THE FABRICATION AND DYNAMIC CHARACTERISTICS OF NOVEL MAGNETIC BUBBLE DEVICES

by

Gerard Ronan

Thesis submitted to
The Victoria University of Manchester
in partial fulfillment of the requirements
for the degree of
Doctor of Philosophy

September 1985.

THE FABRICATION AND DYNAMIC CHARACTERISTICS OF NOVEL MAGNETIC BUBBLE DEVICES

by

Gerard Ronan

Thesis submitted to
The Victoria University of Manchester
in partial fulfillment of the requirements
for the degree of
Doctor of Philosophy

September 1985.

DECLARATION

I declare that no portion of the work referred to in this thesis has been submitted in support of an application for another degree or qualification of this or any other University or other Institution of Learning.

PREFACE

The author graduated from the University of Manchester in 1980 with the degree of B.Sc. (Honours) in Electrical and Electronic Engineering. In 1981 he was awarded the degree of M.Sc. for research on magnetic bubble devices in the above institution. Until 1983 his studies continued towards the degree of Ph.D. with financial support from the Department for Education for Northern Ireland, and following this was awarded a Y.K.K. Japan Scholarship to pursue further research at the Department of Electrical Engineering, Kyushu University, Japan. He returned to Manchester University at the end of 1984 and has recently been appointed to a Royal Society University Research Fellowship.

A Note on Units of Magnetism

Throughout this work the c.g.s. units of magnetism are employed. This, it is felt, is in keeping with the vast majority of internationally-published papers in the field of magnetic bubble devices and physics. A list of commonly-used symbols is included in Appendix 1.1 and, for those who prefer the S.I. nomenclature, standard conversion formulae can be found in Appendix 1.2.

ABSTRACT

Novel concepts in magnetic bubble and related technology have been investigated firstly from a practical point of view by fabrication of current-accessed dual-conductor devices and, secondly, by a theoretical study of domain and domain wall dynamics discussed in the context of a recently-proposed micromagnetic storage method, vertical Bloch line (VBL) memory.

The fabrication of perforated-sheet current-access test devices has involved aluminium - 4% copper sputter deposition, electron beam lithography and dry-etching processes. All geometries for fabrication have been defined using a high-level pattern specification language implemented on the University's CYBER interactive computer rather than photographic methods. Reactive Ion Beam Etching, Reactive Ion Etching, and plasma dry-etching techniques have been evaulated for delineating sub-micron features in the sputtered Al/4% Cu. Test structures of limited quality have been produced together with drive and nucleation circuitry for testing the devices in the DC to 10 MHz range.

Vertical Bloch line memory, in which binary information is coded as a reversal of the domain wall magnetisation rather than by the presence of the domain itself, has been examined in detail. Chip architectures, drive fields and bit-position potential wells have been investigated together with extensive numerical studies of domain wall and Bloch line dynamics. A comparison of VBL-VBL attraction to potential well restoring and drive field gyrotropic forces shows that the originally-anticipated density of 2.0 Gbit/cm^2 will be reduced by

up to a factor of 4. In addition the numerical solution of the equations of motion for a domain wall has been extended for the first time to the three-dimensional case and solved for a translating magnetic bubble. Velocities which include those leading to the punch-through of Bloch curves are simulated, an area of direct interest for the write process in VBL memory.

ACKNOWLEDGEMENTS

I wish to express my thanks to Professor G. R. Hoffman, B.Sc., Ph.D., for providing the facilities within the Department of Electrical Engineering which enabled the work described in this thesis to be carried out. The research was conducted under the overall supervision of W. W. Clegg, M.Sc., Ph.D., to whom I am deeply indebted for his valuable guidance. I shall look forward to working closely with him in the future. The assistance of other members of staff and colleagues is gratefully acknowledged.

Undoubtedly the opportunity provided by Y.K.K. Fasteners Limited, in the form of the Y.K.K. Japan Scholarship Scheme, to study at Kyushu University, Japan, has created one of the most academically and culturally stimulating environments in which I have had the pleasure of working. I am grateful to Y. Fujisaki and A. McKie of Y.K.K. Fasteners Limited, Runcorn, and Dr. J. Richards of the British Council, Tokyo, who ensured the smooth operation of the scholarship scheme and I wish it every success in the future.

Professor S. Konishi of the Department of Electrical Engineering, Kyushu University, Japan, looked after my well-being during my stay at his laboratory. I shall never forget his contagious enthusiasm or the many evenings we spent in discussion. Also the warmth, kindness, and hospitality offered to me by his students and colleagues will remain with me always.

Finally, I thank my parents and sisters, to whom I dedicate this work, for their encouragement when enthusiasm waned.

TABLE OF CONTENTS

5.5 G. Ronan and W. Clegg, "Recent Progress in the Development of Vertical Bloch Line Memory Devices". Paper II, I.O.P. Conference on Current Research in Magnetism, London, April 1985 (unpublished).

5.6 G. Ronan and S. Konishi, "A Three-Dimensional Computer Simulation of a Translating Magnetic Bubble", J. Appl. Phys. Vol. 57(1), pp. 4074-4076, April 1985.

5.7 G. Ronan, W. Clegg and S. Konishi, "Material Considerations for Vertical Bloch Line Memory", To be published, J. de Physique, Sept. 1985.

5.8 G. Ronan, K. Matsuyama, E. Fujita, M. Ohbo, S. Kubota and S. Konishi, "A Three-Dimensional Computer Model of Domain Wall Motion in Magnetic Bubble Materials", To be published, IEEE Trans. Magn., Nov. 1985. (This paper has been extracted from Chapter 4 of this thesis).

CHAPTER I

INTRODUCTION

In the past decade magnetic bubble technology has advanced from initially 92 Kbit devices to the 4 Mbit devices of today. In the continual pursuit of higher performance and density, numerous ingenious schemes of storage and access have been proposed. This thesis presents a study of two such proposals, the perforated-sheet current-access method of propagation which offers potentially an enormous increase in speed of operation and the vertical Bloch line concept of mass memory which promises to be the most dense means of data storage yet considered. This chapter provides a background to magnetic bubble technology and methods of current access propagation. A review of domain and domain wall structures is included from which the VBL concept and methods of VBL study by computer modelling may be considered in subsequent chapters. Finally, in summary, the objectives and organisation of the thesis are described.

1.1 Magnetic Bubble Memory

Magnetic bubbles are cylindrical domains in a thin magnetic film (conventionally epitaxially-grown rare earth garnets) with an easy axis of magnetisation perpendicular to the film plane. These domains are free to move within the film under the influence of externally applied magnetic fields and can represent binary coded data by, in

general, their presence of absence at predetermining storage locations. The technology is now well established, a unique combination of properties (solid state, high density, non-volatile, maintenance-free, low power, radiation hard) making it not just an ideal but in many cases the only choice of storage for certain systems in current use. Magnetic bubbles were first suggested as a computer memory device by Bobeck [1] in the late 1960's although it was not until 1977 that there was a commercial product in the form of a 92 Kbit device from Texas Instruments. After a rather uncertain period in the late 1970's, and early 1980's, when such leading manufactures as Texas Instruments, Rockwell International, National Semiconductor and Plessey Limited stopped production of devices, the magnetic bubble industry has staked out an increasing share of the memory market particularly in portable and airborne equipment. Development and production of bubble memory is now largely dominated by Intel and Motorola in the U.S.A. with strong Japanese competition from Hitachi and Fujitsu. Even though the enormous potential market anticipated in the mid 1970's ($1 billion by 1985) has not been realised, perhaps because bubbles failed to capture the magnetic disc market, the sales are steadily increasing (see Figure 1.1.1) as new uses of bubbles are conceived. In addition, as the major suppliers recoupe their initial investment the cost per bit is decreasing rapidly. This is especially true of the subsystem cost or kit form, as shown in Figure 1.1.2, where higher density single chips and large scale integration of the peripheral support circuitry are making bubble memory more competitive and further widening its potential market.

As well as these commercial manufacturers of bubble devices there

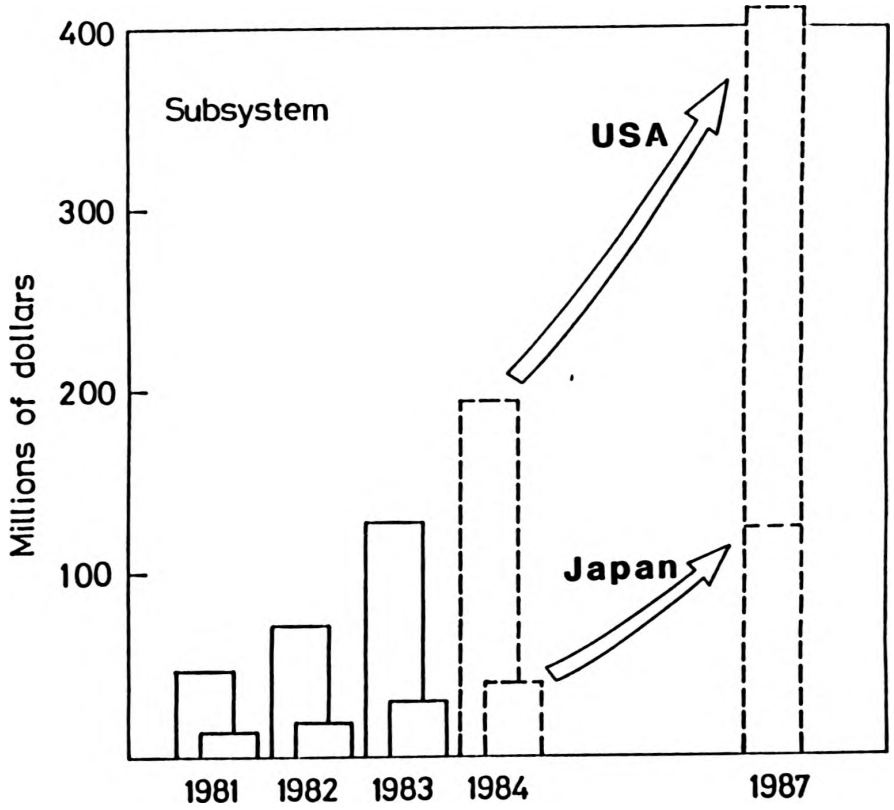

Fig.1.1.1 Sales of bubble memory subsystems.
(Electronics, Jan.12, 1984.)

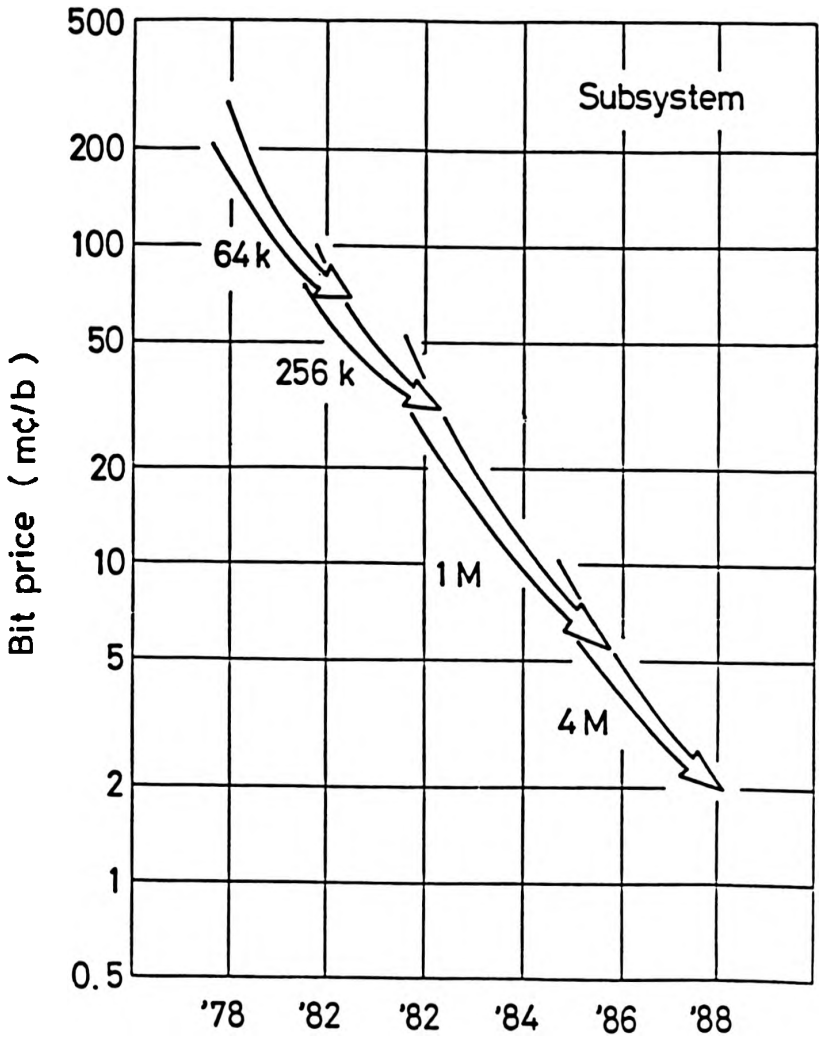

Fig.1.1.2 Bit price of bubble memory subsystems. (After Orihara(33))

are a few smaller concerns producing limited quantities of specialised devices for in-house or military use. In Japan N.E.C. fabricate small numbers of a novel 1 Mbit device which incorporates an on-chip cache memory organisation with an average apparent access time of 2ms and are in the design stages for a 4 Mbit memory [2]. SAGEM of France, who had a second source agreement with National Semiconductor before the latter company retired from the bubble device market, are still supplying military and aerospace applications and have recently started commercially second-sourcing Motorola's 1 Mbit memory. They are also working in conjunction with the French government research laboratories, L.E.T.I., on a 4 Mbit device [3]. Sperry Corporation of the U.S.A. have a small research effort working towards a very high speed (20MHz) high density (8 Mbit) memory which was initially intended for space applications [4]. The Computer Control Institute of the U.S.S.R. was known to be producing 256K bit devices in 1981 [5] presumably for military use although few details on specification or production levels are available. Supplementing this industrial research are large numbers of academic research teams mainly, as one would expect, in Universities of the U.S.A. and Japan, and also in Germany, France and China as well as here in the U.K.

The largest capacity single chip devices now available (in sample quantities at the time of writing) are 4 Mbit memories from Hitachi, Fujitsu and Intel. Typical specifications (Fujitsu FBM64DX, 4 Mbit, 100 kHz bubble memory) are 12.5ms average time to access and an operating power dissipation of 0.26μW per bit. Research on the 16 Mbit device appears to be in an advanced stage of development [6] and sample quantities are expected to become available in 1987. Perhaps

one of the most potentially useful recent advances in bubble technology is the novel package of Hitachi [7]. With careful drive coil and field homogenizer design, a 70% reduction in packaged volume (4 Mbit device) has been achieved with a similar reduction in weight. The package is intended for automated assembly which should ease existing constraints on manufacture. Cost is estimated at being at least comparable and probably less than that of a conventional device.

All commercial devices at this time are of the rotating-field-accessed type. Propagation is brought about by the sequential magnetisation of parts of a repetitive thin-film soft magnetic alloy (permalloy) pattern under the action of an externally-applied rotating in-plane field (typically at a rotational frequency of 100-250 kHz). Input of data is by nucleation of a new bubble, either by a current pulse in a conductor 'hairpin' which locally reverses the material magnetisation or by a stretch and cut action on a seed bubble, again by a current pulse in a conductor. The most common method of detection is by the magnetoresistive effect in a magnetic conductor which causes a change in its electrical resistance when the conductor experiences the external field of a magnetic bubble in its vicinity. Since the net resistance change increases with affected conductor length, bubbles are stretched for stronger signals. The rotating in-plane field will also cause a magnetoresistive change and so dummy detectors are included in a bridge configuration for common-mode rejection. Bubble detection is therefore costly in chip area accounting for about 5% of available space. Memory architecture is typically a block-replicate major-minor loop configuration. Data is sequentially input into a major track and transferred in parallel to a series of minor loops,

these constituting the main storage area. Several spare minor loops are included to provide for redundancy so that the design will be tolerant of defects which might make some of the minor loops inoperative. For non-destructive read, data is replicated, again in parallel, to another major track and sequentially detected. Operation of such a major-minor architecture may be considered somewhat analogous to track and sector organisation of a rotating disc medium.

The most likely successor to permalloy overlay as a propagation pattern is ion-implantation [8]. Here the repetitive propagation pattern is achieved by changing the charcteristics of the top surface of the magnetic medium which supports the bubbles, using typically H_2^+ or He^+ ion bombardment, leaving the exposed areas with in-plane easy axis of magnetisation. Application of a rotating in-plane field sequentially magnetises parts of the pattern thereby propagating a bubble domain. The main advantage of ion-implantation is the closer coupling between bubble and propagation pattern and relaxation of the minimum feature size for fabrication (see Figure 1.1.3) which is rapidly becoming a limiting factor on maximum device densities.

Conventional field-accessed devices are limited in speed of operation to around 250 kHz because of the difficulty of driving the inductance of the drive coils. An alternative proposal for propagation using the current-accessed perforated sheet scheme of Bobeck et al [9] removes this restriction and has been shown to operate at frequencies in excess of 10 MHz. The limiting feature of this technology is power dissipation which may be excessive at high densities. This scheme is, however, well suited to advanced

these constituting the main storage area. Several spare minor loops are included to provide for redundancy so that the design will be tolerant of defects which might make some of the minor loops inoperative. For non-destructive read, data is replicated, again in parallel, to another major track and sequentially detected. Operation of such a major-minor architecture may be considered somewhat analogous to track and sector organisation of a rotating disc medium.

The most likely successor to permalloy overlay as a propagation pattern is ion-implantation [8]. Here the repetitive propagation pattern is achieved by changing the charcteristics of the top surface of the magnetic medium which supports the bubbles, using typically H_2^+ or H_e^+ ion bombardment, leaving the exposed areas with in-plane easy axis of magnetisation. Application of a rotating in-plane field sequentially magnetises parts of the pattern thereby propagating a bubble domain. The main advantage of ion-implantation is the closer coupling between bubble and propagation pattern and relaxation of the minimum feature size for fabrication (see Figure 1.1.3) which is rapidly becoming a limiting factor on maximum device densities.

Conventional field-accessed devices are limited in speed of operation to around 250 kHz because of the difficulty of driving the inductance of the drive coils. An alternative proposal for propagation using the current-accessed perforated sheet scheme of Bobeck et al [9] removes this restriction and has been shown to operate at frequencies in excess of 10 MHz. The limiting feature of this technology is power dissipation which may be excessive at high densities. This scheme is, however, well suited to advanced

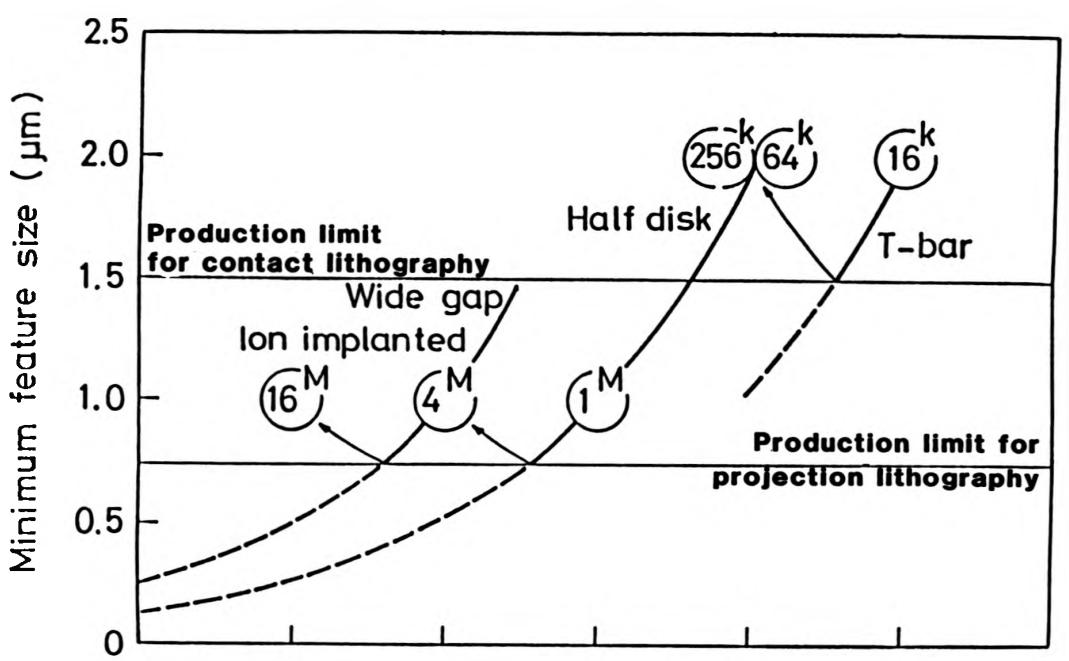

Fig.1.1.3 Projection of minimum feature size with increasing device density. (After Orihara(33))

architectural designs and will be considered in the succeeding sections.

Large increases in device density beyond 16 Mbits are unlikely using conventional technology due to the small (0.5μm) bubble diameter and sub-micron minimum feature size for fabrication. A recent proposal by Konishi [10] has suggested a memory scheme which uses the presence or absence of a vertical Bloch line (VBL) pair in the wall of a magnetic stripe domain to denote binary information as illustrated in Figure 1.1.4. VBL memory shares certain common features, materials, and fabrication processes with conventional bubble devices and is therefore, in principle, an extension of this technology. Because the wall structure is intrinsically of a finer scale than the volume of a domain, substantial increases in storage density (X20) are likely. The development of this novel technology is as yet in the initial stages and even on the most optimistic projections is unlikely to reach a commercial status before the end of the decade. Detailed examination of this concept and projections of performance are considered in Chapter 3.

1.2 Current-Access Magnetic Bubble Memory

The very earliest experiments to control bubble motion used currents in conductors [1]. Copeland et al [11] later employed a meandering conductor with etched stable bubble positions. The first perforated sheet design was proposed by Walsh and Charap [12] although this was not taken up seriously until reintroduced by Bobeck et al [9]. Bubble lattice memory [13], which uses two different bubble types to code data, also used conductors to move bubbles and

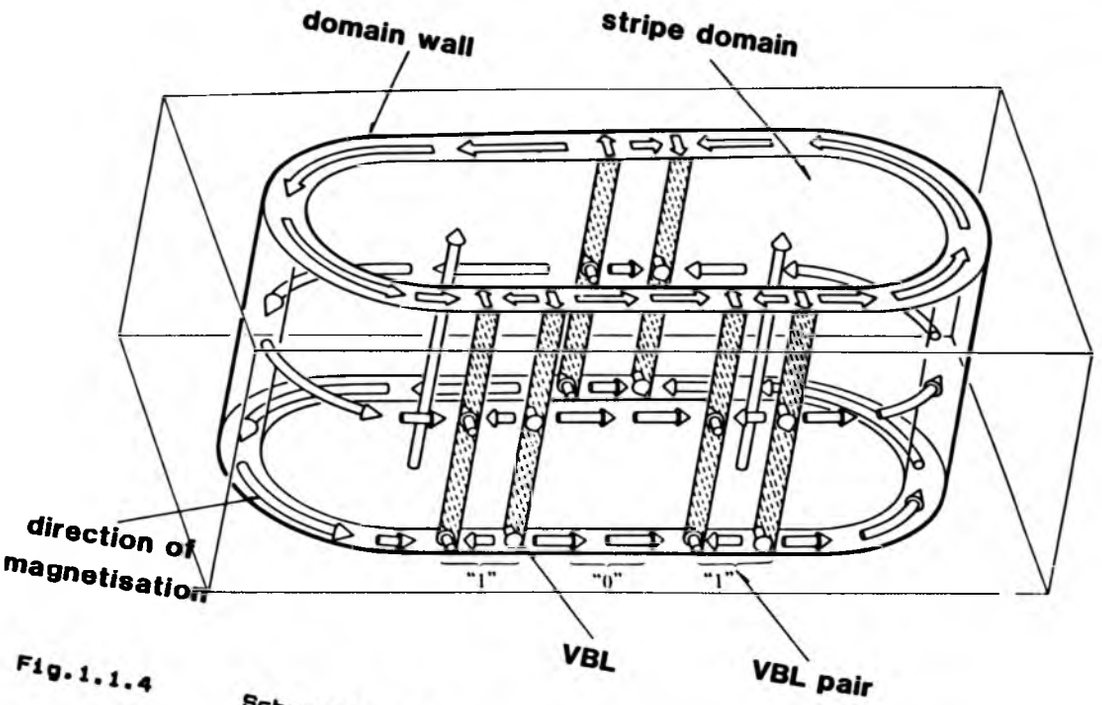

Fig.1.1.4 Schematic of the vertical Bloch line memory concept. (After Konishi and Hidaka(90))

although this has been largely abandoned, recent work by Nelson et al [14] describes a novel approach which appears encouraging for the technology. Advantages of hybrid structures such as field-access minor loop and current-access major loop have been demonstrated by Dekker et al [15] and Takahashi and Urai [16]. Reduction in access time, error rates and power dissipation are possible using such a scheme.

Nowadays due to lower power requirements and relaxation of fabrication process, the meandering conductor has been replaced by apertured-conductor methods as the most promising propagation pattern. A rectangular slot in a conductor sheet as shown in Figure 1.2.1 will distort an otherwise uniform current creating opposite magnetic poles orthogonal to the current flow. These poles will result in one stable and one unstable bubble position similar to a permalloy bar in a magnetic field. Using multilayer conductors with offset apertures and appropriate relative phasing of the currents a travelling potential well can be formed thereby propagating a bubble. Alternatively a single layer approach with a circulating current can produce a travelling potential well in chevron-shaped apertures [9]. Of the multitude of propagation schemes and aperture profiles possible, the dual-conductor rectangular-aperture approach is the most widely studied [17 - 18] and is to be discussed in this work.

There are two classifications of apertured sheet bubble propagators, those that propagate parallel and those that propagate perpendicular to the current flow. Generally a major line runs orthogonal to the minor loops, therefore both types are necessary. These are illustrated in Figure 1.2.2 together with the required current sequences. Propagation parallel to the current flow is

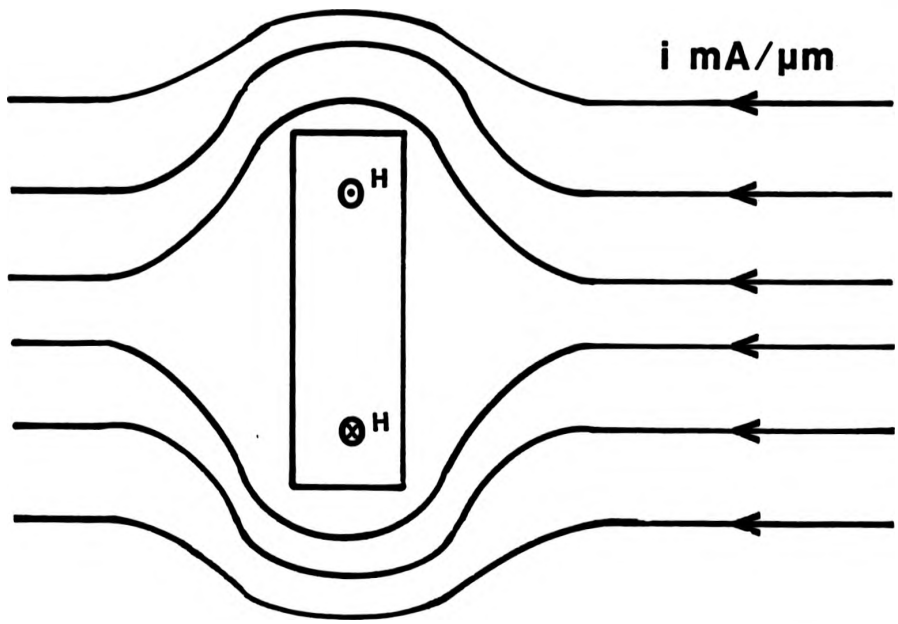

Fig.1.2.1 Current flow around an aperture creating a magnetic dipole.

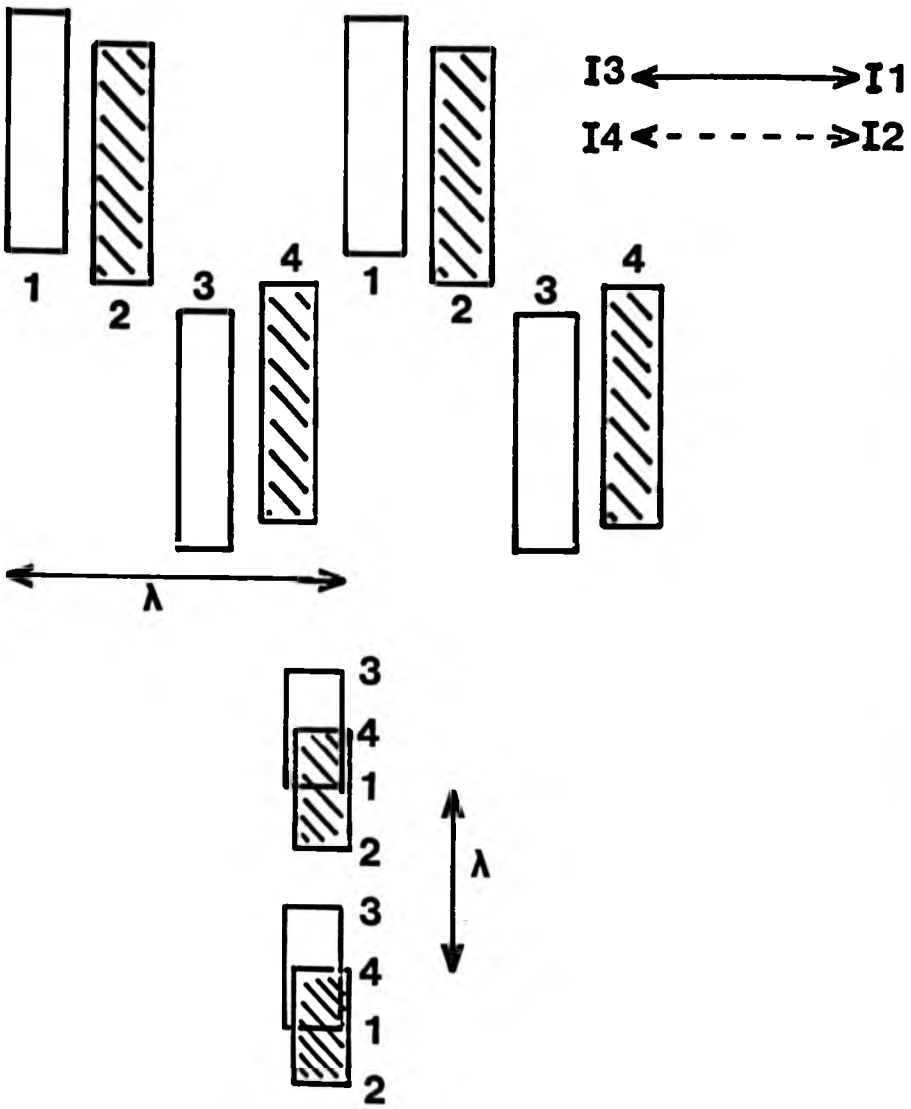

Fig.1.2.2 Propagation parallel (top) and perpendicular (bottom) to the current flow. The shaded regions correspond to apertures in the second conductor level through which I2,I4 flows. The apertures are slightly offset for clarity.

improved if the apertures have a large aspect ratio and are slightly staggered as shown. This however results in a unidirectional propagation pattern.

Propagation perpendicular to the current flow is bidirectional. The optimum aperture shape in this case for a period λ is described by Bobeck et al [9] as 0.3λ by 0.5λ. It should also be apparent that the maximum tolerable layer to layer misalignment of apertures is 0.25λ. Circuit period λ is nominally four times the bubble diameter to reduce bubble-bubble interactions. This gives a minimum feature size for fabrication as being of the order of bubble diameter which is a considerable improvement over permalloy or ion implanted schemes.

The main attraction of current access propagation is the comparatively fast speed of operation. Field-accessed devices are limited to around 250 kHz by the inductance of the orthogonal coil set and need high volt-ampere drivers. In contrast current-accessed circuits can operate from low voltage (5V) supplies and have demonstrated speeds in excess of 10 MHz [19]. It has been shown however, that even with comparatively low drive current densities ($\sim$ 1mA/μm) power dissipation at high device densities may be excessive [20 - 21]. Various methods of reducing power consumption have been described such as partitioning the chip area and using separable drivers although this would increase the silicon overheads for control. Bubble manufacturers are understandably conservative after a rather shaky period in the late 1970's and early 1980's and for the most part designs which increase device complexity have not been welcomed. Research in the Sperry Corporation has, however, adopted a novel approach to power consumption [22]. A

self-structured design using two bubble states to code data permits a closely-packed propagation track ($\lambda \approx 2$ to 2.5 times bubble diameter). For a given density this scheme can therefore use a material with a lower saturation magnetisation thereby reducing power requirements. (< 2 Watts for an 8 x 1 Mbit, 12 MHz device). The closely-packed stream of bubbles has the additional effect of pushing bubbles through otherwise unpassable defects in either the fabrication pattern or the garnet crystal. While this would obviously increase fabrication yield it also suggests that on-chip redundancy could be eliminated, and, as the redundancy control electronics represents a significant (≈ 60%) proportion of the control circuitry, greatly simplify device design and usage. It would appear therefore to have several advantages over previous designs and it will be interesting to see if it will eventually become a marketable product within the next few years as anticipated [23].

Introduction of perforated sheet technology has also brought a revival of magnetic bubble logic. From the earliest days of the technology, it has been realised that the mutual repulsion between bubbles could be used to switch bubbles between tracks and several magnetic logic circuits using permalloy overlays were developed [24 - 25]. With the current-access approach the complex non-linear interactions between the bubble and magnetic overlay are removed allowing greater control. In addition a more precise mathematical treatment is possible which is advantageous for both propagation [26] and logic design [27]. Wu et al [28] have recently fabricated eleven logic elements including XOR/AND, AND/OR, COMPARATOR, LATCH etc., using dual-layer perforated sheet technology. Two practical

applications have been implemented in experimental devices, a bubble string-pattern matcher [29] and a content-addressable memory [30]. There is a high degree of parallelism inherent in such devices providing a 2-3 order of magnitude increase in speed as compared to disk systems, an advantage which increases with data base size. These workers feel that without this approach to memory management such ultra-high density devices as VBL memory will not be practical due to I/O bottlenecks [31]. The reluctance to increase device complexity expressed by most bubble memory manufacturers [31 - 35] has so far resulted in no commercial applications. Notable exceptions are N.E.C., Japan, [36] who have produced small quantities of a cache bubble memory and Sperry Corporation, U.S.A. [23] who anticipate using the saving on silicon overheads mentioned above to enhance memory operation.

A further use of current-accessed propagation is in the proposed major-minor loop organisation of VBL memory (see Chapter 3). Data is coded by reversals of domain wall structure called Vertical Bloch Lines and a rotating in-plane field would adversely disturb them. It is essential to the successful operation of such a memory that the major track, which propagates bubbles, be current access. Work on such a device is still in the elementary stages and though dual-conductor perforated-sheet technology may be adequate, meandering conductors could possibly offer an advantage as will be dicussed in Chapter 3.

1.3 Magnetic Bubble Domains and Domain Wall Structures

1.3.1 Magnetic bubble domains

Magnetic bubbles [37] are cylindrical domains in a thin film of magnetic material, such as rare earth doped garnet, where the preferred magnetic axis is normal to the film plane, the misnomer 'bubbles' coming from their circular appearance when viewed under a microscope using polarised light and the Faraday effect. It was by such optical techniques operated stroboscopically [38] that much of the early device research was undertaken. Structures internal to the domain wall such as Bloch lines are difficult to observe, therefore it is anticipated that mathematical modelling will play a much more significant role in early research in vertical Bloch line memory. In order to familiarise the reader with the basic concepts and terminology of the dynamics of domains and twisted domain wall structures a brief review is included at this stage. For more detailed information the text of Malozemoff and Slonczewski [39] is strongly recommended.

Bubble materials are characterised by a thickness, h (cm); spontaneous magnetisation, M (gauss); exchange constant, A (erg/cm); uniaxial anisotropy constant, K (erg/cm^3); damping parameter, α (dimensionless); and gyromagnetic constant, γ (Oe^{-1} s^{-1}). In addition there are general relationships which a material suitable to support magnetic bubbles must satisfy. Firstly the quality factor Q ($= K/2\pi M^2$) should be greater than one, the significance of which is that the domain magnetisation lies perpendicular to the film plane. Secondly the material coercivity should be very low ($Hc/4\pi M < 0.05$).

This is essential for bubble devices where domains must travel freely within the magnetic medium at low field gradients. Also if coercive loss for example, due to 'pinning', is dominant, domain wall motion tends to be irregular and unpredictable. In the following theoretical framework the coercive field is often assumed to be zero. Finally, the material thickness is comparable to the zero field domain width. Here another parameter, the characteristic material length, l (= $(AK)^{\frac{1}{2}}/\pi M^2$), is introduced where 8l is approximately the zero field domain width.

In the absence of external fields, such a magnetic film will be composed of serpentine (stripe) domains, half with their magnetisation directed parallel and the other half anti-parallel to the film normal which is the 'easy' axis of the material (see Figure 1.3.1a). When a static mangetic field is applied normal to the film plane the region with magnetisation in the direction of applied field will grow at the expense of the other until beyond a critical value the constricted domains will run-in to form cylindrical domains or magnetic bubbles (Figure 1.3.1b-c). A further increase in applied field will decrease the bubble diameter until it collapses leaving the material saturated in one direction. Decreasing the applied field will spontaneously restore the stripe domains and the process can repeat. In general the static dimensions of any domain configuration can be obtained by a minimisation of energy terms or a balance of forces. Ignoring for the present internal domain wall structures, the relevant energy terms are domain wall energy, applied field energy and magnetostatic energy.

Domain wall energy arises from the transition between regions of one direction of magnetisation to another (which we shall henceforth

This is essential for bubble devices where domains must travel freely within the magnetic medium at low field gradients. Also if coercive loss for example, due to 'pinning', is dominant, domain wall motion tends to be irregular and unpredictable. In the following theoretical framework the coercive field is often assumed to be zero. Finally, the material thickness is comparable to the zero field domain width. Here another parameter, the characteristic material length, l (= $(AK)^{\frac{1}{2}}/\pi M^2$), is introduced where 8l is approximately the zero field domain width.

In the absence of external fields, such a magnetic film will be composed of serpentine (stripe) domains, half with their magnetisation directed parallel and the other half anti-parallel to the film normal which is the 'easy' axis of the material (see Figure 1.3.1a). When a static mangetic field is applied normal to the film plane the region with magnetisation in the direction of applied field will grow at the expense of the other until beyond a critical value the constricted domains will run-in to form cylindrical domains or magnetic bubbles (Figure 1.3.1b-c). A further increase in applied field will decrease the bubble diameter until it collapses leaving the material saturated in one direction. Decreasing the applied field will spontaneously restore the stripe domains and the process can repeat. In general the static dimensions of any domain configuration can be obtained by a minimisation of energy terms or a balance of forces. Ignoring for the present internal domain wall structures, the relevant energy terms are domain wall energy, applied field energy and magnetostatic energy.

Domain wall energy arises from the transition between regions of one direction of magnetisation to another (which we shall henceforth

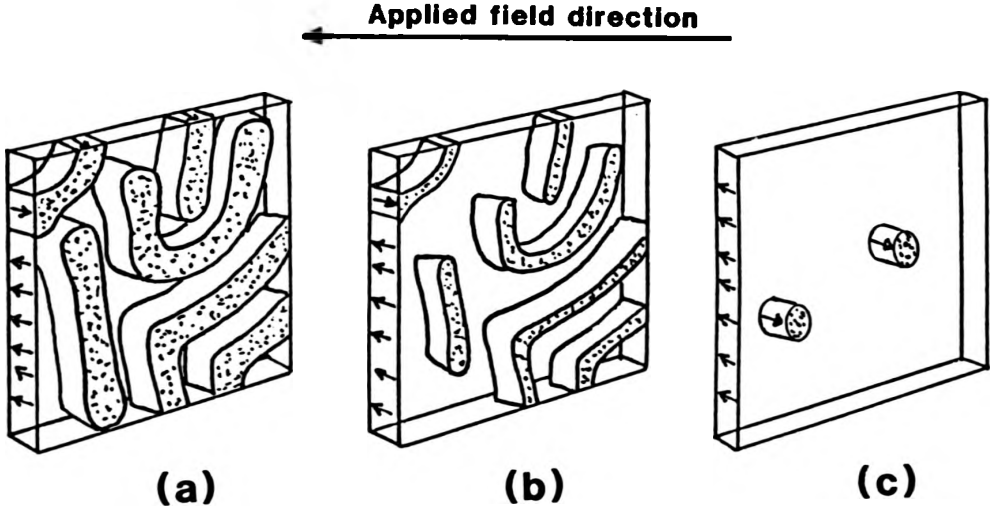

Fig.1.3.1 Domain structures in magnetic garnet materials at a) zero, b) medium, and c) high external field applied normal to the film surface. With further increases in the field the bubble domains seen in (c) collapse and the whole film is saturated in the field direction.

refer to as +Z and -Z directions) resulting in a wall region with magnetisation directed away from the easy axis. This energy is proportional to the wall area and is characterised by a wall energy density $\sigma_0 = 4(AK)^{\frac{1}{2}}$ erg/cm^2. This energy will exert a force per unit area for the case of a bubble, radius r, of σ_0/r tending to reduce the wall area i.e., collapse the bubble.

Applied field energy is proportional to the domain volume and therefore in the case of a bubble domain (magnetised antiparallel to the applied 'bias' field) it acts to compress the bubble. Consider a domain wall which moves δx under the influence of an applied field H. As the domain wall moves, magnetisation reverses, i.e., changes by 2M, and the domain volume increases by δx times the wall area. The energy per unit area increases, therefore, by 2MH δx which may be considered as a force per unit area of simply 2MH.

Magnetostatic energy arises from the interaction between the magnetisation within the domain and the internal fields produced by the domain itself (self-demagnetisation) and surrounding material. It depends in a non-linear manner on the domain size and shape. It acts in opposition to the other forces considered, to expand the domain so as to achieve a demagnetised state in zero external applied field with 50% of the material magnetised in +Z and 50% in -Z. This often proves to be the most difficult term to quantify, but for the case of a bubble the force per unit area acting on the domain wall arising from the magnetostatic energy term may be represented for many purposes by the simplified Thiele force function [40] as

$$\text{Force/unit area} = -8\pi M^2 (1 + 3r/2h)^{-1} \qquad .....1.3.1$$

The equilibrium radius of a bubble is obtained by a balance of forces acting on the domain wall, i.e.,

$$2MH + \sigma_o/r - 8\pi M^2 (1 + 3r/2h)^{-1} = 0 \qquad .....1.3.2$$

This is a quadratic in r which, provided H is within the range of run-out (i.e. bubble to stripe transition) to collapse field, generally gives two solutions, the larger of which is stable. It is often useful to normalise these forces to the applied field magnitude (divide by 2M) and consider effective fields i.e., a surface tension effective field tending to reduce wall curvature, a demagnetising field tending to expand the domain and the externally applied field itself.

Although equation 1.3.1 is useful in simple calculations, a much more general method of calculating the magnetostatic energy or demagnetising field of an arbitrarily-shaped domain is necessary. A versatile approach to this is the equivalent current model of O'Dell [41]. The theory of electromagnetism does not specify the atomic nature of matter and thus we may accurately represent the magnetisation of a material by a large number of elementary equivalent currents which cancel at all points but the domain wall. The demagnetising field may be derived from a current density of 2i emu/cm circulating on the domain wall (i for the closed domain plus i for the surrounding domain). i is given from the definition of magnetism in cgs units as i = M emu/cm. The demagnetising field at a given point on the domain wall is given by integrating Biot-Savart's law over the wall surface.

Similarly, when considering a domain of arbitrary shape the

surface tension effective field derived from wall energy must be calculated using the local radius of curvature of the domain wall. This can be shown by simple trigonometry to be the second order partial differential of wall position, y, at the given point, i.e.,

$$\text{Surface tension effective field} = \frac{\sigma_0}{2M} \nabla^2 y \qquad \ldots\ldots 1.3.3$$

The y axis is assumed normal to the domain wall. Both these techniques are particularly suited to finite element calculations and will be discussed in greater detail in Chapter 4.

Should the three forces or effective fields not balance then the domain will obviously move or change size. In an externally-applied vertical field gradient the bubble will move with a velocity of,

$$v = (\mu_w \Delta H) \quad \text{m/sec} \qquad \ldots\ldots 1.3.4$$

where ΔH is the bias field difference across the bubble radius and μ_w ($= (\gamma/\alpha)(A/K)^{\frac{1}{2}}$) is the domain wall mobility.

1.3.2 Domain wall structures

So far we have considered domain walls merely as surfaces with an associated energy density. A wall is, however, a continuous three-dimensional transition region through which the magnetisation vector $\vec{M}$ changes from pointing in the +Z to the -Z direction or vice-versa and as such has a variety of possible twist structures. The preferred configuration of the domain wall is, as before, simply a minimisation of the relevant energy terms which may be considered as a balance of forces or torques on $\vec{M}$. The width of the transition

region is a compromise between uniaxial anisotropy favouring an abrupt change with magnetisation always in the preferred perpendicular orientation, and exchange stiffness which favours a gradual rotation. Minimising exchange and anisotropy energies, one solution is given for a wall in the YZ plane as (Ref. 39, Chapter 7)

$$\phi(y) = \text{constant} \qquad \text{.....1.3.5}$$

$$\theta(y) = \pm 2 \arctan \exp (y/\Delta_0) \qquad \text{.....1.3.6}$$

where

$$\Delta_0 = (A/K)^{\frac{1}{2}} \qquad \text{.....1.3.7}$$

and ϕ, θ are the polar co-ordinates of magnetisation measured from the X and Z axis respectively. Including local magnetostatic energy, the minimum wall energy occurs when $\phi(y) = 0, \pi$ i.e., when magnetisation lies in the plane of the wall. This is called a 'Bloch wall' and corresponds to a screw rotation in either a clockwise or anticlockwise direction through the wall, as shown in Figure 1.3.2a. This sense of rotation is known as the wall chirality. Most of the transition occurs within a width $\pi\Delta_0$, as shown in Figure 1.3.2b, where Δ_0 is known as the wall width parameter. At this point it is instructive to note that $\theta(y)$ may be substituted by wall position, y, defined at the wall centre, $\theta = \pm \pi/2$, and

$$\frac{\partial\theta}{\partial y} = \Delta_0^{-1} \qquad \text{.....1.3.8}$$

$$\dot{\theta} = \frac{d\theta}{dt} = \frac{\partial\theta}{\partial y} \cdot \frac{\partial y}{\partial t}$$

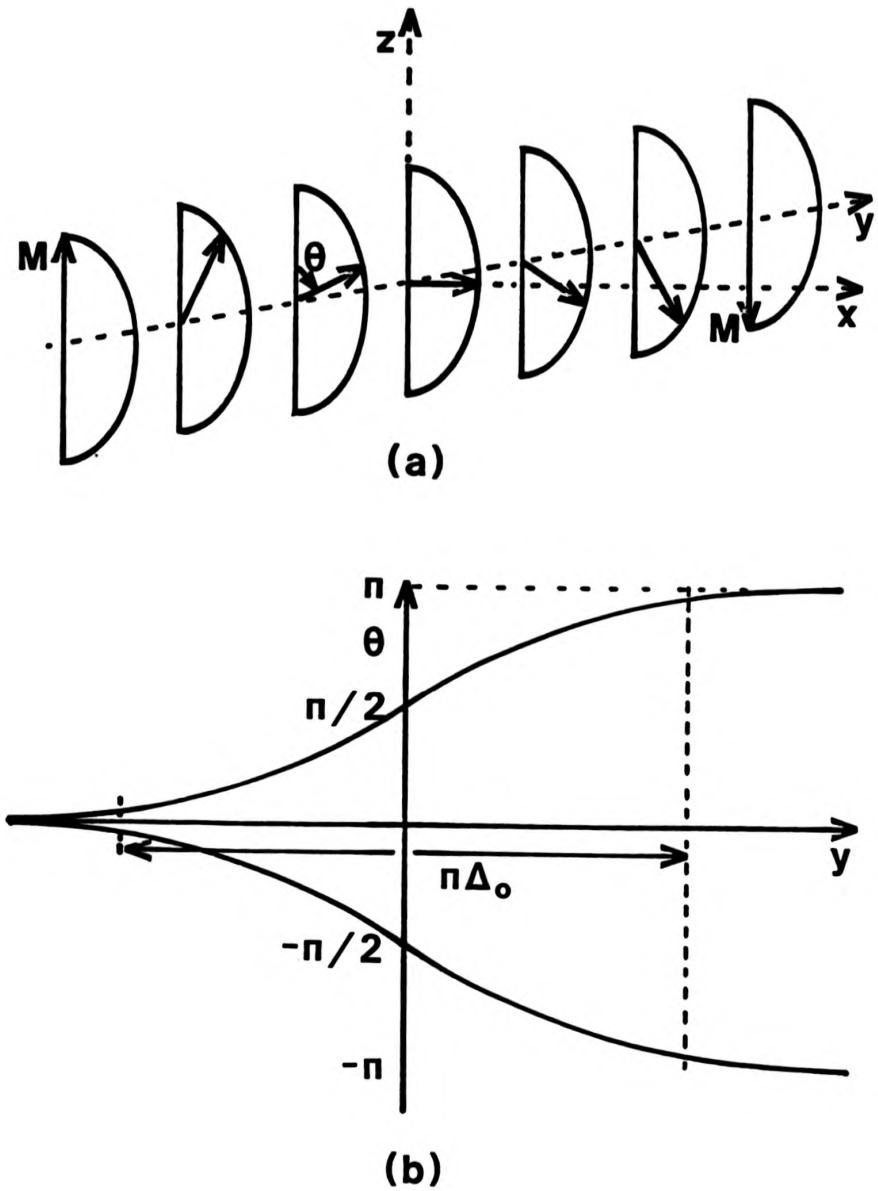

Fig.1.3.2 a) Rotation of magnetisation through a Bloch wall, b) Variation of magnetisation polar angle (θ) through the wall thickness. The two possible chiralities of Bloch wall are shown.

$$= \Delta_o^{-1} \dot{y} \qquad \text{.....1.3.9}$$

It is often useful, especially when determining wall dynamics, to consider only the wall centre position and magnetisation structure at that position.

Under the influence of an external in-plane field, Hp, ϕ deviates from the plane of the wall towards the azimuthal angle of Hp. The degree to which ϕ deviates from the plane of the wall depends upon the magnitude of Hp and is given for Hp perpendicular to the wall as

$$\phi = \arcsin(Hp/8M) \qquad |Hp| < 8M \qquad \text{....1.3.10}$$

$$= \pm \pi/2 \qquad |Hp| \geq 8M \qquad \text{....1.3.11}$$

For $|Hp| \geq 8M$ the magnetisation rotates through the wall in a head-on fashion forming what is called a 'Neel wall'. As |Hp| decreases the wall magnetisation gradually returns to the plane of the wall (see Figure 1.3.3). It should also be apparent that as the Neel wall structure is a higher energy transition the wall width will reduce somewhat.

The boundary conditions of an isolated domain wall are at the film surfaces. Using the equivalent current model the demagnetising field of a planar wall, Hy, (often called the in-plane stray field) can be shown to be perpendicular to the wall and is given approximately by,

$$Hy(Z) = 4M \ln [Z/(h-Z)] \qquad \text{....1.3.12}$$

(This is calculated for a bubble domain in Chapter 4). Hy is zero at the film centre, $Z = \frac{1}{2}h$, and logarithmically diverges in opposite

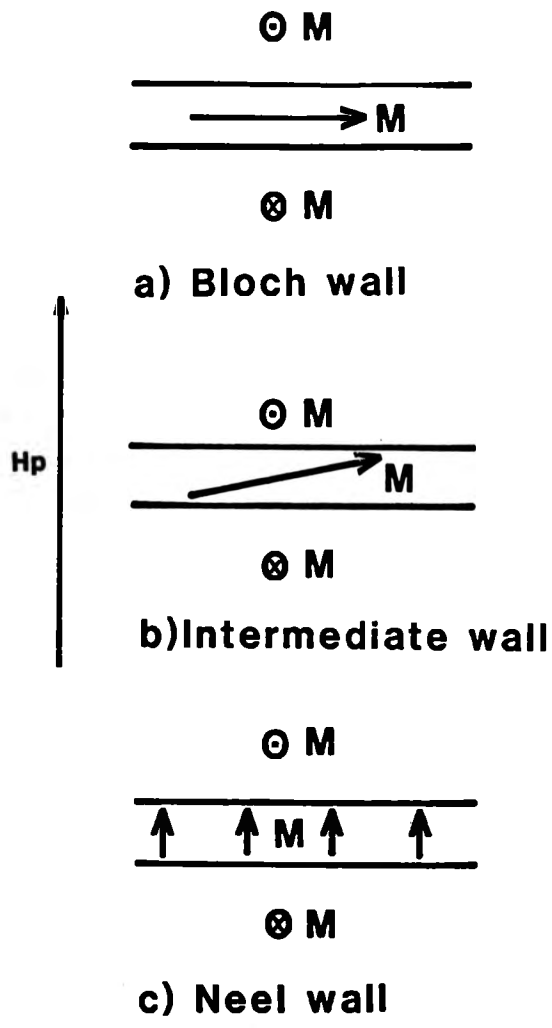

Fig.1.3.3 The wall structures for an in-plane field, Hp, a) zero, b) $|Hp| \leq 8M$, c) $|Hp| \geq 8M$.

directions near the two surfaces. (This model is only accurate at a distance > $\pi\Delta$ from the surfaces). From the inequality of equation 1.3.11 it can be seen that Neel wall orientations are preferred when

$$0 < Z < h/(1 + e^2) \qquad ....1.3.13$$

and $$he^2/(1+e^2) < Z < h \qquad ....1.3.14$$

where $Z = h/(1 + e^2)$ and $Z = he^2/(1 + e^2)$ are the 'critical points'. The angle of wall magnetisation, ϕ, therefore rotates by 180^o through the film thickness, as shown in Figure 1.3.4, and has two senses of rotation corresponding to the different Bloch wall chiralities.

The transition region between Bloch walls of opposite chirality is known as a Bloch line. The static configuration is perpendicular to the film plane, minimising its length and energy, and is known as a vertical Bloch line (VBL). Experimental confirmation of such a structure has been demonstrated by Lorentz microscopy [42]. Minimising local exchange and magnetostatic energies the static structure is given at the centre of a wall in an infinite X-Z plane as,

$$\phi(x) = \pm 2 \arctan \exp (x/\Lambda_o) \qquad ....1.3.15$$

where Λ_o is known as the Bloch line width parameter, defined as:

$$\Lambda_o = (A/2\pi M^2)^{\frac{1}{2}} \qquad ....1.3.16$$

This is the same form as equation 1.3.6 for a domain wall transition region where most of the 180^o rotation occurs within $\pi \Lambda_o$. The

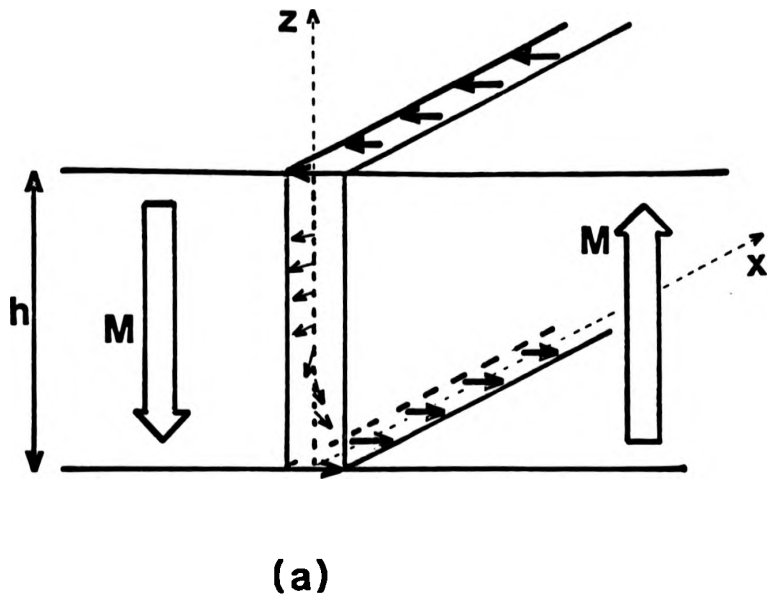

(a)

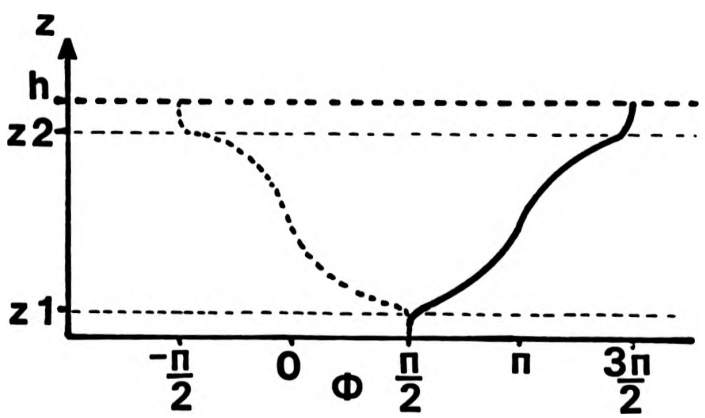

(b)

Fig.1.3.4 a) Rotation of azimuthal angle of magnetisation (ϕ) at wall centre through the material thickness due to the stray field at the film surfaces. b) Variation of ϕ with position through the thickness. The Bloch wall of opposite chirality is included in dotted line and the critical points, Z1 and Z2, are marked.

Bloch line width parameter is independent of uniaxial anisotropy as anisotropy energy is constant along the X axis. In the same way that a wall has chirality, a vertical Bloch line will have one of two possible directions of twist classed as positive and negative. These are defined in Figure 1.3.5, with ϕ increasing for a positive and decreasing for a negative Bloch line, moving anticlockwise round a closed domain of -Z magnetisation. There must always be zero or an even number of Bloch lines in a domain as ϕ must be continuous on the wall. Whereas Bloch lines of opposite polarity can combine to give a net zero twist, Bloch lines of like polarity cannot as compression only serves to increase the exchange energy between them. When the effect of stray field is included, the structure of Figure 1.3.6 is obtained, where the vertical Bloch line consists of a 2π rotation at one surface, zero at the other and a gradual transition at intermediate stages. Although it is often useful to consider the thickness averaged form, it should be remembered that it is a three-dimensional structure with the 'head' (2π rotation) and 'tail' (zero rotation) being unlikely to behave dynamically in an identical manner.

Similarly Bloch lines of some form will occur anywhere there is a transition between Bloch walls of opposite chirality. A horizontal Bloch line (HBL) is shown in Figure 1.3.7 lying parallel to the X axis separating opposite Bloch wall chiralities above and below it. The corresponding plot of ϕ through the thickness, Figure 1.3.7b, illustrates the HBL separating the two minimum energy contours of the Bloch wall chiralities. The total rotation of ϕ in a HBL and therefore the Bloch line energy is a function of position through the thickness. As such a HBL is not generally a statically-stable

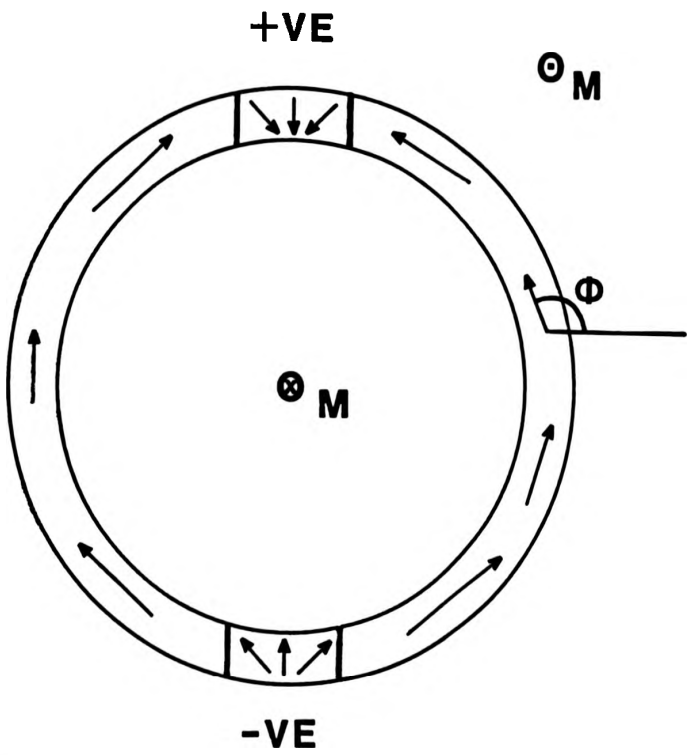

Fig.1.3.5 Definition of positive and negative vertical Bloch lines in the wall of a bubble domain.

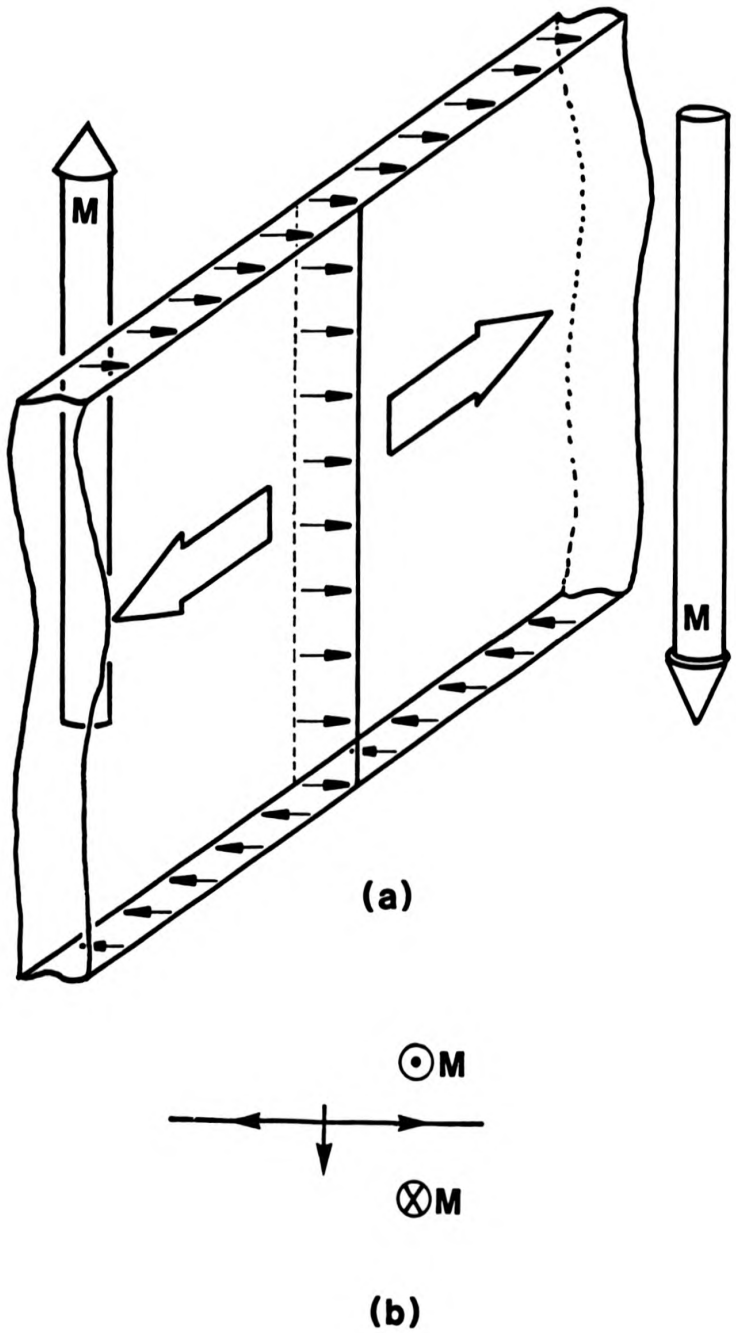

Fig.1.3.6 a) Cross section of a VBL, b) thickness averaged representation of a VBL.

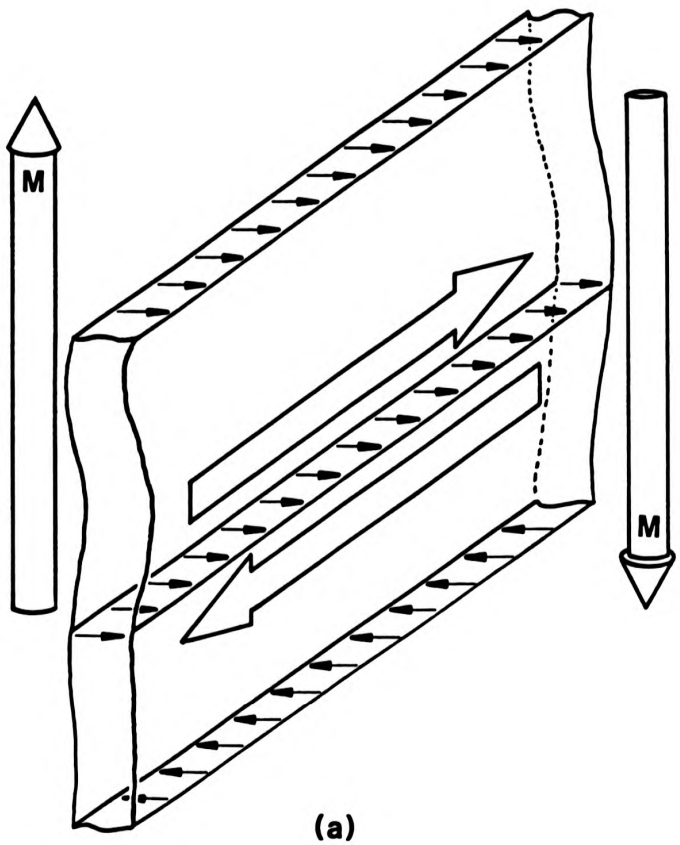

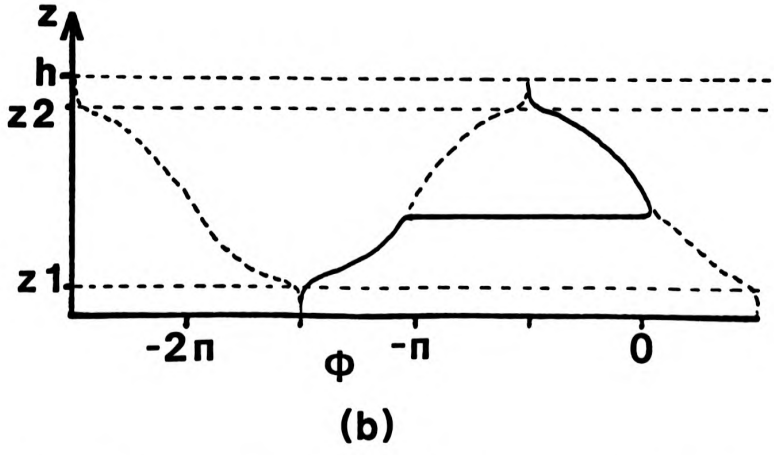

Fig.1.3.7 a) Cross section of a domain wall with a horizontal Bloch line, b) Rotation of azimuthal angle of magnetisation at the wall centre, ϕ, through the film thickness with a HBL in the wall.

structure and in the absence of externally applied forces (in-plane fields or gyrotropic forces) would receed to the critical point at which there is a zero twist (Z2 in Figure 1.3.7b). A HBL at the centre of the film with a net twist of π would be of the same form as equations 1.3.15, and 16 with Z replacing X. Should sufficient energy be applied to the wall such that the HBL reaches the critical point at which there is a 2π twist, two possibilities occur. Firstly, as is more likely in thicker films, a second HBL can nucleate and travel in the opposite direction towards the other critical point, or, secondly, the magnetisation at the film surface spontaneously flips through 2π leaving a Bloch wall of now completely-opposite chirality. The latter process is known as 'punch-through' and is an important phenomenon in wall dynamics.

While examining a HBL, the discussion has so far been limited to plane walls such as those running the length of a stripe domain. Including a curved wall, such as that in a stripe domain head or a bubble domain, the component normal to the wall of any externally applied force arising from in-plane fields or perpendicular field gradients will vary around the curved wall. At those points where the applied field component drops to zero any horizontal Bloch line would receed to a critical point. Thus one arrives at the structure of Figure 1.3.8 with a Bloch curve separating the opposite Bloch wall chiralities. Following the previous discussion, should the Bloch curve reach the critical point corresponding to a 2π rotation a punch-through process can occur. This will however only occur at the 'top' of the Bloch curve leaving one section of the wall with a completely reversed wall chirality. The flanks of the Bloch curve will now prefer a perpendicular orientation minimising the total

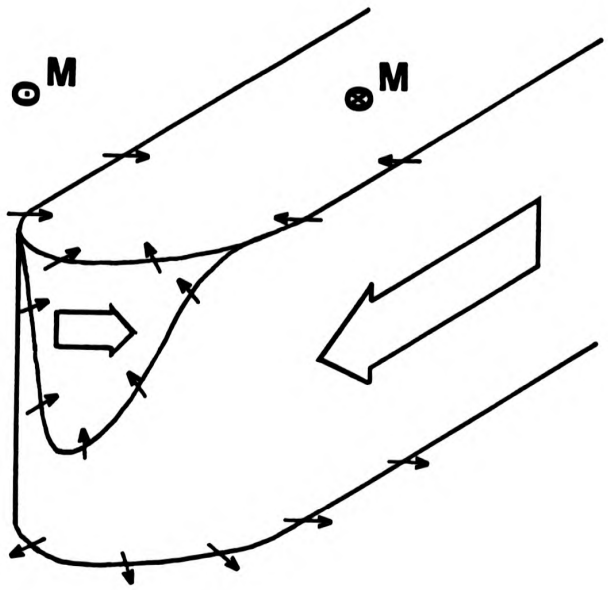

Fig.1.3.8 Formation of a Bloch curve at a stripe domain head.

Bloch line length and energy, resulting in two VBL's of opposite polarity on either flank of the domain wall. The formation of VBL's by the punch-through of Bloch curves has been extensively studied by experiment [43 - 44] and theoretically by the quasi-static state approximation [45] as well as the numerical solution of this work in Chapter 4 [46 - 47].

The final domain wall structure to be considered is the transition between Bloch lines of opposite polarity known as a Bloch point (Ref. 39, Chapter 9). This structure differs significantly from those previously mentioned as it represents a singularity, i.e., the magnetisation vector does not vary continuously with position. Rather magnetisation spontaneously changes by a finite angle in every axis through the Bloch point. As such therefore it cannot have a finite radius but represents a transition on a molecular scale where the continuous magnetisation model is no longer valid. The structure of Figure 1.3.9, which includes a Bloch point at Z = h/2, can be seen to be stable if the total energy of the Bloch line is considered. In comparison to the VBL of Figure 1.3.6 there is now no head (2π twist) but two tails with a maximum twist of π at the centre. Should the Bloch point move closer to either surface the VBL maximum rotation along the X axis, and therefore the Bloch line energy, will increase. In the presence of an in-plane field normal to the wall, one polarity of Bloch line is favoured at the expense of the other and the Bloch point will move closer to one surface. Should the field be sufficiently large the Bloch point will punch-through at the surface, reversing the polarity of the Bloch line. A detailed analysis of Bloch points is beyond the scope of this work. It is mentioned only in so far as it is a highly

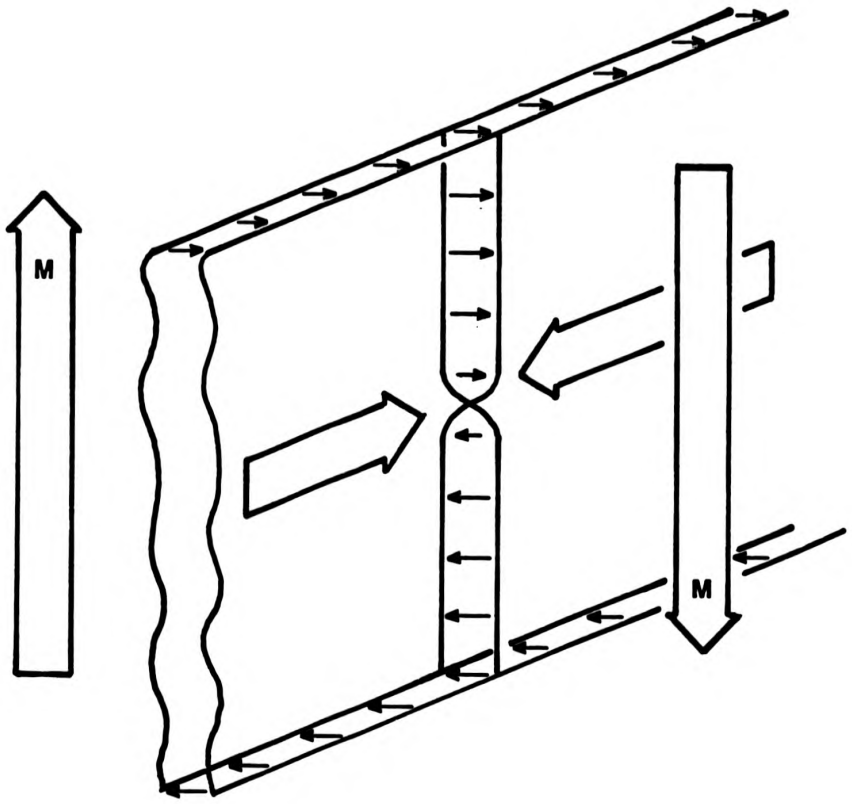

Fig.1.3.9 Cross section of a domain wall with a Bloch point separating two regions of Bloch line of opposite polarity.

undesirable structure in vertical Bloch line memory where data integrity relies upon the stability of VBL's of like polarity.

1.3.3 Domain wall dynamics

The dynamics of domain walls and wall structures are based on the equations of Landau and Lifshitz [48]. Expressed in a simplified form these state firstly that magnetisation $\vec{M}$ will precess around a field, $\vec{H}$, at an angular velocity given by (see Figure 1.3.10)

$$\omega = \gamma H \qquad \ldots.1.3.17$$

Secondly, the precession amplitude will decrease due to dissipative effects until the vector product $\vec{M} \times \vec{H}$ is zero. It is useful to express these effects in the terms of Thiele [49] i.e.,

$$\gamma\vec{M} \times \left[\vec{H} - \frac{1}{\gamma|M|^2} \vec{M} \times \frac{d\vec{M}}{dt} - \frac{\alpha}{\gamma|M|} \frac{d\vec{M}}{dt} \right] = 0 \qquad \ldots.1.3.18$$

where the second and third terms of equation 1.3.18 are effective fields of a gyrotropic and dissipative nature respectively.

With reference to the simple Bloch wall of Figure 1.3.11a a field, Hz, normal to the film will cause magnetisation at the wall centre to precess out of the plane of the wall. The rate of change of $\vec{M}$ is given by

$$\frac{d\vec{M}}{dt} = |M| \frac{d\theta}{dt} \qquad \ldots.1.3.19$$

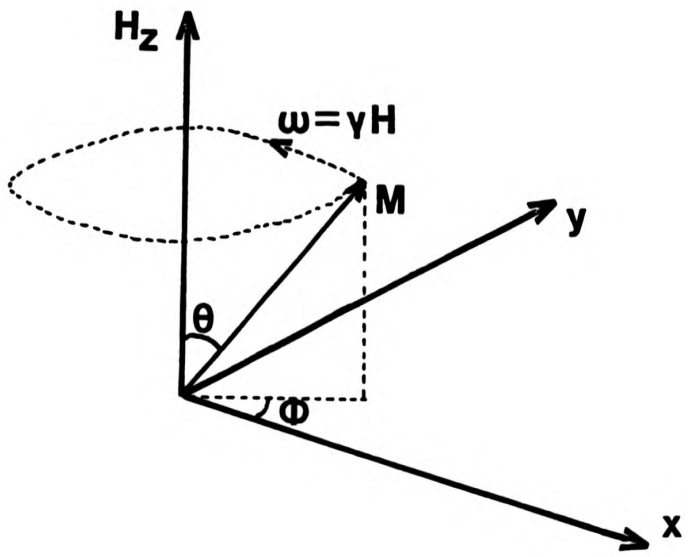

Fig.1.3.10 Magnetisation M will precess at an angular velocity of ω in the presence of a field H in the direction given by the right hand rule.

and therefore there is a dissipative effective field acting in opposition to this precession given by

$$H\alpha = \frac{\alpha}{\gamma} \dot{\phi} \qquad \ldots.1.3.20$$

In addition, as magnetisation precesses out of the plane of the wall, magnetostatic energy increases giving rise to a local demagnetising field which, resolved normal to the direction of magnetisation (Figure 1.3.11b), is approximated by

$$Hd = 4\pi M \sin \phi \cos \phi \qquad \ldots.1.3.21$$

$$= 2\pi M \sin 2\phi \qquad \ldots.1.3.22$$

As this also acts in opposition to the motion there is a total field of $H\alpha + Hd$ which causes a precession out of the film plane, towards the Z axis of

$$\dot{\theta} = \gamma (H\alpha + Hd) \qquad \ldots.1.3.23$$

which with the substitution of equation 1.3.9 gives the wall centre velocity as,

$$\dot{y} = \gamma\Delta_0 (2\pi M \sin 2\phi + \frac{\alpha}{\gamma} \dot{\phi}) \qquad \ldots.1.3.24$$

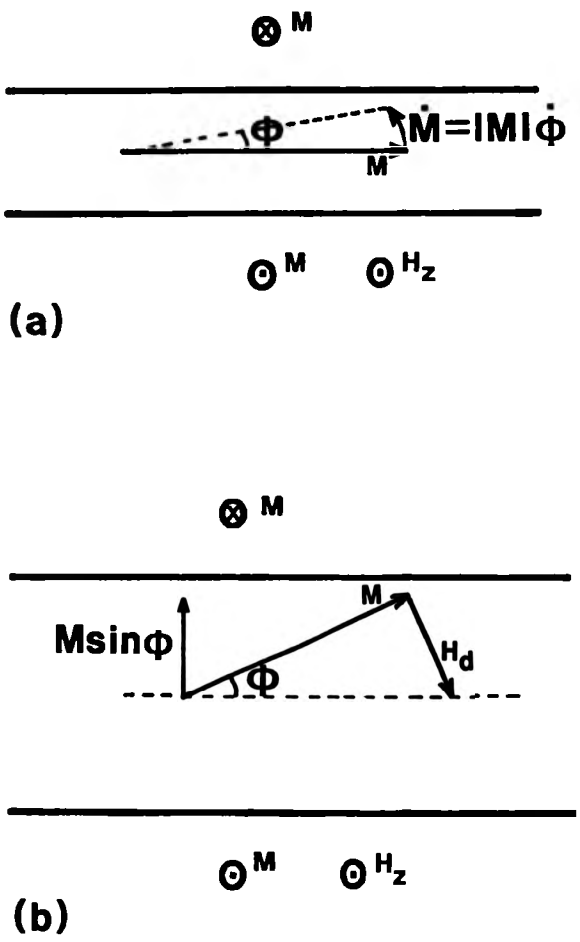

Fig.1.3.11 a) Precession within a simple Bloch wall.
b) The local magnetostatic energy increases as magnetisation rotates out of the plane of the wall giving rise to a local demagnetising field, Hd.

In a similar manner to equation 1.3.20, the precession of magnetisation towards the Z axis causes a dissipation effective field, $(\alpha/\gamma)\dot{\theta}$, acting in opposition to the applied field Hz. This in turn causes ϕ to rotate at an angular velocity of

$$\dot{\phi} = \gamma \left(Hz - \frac{\alpha}{\gamma} \dot{\theta}\right) \qquad \ldots.1.3.25$$

$$= \gamma \left(Hz - \frac{\alpha}{\gamma \Delta_0} \dot{y}\right) \qquad \ldots.1.3.26$$

Equations 1.3.24 and 1.3.26 give rather simply the equations of motion for a domain wall with an associated wall structure. It should be remembered that Hz is the sum of effective fields normal to the film, as in section 1.3.1, involving fields of magnetostatic, domain wall and external origin. Although a more precise mathematical treatment, as in Chapter 4, is strictly necessary, these equations can provide a significant insight to domain wall dynamic behaviour.

A simple Bloch wall moving at a constant velocity will have an equilibrium structure at the wall centre, i.e., $\dot{\phi} = 0$, and therefore from equation 1.3.26,

$$\dot{y} = (\gamma/\alpha)\, \Delta_0\, Hz \qquad \ldots.1.3.27$$

$$= (\gamma/\alpha)(A/K)^{\frac{1}{2}}\, Hz, \qquad \ldots.1.3.28$$

and equation 1.3.4 is derived. Conversely if the wall of Figure 1.3.12 which contains VBL's is considered, $\dot{\phi} \neq 0$, and the wall

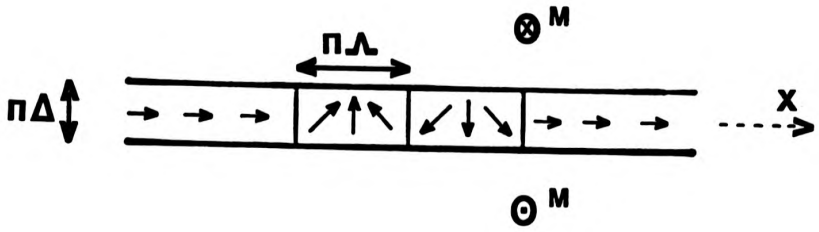

Fig.1.3.12 A pair of VBL in a domain wall.

velocity is given by combining equations 1.3.24 and 1.3.26 (assuming the spatial average of local demagnetising field, $2\pi M \sin 2\phi$, is zero) by,

$$\dot{y} = \frac{\alpha\gamma}{(1 + \alpha^2)} (A/K)^{\frac{1}{2}} \text{ Hz} \qquad \ldots.1.3.29$$

Consequently as $\alpha << 1$ the mobility of a section of wall containing VBL's (known as a 'hard' wall) is very much less ($\approx \alpha^2$) than that of a simple Bloch wall (or 'soft' wall). Also if the VBL transverse velocity within the wall is taken from equation 1.3.16 as,

$$\dot{x} = \Lambda_0 \dot{\phi} \qquad \ldots.1.3.30$$

an approximate relationship between domain wall and VBL velocities can be derived from equation 1.3.24 as

$$\dot{y} \approx \frac{\alpha}{\sqrt{Q}} \dot{x} \qquad \ldots.1.3.31$$

Again, as $\alpha << 1$, this indicates that the VBL velocity within the wall is much larger than the domain wall velocity. A segment of hard wall in an otherwise soft wall will therefore be displaced rapidly along the wall and appear to retard the wall motion. A bubble domain with a large number of VBL's will hardly move in response to a field gradient as most of the energy is funnelled into rotating the VBL's

around its circumference. Because of this behaviour, considerable effort is taken, by using ion-implanted capping layers [50], to ensure hard bubbles are not present in conventional bubble devices. Conversely these phenomena are fundamental to the concept of VBL memory.

Before finishing this section, gyrotropic force is introduced. So far only forces normal to the wall, applying a pressure to displacing the wall have been discussed. By symmetry there must be a force acting orthogonal to the wall velocity, applying a pressure to displace a VBL. This can be shown from the above equations to be proportional to the wall velocity and the force per unit length on the VBL is:

$$F_g = \frac{2\pi M}{\gamma} \dot{y} \qquad \ldots.1.3.32$$

This creates some remarkable dynamic behaviour in bubble motion such as deflection from the field gradient by acute skew angles [51] or gradientless propagation in a pulsed bias field (automotion) [52].

1.4 Summary

All commercially available magnetic bubble devices at this time are of the simple major-minor loop architecture with most industrial research being aimed at increasing device density. It is felt however, that as the limits of device density are reached attention will turn to improving operating characteristics and towards the design of high performance bubble memory devices. These are most

likely to use the dual-conductor apertured-sheet technology as it provides flexibility and ease of design. However as the current densities required are large (1-10mA/μm) power dissipation and electromigration problems are envisaged.

An alternative form of mass storage, VBL memory, which codes data in the micromagnetic wall structure of bubble materials, offers the potential of very much greater storage capacities than bubble memory. The observation of such wall structures is very difficult due to their fine scale, at best their dynamic effect on wall motion gives an indication of their presence in a wall [53]. These techniques are not as useful to the study of device operation as they intrinsically have a disruptive effect on the coded data. Fortunately the dynamic characteristics of wall structures are well defined mathematically and this, coupled with the much more powerful computational capabilities nowadays, suggests that simulation of device behaviour will play a much more significant role in the early development of such a memory. The complex non-linear interactions resulting from magnetic overlays which hampered earlier bubble simulation work are not necessary and therefore there is a high degree of confidence in such theoretical research.

In general terms the aims of this work are two fold. Firstly, a facility for fabrication and testing of dual-layer apertured-sheet current-accessed propagation patterns was deemed necessary in the study of high performance bubble memory and so work was undertaken to establish one. As will be described, fabrication entailed electron beam lithography and dry-etching techniques although as work here proved only partially successful due primarily to the difficulty of dry-etching the metallisation layers, devices of only limited quality were produced.

Secondly, the concept of vertical Bloch line memory which promises ultra-high densities has been examined. It is found that although the ultimate storage density may be a factor of four less than that initially anticipated, considerable advantages over conventional bubble technology remain. Methods of studying domain wall motion by computer simulation using numerical analysis have been investigated. The numerical solution has been extended to the three-dimensional case and applied to a translating bubble at velocities that include the formation of VBL by Bloch curve punch through, an area directly relevant to the write process in VBL memory.

Chapter 2 outlines the fabrication of current-access propagation patterns, concluding with the limitations of the existing process and recommendations for future work. The concept of VBL memory is given in Chapter 3 with some initial projections of device density and performance, together with some considerations for fabrication of experimental devices. Methods of numerical analysis of domain wall motion and the three-dimensional solution in the case of a translating bubble are included in Chapter 4. Uses and limitations of these techniques for the study of VBL memory are considered. In conclusion the results of this work are reviewed and recommendations for future research are suggested.

CHAPTER II

FABRICATION OF DUAL-LAYER APERTURED-CONDUCTOR CURRENT-ACCESSED PROPAGATION PATTERNS

2.1 Introduction

The electron beam machine (EBM) used for high-resolution lithography in the Department of Electrical Engineering is based on a Cambridge Instruments S150 electron optical column and chamber. The precision wafer-stage assembly and laser interferometer positioning system has previously been described by Garside and Pickard [54]. The (fabrication) beam deflection coils are driven by a vector-scan pattern generator and the installation is principally used for direct write on wafer. The typical operation of the facility for an application such as the definition of the final metallisation layer of an Uncommitted Logic Array has been reported by Hardy et al [55].

The particular attractiveness of electron beam fabrication is the potential for very quick turn-around time from design to device. In addition, even the initial current-accessed bubble propagation patterns described here comprised dimensions which would have been very difficult to delineate by photolithography with the equipment which was available. If the design of devices was to be extended to smaller diameter bubbles it was considered essential to have a capability for sub-micron fabrication and so the EBM facility was used from the outset.

Having delineated a pattern mask in a resist layer, the mask features must be reproduced in the metallisation layer by etching. This should be an anisotropic process or undercutting will destroy the finer detail. Wet chemical etches are unsuitable for this reason and so only dry-etching techniques were therefore considered i.e., ion milling, reactive ion beam etching (RIBE), reactive ion etching (RIE), and plasma etching. Ion milling [56] is a purely physical process whereby an incident beam of high energy ions (e.g., Argon) erodes the exposed areas of material. This can produce very controllable etch profiles, although it has the disadvantage of eroding the mask at a similar rate to the underlying layer. RIBE [57] combines a chemical etch with the physical milling process by using a reactive gas or gas mixture thereby increasing the etch rate and improving the selectivity between resist and underlying layer and/or the latter and other layers in the device. A variation of RIBE is chemically-assisted ion beam etching [58] where a reactive gas is injected into an inert ion beam near the substrate, again giving very high etch rates and selectivities. Alternatively, RIE [59] is a higher pressure process ($\sim 10^{-2} - 10^{-1}$ mbar as opposed to $10^{-4} - 10^{-3}$ mbar for RIBE), whereby a reactive gas mixture is excited by an r.f. power supply in a parallel plate reactor. The r.f. power is capacitively coupled to the discharge by an electrode (cathode) within the system. The wafer sits on the cathode on which a negative bias (100-600V) appears as a function of the discharge process if the cathode is allowed to 'float' electrically. Therefore RIE includes both ion bombardment perpendicular to the sample surface and chemical reactions. Anisotropic etching is generally obtainable. Plasma etching [60] can also be achieved by a r.f. discharge in a parallel

plate reactor. The pressure is usually high, 10^{-1} - 1 mbar, and the sample reats either in the plasma itself or on the anode. Although anisotropic profiles may be achieved [61] the incident ion energy is low, generally resulting in an isotropic etch. While this is, therefore, not a suitable process for the pattern delineation under discussion it was found useful in removal of resist after etching.

Choice of etching process again depends on the nature of the layer to be etched. Al/4% Cu was chosen for metallisation as the copper content reduces the electromigration problem, i.e. the tendency for conductors to creep at high current densities, associated with pure aluminium [62]. It also has an advantage over chemically more inert layers, such as gold, in that chemically-assisted etching is possible. The high copper content coupled with the need to remove an oxide layer suggests that a highly physical process such as RIBE would be suitable. This was evaluated using a capillary source [63], to be described in section 2.4, as opposed to the more common saddle field source [64] although the results were disappointing due to the low power density available. Rather than uprate the RIBE system to one of greater power, pattern delineation was finally achieved by RIE, this choice being related to the relative cost (a factor of approximately four) of the two systems. Of the main reactive gases for aluminium etching, CCl_4 and BCl_3 [65], CCl_4 was chosen as it was considered the less hazardous of the two.

In the succeeding sections the fabrication process is outlined. To economise on the garnet wafers available, processing of individual 7mm square chips has been undertaken. Test devices of limited quality were fabricated. End-point detection and resist hardening techniques

were studied in an effort to improve the processing. Test equipment for the current-accessed devices was constructed. In conclusion, the limitations of the fabrication process are discussed together with recommendations for future work.

2.2 Patterns for Current-Access Propagation

Patterns for dual-layer apertured-conductor bubble propagation circuits have been written on the University's CYBER interactive computer using a high level pattern language developed by Patel and Hardy [66] of the Electrical Engineering Department. The patterns are based on those of Bobeck et al [9], including tracks parallel and perpendicular to the current flow, a bubble nucleator, registration marks, bonding pads and some resolution lines of width 2.0 to 0.5μm. Figure 2.2.1a-c and Figure 2.2.2a-c are, at increasing magnification, the first and second metallisation layers respectively, and Figure 2.2.3a-c combines the two illustrating the intended alignment between layers.

The bonding pads for the first layer (Figure 2.2.1a) include those for nucleation at the bottom centre, the remaining two being for current drive. As the devices were intended to be tested by stroboscopic observation a detector was not included. The bonding pads are large enough for three probe contacts to each thereby maintaining low contact resistance. Current is funnelled into the central 200μm x 200μm area, the active test area being 100μm x 130μm (Figure 2.2.3c). The anticipated drive current density is 2-3mA/μm therefore requiring drive circuitry capable of supplying 0.4 - 0.6A. With reference to Figure 2.2.3c the two types of

were studied in an effort to improve the processing. Test equipment for the current-accessed devices was constructed. In conclusion, the limitations of the fabrication process are discussed together with recommendations for future work.

2.2 Patterns for Current-Access Propagation

Patterns for dual-layer apertured-conductor bubble propagation circuits have been written on the University's CYBER interactive computer using a high level pattern language developed by Patel and Hardy [66] of the Electrical Engineering Department. The patterns are based on those of Bobeck et al [9], including tracks parallel and perpendicular to the current flow, a bubble nucleator, registration marks, bonding pads and some resolution lines of width 2.0 to 0.5μm. Figure 2.2.1a-c and Figure 2.2.2a-c are, at increasing magnification, the first and second metallisation layers respectively, and Figure 2.2.3a-c combines the two illustrating the intended alignment between layers.

The bonding pads for the first layer (Figure 2.2.1a) include those for nucleation at the bottom centre, the remaining two being for current drive. As the devices were intended to be tested by stroboscopic observation a detector was not included. The bonding pads are large enough for three probe contacts to each thereby maintaining low contact resistance. Current is funnelled into the central 200μm x 200μm area, the active test area being 100μm x 130μm (Figure 2.2.3c). The anticipated drive current density is 2-3mA/μm therefore requiring drive circuitry capable of supplying 0.4 - 0.6A. With reference to Figure 2.2.3c the two types of

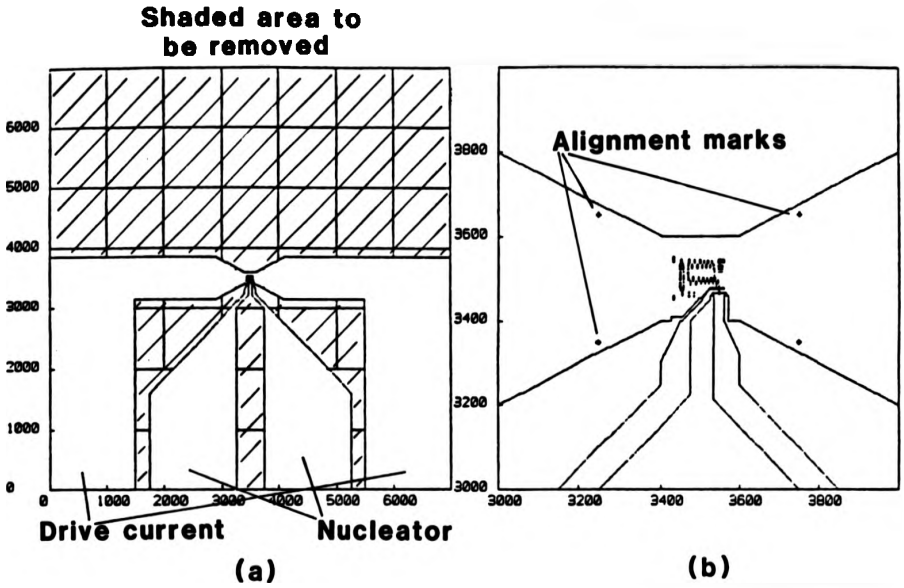

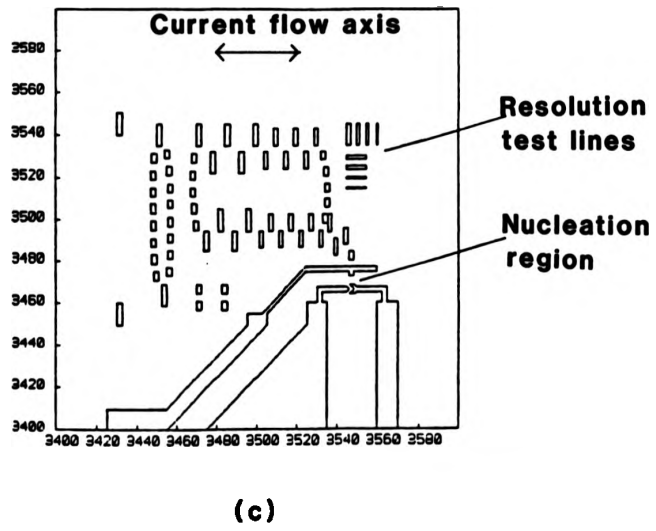

Fig.2.2.1 (a)The first layer metallisation pattern. Dimensions are in microns. (b)The central 1 mm of the first layer pattern. (c)The first layer test pattern.

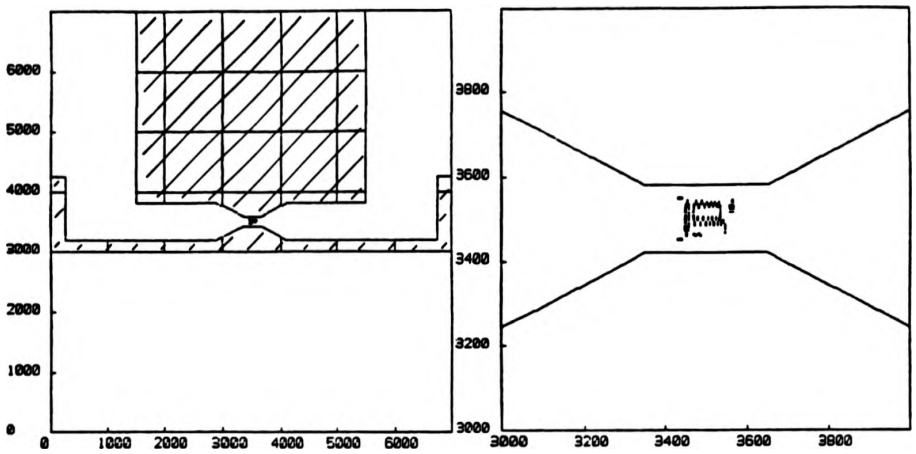

(a) (b)

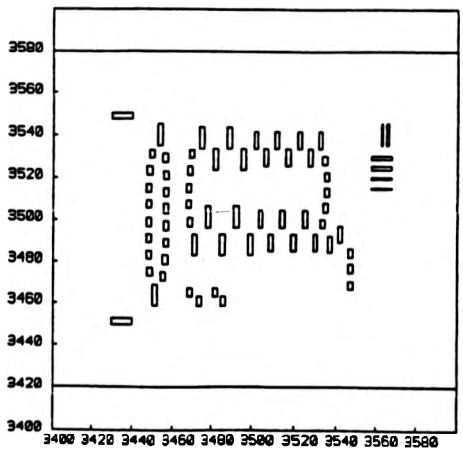

(c)

Fig.2.2.2 (a)The second layer metallisation pattern. (b)The central 1 mm of the second layer pattern. (c)The second layer test area.

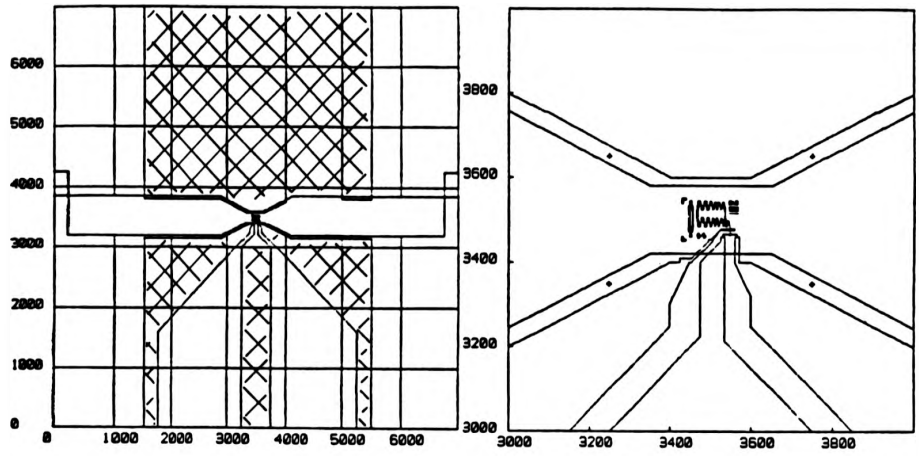

(a) (b)

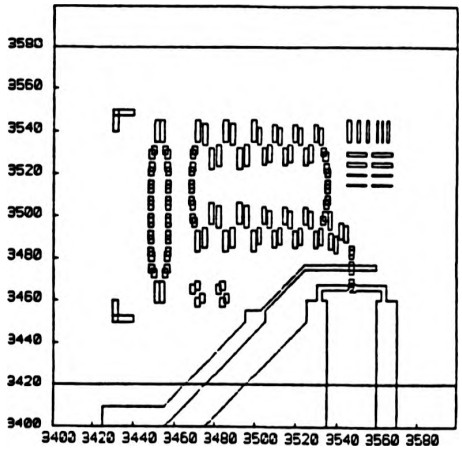

(c)

Fig.2.2.3 (a)Both metallisation layers. (b)The central 1 mm of both layers. (c)The central test area.

racetrack can be seen. At the left side of the test area there are tracks perpendicular to the current flow with 180° turns at each end. The propagation period, λ, is 8μm and the aperture size is 2.5μm x 4μm. The central loop has tracks parallel to the current flow (as well as perpendicular), with periods of 10μm and 14μm. A range of track periods were therefore included which were intended to be evaluated using 2-3.5μm diameter bubbles. The nucleate circuit, bottom right, is designed either to divert a fraction of the drive current or act in a manner similar to a conventional hairpin nucleator. The current path is through a 1.8μm conductor which is, excluding the resolution lines at the top right, the minimum linewidth of the test circuits. Also included at the bottom left are two single bubble idler loops, one with slightly overlapping apertures. Registration marks for second layer alignment are included within the central $1mm^2$ subfield (Figure 2.2.1b, Figure 2.2.3b). These are positioned outside the second metallisation layer so they may be examined by the EBM in SEM mode without exposure of the electron sensitive resist in critical areas and, therefore, without any adverse effect on the second layer pattern.

The 7mm x 7mm pattern was subdivided into 49, $1mm^2$ subfields for exposure by the EBM. After each subfield was exposed the EBM stage was repositioned for the next. The fine detail in the test area was exposed firstly using the electron beam focussed to a small spot, 0.3μm diameter, the drawback being that beam current is limited to approximately 10nA. This means that the exposure time per spot must be greater than 8μs as the resist used (Isofine E-B positive) requires $112\mu C/cm^2$ for correct exposure and the spot increment distance is 0.25μm. The subsequent bonding pad area was exposed

using a gross spot (~2μm diameter) and beam current (30nA), thereby reducing the overall exposure time. Even so, one layer exposure required 15-20 minutes.

2.3 Sample Preparation and Sputter Deposition

Samples of device quality garnet substrates have been provided by Plessey Limited (Allen Clark Research Centre, Caswell), Bell Laboratories (Murray Hill, New Jersey), and Philips Laboratories (Eindhoven, Holland), those from the latter two being high mobility samples specifically for current-accessed devices. For fabrication of the initial test devices, however, the lower quality Plessey garnets were used, these having zero bias stripe widths of 2 - 3.5μm and of nominal composition $Sm_{0.2}$ $Lu_{0.2}$ $Y_{1.7}$ $Ca_{0.9}$ $Ge_{0.9}$ $Fe_{4.1}$ O_{12}. Techniques were developed to allow processing on a chip-by-chip basis to conserve garnet material. The wafers were waxed to a holder and cut with a diamond saw into 7 x 7mm^2 chips. To remove the wax and clean the samples, multiple ultrasonic rinses in hot water and Teepol followed by multiple ultrasonic rinses in high purity Isopropyl alcohol were used, concluding with a 45 minute ultrasonic agitation in flowing 10MΩcm deionised water. The samples were baked at 100^{o}C for 10 minutes to remove moisture immediately before insertion into the sputter deposition system.

R.F. sputter deposition [67] was chosen for metallisation and insulating layers as it provides a good step coverage as compared to more directional deposition methods at lower pressures such as evaporation. This is essential for dual-layer conductors when a planar process [68] is not used. The Nordiko SG1250 13.56MHz system

used (see Figure 2.5.1a) was previously commissioned [69] and therefore was only briefly characterised for the specific needs of Al/4% Cu and SiO_2 deposition.

The optimum Argon pressure at deposition, 1.8×10^{-2} mbar, was determined from the measured variation of deposition rate as a function of pressure, (see Appendix 2.1). All thicknesses were obtained from measurements made on a Talystep 1 system (Rank Taylor Hobson Ltd.). Power was limited to 100 Watts for Al/4% Cu deposition as the thickness uniformity rapidly degraded above this value as can be seen in Appendix 2.1. A deposition rate of 21.7nm/min was obtained requiring 11.5 minutes deposition time for 250nm of Al/4% Cu. A power of 150 Watts was chosen for the SiO_2 layer as the deposition rate was much lower (see also Appendix 2.1). A 30-minute sputter was used for a 240nm insulating layer and 35 minutes for a 280nm final passivation coating. All processes were preceeded by a 20-minute sputter clean of the target surface. $7 \times 7mm^2$ substrate holders were constructed as well as a series of masks to ensure (i) the metallisation layer bonding pads were not covered in SiO_2 and (ii) the 2nd layer metallisation did not overlap the insulating layer causing short circuits to the first conductor layer.

Hillock formation [85] was sometimes observed in the Al/4% Cu layers due to a poor mechanical contact between substrate and holder although this is not considered a major problem (see also Figure 2.9.3). An antistress PTFE pre-layer [70] was not deposited although for the highly magnetostrictive samples of Philips this would be essential. The various deposition parameters are summarised in Figure 2.3.1.

SPUTTER PROCESSES

1st metallisation layer Al/4% Cu

Deposition time	11.5 mins
Inlet pressure	1.8×10^{-2} mbar
Input power	100 Watts
Deposition thickness	250 nm

Insulating layer SiO_2

Deposition time	30 mins
Inlet pressure	1.8×10^{-2} mbar
Input power	150 Watts
Deposition thickness	240 nm

2nd metallisation layer Al/4% Cu

Deposition time	12 mins
Inlet pressure	1.8×10^{-2} mbar
Input power	100 Watts
Deposition thickness	260 nm

Passivation layer SiO_2

Deposition time	35 mins
Inlet pressure	1.8×10^{-2} mbar
Input power	150 Watts
Deposition thickness	280 nm

Sputter targets purity (4")

Al/4% Cu	99.999%
SiO_2	99.9%

Sputter gas purity

Argon	99.999%

Figure 2.3.1 The Sputter Deposition Parameters

2.4 Reactive Ion Beam Etching

A reactive ion beam etching (RIBE) system has been evaluated for Al/4% Cu lithography using a capillary ion source (Oxford Applied Research Microdischarge Source). A diagram of the ion source is included in Appendix 2.2. The system comprised the ion gun which had a fine capillary nozzle, fed from a stainless steel reservoir containing CCl_4 liquid and/or an Argon supply and was powered by a 0-10kV, 0-3mA, H.V. generator (Wallis VCS 103/3). Initial results were disappointing, an etch rate of the order of 0.5nm/min was obtained, and problems were encountered due to breakdown of the ion source insulation. The low etch rate was attributed to the low power of the source and an aluminium oxide barrier on the sample surface. This was constantly reformed as the low flow rate of CCl_4 through the capillary orifice caused a relatively high percentage of oxygen to be present at the target.

Modifications to the gun insulator (see Appendix 2.2) improved the operating margins and reliability of the source. A separate pump was introduced at the input of the source to increase the flow rate of CCl_4 through the gas feed network, and the capillary cross section was increased by a factor of 16, greatly enhancing the CCl_4 flow rate through the source itself and so reducing the relative effect of oxygen contamination. Further modifications included a substrate heater with thermocouple feedback control to increase the speed of reaction and to prevent the accumulation of $AlCl_3$ which is non-volatile at room temperature, and tilting the substrate to 40-45^{o} with respect to the beam to increase sputtering yields [71].

Although these measures did increase the etch rate by a factor of

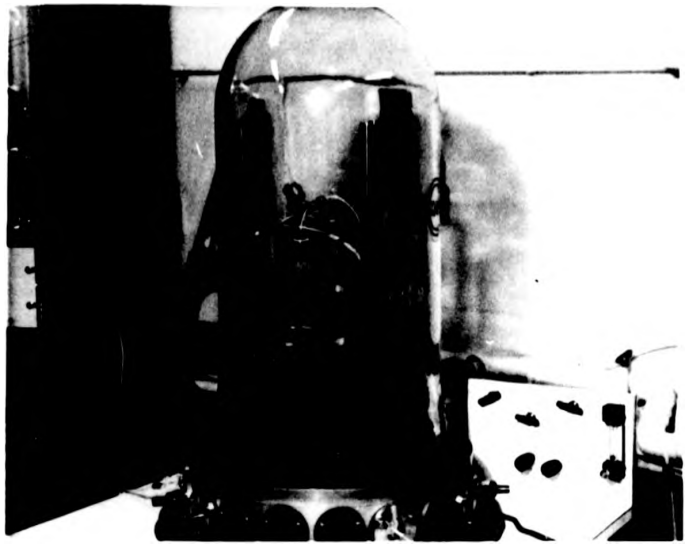

Fig.2.4.1a The capillary ion source and vacuum system.

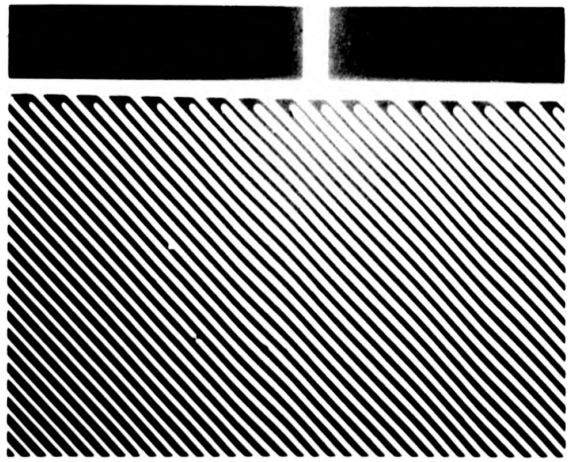

Fig.2.4.1b A magnetometer pattern ion milled in nickel-iron. Minimum feature size is 10μm.

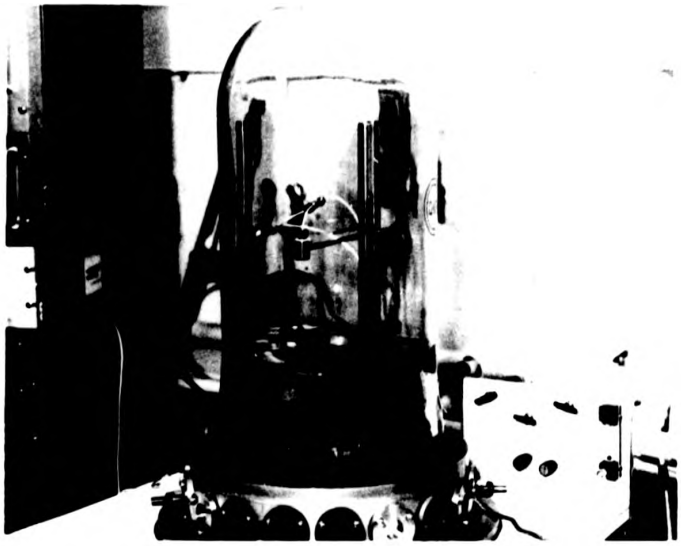

Fig.2.4.1a The capillary ion source and vacuum system.

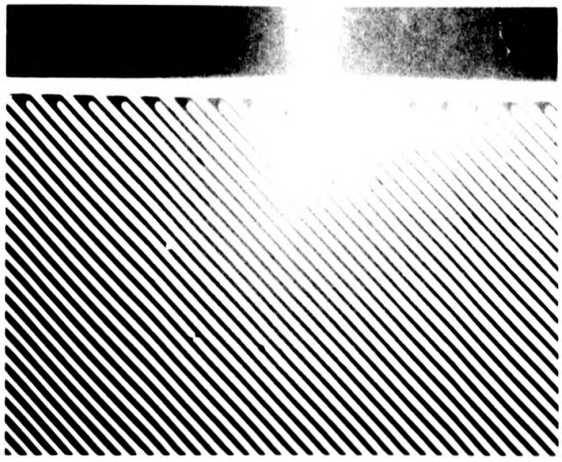

Fig.2.4.1b A magnetometer pattern ion milled in nickel-iron. Minimum feature size is 10μm.

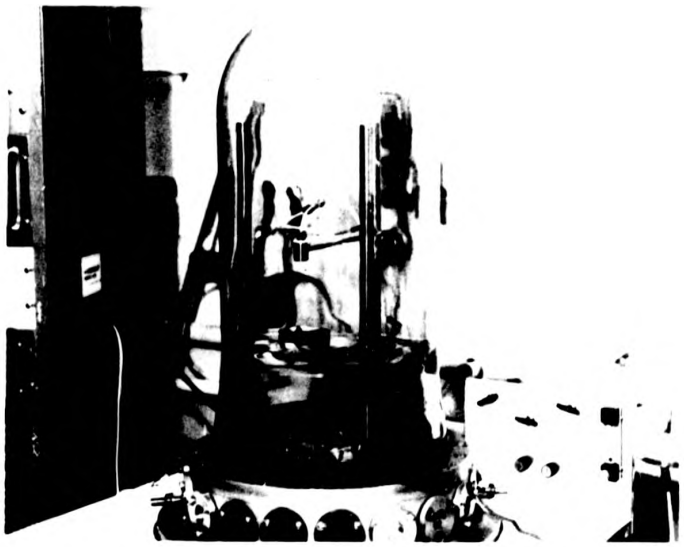

Fig.2.4.1a The capillary ion source and vacuum system.

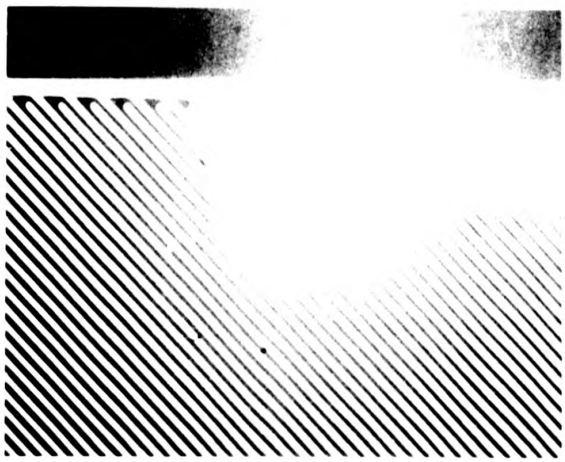

Fig.2.4.1b A magnetometer pattern ion milled in nickel-iron. Minimum feature size is 10μm.

10 this was considered insufficient for our purposes and so the source was abandoned in favour of a parallel plate reactor. The usefulness of the source was briefly evaluated for ion milling of nickel-iron using Argon alone. In this case, the source could only be used in an ion milling capacity as nickel-iron does not form volatile products with a relative gas. The samples provided from a project on thin film magnetometers [72] were sufficiently thin (30nm) that etching using the capillary source was practical. An etching time of 30 minutes produced the results shown in Figure 2.4.1b. The vacuum system and gas feed network were maintained for use in the parallel plate reactor described in the next section.

2.5 Reactive Ion Etching

A reactive ion etching (RIE) 10cm diameter, parallel plate reactor (Nanotech NRM1 and NRF1-2 13.56 MHz r.f. power supply) has been commissioned for etching the current-access propagation patterns in Al/4% Cu. Due to the highly corrosive nature of the etchant (CCl_4) it was necessary to replace some of the more critical components with stainless steel parts, replace nitrile O-ring seals with those of Viton, and warm the system with a hot water supply ($65^{o}C$) thereby decreasing contamination buildup and increasing the overall durability. Figure 2.5.1 is a photograph of the reactor. The samples rest on the lower electrode and power can be applied to either the lower (RIE mode) or upper (Plasma etch mode) plate. The gas feed network constructed for RIBE was incorporated with an additional inlet to allow an air plasma for resist ashing (see Figure 2.5.2).

Fig.2.5.1a The parallel plate reactor RIE system and vacuum controller. The Nordiko sputter system is in the background.

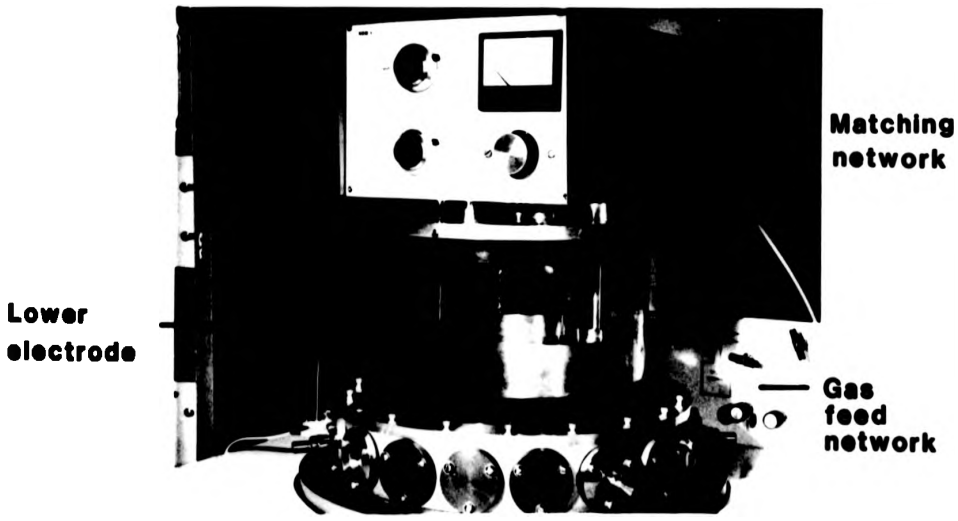

Fig.2.5.1b The parallel plate reactor RIE system.

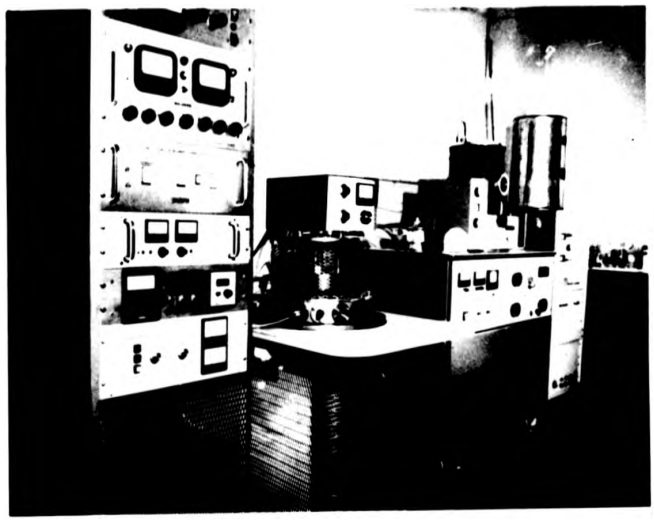

Fig.2.5.1a The parallel plate reactor RIE system and vacuum controller. The Nordiko sputter system is in the background.

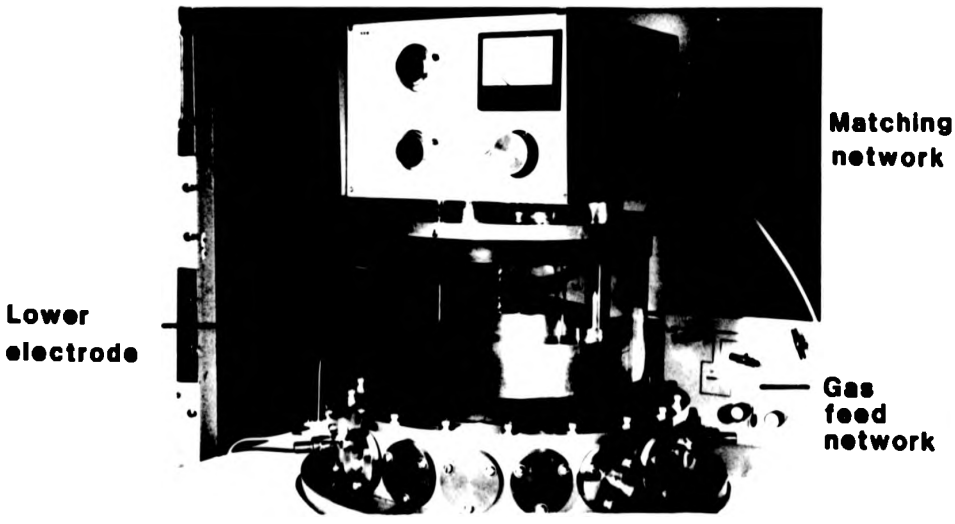

Fig.2.5.1b The parallel plate reactor RIE system.

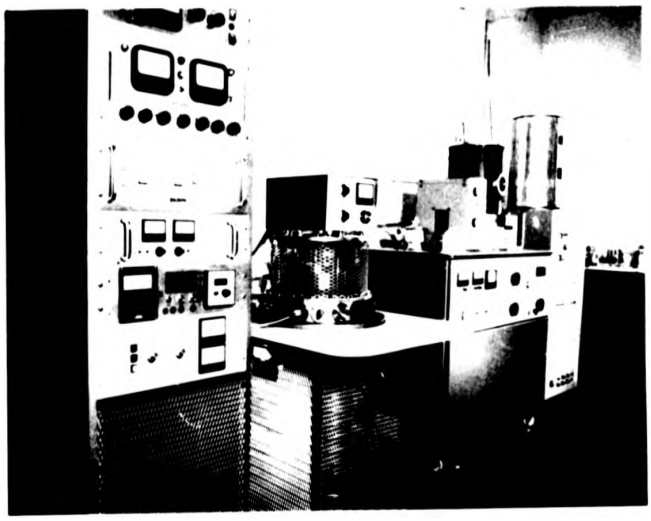

Fig.2.5.1a The parallel plate reactor RIE system and vacuum controller. The Nordiko sputter system is in the background.

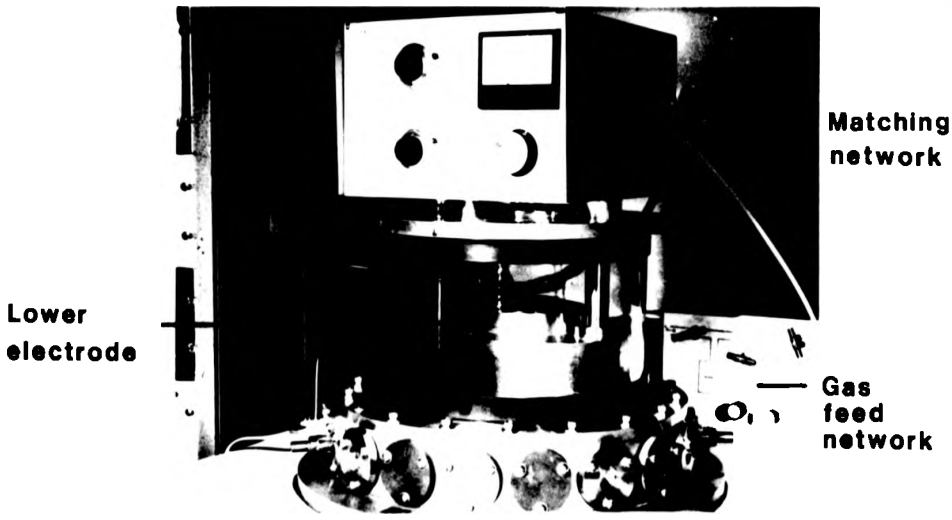

Fig.2.5.1b The parallel plate reactor RIE system.

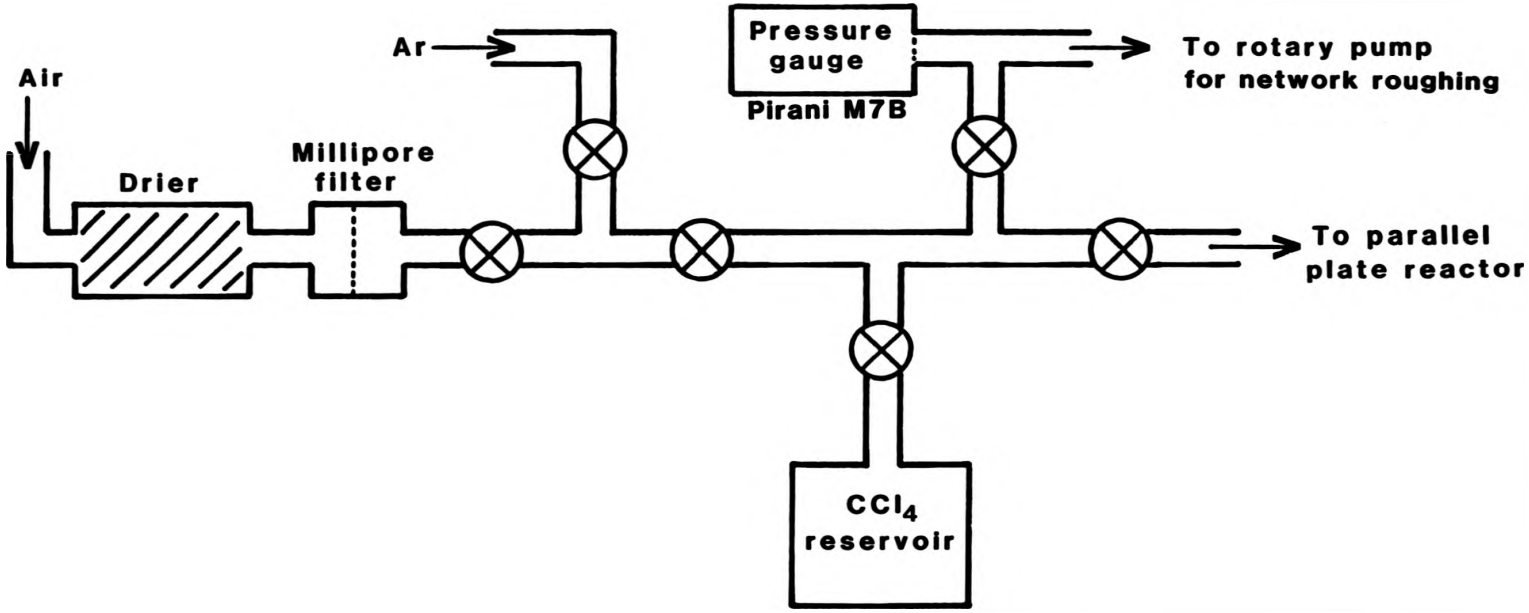

Fig.2.5.2 The gas feed network.

The etching of aluminium in CCl_4 involves two distinct processes. Firstly an Al_2O_3 barrier layer (estimated at ≈45nm thick), which does not form volatile chloride products, is removed by a milling process. Oxide removal is comparatively slow and the time required to expose the underlying aluminium was found to be greatly increased by plasma contaminants such as moisture or air (see also section 2.6). Secondly, as shall be shown below, the exposed aluminium is removed by an ion-bombardment assisted chemical reaction at etch rates far in excess of those for oxide removal. There can, therefore, be a considerable difference in apparent etch rates for samples of different thicknesses. For this reason, unless otherwise stated, the etch rates given below are for samples 250nm thick.

The chemical reaction of primary importance is believed to be [75]

$$\frac{3}{2} Cl_2 + Al \text{ (solid)} \rightarrow AlCl_3 \qquad \ldots.2.5.1$$

where Cl_2 is dissociated from CCl_4 in the plasma discharge. While molecular chlorine is not the only rective dissociation product of CCl_4, the above reaction was verified by observation of the reduction in intensity of the optical emission of the plasma at a wavelength of 255nm (characteristic of Cl_2) during etching. This will be described in section 2.6. The reaction was found to be very pressure dependent. At high pressures collisions within the plasma are more frequent and the density of reactive species at the substrate increases although the incident ion energy is reduced. Above a critical pressure the ion energy is insufficient to remove the native

oxide layer and the etch rate reduces to zero. It was anticipated that the cathode bias voltage would have a significant effect on etching times as the accelerating potential determines ion energy. In practice, however, little or no control of the bias potential was available and it remained in the 50-100V region. This was suspected to be a fault on the voltage metering system although none could be traced. As the reactor was found capable of etching aluminium it was used with the limited bias potential control.

The initial system characterisation was undertaken using 100% Al evaporated samples. Figure 2.5.3 shows the variation of etch rate with sample thickness for four values of pressure. At low pressure ($1.5 - 2 \times 10^{-2}$ mbar) etch rate is independent of sample thickness. This indicates that both the oxide layer and the underlying aluminium are removed at the same rate and therefore the process is largely a milling one with little or no reactive etch. As the pressure increases ($2.25 - 5.25 \times 10^{-2}$ mbar) the etch rate increases considerably with thickness. This is indicative of a slow oxide removal by ion milling followed by fast removal of aluminium by reactive ion etching. As can be seen from the gradient at higher pressure, the oxide requires a large proportion of the overall etch time. At still higher pressures, as shown in Figure 2.5.4, the etch rate cuts off sharply as the RIE gives way to a plasma process. The oxide layer is then an effective barrier as the ion milling process is negligible. The reactor plate separation was optimised at 4cm as shown in Figure 2.5.5.

Similar characteristics were observed for Al/4% Cu although the copper content was an additional problem as it requires a milling process for removal i.e. it does not form a volatile chloride which

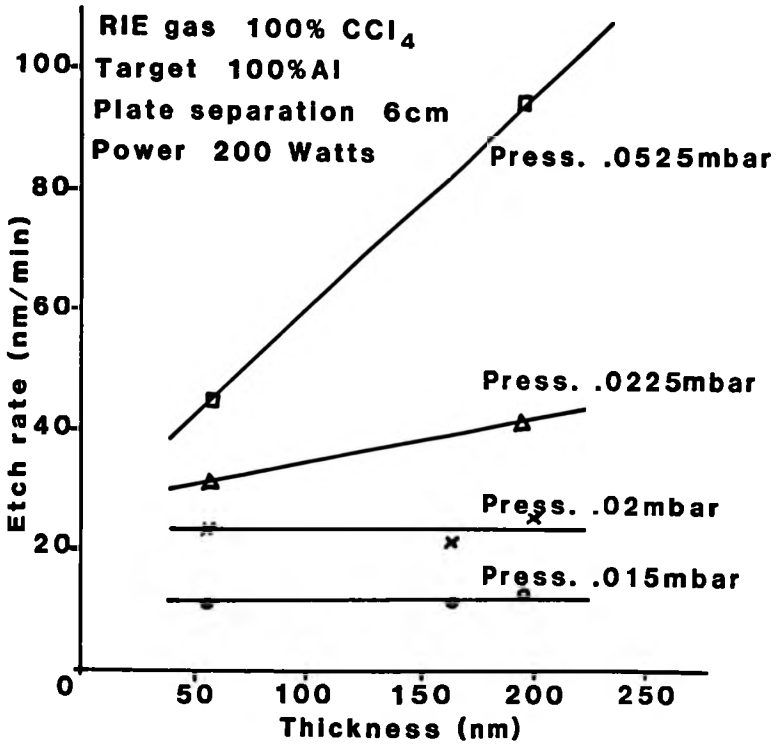

Fig.2.5.3 Etch rate as a function of sample thickness.

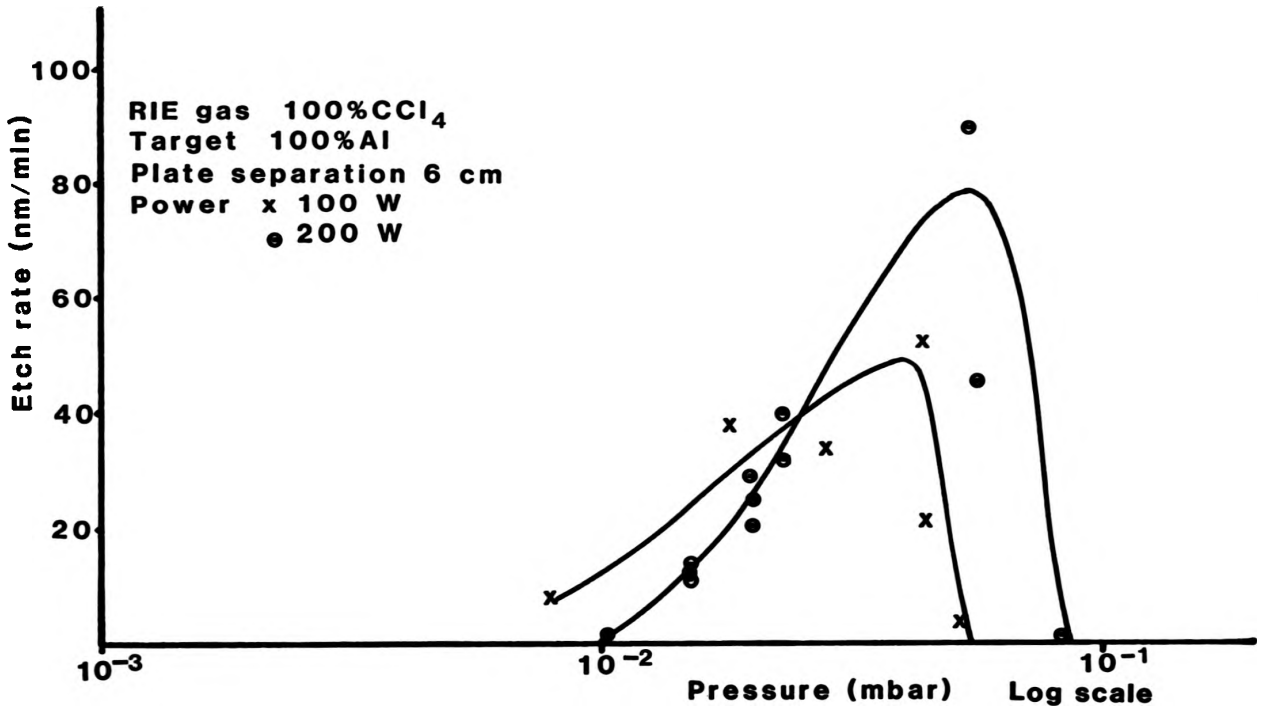

Fig.2.5.4 Etch rate as a function of pressure for RIE of evaporated Al samples.

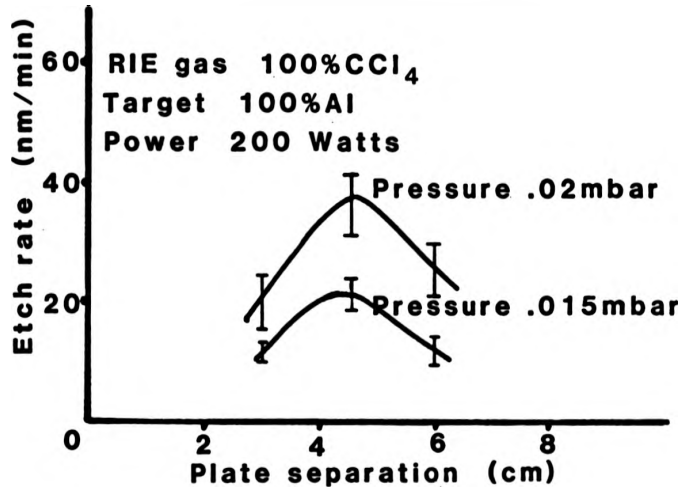

Fig.2.5.5 Etch rate as a function of reactor plate separation.

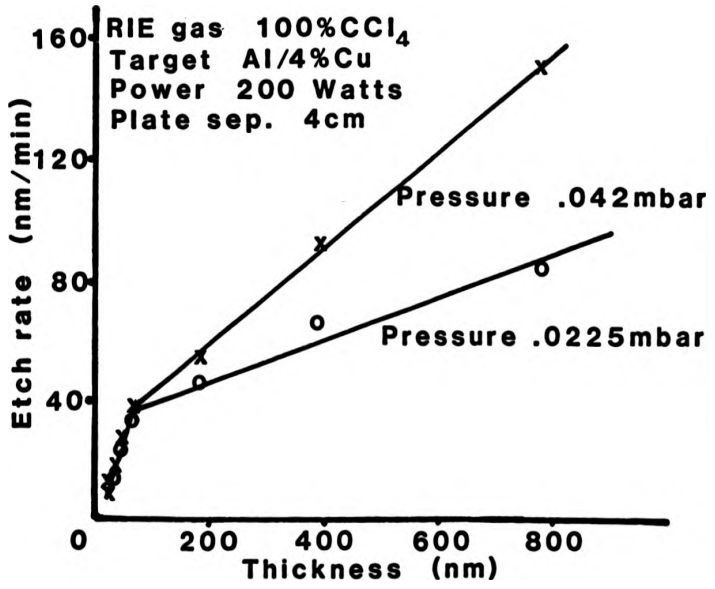

Fig.2.5.6 Etch rate as a function of sample thickness for Al/4% Cu.

can be pumped off. Figure 2.5.6 demonstrates the change of etch rate with sample thickness for two pressures. At very low thickness, < 45nm, etch rate is largely independent of pressure although it increases with thickness. This is caused by the inherent 'dead time' at the start of the etch, during which the plasma has not reached an equilibrium state. One would, therefore, expect an apparent increase in etch rate with etching time which here is noticeable at low thickness. This phenomenon was also noticed with detrimental effects on resist erosion as discussed in section 2.7. At thicknesses above 45nm the etch rate varies considerably with pressure as RIE becomes an additional influencing factor. Figure 2.5.7 illustrates the etch rate as a function of pressure for 100 and 200 Watts r.f. power as obtained for the original system and at 200 Watts for the system in its final form. A combination of factors, including the above-mentioned modifications and improvement of pumping efficiencies and general vacuum techniques, e.g. removal of contaminants and leaks, increased the useful operating range of the system. An operating pressure of 10^{-1} mbar and working power of 200 Watts were chosen for delineation of patterns. At lower powers the operating range and etch rates are too low to be of practical use, while at higher powers the etching time is too short to allow reproducible results due not only to the inaccuracy of end-point detection but also now to the large proportion of the etch time being the initial 'dead time'. The final pattern delineation was achieved with a CCl_4/Ar gas mixture at a CCl_4 partial pressure of 1.5×10^{-2} mbar, i.e. a concentration of 15%. The effect of gas composition can be seen from Figure 2.5.8. As such a large proportion of the etching time is used in oxide removal by ion milling, dilution of the

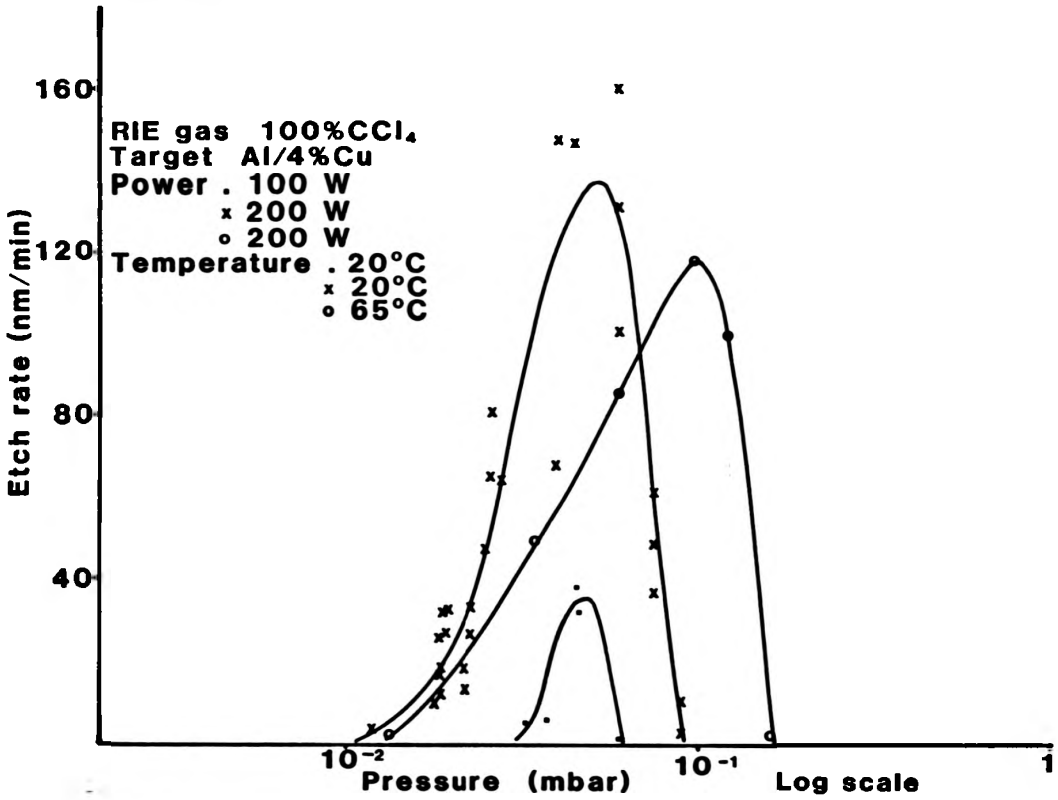

Fig.2.5.7 Etch rate as a function of pressure for Al/4% Cu.

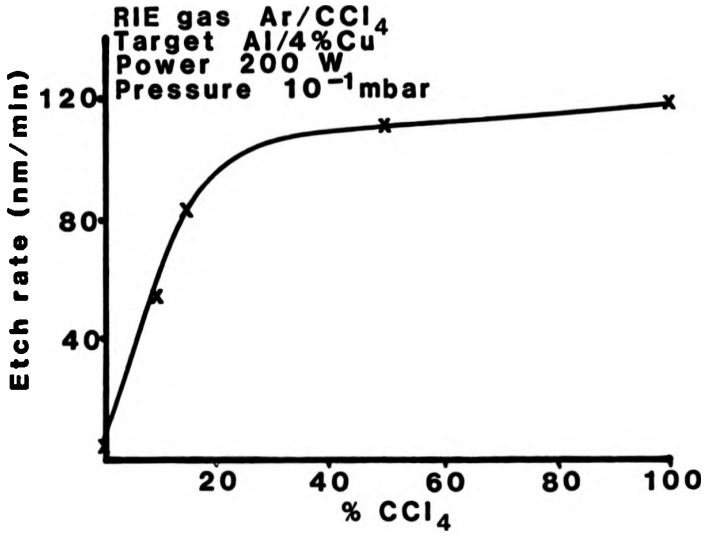

Fig.2.5.8 Etch rate as a function of gas composition.

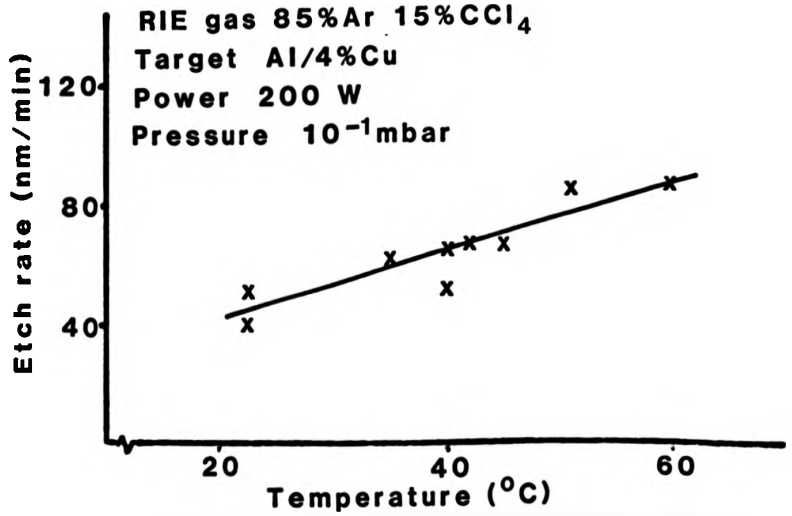

Fig.2.5.9 Etch rate as a function of reactor temperature.

reactive gas does not significantly effect etch rates until very low concentrations are reached. At the chosen partial pressures, etch rates in excess of 80nm/min were obtained. In contrast, resist erosion is reduced considerably at low CCl_4 concentrations (see section 2.7) and therefore higher Al/4% Cu: resist selectivities are obtained. Etch rate as a function of temperature, Figure 2.5.9, gives a gradual increase with temperature at this CCl_4 concentration as expected. Warming the reactor also decreases pump down time and prevents moisture condensing on the reactor when exposed to air. Correlation between CCl_4/Ar flow rate was not quantified although it was noticed that best etches were obtained at maximum flow rates. It was also noted that a high quality vacuum, $< 6 \times 10^{-6}$ mbar, was necessary before RIE commenced, again presumably due to the relative percentage of air or moisture present in the reactor.

A large overetch, an additional 30% of the etch time, was found to be necessary as there was a considerable amount of residue left on the substrate. This was not removed by heating the substrate at 200^{o}C and would therefore appear to be due to the large copper content. The overetch was limited by the relatively poor selectivity of the electron beam resist. It was hoped that there would be sufficient milling action during resist removal by air plasma to clean the substrate although this was not the case and residue remained a problem throughout the project. A more serious concern was deterioration of the metallisation layer by corrosion upon exposure to atmosphere. Any residual chlorine compounds tend to form hydrochloric acid with detrimental effects on the sample as well as the reactor itself. Various techniques were tried to combat this, such as substrate heating, quenching, long pump down before exposure

RIE of Al/4% Cu

Initial reactor pressure	$< 6 \times 10^{-6}$ mbar
Gas mixture	15% CCl_4 85% Ar
Chamber pressure	10^{-1} mbar
Rf. power	200 Watts
Temperature	$> 60^{o}C$
Overetch	30%

Removal (ashing) of Isofine positive electron beam resist

Gas mixture	80% N_2 20% O_2 (Atmosphere)
Chamber pressure	10^{-1} mbar
Rf. power	200 Watts
Temperature	$20^{o}C$
Time	5 mins
Final Passivation layer	280nm SiO_2

Figure 2.5.10 The final etch process for Al/4% Cu

to atmosphere, all with minimal effect. Resist ashing did alleviate the problem slightly as there was a rapid formation of a passive oxide layer and plasma-assisted removal of reaction products, although it was still found essential to coat the samples immediately with a passivation SiO_2 layer. Even so, all samples etched demonstrated some corrosion problems.

Figure 2.5.10 summarises the conditions chosen for pattern delineation.

2.6 End-Point Detection

As previously mentioned, the overetch was limited by the high erosion rate of the electron beam resist. Accurate determination of the end of etch would alleviate the problem and so optical spectroscopy as a form of end-point detection [73 - 75] was evaluated for the RIE of Al/4% Cu. In optical spectroscopy the intensity of optical radiation from excited species within the plasma is monitored at wavelengths corresponding to reactant or product species. During the etch, there is a reduction in reactant species within the plasma and a reduction in optical intensity at the corresponding wavelength. Conversely, as the product species enter the plasma there is an increase in optical intensity at the corresponding wavelength. In either case, the end-point of the etch is determined by the return of emission intensity to its original value. A system was constructed consisting of a photomultiplier, a motor-driven monochromator, a chopper noise-reduction circuit (see Appendix 2.3), and an X-Y plotter for recording the optical spectrum of the discharge. Although spectrum lines characteristic of Al were encountered at

309nm and 396nm the sensitivity of the system at wavelengths below 400nm was insufficient for practical use as a quartz window was not included.

A commercial spectroscopy system (UTI Instruments Company model 1011) which was available on temporary loan, has also been used with significantly better results. Unlike the above system, the UTI model incorporated a quartz window allowing wavelengths as low as 240nm to be transmitted via a quartz optical fibre to a monochromator. The optical emission at the wavelength of 255nm, corresponding to molecular chlorine [75], was found to be most useful in indicating a reduction in available chlorine during etching. The system was, however, not incorporated as a permanent feature not only due to the cost (approximately £8000) but also due to the lack of reliability (intermittent electronic faults) and reproducibility of the equipment.

Figure 2.6.1 shows an example of the reduction in optical emission at 255nm during 100% CCl_4 RIE of 250nm of Al/4% Cu using a power of 300 W, plate separation of 4cm, and a pressure of 1×10^{-2} mbar. For the first minute the emission remains constant indicating a non-chemical removal of the oxide barrier. The subsequent sharp fall and slow rise demonstrates the depletion of the molecular chlorine during the etch process, the end-point arriving at 5.5 minutes. In contrast Figure 2.6.2 was taken during a 'bad' etch under similar conditions (pressure = 2.3×10^{-2} mbar). The source of contamination was traced to the deterioration of an O-ring in the target water-cooling system which allowed small quantities of moisture to be present in the plasma, dissociating to leave oxygen ions. The oxide barrier was, therefore, replaced almost as quickly

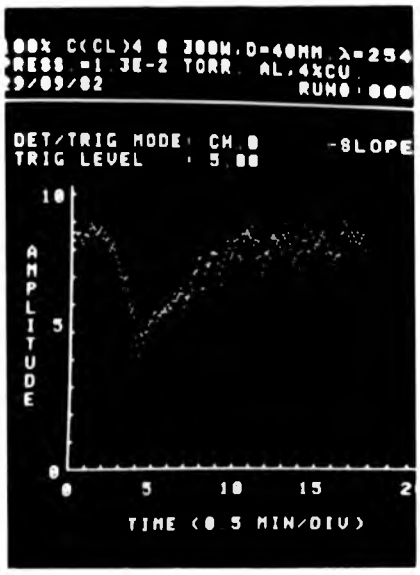

Fig.2.6.1 Reduction of optical emission at 255nm during RIE of Al/4% Cu.

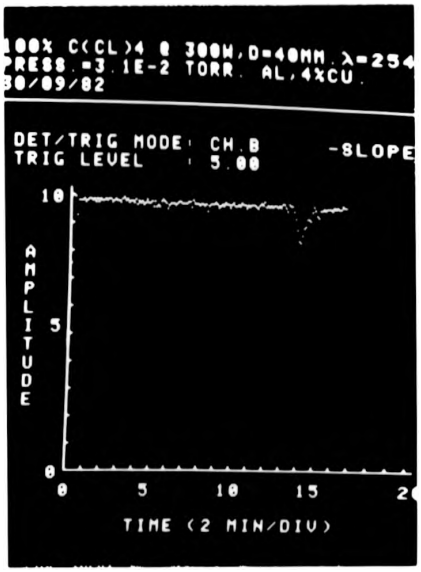

Fig.2.6.2 Reduction of optical emission at 255 nm during RIE of Al/4% Cu while there was a small system leak.

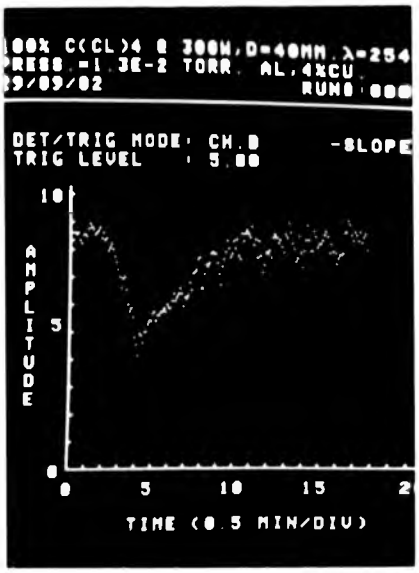

Fig.2.6.1 Reduction of optical emission at 255nm during RIE of Al/4% Cu.

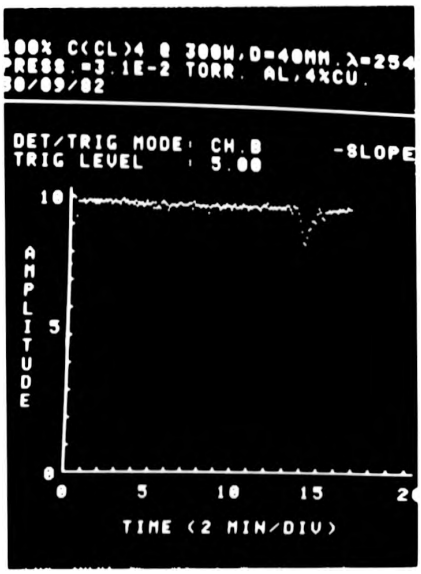

Fig.2.6.2 Reduction of optical emission at 255 nm during RIE of Al/4% Cu while there was a small system leak.

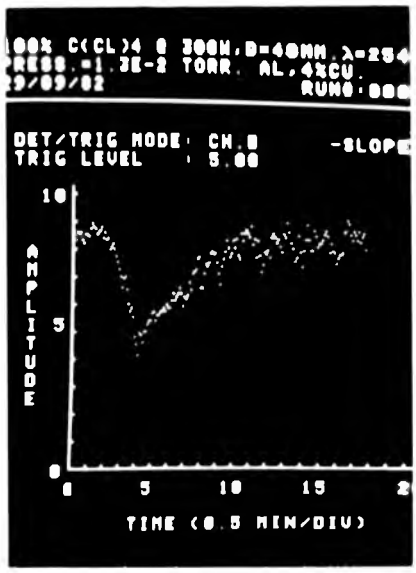

Fig.2.6.1 Reduction of optical emission at 255nm during RIE of Al/4% Cu.

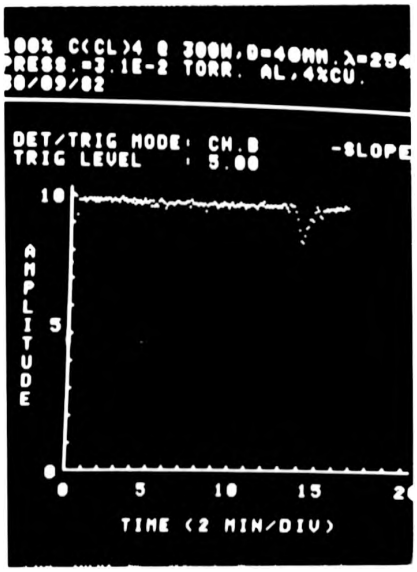

Fig.2.6.2 Reduction of optical emission at 255 nm during RIE of Al/4% Cu while there was a small system leak.

as it was removed [59] and the actual reactive etch did not take place until 26 minutes. Even assuming that all the aluminium was converted to oxide this would still indicate that the removal rate of oxide is less than 10nm/min. This dramatically illustrated the necessity of good vacuum quality and techniques during RIE of aluminium.

The use of a mass spectrometer as an end-point detector was considered although lack of time necessitated abandoning this in favour of device fabrication. End-point detection was finally determined by simple observation of the sample becoming optically transparent during etching. Large unused areas of the test devices were exposed to etching to facilitate this process. As a consequence of this rather crude method of end-point detection, the reproducibility of the etch was not good. It was difficult to determine with greater than 25% accuracy when the end-point had arrived and often the patterns would be under or overetched.

2.7 Electron Resists

In all three electron resists were used while establishing the fabrication process these being Isopoly E-B negative resist -NS (12.5), Isofine E-B positive resist -PM (15), both manufactured by Micro-Image Technology Limited, and a poly-methyl-methacrylate (PMMA) positive resist of 4% weight in methyl isobutyl ketone, produced within the Department of Electrical Engineering [76]. After development, negative resist remains and positive resist is removed where it has been exposed. The negative resist was included only for comparison as a positive resist is more practical for etching holes

as in the apertured-conductor devices.

Before spin coating, the substrates were baked at 150°C. The thickness of resist spun on 7mm x 7mm substrates was experimentally determined as a function of spin speed (see Appendix 2.4) giving 0.6μm for both the negative and Isofine positive and 0.2μm for PMMA at 2750 r.p.m. After spinning the substrates were baked at 120°C for negative resist and 170°C for both positive resists. At the above thicknesses, the best electron exposures were obtained at 20kV accelerating potential as 24.6μC/cm^2, 112μC/cm^2 and 840μC/cm^2 for the negative, Isofine positive and PMMA respectively. The Isopoly negative and Isofine positive resists were spray developed using the manufacturer's recommended developers after which they were baked at 150°C. The PMMA was spray developed in one part methyl isobutyl ketone, three parts isopropyl alcohol, after which it was baked at 170°C. No significant loss of thickness due to development was observed for the negative and Isofine positive resist, although a 20-30% loss occurred in PMMA.

Resilience of electron resists to RIE is known to be poor [77] and was indeed a major problem with both positive resists. The negative gave comparatively good results, selectivities (Al/4% Cu: Resist) of 4:1 being obtained without difficulty. This was attributed to the higher degree of random cross-linkage between molecular chains in the exposed regions of negative resist than unexposed regions of positive resist [78]. Both positive resists gave selectivities of the order 0.5:1 in a 100% CCl_4 RIE. Introduction of Argon as a dilutant for CCl_4 in the parallel plate reactor improved matters somewhat. Figure 2.7.1 illustrates etch rate as a function of CCl_4 concentration for Isofine positive. The erosion rate drops

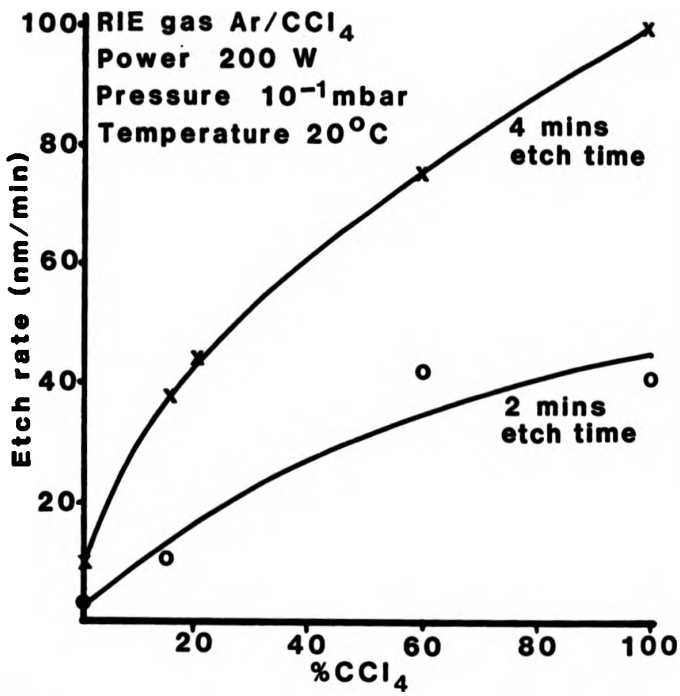

Fig.2.7.1 Etch rate as a function of gas composition for Isofine positive electron beam resist.

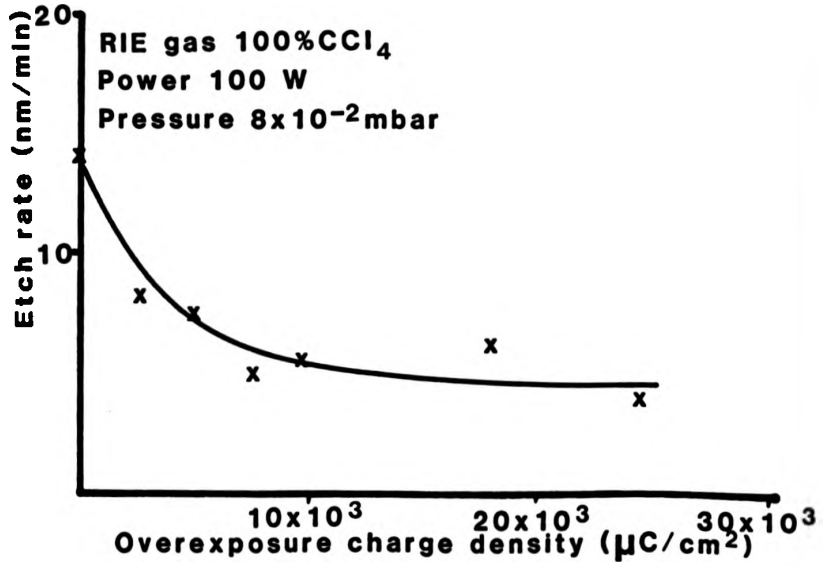

Fig.2.7.2 Etch rate of PMMA as a function of overexposure charge density.

more quickly with decreasing CCl_4 concentration than that observed for Al/4% Cu due to the oxide layer as previously mentioned. Also evident from Figure 2.7.1 is the increase of erosion rate with etch time which became a limiting factor on the percentage overetch possible. The etch rate for an etching time of 4 minutes is twice that for an etching time of 2 minutes. This is attributed to the system dead time mentioned in section 2.5 and an increase in the substrate temperature with time.

It is known that under gross overexposure conditions, positive resist demonstrates a higher degree of cross-linkage and effectively acts as a negative resist [78]. During RIE of exposure test patterns in PMMA, it was observed that grossly overexposed regions had not been removed during development and displayed greater resilience to the plasma than unexposed regions. It would, therefore, appear feasible to harden the resist by flooding the developed pattern with electrons in vacuum. This was briefly evaluated using the electron beam machine so as to quantify exposure dosages and spot energies, although a separate vacuum system and a simple filament would suffice. A similar technique is applied in photolithography where developed photoresist patterns are exposed to deep ultra violet radiation to improve hardness [79]. Ultra violet light was not, however, found to have any effect on the resilience of electron resists in this work.

Figure 2.7.2 outlines the decrease in erosion rate of PMMA as a function of overexposure charge density. As expected the resist gradually becomes less susceptible to erosion, the change becoming less noticeable above 10×10^3 $\mu C/cm^2$. The increased resilience was also accompanied by a reduction in resist thickness of up to 50% as

shown in Figure 2.7.3. The reduction in thickness appears closely to follow the decrease in erosion rate again becoming less noticeable above 10 x 10^3 $\mu C/cm^2$. A further influencing factor was found to be the energy per exposure spot as can be seen from Figure 2.7.4. In this case the charge density and, therefore, the total energy per unit area was maintained at a constant value and the electron beam energy increased by exposing at higher currents for shorter times. Again, above a given energy, 120 pJ, this effect becomes less noticeable. No degradation of the resist such as flowing of the pattern or physical damage could be seen over this range of exposures although at much higher energies (> 800 pJ) both the resist and underlying Al/4% Cu layer were destroyed by thermal evaporation. It would seem reasonable to assume the reduction in thickness is not by resist removal but by resist compaction associated with increased cross linkage, increasing its density which would account for its increased etch resistance. By this method selectivities of 2.5-3:1 were obtained for thickness reduced PMMA in a 100% CCl_4 RIE which, even accounting for the reduction in thickness, gave a significant improvement. Initial indications are that a similar effect to a lesser extent is also evident in the Isofine positive althought this was not quantified. The resist hardening technique was eventually abandoned as the large electron beam currents were not considered beneficial to the long term quality of the very much finer pattern exposures as they damaged the filament and, in one instance, the blanking coils. Rather than construct a separate vacuum system for resist hardening the patterns were exposed in Isofine positive and etched at low, 15%, CCl_4 concentrations.

Ashing of resist [80] after etching has been achieved in a plasma

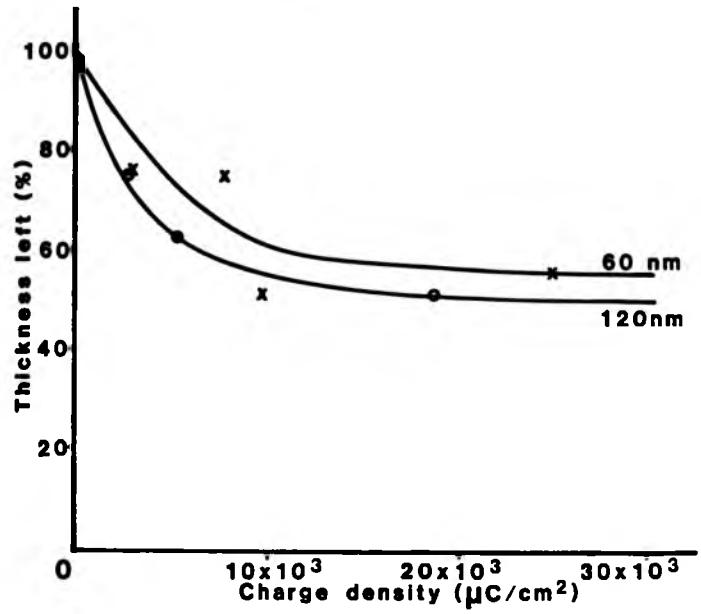

Fig.2.7.3 Reduction of PMMA thickness with overexposure charge density.

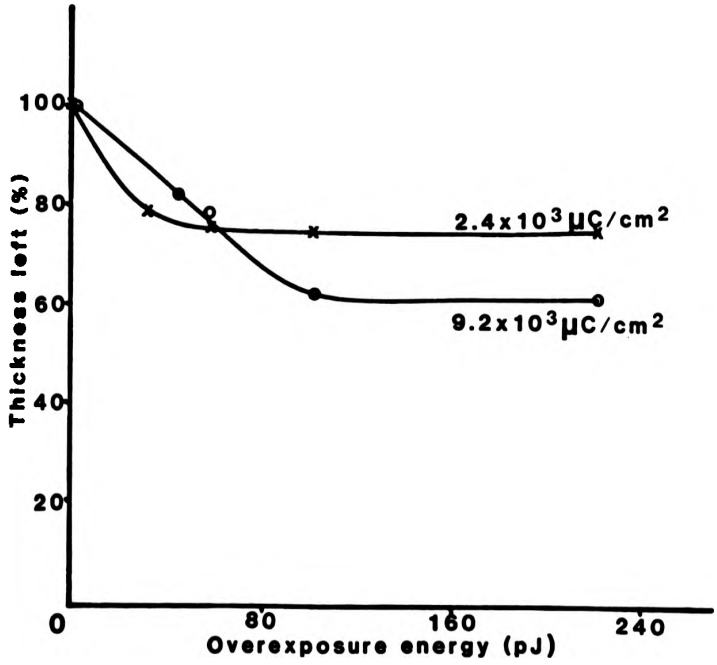

Fig.2.7.4 Reduction of PMMA thickness with increasing electron beam energy.

discharge of N_2/O_2 in an atmospheric ratio. Using the same parallel plate reactor, air was bled into the system through a silica gel drier and a 0.25μm aperture Millipore filter (see Figure 2.5.2). Figure 2.7.5 demonstrates that 50-60 nm/min removal rate of Isofine positive is possible using this method. In comparison the removal of Isopoly negative is more difficult, 20-30 nm/min, this being another indication of the increased hardness of a negative resist. No degradation of the underlying Al/4% Cu layer was noticed. Indeed, it was hoped that formation of an oxide layer in this manner would be beneficial in reducing the effect of pinholes in the SiO_2 insulation and de-scum and passivate the substrate. In practice both corrosion and residue problems remained due to the higher pressure of the ashing plasma and therefore reduced milling effect on the target. Final passivation of the samples was achieved by a 280nm top layer of SiO_2. The ashing process does have the advantages of being non-critical and performed in-situ, removing a handling step.

2.8 Current-Accessed Circuit Test Equipment

The test devices were intended to be studied dynamically using the high speed stroboscopic sampling system [38] and video measuring equipment [81] previously described. As the existing bubble controller [82] is only for conventional field-accessed devices, a current-accessed drive and bubble nucleator were constructed. The controller specifications required a four-phase clock capable of supplying 0-1 Ampere currents from D.C. to 10 MHz, and a bubble nucleator capable of generating an eight bit bubble pattern with 200-400mA pulse currents. In addition, a probe card was incorporated

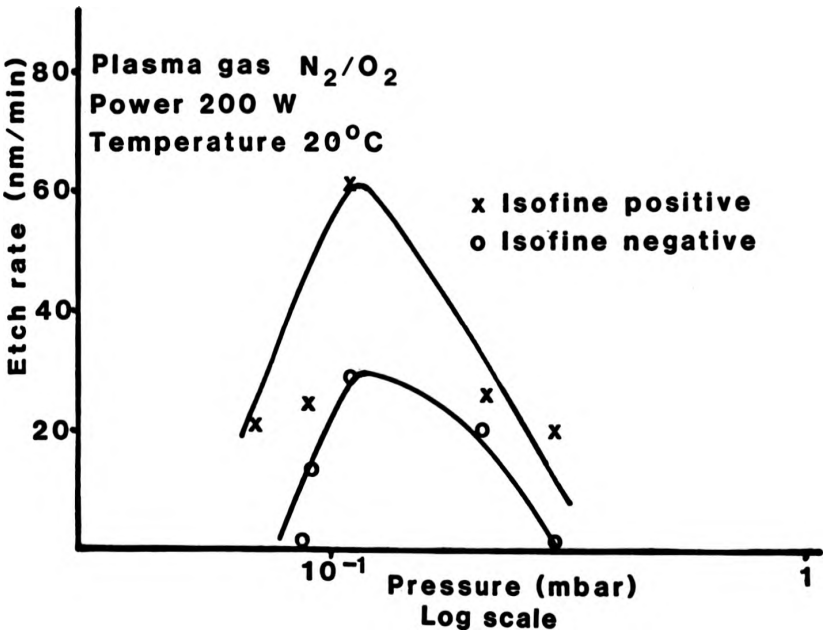

Fig.2.7.5 Etch rate of electron beam resist in a nitrogen/oxygen plasma.

in a microscope stage for easy insertion of the 7mm x 7mm test devices. Photographs of the controller and probe card are shown in Figure 2.8.1 and the controller circuit diagrams are included in Appendix 2.5.

The clock generator circuit was designed to provide a four-phase clock from an external one of twice the frequency. The design is non-synchronous and care has been taken to ensure switching of clock edges at non-critical times to avoid spurious output. Features of the design include on/off (S1), forwards/backwards (S2), and 0%/50% overlap (S3). The latter permits a 50% overlap between adjacent pulses and is intended to assist bubble propagation by repelling the bubble from its previous potential well, as the subsequent one becomes available.

The bubble nucleator generates an eight bit bubble pattern by passing a current through an on-chip hairpin nucleator. The bit pattern is manually set (S5-S12), loaded by a divide-by-eight counter (IC11) and used to trigger one of two monostables (IC9(b)). The input trigger is gated with a second monostable (IC9(a)) and adjustment of both monostable pulse widths (VR1, VR2) can set not only the nucleate pulse width but also a delay from the input clock trigger. Additional features include adjustable output current amplitude (VR3), enable/disable (S14) and choice of triggering clock pulse (S4).

The pairs of clock outputs corresponding to the two conductor layers are output to the device via two push-pull current amplifiers. A variable (VR4, VR5) 0-1A output pulsed current is obtained. The circuit has been tested in the 0-10MHz 0-1A range. Although at the top of the frequency range at maximum current the waveforms become

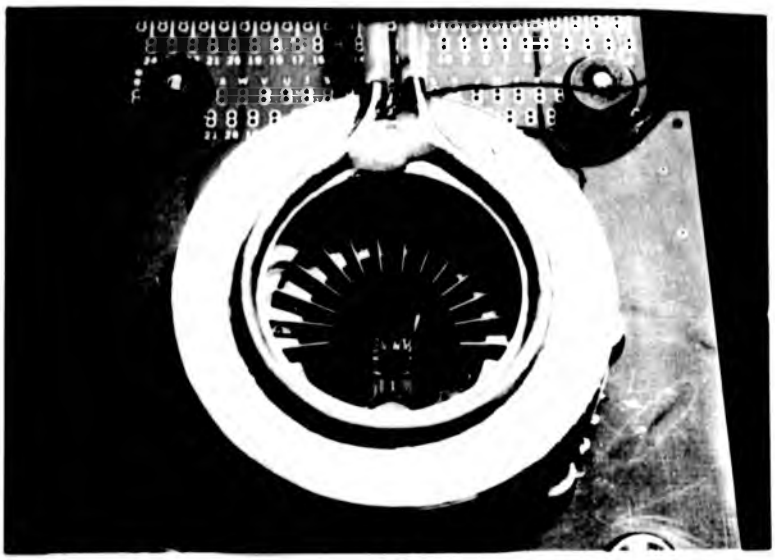

(a)

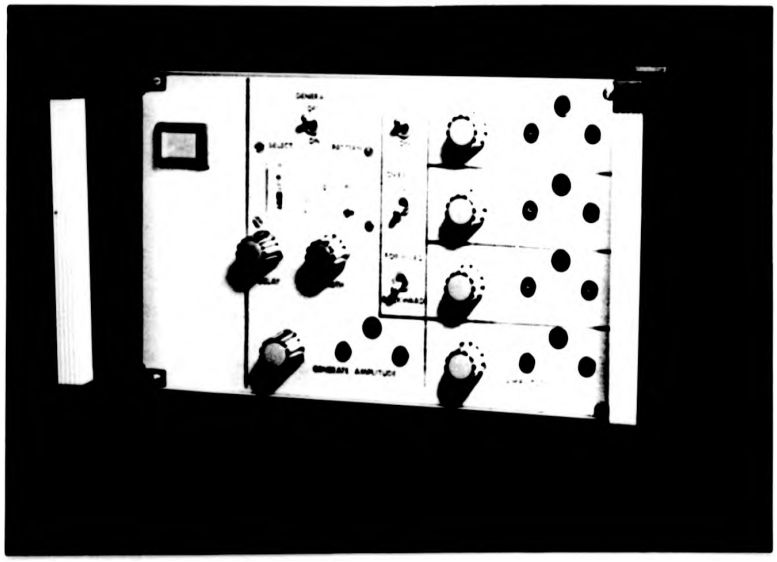

(b)

Fig.2.8.1 (a) The probe card. (b) The current-access bubble memory controller.

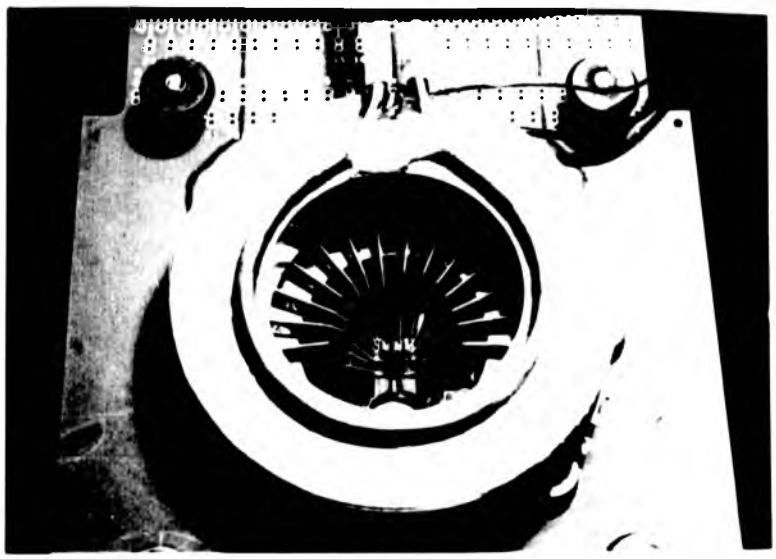

(a)

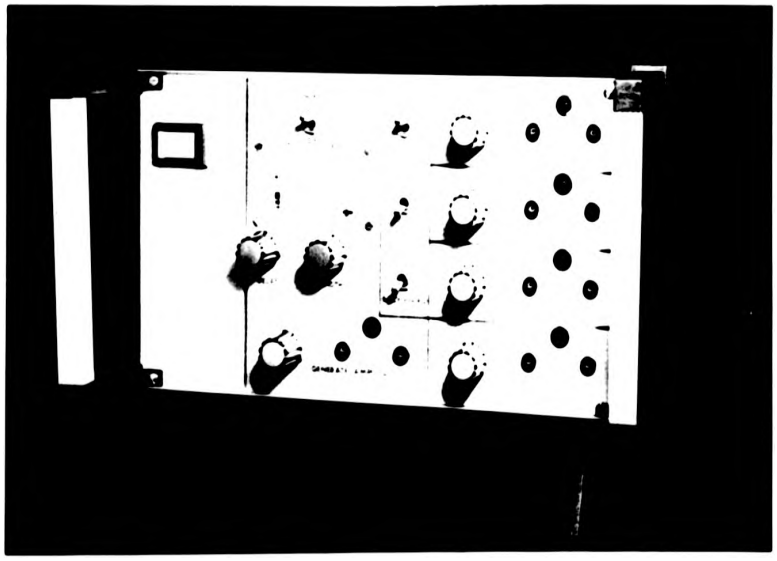

(b)

Fig.2.8.1 (a) The probe card. (b) The current-access bubble memory controller.

(a)

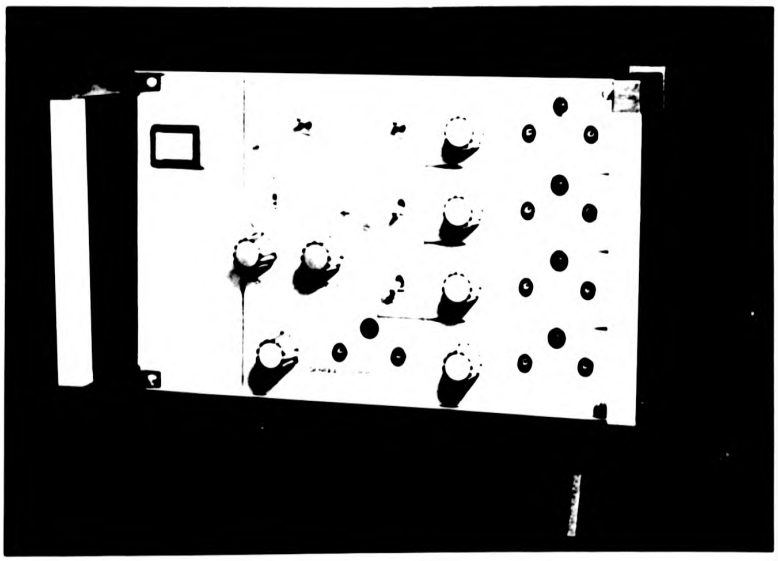

(b)

Fig.2.8.1 (a) The probe card. (b) The current-access bubble memory controller.

slightly degraded, it was considered perfectly adequate for devices of up to twice the cross-sectional width of the initial test devices (see section 2.2).

A probe card (Wentworth Laboratories Limited) was incorporated in a microscope stage to facilitate testing. The stage is hinged for easy insertion of samples and includes water-cooled bias coils. The fourteen probe pins are arranged such that three pins per probe are available for the high current-drive inputs.

2.9 Discussion and Summary

A process for delineating current-access propagation patterns in Al/4% Cu has been established, entailing Electron Beam Lithography and RIE using CCl_4-Argon gas mixtures. An anisotropic etch profile was obtained enabling 1μm lines to be delineated although corrosion and residue presented some problems, see Figure 2.9.1. Sub-micron features were fabricated although, in general, the electron resist in those regions was underexposed as there was no proximity-effect correction [83] of the patten data i.e. adjustment of the exposure charge density at pattern edges. Using an N_2/O_2 plasma to remove the resist did alleviate some of the residue and corrosion problems although it was essential immediately to coat the devices with a final SiO_2 passivation layer. A flowing N_2 glove box over the RIE reactor would have helped prevent the samples from coming into contact with the atmosphere and is highly recommended for future work using this system.

Figure 2.9.2 and Figure 2.9.3 illustrate two typical devices fabricated. The limiting factor of all devices fabricated was the

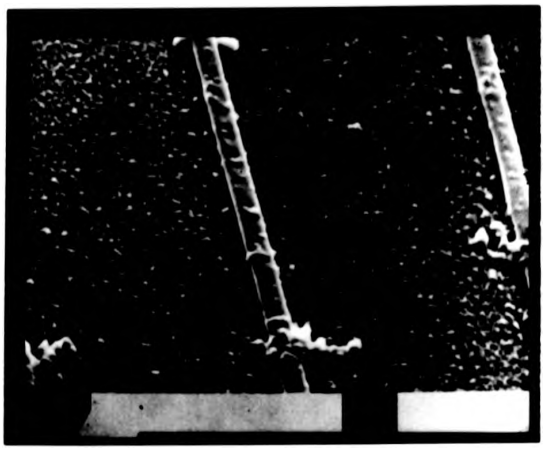

Fig.2.9.1a 1 μm lines etched in Al / 4% Cu. The resist (Isopoly negative) has not been removed and there is considerable corrosion and residue.

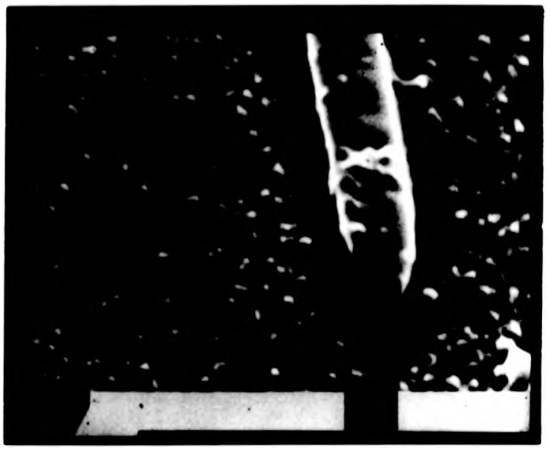

Fig.2.9.1b As above. An anisotropic etch profile is obtained with the RIE process.

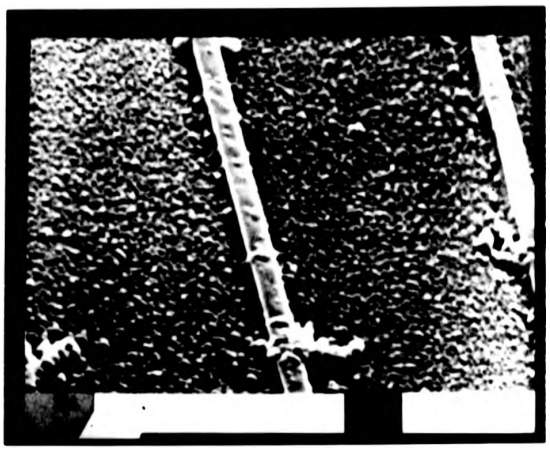

Fig.2.9.1a 1 μm lines etched in Al /4% Cu. The resist (Isopoly negative) has not been removed and there is considerable corrosion and residue.

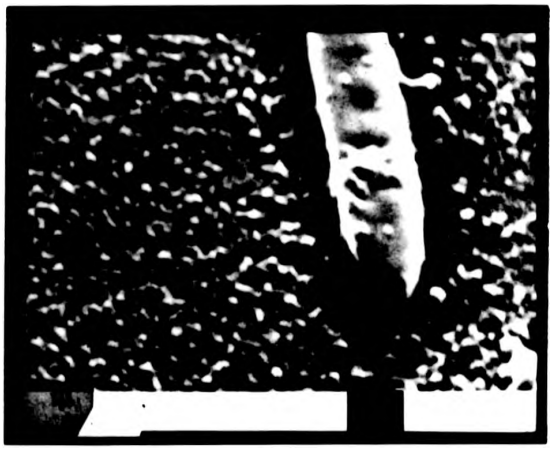

Fig.2.9.1b As above. An anisotropic etch profile is obtained with the RIE process.

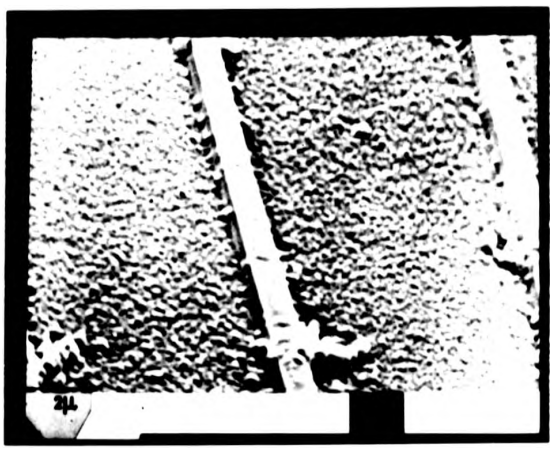

Fig.2.9.1a 1 μm lines etched in Al / 4% Cu. The resist (Isopoly negative) has not been removed and there is considerable corrosion and residue.

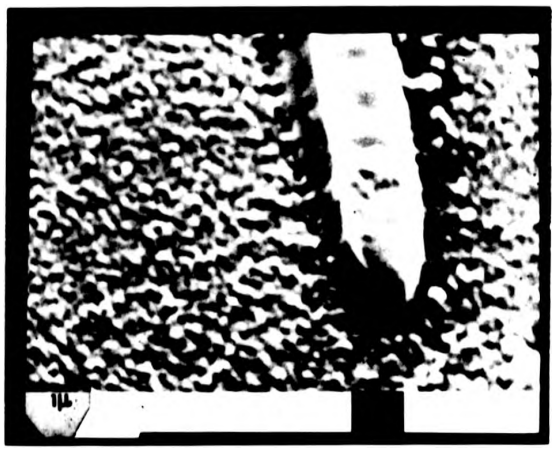

Fig.2.9.1b As above. An anisotropic etch profile is obtained with the RIE process.

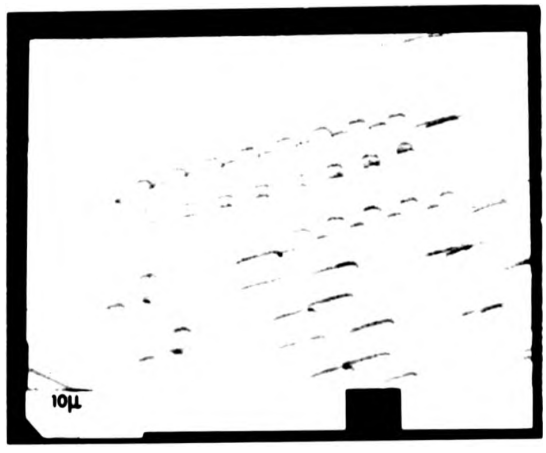

Fig.2.9.2a An example of the current-accessed devices fabricated. Alignment between layers is poor but corrosion and residue are minimal.

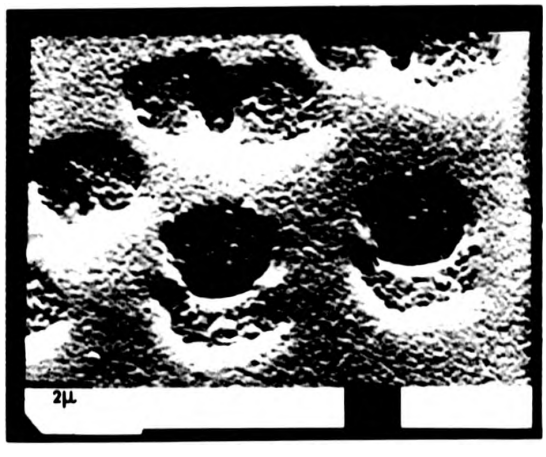

Fig.2.9.2b As above illustrating the good step coverage obtained by sputter deposition.

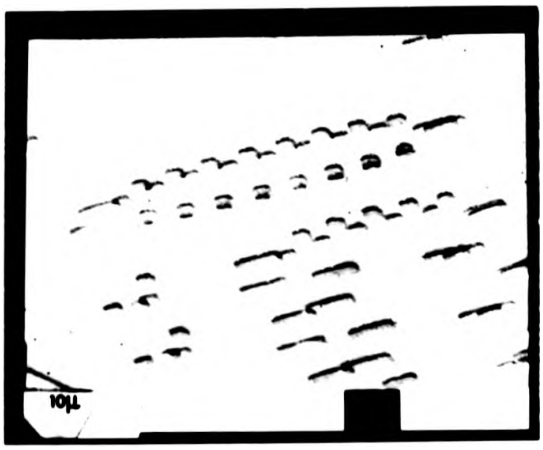

Fig.2.9.2a An example of the current-accessed devices fabricated. Alignment between layers is poor but corrosion and residue are minimal.

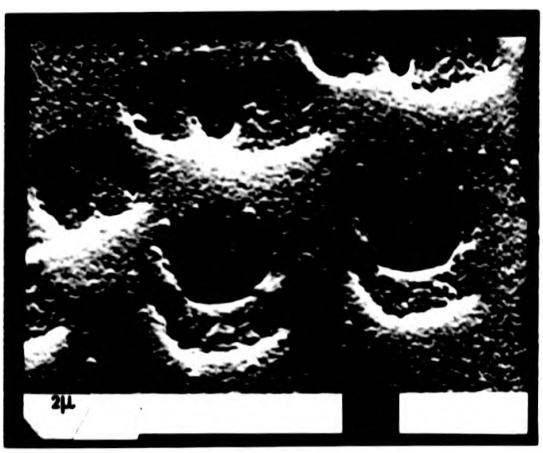

Fig.2.9.2b As above illustrating the good step coverage obtained by sputter deposition.

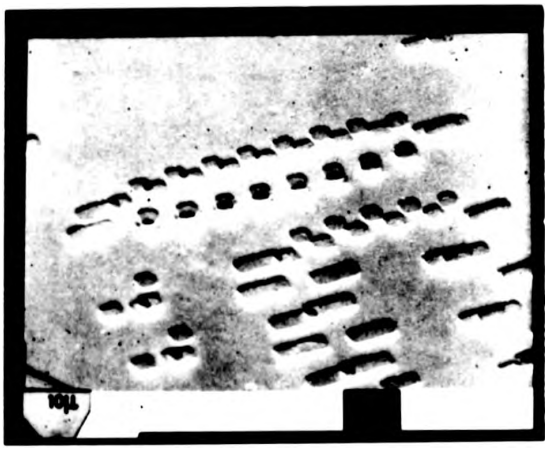

Fig.2.9.2a An example of the current-accessed devices fabricated. Alignment between layers is poor but corrosion and residue are minimal.

Fig.2.9.2b As above illustrating the good step coverage obtained by sputter deposition.

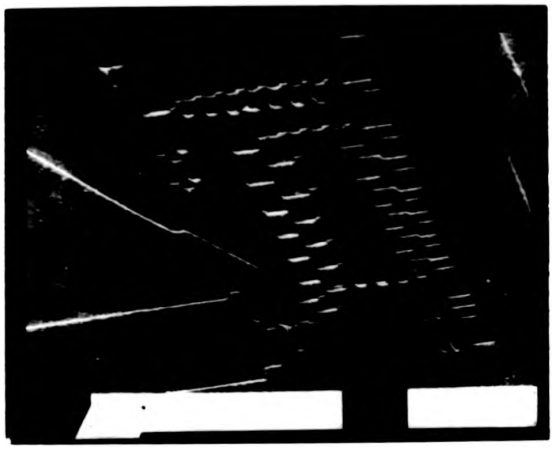

Fig.2.9.3a A further example of the fabricated devices. Again second layer alignment is poor.

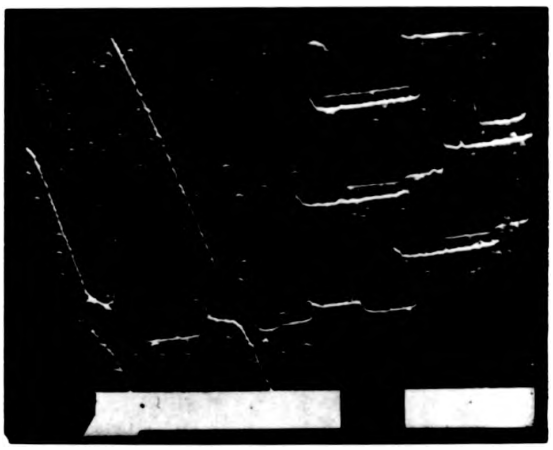

Fig.2.9.3b The generator section of the above sample. The large 'hillock' formation is attributed to the poor thermal contact of the substrate holder during sputter deposition.

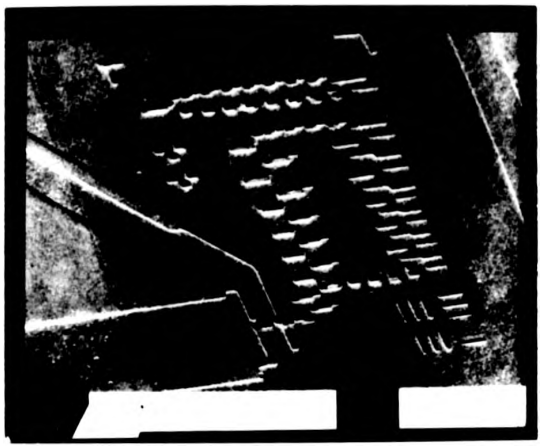

Fig.2.9.3a A further example of the fabricated devices. Again second layer alignment is poor.

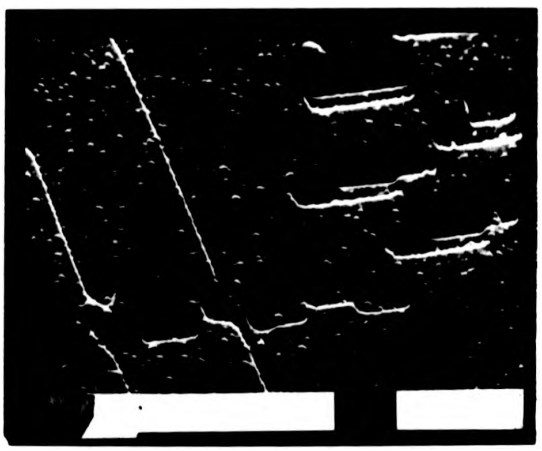

Fig.2.9.3b The generator section of the above sample. The large 'hillock' formation is attributed to the poor thermal contact of the substrate holder during sputter deposition.

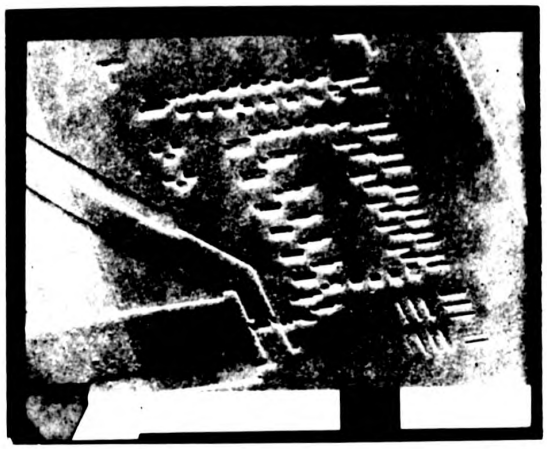

Fig.2.9.3a A further example of the fabricated devices. Again second layer alignment is poor.

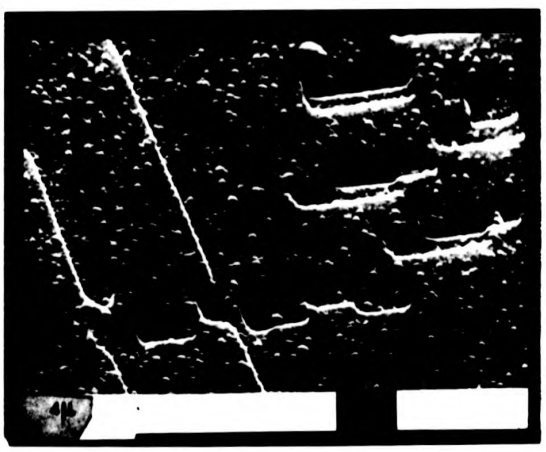

Fig.2.9.3b The generator section of the above sample. The large 'hillock' formation is attributed to the poor thermal contact of the substrate holder during sputter deposition.

poor alignment of the second layer. This was due to the rather poor quality of the registration pictures obtained from the EBM in SEM mode and its somewhat temperamental operation at the time of this project. This was due to a number of reasons. The beam deflection in SEM mode was non-linear giving significant picture distortion. The beam blanking at flyback was not effective resulting in severe loss of picture contrast. In addition, due to the physical dimensions of the exposure chamber, the electron detector was positioned at a distance from the exposure area which was too great to give an acceptable signal-to-noise ratio. Subsequently a new exposure chamber has been constructed by Pickard of this Department with provision for a backscattered electron detector (K. E. Developments Limited). This has now been fitted to the EBM greatly improving the quality of registration pictures. Misalignment is not expected to present a problem to future work [84]. However the devices fabricated were aligned to no better than 2μm ($\tilde{}$ $\frac{1}{4}\lambda$) and were not expected to work at anything other than quasi-static state at best.

By far the most difficult fabrication process was the RIE of Al/4% Cu. The etch was not very reproducible due to the difficulties of oxide removal and required a reasonably high quality vacuum. In addition an unacceptably large proportion of the project time was spent on vacuum maintenance due to the highly corrosive nature of CCl_4 and its detrimental effects on vacuum seals and pumping fluids. The main benefit of RIE, the ability to increase the selectivity between mask and metallisation layer, was not realised for this process. RIBE would not necessarily improve any of these factors. The reproducibility of the etch could be increased if gas flow

controllers maintaining an accurate gas composition were used together with end-point detection although this would increase the basic reactor cost by a factor of six and in no way improve the vacuum system reliability. An alternative which should seriously be considered for future work is ion beam milling with an inert gas such as Argon. This would remove the system reliability problems associated with CCl_4 operation and would give selectivities of the same order as those obtained. A conceivable problem with ion milling is the inability to discriminate between etched layer and underlying material. However, as the etch rates of aluminium and oxide are similar, the reproducibility of the etch could be maintained without end-point detection. In addition, the corrosion and residue problems would be removed. A final SiO_2 passivation layer would still be desirable. The disadvantage is the high cost of a sufficiently powerful ion source although it should be mentioned that such a system would not be limited to any one etching process, as is the RIE of Al/4% Cu using CCl_4, and therefore the cost could possibly be shared with alternative projects requiring high quality lithography. Furthermore the price of such equipment is falling as it becomes more widely used in industry and may well prove a cost-effective solution in the future.

In conclusion, the limiting factors to device fabrication were the poor alignment of second layer and the difficulty of RIE using CCl_4. Steps have subsequently been taken to improve alignment and this is no longer considered a problem. RIE of Al/4% Cu has been demonstrated to be possible although the process, using the equipment available, was unreliable and unreproducible. A non-reactive ion-milling process would appear more attractive for this type of

lithography. The remaining processes, sputter deposition and resist ashing gave good results and there inclusion in future work is recommended. The test devices fabricated were not of a sufficiently high quality to be tested.

CHAPTER III

VERTICAL BLOCH LINE MEMORY

3.1 Introduction

For many years now it has been known that vertical Bloch lines (VBLs) could be injected into a domain wall [86] and that VBLs are controllable and movable within the domain wall [87]. It was not, however, until Konishi [10] conceived a method of detecting VBLs that the concept of using them in a stripe domain wall as a form of serial storage was proposed. Although such a device is likely to share certain common features, materials and fabrication processes with conventional bubble devices and as such is naturally regarded as a development or offshoot of bubble technology, it should be stressed that the basic storage mechanism is quite different. Because the wall structure is intrinsically of a finer scale than the volume of a domain, substantial increases in storage density over bubble memory are anticipated. The concept of coding data using domain wall structures is, however, not new. Schwee [88] proposed using the presence or absence of "cross-ties" in films thin enough to support both Bloch and Neel walls to represent binary information. VBL memory uses a material with a comparatively low magnetisation and with lower demagnetising effects so that smaller structures are possible. Also, the bubble "lattice" memory [13] use different domain wall structures to code data and although increases in storage

density over conventional bubble memory are possible the basic storage mechanism uses a domain to denote only one bit as opposed to thousands of bits per domain for VBL memory.

The proposed chip architecture for VBL memory is similar to the major-minor loop organisation of a bubble memory. The main storage area, i.e., the minor loops, are made of stripe domains where the presence or absence of a pair of negative VBLs in the stripe domain wall denotes binary information. VBL pair bit position is defined by a periodic in-plane field potential well and a perpendicular drive field provides a gyrotropic force to propagate the VBLs around the stripe domain wall. The major loop comprises a bubble propagation track with a nucleator, detector, and bubble-VBL read/write gates. At the time of writing, a device including all three basic functions, write, propagate and read, has not yet been produced although the individual functions have been experimentally confirmed [89 - 90] in work associated with the initial VBL memory proposal of Konishi. In addition, Hidaka and Matsutera [91] have demonstrated that shallow ion implantation can be used to define VBL bit positions and Klein and Engemann [92] have shown that the stripe domains, i.e., minor loops, may be confined by local material thinning. Wu and Humphrey [93] have fabricated a VBL write gate which demonstrated good operating margins and although as yet a fully operational read gate has not been fabricated it is anticipated to be similar in design to the write gate. One of the greatest problems for experimental work on VBL memory is the difficulty of observing such fine structures. By far the most practical method of determining Bloch line position is by disturbing the wall with a perpendicular pulse field [87] or field gradient [94] and observing the wall distortion associated with

the low mobility of a region of wall containing Bloch lines. This method suffers from the drawback that to distort the wall sufficiently to be observed by polarised light a comparatively large force has to be applied, thereby disturbing the very structure that is to be examined. Consequently the resolution is somewhat limited. Fortunately, bubble wall physics has been extensively developed over the past decade and the static and dynamic characteristics of Bloch lines can be mathematically predicted with a high degree of confidence. It is by such device modelling that much of the early research on VBL memory is being undertaken and the design of experimental devices being achieved.

In the following sections the detailed operation of VBL memory is discussed. Many of the ideas presented have resulted from group research in the Department of Electrical Engineering at Kyushu University to which the author contributed. When it is possible to identify the contributions of other individuals, credit is given to specific members of this research group. A simple model of a VBL is used to compare forces acting on a VBL and thereby project theoretical performance. Possible chip architectures, problems and future developments are explored and in conclusion the usefulness of such a device is examined.

3.2 VBL Memory Operation

3.2.1 The write process

To write one bit in a stripe domain wall a pair of negative VBLs is injected by the punch-through process discussed in Chapter 1.

Consider the azimuthal angle of magnetisation, ϕ, at a stripe head as it expands in a perpendicular field, Hz. Equation 1.3.17 states that ϕ will precess around Hz. If the chirality of the wall and polarity of Hz are such that ϕ will increase as shown in Figure 3.2.1, at a critical Hz a portion of the wall will prefer the minimum energy contour of B as opposed to the original contour, A, and a HBL will nucleate. As the stripe head continues to expand a gyrotropic force acts on the HBL propagating it to the opposite surface in a similar manner as that discused with respect to VBLs in Chapter 1. If Hz is increased further, the HBL will punch-through at the surface, totally reversing the chirality of the stripe head and leaving VBLs of opposite polarity on either flank of the stripe head. The critical wall velocity for punch-through is given by [45]

$$v_p \simeq 24\ \gamma A/(hK^{\frac{1}{2}}) \qquad .....3.2.1$$

The positive and negative VBLs at the stripe head are an unwinding pair which could recombine, and so to create a stable winding pair (representing one bit of data) the positive VBL is replaced by a negative VBL using a chopping process. This is illustrated in Figure 3.2.2. A negative VBL is included in the initial stripe head making both flanks symmetrical as will be discussed later. After punch-through, (c), the positive VBL is placed at the stripe head and the head of the stripe is removed by a chopping action, (e-f). The direction of magnetisation in the merging walls, e, is such that a negative VBL is formed by the chop. It is for this reason that negative as opposed to positive VBLs have been defined as information carriers. The final stripe, f, now has an additional pair of

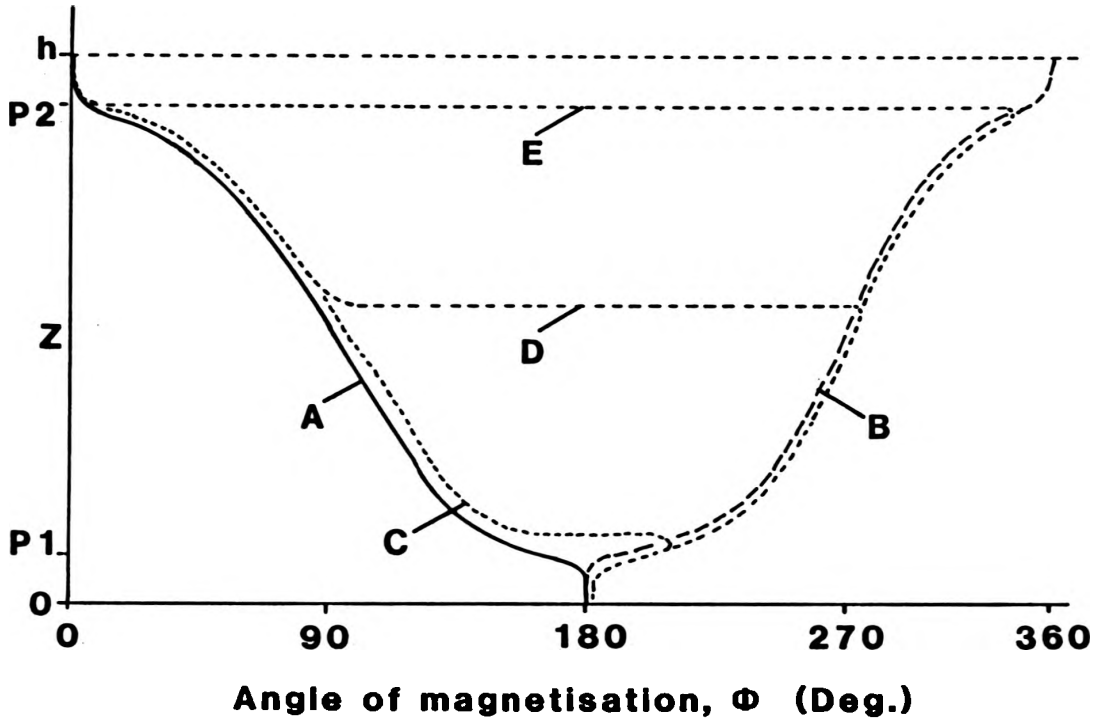

Fig.3.2.1 Azimuthal angle of magnetisation ϕ at wall centre (A,B) through the thickness, (C) as a HBL nucleates and, (C-E) as a HBL propagates through the material thickness.

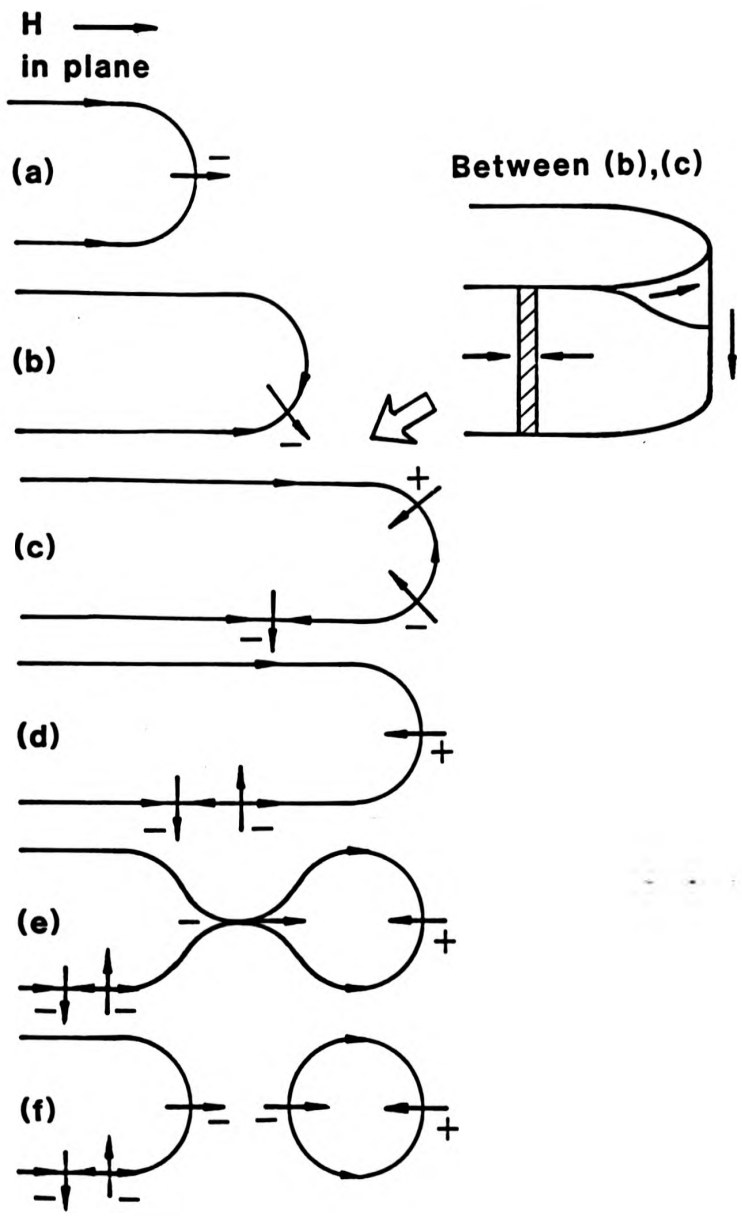

Fig.3.2.2 The VBL write process by expansion and chopping the stripe head. (See Fig.3.2.8 for explanation of in-plane field in (a).)

negative VBLs or a logical '1'. To write a logical zero the stripe head is simply prevented from expanding. To swop old data for new the VBLs are positioned at the stripe head and removed by a chopping action before new data is written.

A practical method of controlling stripe head expansion [10] is shown in Figure 3.2.3. The mutual repulsion between a bubble domain in a major line and the stripe domain comprising the minor loop will prevent the stripe head expanding. The presence of a bubble is thereby converted to the absence of a VBL pair. A meandering conductor for stripe expansion and a pair of chopping conductors, shown in Figure 3.2.4, as in the design of Wu and Humphrey [93] provide the necessary fields for VBL generation. Wu and Humphrey's VBL write gate also has an asymmetry in the expander meandering conductor which deflects the stripe head, on expansion automatically positioning the positive and negative VBLs on opposite sides of the chopping conductors. A further point to notice from Figure 3.2.3 is that the major line period should conventionally be four times the bubble diameter or twice the stripe domain equilibrium period. However, this would halve the potential storage density. One possible solution might be to fold the stripe domains in much the same manner as minor loops are folded in conventional bubble devices although this could create difficulties in propagation and fabrication as will be discussed later. A much more attractive alternative is shown in Figure 3.2.5 where two major tracks are combined with alternate stripe domains to create two major-minor loop memories which operate in parallel. Inherent in this interleaved design is that both the VBL write and read gates be similar, a consideration which will be covered in the read section.

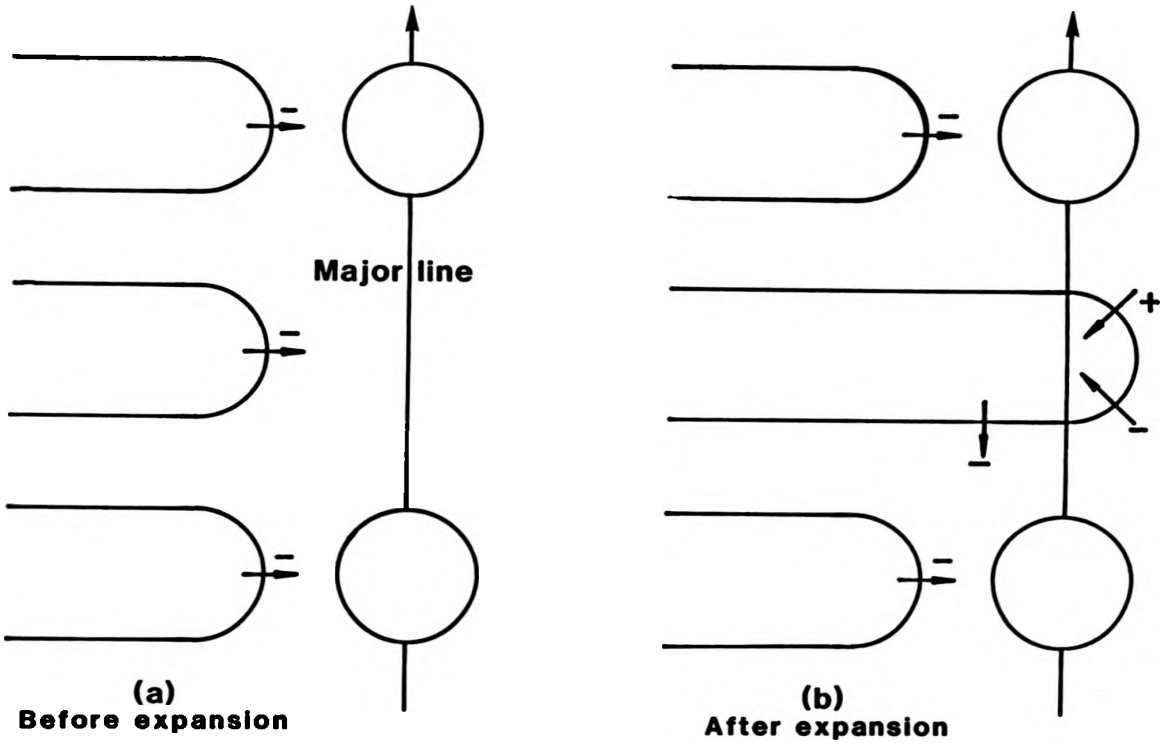

Fig.3.2.3 Conversion of a bubble to the absence of VBL by mutual repulsion between stripe and bubble domains.

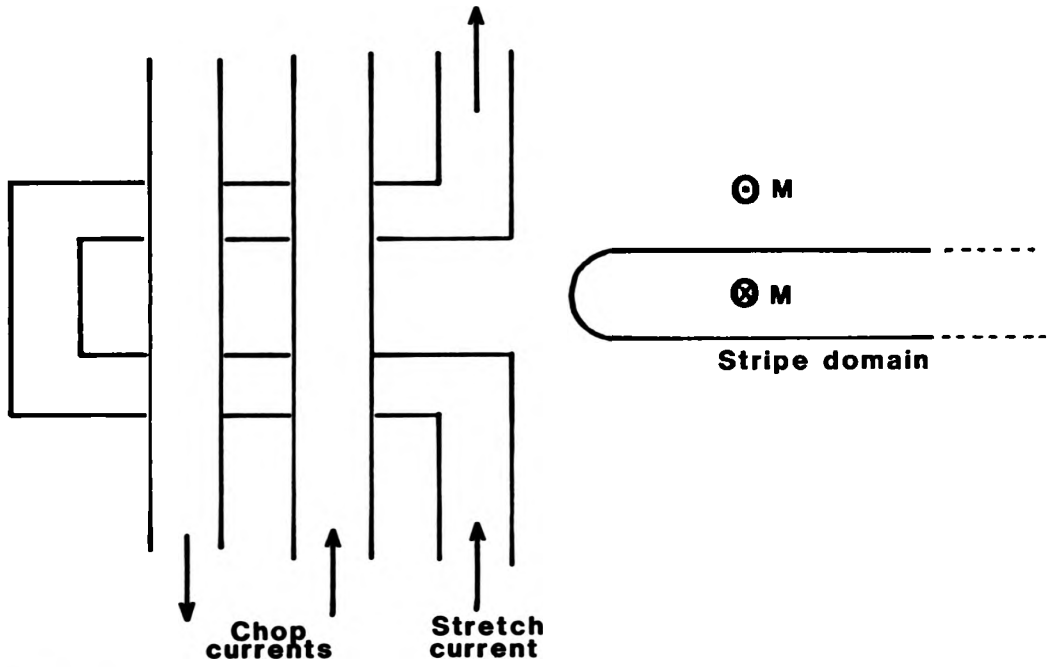

Fig.3.2.4 Stretch and chop conductors for VBL injection at the stripe head.

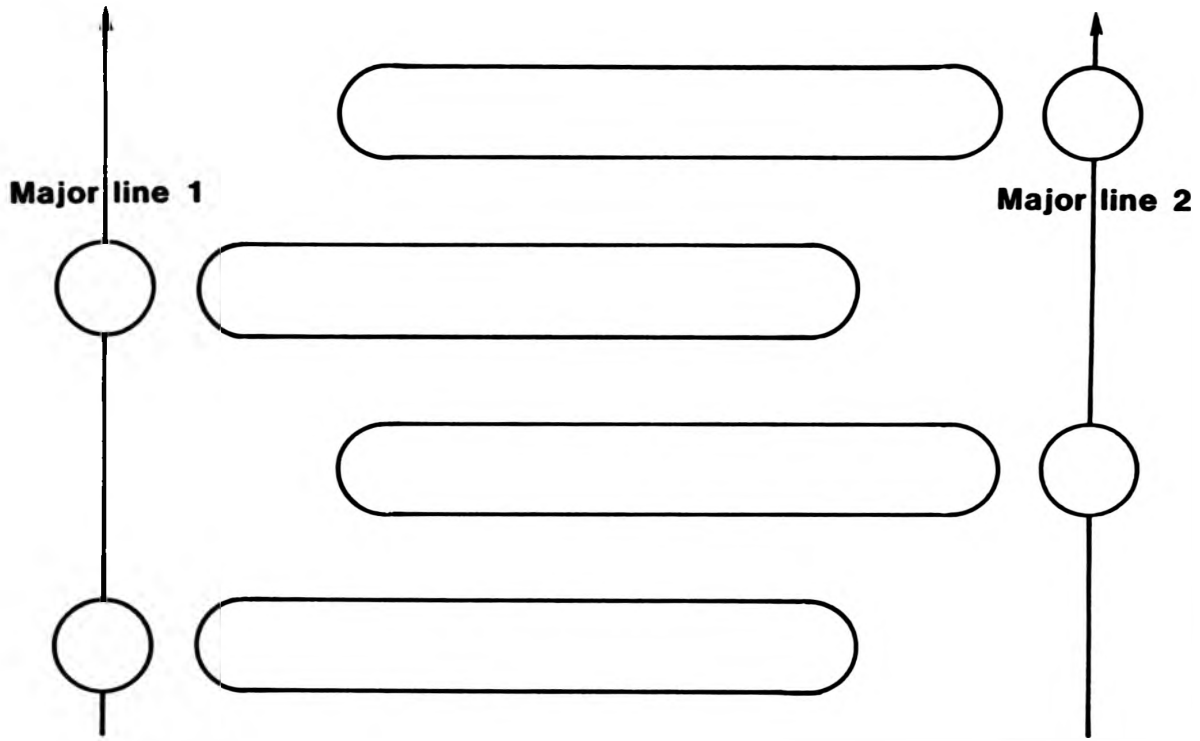

Fig.3.2.5 A major-minor loop organisation which has a track period of four times the bubble diameter.

Finally, it should be mentioned that there are a number of combinations of wall chirality and Hz polarity which will expand or contract, or cause punch-through at the top, Z=h, or bottom, Z=0, surface. It is fairly obvious that an expanding pulse is preferable to a collapsing one as the large fields necessary to cause punch-through and a domain chop should be as far from the VBL-coded data as possible to maintain data integrity. It may well be advantageous to choose chirality such that punch-through occurs on the top surface, closest to the expanding conductor, although it is doubtful if any significant saving in power dissipation would be achieved.

3.2.2 VBL propagation

VBLs may be propagated in a stripe domain wall by applied perpendicular pulse fields or in-plane field gradients. Consider first the effect of an in-plane field, Hip, acting parallel to a domain wall as in Figure 3.2.6. Each VBL is symmetrical about a section of Neel wall at the VBL centre of area equal to the domain wall cross-sectional area, upon which the in-plane field will exert a force per unit area of ±2M Hip. (See also section 3.3). The VBL pair in Figure 3.2.6a will therefore be compressed with the direction of Hip shown. This can also be seen from the overall wall energy which is minimised if the region of wall between the two VBLs, with magnetisation in opposition to Hip, is minimised. Similarly the VBLs will separate for Hip of opposite polarity. It is likely that a small static in-plane field bias will be used to compress the VBL pairs and that local in-plane fields will separate VBL pairs using

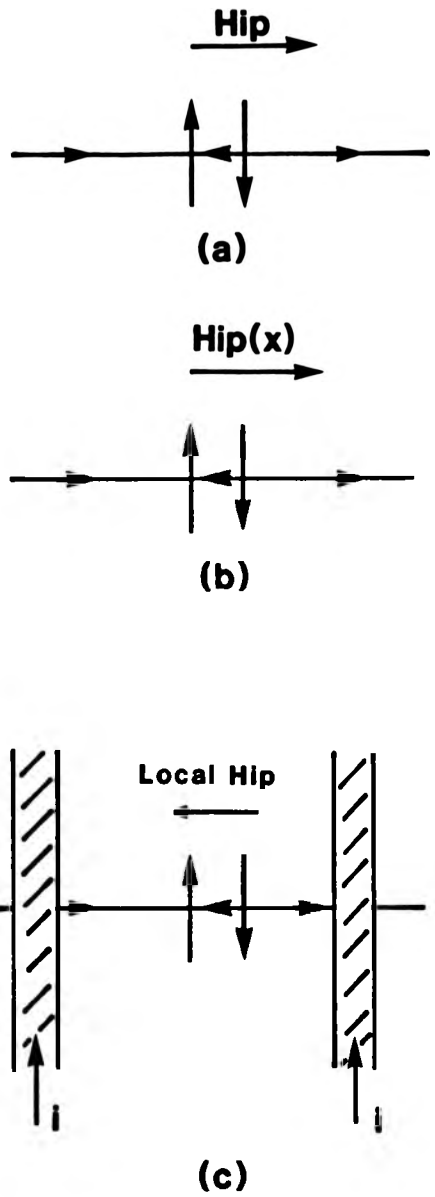

Fig.3.2.6 Control of VBL by in-plane fields. a) compression, b) propagation, and c) separation of VBL using in-plane fields from, for example, current-carrying conductors.

conductors as in Figure 3.2.6c for the read function of Konishi [10]. Should Hip vary as a function of position along the domain wall, as in Figure 3.2.6b, the VBL pair will tend towards the minimum Hip. Propagation of VBLs could therefore be obtained by a travelling in-plane field potential well caused by current-carrying conductors or apertured sheets. Such a structure may indeed prove useful in the early development of devices but the fabrication tolerances and power dissipation would probably be unrealistic at optimum device densities. A periodic in-plane field potential well structure defining the bit positions and a perpendicular drive field providing a gyrotropic force sufficient to propagate a VBL pair out of one potential well and into the next is a more likely arrangement. Such a potential well again could be produced by current-carrying conductors although a passive structure using shallow ion implantation, as discussed by Hidaka and Matsutera [91], would be more desirable. Ion implanted stripes, as shown in Figure 3.2.7 are exposed orthogonal to the stripe domain, inducing an in-plane magnetic anisotropy field which stabilises the VBL pair. The domain wall magnetisation immediately under the implanted region is exchange coupled to the in-plane magnetisation of such capping layers and can induce a reversal of magnetisation within a VBL, i.e. a Bloch point. Obviously the implantation must be much lower than that for Bloch point injection or VBL annihilation will occur at the interface between the implanted layer and underlying garnet as discussed in Chapter 1. Hidaka and Matsutera also found that a small in-plane field (< 10 Oe) parallel to the stripe domains helped to make the in-plane magnetic anisotropy unidirectional, thereby reducing VBL pair propagation errors. Application of an in-plane static field

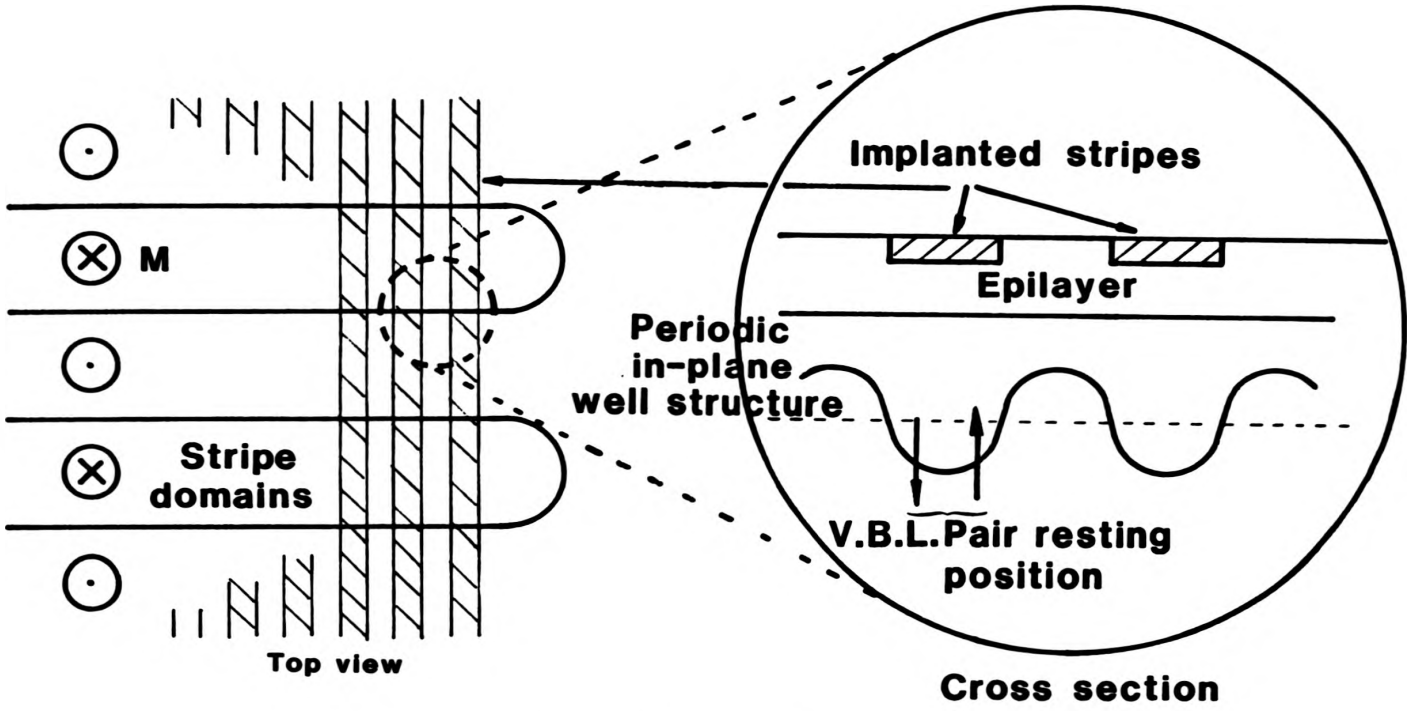

Fig.3.2.7 A periodic in-plane field potential well structure defining VBL pair bit position.

also induces a potential well at the stripe head. With reference to the structure of Figure 3.2.8, the component of Hip tangential to the domain wall is maximum on the stripe flanks and zero at the stripe head. The stripe head is therefore a stable position for an isolated (or odd number of) VBL which is one of the considerations for maintaining a VBL at this position. The symmetry of the wall magnetisation between VBL pairs on opposite flanks of a stripe including a VBL at the stripe head is also advantageous considering the symmetry of the very simple potential well structure of Figure 3.2.7.

An externally-applied perpendicular field pulse will induce a gyrotropic force on the VBLs and hence circulate them around the stripe domain wall. It should be remembered that it is the effective field on the domain wall resulting from demagnetising and wall energy effects as well as the applied field that provides the gyrotropic force. While the applied field is removed an effective field of opposite polarity is being induced and the VBLs tend to return to their original positions. The gyrotropic force on a VBL is given by equation 1.3.32 and is proportional to the domain wall velocity. To produce a net forward motion of the VBLs the perpendicular field is shaped as in Figure 3.2.9 with fast rise and slow fall times to give a high forward gyrotropic force to propagate a VBL pair out of a potential well and a low backward force insufficient to return the VBL pair to its original position. The magnitude and shape of the drive field has been the subject of extensive computer simulations of domain wall motion [95 - 97] which at present indicate that the typical values of Figure 3.2.9 are suitable for propagation of VBL pairs in 5μm bubble garnets with in-plane field potential wells of

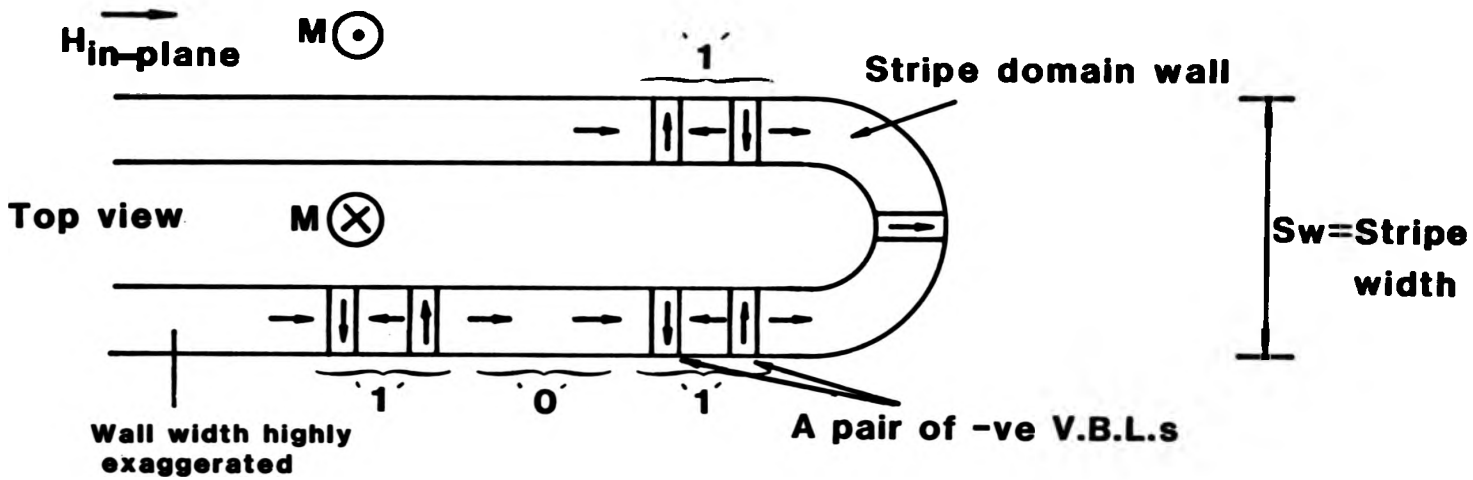

Fig.3.2.8 Stabilising an isolated VBL at the stripe head.

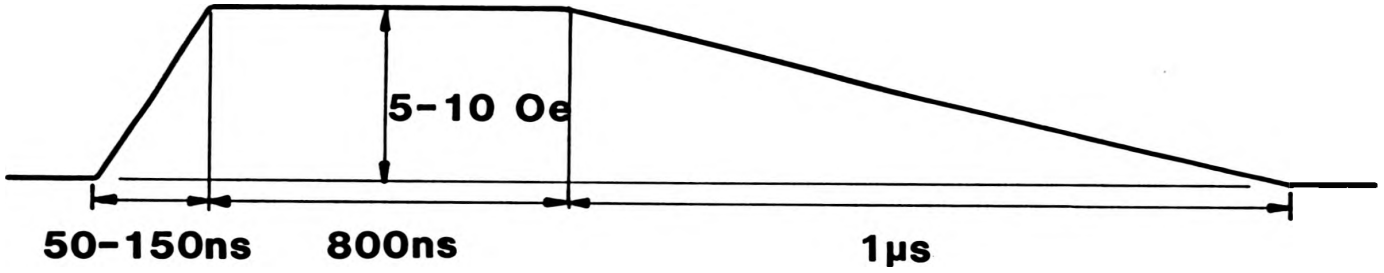

Fig.3.2.9 Typical perpendicular pulse field shape for propagation of VBL pairs in 5 m bubble garnet films with 1-2 Oe potential wells to define VBL bit position.

1-2 Oe in magnitude. A comparatively long constant drive field was found to be necessary to allow the wall to reach an equilibrium state [95]. This is discussed in more detail in section 3.3.8.

Reverse propagation can be obtained by using a slow rise and fast fall time for the pulse shape of Figure 3.2.9 or by reversing the drive field polarity. If bidirectional propagation is to be practical, the domain wall displacement during both forward and reverse VBL motion should be in the same direction so that the drive field amplitudes are the same. Reversal of drive field rise and fall times, as opposed to drive field polarity, is therefore preferable for reverse propagation (see also section 3.3.9).

As the VBL velocity is approximately proportional to the wall velocity, equation 1.3.31, it was originally anticipated that the VBL pair displacement could be restricted to one bit position by confining the total wall displacement with a physical barrier such as an ion milled step in the garnet [98]. This would suggest that the rise time and maximum amplitude of the perpendicular drive field would be non-critical. However, as the wall displacement is very much less than the VBL displacement this would entail fabrication tolerances less than that for bit position structures. The drive field rise time was also found to be critical in propagating random bit patterns [96]. Consider a stripe domain with one straight wall section containing a large number of VBLs and the other containing none. If the drive field rise time is very fast, < 10ns, the stripe domain will quickly reach an equilibrium state by moving only the soft wall which has a high mobility and therefore the gyrotropic forces on the VBLs are minimal. At present a 50-150ns rise time, as shown in Figure 3.2.9, is considered suitable for typical 5μm bubble garnet materials [96].

The most promising technique for stabilising the stripe domain minor loops now appears to be by material thinning as studied experimentally by Klein and Engemann [92] and included in the simulations of Matsuyama et al [97]. Arnaud and Boileau [99] suggested the use of ion implantation to confine stripe domains although Bloch point injection becomes a danger in such a scheme. A groove of up to 50% material thickness and 50% of the zero-field stripe width, positioned inside the stripe domain, will stabilise the stripe at zero-field stripe width in the presence of a collapsing perpendicular bias field. The bias field is necessary to stabilise the bubble domains in the major loop. The propagation of VBL pairs under the collapsing pulse field of Figure 3.2.9 has been theoretically demonstrated [96]. Propagation through the stripe head is expected to be more difficult than that in the straight wall region and although again it has been examined theoretically [92], operating margins are still to be improved. The reasons for this are twofold. Firstly, the stripe head represents a potential well for VBLs, which has to be overcome if the VBL pair is to propagate from one straight wall region to the other. Although this could be done by using the stripe head as a bit position itself, it is not desirable as it complicates the design of Konishi's VBL-bubble gate at the stripe head. Secondly, the distance that a VBL pair has to travel to pass the stripe head is much greater than the bit period in the straight wall region. The domain wall at the stripe head must therefore be displaced a greater distance than that in the straight wall region. While this may be possible at the stripe head it is not possible round a curved wall region in a folded stripe domain, and so a folded loop major-minor organisation is not considered practical in

this application. Matching operating margins for the straight wall region and the stripe head is a difficult but not insurmountable problem [97].

Use of orthorhombic garnets with a large in-plane anisotropy has been suggested as a possible method for stabilising the stripe domains [100]. The stripe domains align parallel to the in-plane easy axis of magnetisation without the need for a fabricated structure. In addition, the damping parameter of typical orthorhombic garnet materials is very low, < 0.01, which suggests that large increases in speed of operation may be possible. However, the large in-plane anisotropy is likely to exacerbate the difficulty of propagation through the stripe head.

3.2.3 The read process

The read function as proposed by Konishi uses the principle that the direction of wall magnetisation changes by π around the stripe head in the absence of a VBL and by 2π with a VBL at the stripe head. Wall magnetisation on opposite flanks of a stripe head is therefore parallel or antiparallel depending on whether or not there is a VBL at the stripe head, and hence there is a difference in the energy required to merge the two configurations of walls when the stripe head is chopped. Figure 3.2.10 demonstrates the operation of the read function. The stripe head is expanded to a region well removed from the storage area, probably by a meandering conductor similar to the write gate. The VBL pair, if present,is separated by a local in-plane field created by, for example, current carrying conductors as shown in Figure 3.2.10c. If a VBL pair was present there is,

this application. Matching operating margins for the straight wall region and the stripe head is a difficult but not insurmountable problem [97].

Use of orthorhombic garnets with a large in-plane anisotropy has been suggested as a possible method for stabilising the stripe domains [100]. The stripe domains align parallel to the in-plane easy axis of magnetisation without the need for a fabricated structure. In addition, the damping parameter of typical orthorhombic garnet materials is very low, < 0.01, which suggests that large increases in speed of operation may be possible. However, the large in-plane anisotropy is likely to exacerbate the difficulty of propagation through the stripe head.

3.2.3 The read process

The read function as proposed by Konishi uses the principle that the direction of wall magnetisation changes by π around the stripe head in the absence of a VBL and by 2π with a VBL at the stripe head. Wall magnetisation on opposite flanks of a stripe head is therefore parallel or antiparallel depending on whether or not there is a VBL at the stripe head, and hence there is a difference in the energy required to merge the two configurations of walls when the stripe head is chopped. Figure 3.2.10 demonstrates the operation of the read function. The stripe head is expanded to a region well removed from the storage area, probably by a meandering conductor similar to the write gate. The VBL pair, if present,is separated by a local in-plane field created by, for example, current carrying conductors as shown in Figure 3.2.10c. If a VBL pair was present there is,

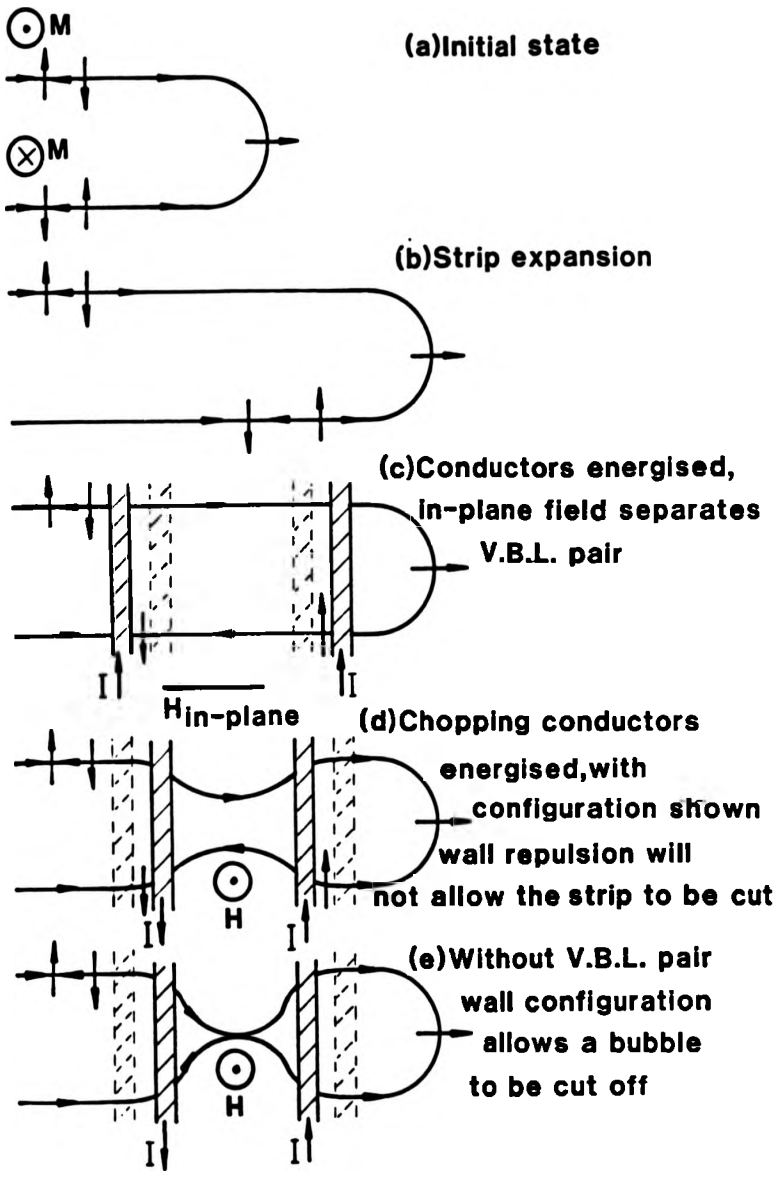

Fig.3.2.10 The read process as proposed by Konishi(10). An odd number of VBLs at the stripe head can easily be converted to a bubble by a chopping action.

including the resident VBL at the stripe head, two VBLs at the stripe head and the wall magnetisation on opposite flanks is antiparallel, see Figure 3.2.10d. If the stripe head is chopped, again by current carrying conductors, the increase in exchange energy between the merging walls will make the chop comparatively difficult. In the absence of a VBL pair the merging wall magnetisation is parallel, with a reduced exchange energy, and the stripe head is easier to remove. In this manner the absence of a VBL pair is converted to the presence of a bubble domain which can be propagated down a major track and detected using a standard magnetoresistive detector. The discrimination between chop and no chop has been shown to be reproducible with operating margins of greater than 20% [89], although as yet a fully-functioning read gate has not been fabricated. When a bubble is removed from the stripe head the direction of magnetisation in the merging walls is such that the isolated negative VBL is replicated in the new stripe head, see Figure 3.2.10e. In the presence of a VBL pair the stripe head is not removed so the number of VBL pairs is unchanged. The process is therefore a non-destructive readout.

An alternative readout scheme which has been recently suggested [101] is simply to expand the stripe domain head and remove it by chopping without the difficulties of VBL manipulation. The removed bubble would therefore have a different winding state (number of 2π rotations in wall magnetisation around the circumference) depending on the presence or absence of a VBL pair in the stripe head at the time of chopping. Detection would necessitate the inclusion of a state discriminator and annihilator in the major track before magnetoresistive detection of the selected bubble state. However, as

the VBL pair is a removed from the host stripe domain this method is a destructive readout. While a non-destructive process is more desirable, should the manipulation of VBL at the stripe head prove more difficult than at present anticipated this technique will provide a viable alternative. It should be mentioned that such an enforced chop will be necessary before the write process since the replacement of old data in the stripe domain with new data will require the initial removal of existing VBL pairs. In either case the read function is controlled by an expansion and chop of the stripe domain, functions which are inherent in the write process, and so the interleaved major-minor loop architecture of Figure 3.2.5 is realistic.

3.2.4 Summary

The concepts and difficulties involved in the fundamental functions of write, propagate, and read for VBL memory have been outlined. Although research on such a memory is in the elementary stages and as yet a fully functioning VBL memory does not exist, no major flaws in its conception have been identified. Computer simulation has been used extensively to formulate the initial design of device structures and operations. In the succeeding sections device performance and usefulness are examined.

3.3 Projections of Performance

3.3.1 Introduction

For this discussion we assume a simplified model of a domain wall

to consider some of the material requirements that would tailor a typical bubble garnet film to the specific needs of VBL memory. A VBL is represented as a point magnetic charge and we consider the in-plane field component parallel to the wall arising from convergence (or divergence) of magnetisation in the flanking Bloch wall regions.

This so called 'σ-charge' gives rise to a non-local effect which interacts with similar poles at different positions on the wall. If we consider a VBL as a point with regions of wall magnetisation angle ϕ_w=0 and π on either flank, then the magnetic moment of the VBL is simply 2M. Including the wall width, $\pi\Delta_0$, and the material thickness, h, then the total magnetic charge, m, is given by $2\pi M\Delta_0 h$. m is assumed to be a point charge as opposed to a charge distribution which would require a more detailed study, and the variation of charge through the thickness is ignored. (This latter point will be considered in conclusion). The magnetic field parallel to the wall at distance r resulting from this point charge is m/r^2, and the force acting on the charge due to a magnetic field H is m.H.

3.3.2 Attractive force between VBL pairs

Consider the effective field resulting from a pair of negative VBLs as shown in Figure 3.3.1. The field at p, a distance x from the centre of the VBL pair, is

$$H(p) = 2M\pi\Delta_0 h \left[\frac{1}{\left(x + \frac{\pi\Lambda}{2}\right)^2} - \frac{1}{\left(x - \frac{\pi\Lambda}{2}\right)^2} \right] \qquad .....3.3.1$$

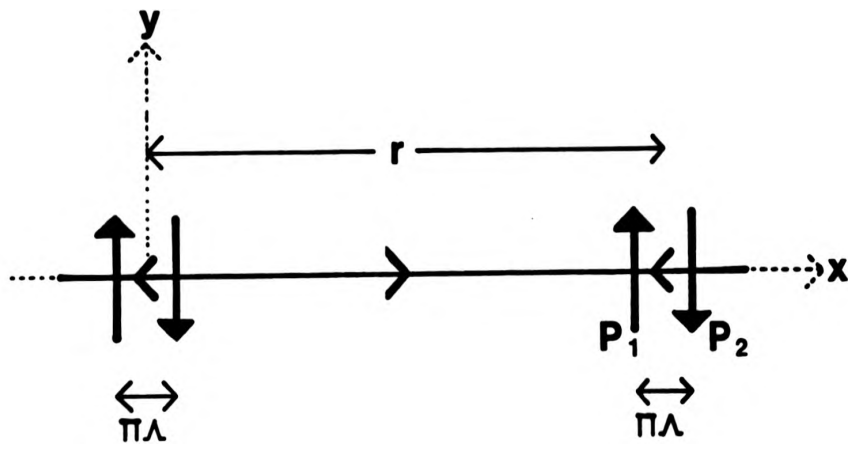

VBL magnetic charge, $m = 2M\pi\Delta_0 h$

Field due to charge, $H = m/r^2$

Force on point charge, $F = m.H$

Fig.3.3.1 VBL pairs in adjacent bit positions at a separation r.

$$\approx -4\pi M\Delta_o \pi\Lambda\ h/x^3 \qquad .....3.3.2$$

for the VBL spacing, $\pi\Lambda$, << x. With reference to Figure 3.3.1 the attractive force on a pair of VBL a distance r from the initial pair is given by,

$$F_{att} = 2\pi M\Delta_o h\ H(p_1) - 2\pi M\Delta_o h\ H(p_2) \qquad .....3.3.3$$

Therefore,

$$F_{att} = 2\pi M\Delta_o h.\pi\Lambda.\ \frac{\delta H}{\delta x}\Big|_{x=r} \qquad .....3.3.4$$

which from equation 3.3.2 is

$$F_{att} = 24\pi^4 M^2\Delta_o{}^2\Lambda^2 h^2/r^4 \qquad .....3.3.5$$

Substituting $\Delta_o = 1/2Q$ 3.3.6

and $\Lambda = 1/2\sqrt{Q}$ 3.3.7

the attractive force between VBL pairs is,

$$F_{att} = 3\pi^3 \frac{A}{Q^2}\ \frac{l^2h^2}{r^4} \qquad .....3.3.8$$

3.3.3 Potential well restoring force

If we assume a sinusoidal potential well of the form

$$H_W = H_m \cos \frac{2\pi}{r} x \qquad .....3.3.9$$

then in a similar manner to equation 3.3.4 the restoring force on a VBL pair is

$$F_R = -2\pi^2 M\Delta_0 \wedge h \frac{2\pi}{r} H_m \sin \frac{2\pi}{r} x \qquad ....3.3.10$$

which is a maximum at x = r/4 and x = 3r/4. Ideally as $F_{att} \propto 1/r^4$ it would be preferable to have the maximum restoring force at x = 0 and x = r, hence reducing the required amplitude of H_m and thus the magnitude of the drive field. A simple solution would be a triangular potential well [91]. For the present, however, we shall consider the case of maximum restoring force at x = 0,r and with the substitutions of equation 3.3.6 and 3.3.7,

$$F_{Rmax} = 2\pi^2 M\Delta_0 \wedge h 2\pi H_m/r \qquad ....3.3.11$$

$$= \frac{-\pi^2}{Q} \frac{\sqrt{2\pi A}}{r} H_m lh \qquad ....3.3.12$$

3.3.4 Drive field gyrotropic force

The gyrotropic force associated with a perpendicular drive field is more difficult to define as it is directly related to the density of VBL in the domain wall. The gyrotropic force on a VBL is,

$$F_g = \frac{2\pi M}{\gamma} h v_y \qquad ....3.3.13$$

v_y is the domain wall velocity which from the mobility of a 'hard' wall (i.e., $r = 2\pi A$) is,

$$v_y = \alpha\gamma\Delta_0 Hz \qquad \ldots.3.3.14$$

where Hz is the sum of perpendicular components of effective fields, i.e., demagnetising, wall curvature and applied fields. Our initial assumption for F_{att} however was that $r \gg \pi A$ which would suppose that the wall would move at a higher velocity although not that of a 'soft' wall given by,

$$v_y = \frac{\gamma\Delta_0}{\alpha} Hz \qquad \ldots.3.3.15$$

As $\alpha \ll 1$ there would appear to be a considerable uncertainty as to the magnitude of the gyrotropic force (although this may be estimated by numerical solutions of domain wall motion [95]). Combining equation 3.3.13 and 3.3.14 one can however say that this force is in excess of,

$$F_{gmin} = 2\pi M\alpha\Delta_0 hHz \qquad \ldots.3.3.16$$

$$= \sqrt{\frac{2\pi A}{Q}}\ \alpha hHz \qquad \ldots.3.3.17$$

3.3.5 Material considerations

The principle requirements of VBL memory are that the bit period, r, is small thereby maintaining a high density, and that the gyrotropic force for propagation is low so that the drive field magnitude is minimised. To satisfy these conditions, $F_{att} << F_{Rmax}$ and $F_{Rmax} << F_{gmin}$. While comparing these three forces, equations 3.3.8, 3.3.12 and 3.3.17, l can be taken as Sw/8 and the exchange constant A can be assumed constant at approximately 2×10^{-7} erg/cm. Immediately obvious is that a low h (≈ 3-4l), high Q (≈4) material reduces the relative effect of F_{att} and that a high α (≈ 0.1 - 0.2) increases F_{gmin}. This latter one would intuitively expect as large damping decreases both domain distortion and large VBL oscillatory effects during propagation [95]. The upper limit on α can be seen from the ratio of VBL velocity to wall velocity (equation 1.3.31).

$$v_{wall}/v_{VBL} = \text{constant}.\alpha \qquad \ldots.3.3.18$$

i.e., a large damping increases the ratio v_{wall}/v_{VBL} increasing the required wall displacement and thus Hz (remembering that Hz is an effective field resultant from drive, demagnetising and wall bending effects). The criterion of high Q is straightforward as one would require large Q to maintain domain stability (see section 1.3.1). A possible disadvantage of a thin material (h ≈ 3-4l) might be in detection (magnetoresistive detection of bubble domains), although as it is only the detector which will be fabricated from permalloy then a thin-film detector with high signal-to-noise performance can be employed.

In summary therefore, to estimate storage density in the following section we shall consider a material with $\alpha = 0.1$, $Q = 4$, $h = 41$, $l = S_w/8$ and $A = 2 \times 10^{-7}$ erg/cm.

3.3.6 Data storage density

It would clearly be desirable to have $F_{Rmax} >> F_{att}$ not only to ensure stability of the bit positions, but also for successful propagation of a random bit pattern. Taking therefore $F_{Rmax} = 10\ F_{att}$ and combining equations 3.3.8 and 3.3.12, a relationship between potential well depth (H_m) and bit period:stripe width ratio (r/S_w) can be obtained as shown for various stripe widths in Figure 3.3.2. The expected potential well depth for decreasing stripe width is shown approximately as an arrow from which an estimation of the bit period can be made. The position of this arrow, i.e. the potential wall depth, is rather uncertain as yet. However, assuming a potential well of approximately 1.5-2Oe for 5μm bubble garnet materials, as discused by Matsuyama et al [96], it would be reasonable to predict that this would scale approximately as a function of $1/h$ and, therefore, $1/S_w$ as it is the thickness-averaged in-plane field that is being considered. As shown, this corresponds approximately to the 'knee' of the curves. As expected, potential well depth increases sharply with decreasing bit period and the corresponding densities ($= 1/r \times S_w$ bits/cm^2) vary approximately as a function of $1/S_w^2$. (See Figure 3.3.3).

A more detailed estimation of VBL magnetic charge, accounting for the variation of ϕ_w through the thickness, gives a reduction in the σ-charge. With reference to the three-dimensional VBL of Figure

In summary therefore, to estimate storage density in the following section we shall consider a material with $\alpha = 0.1$, $Q = 4$, $h = 4l$, $l = S_w/8$ and $A = 2 \times 10^{-7}$ erg/cm.

3.3.6 Data storage density

It would clearly be desirable to have $F_{Rmax} >> F_{att}$ not only to ensure stability of the bit positions, but also for successful propagation of a random bit pattern. Taking therefore $F_{Rmax} = 10\ F_{att}$ and combining equations 3.3.8 and 3.3.12, a relationship between potential well depth (H_m) and bit period:stripe width ratio (r/S_w) can be obtained as shown for various stripe widths in Figure 3.3.2. The expected potential well depth for decreasing stripe width is shown approximately as an arrow from which an estimation of the bit period can be made. The position of this arrow, i.e. the potential wall depth, is rather uncertain as yet. However, assuming a potential well of approximately 1.5-2Oe for 5μm bubble garnet materials, as discused by Matsuyama et al [96], it would be reasonable to predict that this would scale approximately as a function of $1/h$ and, therefore, $1/S_w$ as it is the thickness-averaged in-plane field that is being considered. As shown, this corresponds approximately to the 'knee' of the curves. As expected, potential well depth increases sharply with decreasing bit period and the corresponding densities ($= 1/r \times S_w$ bits/cm^2) vary approximately as a function of $1/S_w^2$. (See Figure 3.3.3).

A more detailed estimation of VBL magnetic charge, accounting for the variation of σ_w through the thickness, gives a reduction in the σ-charge. With reference to the three-dimensional VBL of Figure

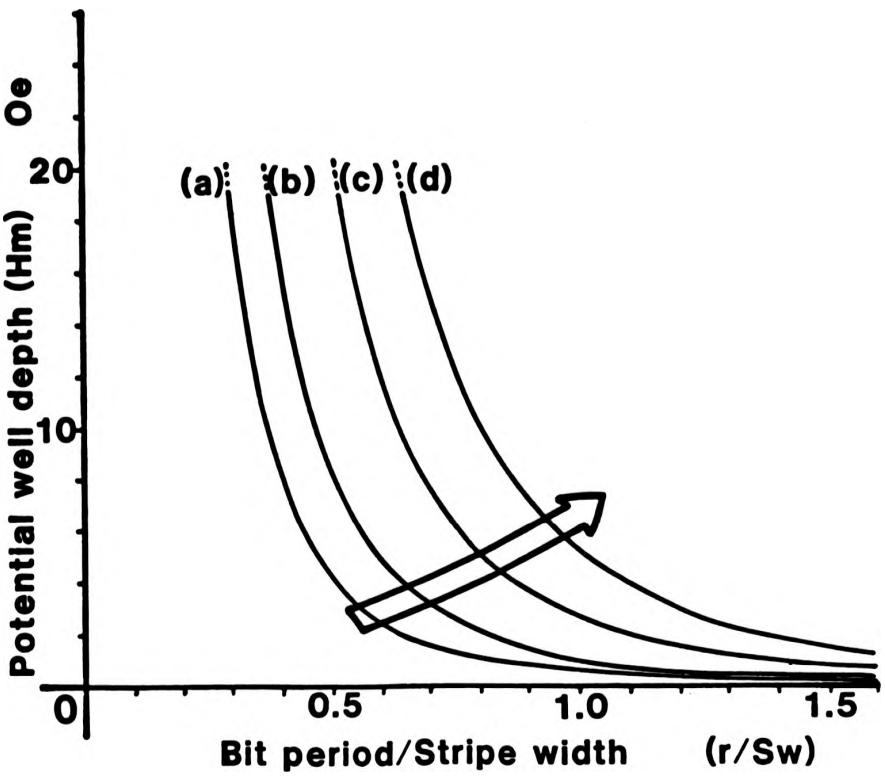

Fig.3.3.2 Potential well depth as a function of bit period:stripe width ratio for stripe widths of a) 5.0 μm, b) 2.5 μm, c) 1.0 μm, and d) 0.5 μm. The position of the arrow shows the expected potential well depth.

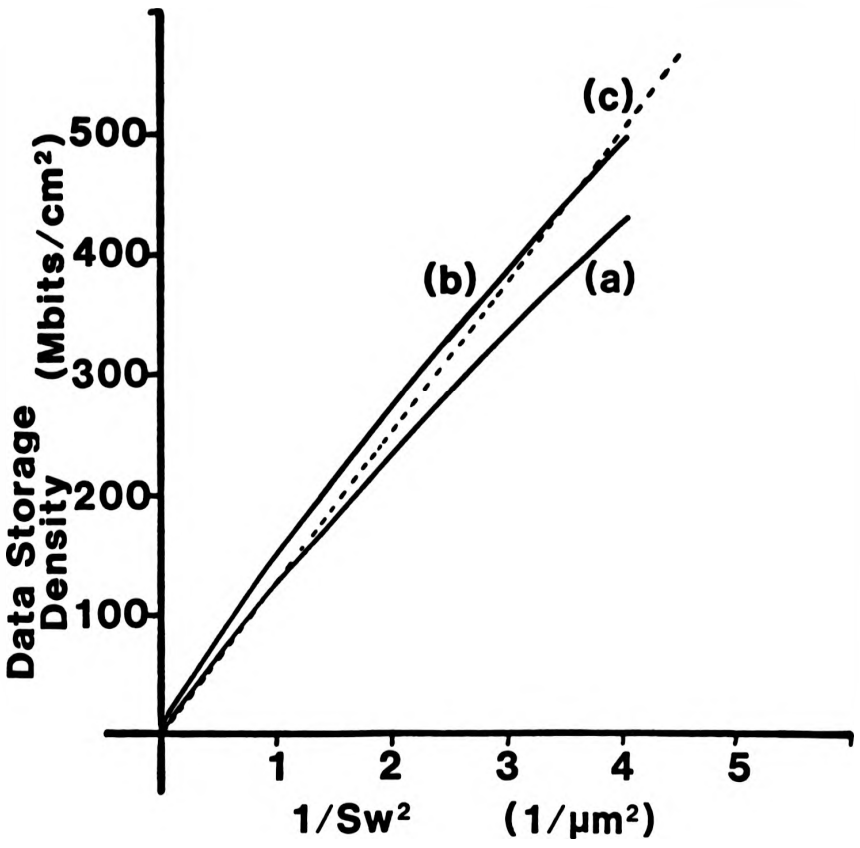

Fig.3.3.3 Data storage density as a function of 1/Sw for a) the simple charge model, b) the revised charge model accounting for charge variation through the material thickness, and c) r = 0.88w.

1.3.6, the magnetic moment of the head and tail of the VBL is zero rising to a maximum of 2M at the centre of the film thickness. The magnetic moment at a given thickness is given from equations 1.3.10 and 1.3.12 as

$$m = 2M \cos \phi_w = 2M \sqrt{(1 - \tfrac{1}{4}(\ln(Z/(h-Z))^2} \qquad ....3.3.19$$

The thickness-averaged magnetic moment is given as

$$m = \frac{2M}{h} \int_{h/1+e^2}^{he^2/1+e^2} \sqrt{1 - \tfrac{1}{4}(\ln(Z/(h-Z)))^2}\ dZ \qquad ....3.3.20$$

which is 1.28M or 64% of that used in the original model. Using the same argument as above the corresponding theoretical density is plotted as curve (b) in Figure 3.3.3 and is seen to approach 500 Mbits/cm^2 for 0.5μm stripe width. The original point charge model would therefore appear to be conservative and in practice some gain in density would be achieved. However, as a rule of thumb, bit spacing of the order 0.8Sw (four times the VBL pair width) could be used. This may be considered somewhat analogous to the required bit spacing of four times the bubble diameter in a conventional bubble device, although in that case the relevant force is repulsive. The density derived in these calculations is a factor of four smaller than that originally anticipated [10, 101], although it does not exclude the possibility of Gbit single-chip devices using chip areas comparable to those of today's bubble memories. In comparison to a conventional bubble memory cell area, 16Sw^2, an increase in density

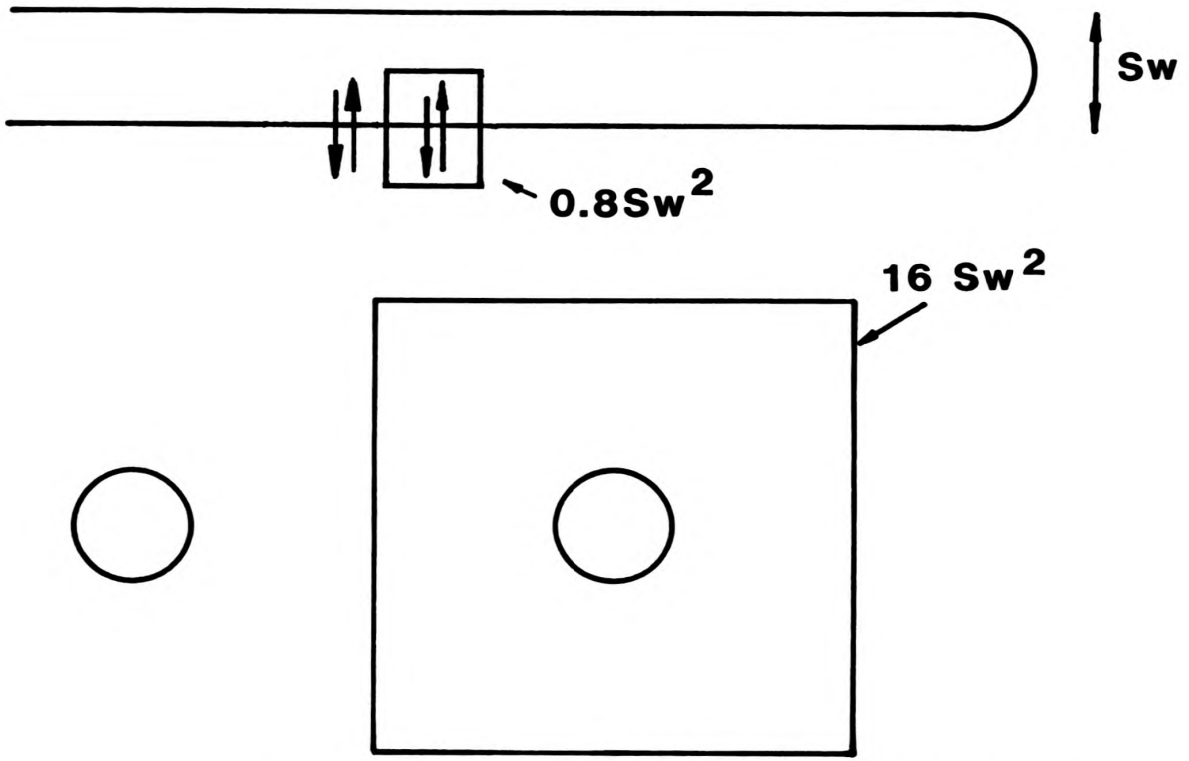

Fig.3.3.4 Comparison of bubble and VBL memory storage cell areas.

of twenty-fold is expected as shown in Figure 3.3.4.

3.3.7 Fabrication Requirements

The features in a VBL memory to be fabricated are a current-access major track with a bubble detector and nucleator, VBL bit potential wells, stripe domain stabilisation grooves, and VBL write/read gates. Of these, the major track, including the detector and nucleator, and the write/read gates are concerned with the manipulation of domains either in the form of bubbles or the stripe heads and the fabrication requirements should be not so stringent as elsewhere. Typically, dual-layer apertured-conductor minimum linewidths and alignment are of the order of Sw and the VBL write gate of Wu and Humphrey has a minimum linewidth of 1.25Sw which it would seem reasonable to assume would be similar for a read gate. This write gate does however have an asymmetric feature for deflection of the stripe head during expansion corresponding to a minimum feature size of about 0.5Sw, although the tolerances on this are unknown. The goove for stripe stabilisation discussed by Matsuyama et al [97] is of width 0.5Sw although the period is equal to that of the stripe domains, i.e. 2Sw. Yonekura et al [102] have reported a novel technique for fabrication of narrow gaps as small as one tenth of the pattern period with a basic photolithographic requirement of half the pattern period. In this process, photoresist patterns were coated with evaporated copper and the gaps between patterns were reduced by the side deposition of the copper film. Such a technique is only possible for a simple single line structure as intended for stripe stablisation which, if used, would relax

fabrication requirements for grooving to a minimum linewidth of Sw. Grooving the substrate can be achieved by ion milling [92]. The minor loop bit period would therefore, as expected, be the limiting fabrication requirement. Using the previously-recommended bit period of 0.8Sw and the simple potential well structure of Figure 3.2.7 the linewidth required for VBL potential wells is 0.4Sw. To reach 500 Mbits/cm^2 using 0.5μm bubble material this would require 0.2μm fabrication capability. While this is certainly beyond that capable using today's industrial fabrication techniques, it is not altogether unreasonable considering the very simple grating design of the potential well structure. The resolution of electron beam lithography is less than 0.1μm providing the pattern is as simple as that under discussion.

Intel's 4Mbit bubble memory has a 0.75μm minimum feature size [103] which, if applied to VBL memory, offers the possibility of 36Mbits/cm^2. If the minimum feature size for bit period is increased to that for the remaining chip functions, i.e. Sw, the maximum density for a given fabrication linewidth capability can be obtained. Optimum device density is obtained, therefore, using a bit period of 2Sw. This assumes that the VBLs will have to be displaced at a much greater distance than before and the drive field is likely to be of greater magnitude and duration than that previously discussed. However, if this is possible, a density of 88 Mbits/cm^2 could be expected using a 0.75μm minimum linewidth.

3.3.8 Speed of operation

To estimate a mean time to access for VBL memory the simple

interleaved architecture of Figure 3.2.5 is assumed with a current-access major track of clock period t_{major}, and a minor loop perpendicular pulse field period of t_{minor}. If the chip is square of area A, stripe width Sw, and cell period 0.8Sw, then

$$\text{No. of bits/major track} = \frac{\sqrt{A}}{4Sw} \qquad \ldots.3.3.21$$

and

$$\text{No. of bits/minor loop} = \frac{2\sqrt{A}}{0.8Sw} \qquad \ldots.3.3.22$$

As bidirectional propagation is possible, the worst-case access time is when the bit is $\sqrt{A}/0.8Sw$ bits from the read gate and $\sqrt{A}/4Sw$ from the detector with mean time to access occurring at half these values. The read function occurs in parallel for all the minor loops and is not expected to be a significant factor in access times. However, even pessimistically assuming 0.1ms for VBL-bubble conversion, the mean time to access would be:

$$T_{mean} = \frac{\sqrt{A}}{2 \times 0.8Sw} \times t_{minor} + \frac{\sqrt{A}}{2 \times 4Sw} \times t_{major} + 0.1 \text{ ms} \quad ..3.3.23$$

Kryder [20] has stated that if the bubble mobility and the material coercivity are held constant for decreasing bubble diameter, the clock period for a current-accessed track is proportional to the bubble diameter. Therefore, if we assume an operating frequency of 1 MHz for a 2μm bubble diameter [28] [30] then for 5um and 0.5μm

bubble diameters, t_{major} is assumed to reduce from 2.5μm to 0.25μs.

To estimate the minor loop clock period the relaxation time of a domain wall has to be calculated. In section 1.3, the effective field acting on a bubble domain, equation 1.3.2. For a regular stripe array, as in the minor loop storage area in VBL memory, the domain walls may be assumed to be straight ($\sigma_0/r = 0$) and for small wall displacement, y, in a bias field, ΔH, the equilibrium stripe width, Sw ± 2y, is obtained when

$$2M\Delta H + 2MH_d = 0 \qquad .....3.3.24$$

where H_d is the demagnetising field from the stripe array. This implies that there is a restoring force of $2MH_d$ acting on the domain wall.

An approximation to the demagnetising field, valid for Sw >> h, can be obtained using the equivalent current model (see section 1.3.1) and representing the stripe domain walls by conductors carrying currents of ± 2Mh emu, as shown in Figure 3.3.5. The contribution to demagnetisng field from domain walls other than those adjacent to the wall in question, A, cancel and therefore,

$$H_d = \frac{4Mh}{Sw + 2y} - \frac{4Mh}{Sw - 2y} \qquad ....3.3.25$$

$$\approx -4Mh \cdot \frac{4y}{Sw^2} \qquad ....3.3.26$$

The restoring force is therefore

bubble diameters, t_{major} is assumed to reduce from 2.5μm to 0.25μs.

To estimate the minor loop clock period the relaxation time of a domain wall has to be calculated. In section 1.3, the effective field acting on a domain wall was discussed for a bubble domain, equation 1.3.2. For a regular stripe array, as in the minor loop storage area in VBL memory, the domain walls may be assumed to be straight ($\sigma_o/r = 0$) and for small wall displacement, y, in a bias field, ΔH, the equilibrium stripe width, Sw ± 2y, is obtained when

$$2M\Delta H + 2MH_d = 0 \qquad \text{.....3.3.24}$$

where H_d is the demagnetising field from the stripe array. This implies that there is a restoring force of $2MH_d$ acting on the domain wall.

An approximation to the demagnetising field, valid for Sw >> h, can be obtained using the equivalent current model (see section 1.3.1) and representing the stripe domain walls by conductors carrying currents of ± 2Mh emu, as shown in Figure 3.3.5. The contribution to demagnetisng field from domain walls other than those adjacent to the wall in question, A, cancel and therefore,

$$H_d = \frac{4Mh}{Sw + 2y} - \frac{4Mh}{Sw - 2y} \qquad \text{....3.3.25}$$

$$\approx -4Mh \cdot \frac{4y}{Sw^2} \qquad \text{....3.3.26}$$

The restoring force is therefore

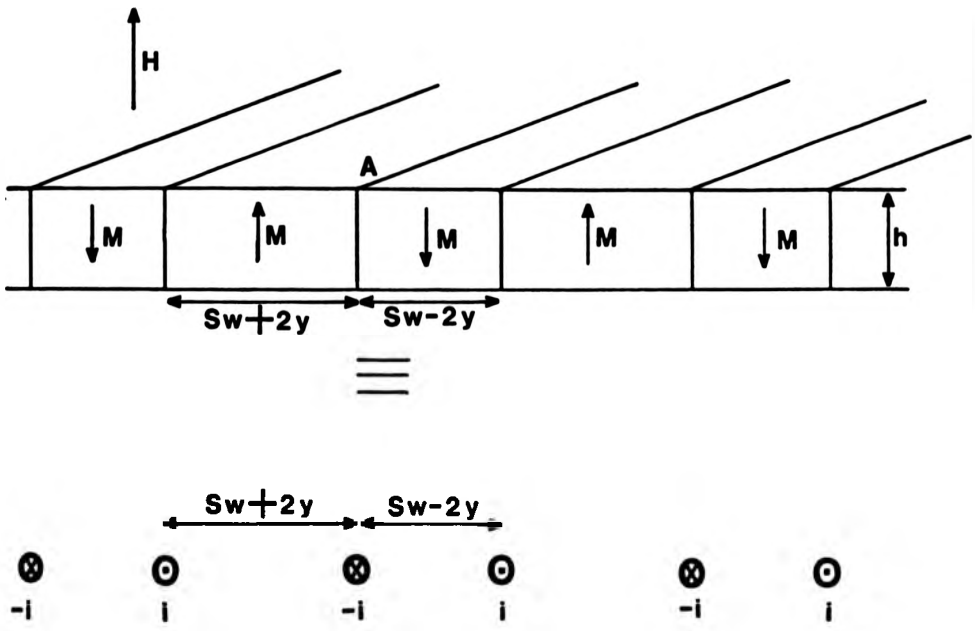

$$i = 2Mh$$

Fig.3.3.5 The equivalent current model of a stripe array.

$$F_R = - \frac{32M^2h}{Sw^2} y \qquad \ldots.3.3.27$$

If the applied field is removed there is an effective field, H_{eff}, acting on the wall so as to return it to its original position, y=0. Therefore, $H_{eff} = H_d$ and the wall moves with a velocity of

$$\dot{y} = \mu H_{eff} \qquad \ldots.3.3.28$$

This implies a viscous damping force, F_D, where

$$F_D = 2MH_{eff} \qquad \ldots.3.3.29$$

$$= \frac{2M}{\mu} \dot{y} \qquad \ldots.3.3.30$$

At a given instant, dynamic and static forces balance and so,

$$\frac{2M}{\mu} \dot{y} = - \frac{32M^2}{Sw^2} h y \qquad \ldots.3.3.31$$

$$\frac{\dot{y}}{y} = - \frac{16Mh\ \mu}{Sw^2} \qquad \ldots.3.3.32$$

and

$$y = C\, e^{- \frac{16Mh\ \mu}{Sw^2} t} \qquad \ldots.3.3.33$$

where C is a constant. This corresponds to an exponential decay with time constant,

$$\tau_c = \frac{Sw^2}{16Mh\ \mu} \qquad \ldots.3.3.34$$

where the mobility, μ, of a hard wall is $\alpha\gamma\Delta_0$ (equation 1.3.29). Using the substitutions of section 1.3 and the parameters of section 3.3.5 with $\gamma = 1.8 \times 10^7$ Oe^{-1} s^{-1} [116], τ_c becomes

$$\tau_c = 4\sqrt{\frac{2\pi Q}{A}}\ \frac{l^2}{\alpha\gamma h} \qquad \ldots.3.3.35$$

$$= 6.6 \times 10^{-3}\ l \qquad \ldots.3.3.36$$

The wall relaxation time constant is therefore proportional to the characteristic material length and the pulse bias field frequency for VBL propagation is expected to be inversely proportional to the stripe width. Taking the total wall relaxation time as approximately $3\tau_c$ and the pulse bias field period as $6\tau_c$, t_{minor} can be taken as approximately 2.5μs and 0.25μs for 5μm and 0.5μm bubble garnet materials respectively.

As both t_{major} and t_{minor} are proportional to the bubble diameter, from equation 3.3.23, the mean time to access is approximately constant for increasing device density and is proportional to the square root of the chip area. A 5 Mbit device with A = $1cm^2$ and Sw = 5μm would have a mean time to access of 3.85ms while for a 1 Gbit device with Sw = 0.5μm and A = $2cm^2$ it would be 7.6ms. These times could be reduced by a few ms if advantage is taken of the fact that major and minor loop propagation are independent and pipelining is possible. Data transfer is at 800 kHz

and 8 MHz for 5μm and 0.5μm bubble garnet materials respectively as there are two major tracks.

To put these figures in perspective, Intel's 4 Mbit device has a mean time to access of 41ms [103] while Hitachi's and Fujitsu's 4 Mbit devices have a mean time to access of 12.5ms and readout data rates of 400 kbits/sec [104]. The above values for VBL memory would therefore compare favourably even at the much higher densities calculated.

Further increases in speed of operation and data output could easily be achieved by partitioning the chip. Four separate memory sections, each with the interleaved architecture operating in parallel, would produce a byte-wide memory with obvious improvements in access times and data rates. The large number of detectors for such an architecture would not necessarily be excessive. There is no rotating in-plane field in VBL memory, therefore signal-to-noise ratios would be acceptable with much smaller detector areas than those in conventional bubble devices. Also as the detector is the only permalloy feature on the device it can be tailored more specifically to the requirements of magnetoresistive detection, i.e. using thin films, again improving signal strength.

Magnetic bubble logic when combined with bubble memory has been shown to offer significant speed advantages by reducing I/O bottlenecks [30] and would also appear compatible with VBL memory. While VBL-VBL logical operations are possible, data is restricted to the domain wall and has therefore only one-dimensional freedom of movement. The two-dimensional interaction as in bubble-bubble logic is not possible which would suggest that no significant advantages could be gained from VBL-VBL logic. All the possibilities of, for

example, using current-access cache loops or magnetic bubble logic for searches or error correction/redundancy control are available to improve performance and will no doubt be investigated in the near future.

3.3.9 Power requirements

To estimate power requirements of VBL memory, the previous interleaved architecture and drive field are assumed for a 5 Mbit and 1 Gbit device. Read, write and swop functions for VBLs operate for very low duty cycles and power dissipations for these areas are therefore neglected. On-chip power dissipation is hence principally divided in two sections, minor loop storage area and major loop tracks. The potential well structure for VBL bit position is passive and power requirements for the minor loop storage area are determined by the drive-field coil design. As bubble garnet films are very low-loss materials and the domain wall displacement per propagated bit is very much lower than that in bubble memory, the on-chip power dissipation in the minor loop storage region is also negligible. Typical power dissipation in a major track running the length of the chip is estimated as 0.25 Watts [9] [22] (See Appendix 3.1). The interleaved architecture of Figure 3.3.4 has two major tracks which therefore alone require 0.5 Watts. For the 5 Mbit device using 5μm bubble garnet, generate and detection power dissipations are also assumed small in comparison to this figure, and so the on-chip power dissipation is estimated as 0.5 Watts due almost entirely to the major tracks. The major track width is proportional to the bubble diameter, therfore for a constant current density the total current

is proportional to the bubble diameter. The major track resistance depends on both width and thickness and is approximately inversely proportional to the square of bubble diameter. To a first approximation the power dissipation (I^2R) is therefore independent of bubble diameter and is proportional only to the total length of major track [20]. The major track power dissipation for a $2cm^2$, 1 Gbit device would be approximately $\sqrt{2}$ times that for a 5 Mbit device. If the major tracks are not operated in parallel these figures could be reduced by 50% although data rates would decrease accordingly. Access times would not necessarily be affected by such asynchronous operation. At small bubble diameters, generate and detection power dissipations become more relevant [20] and careful design will be necessary to prevent these values becoming dominant.

The perpendicular fields to be produced by the drive coils, ~10 Oe, are much smaller than the rotating in-plane fields of a bubble memory, ~60 Oe, and power dissipation will be lower. Also, the major and minor loop drives are asynchronous and therefore to input or output data continuously the minor loops need only be cycled one bit position while the major track is filled or emptied. Given the above interleaved architecture with 500 bits per major track (5 Mbits/cm^2) and major and minor drive periods of 2.5μs, the minor loop drive field duty cycle is only 0.2%. During reverse propagation this is reduced even further, i.e. when the drive field of Figure 3.3.6 is used. The rate of change of drive field in the fast wall contraction and slow wall expansion are as before. The VBL motion is identical in the reverse direction provided there is a long relaxation period immediately after the rapid wall and VBL motion to allow the domain to reach static equilibrium. A further 50% reduction in duty cycle

is proportional to the bubble diameter. The major track resistance depends on both width and thickness and is approximately inversely proportional to the square of bubble diameter. To a first approximation the power dissipation (I^2R) is therefore independent of bubble diameter and is proportional only to the total length of major track [20]. The major track power dissipation for a $2cm^2$, 1 Gbit device would be approximately $\sqrt{2}$ times that for a 5 Mbit device. If the major tracks are not operated in parallel these figures could be reduced by 50% although data rates would decrease accordingly. Access times would not necessarily be affected by such asynchronous operation. At small bubble diameters, generate and detection power dissipations become more relevant [20] and careful design will be necessary to prevent these values becoming dominant.

The perpendicular fields to be produced by the drive coils, ~10 Oe, are much smaller than the rotating in-plane fields of a bubble memory, ~60 Oe, and power dissipation will be lower. Also, the major and minor loop drives are asynchronous and therefore to input or output data continuously the minor loops need only be cycled one bit position while the major track is filled or emptied. Given the above interleaved architecture with 500 bits per major track (5 Mbits/cm^2) and major and minor drive periods of 2.5μs, the minor loop drive field duty cycle is only 0.2%. During reverse propagation this is reduced even further, i.e. when the drive field of Figure 3.3.6 is used. The rate of change of drive field in the fast wall contraction and slow wall expansion are as before. The VBL motion is identical in the reverse direction provided there is a long relaxation period immediately after the rapid wall and VBL motion to allow the domain to reach static equilibrium. A further 50% reduction in duty cycle

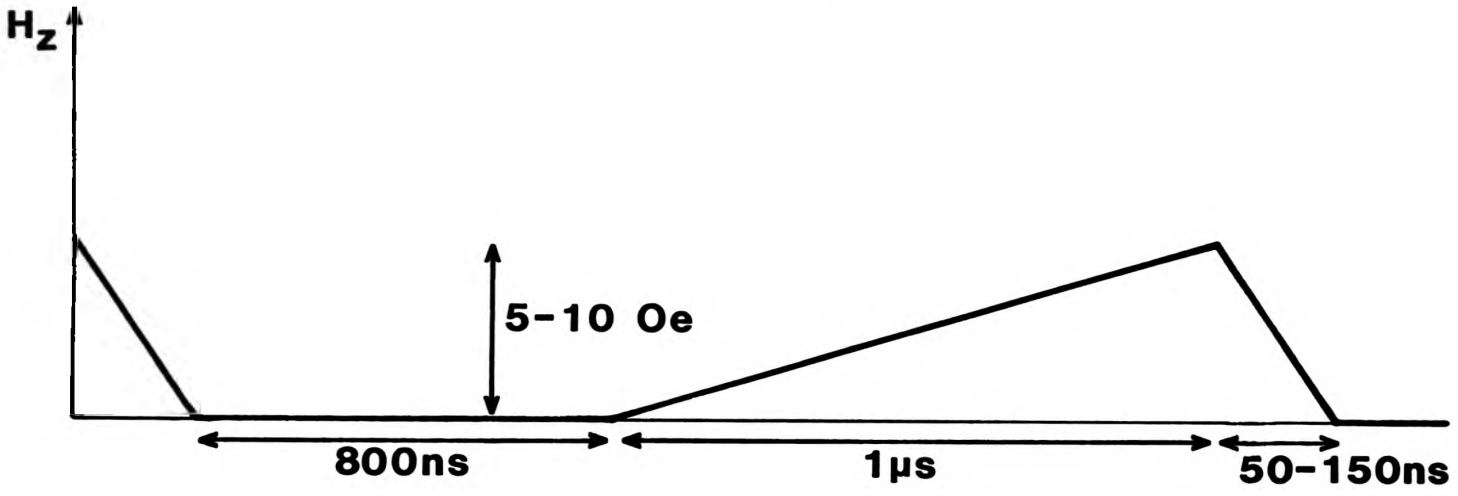

Fig.3.3.6 Reverse drive field pulse shape which offers lower power dissipation.

to 0.1% is therefore achieved which, in total, is of the order 1-2m Watts. At higher densities the minor loop drive field duty cycle is the same and drive coil power dissipation remains negligible. In addition, as the duty cycle of the minor loop storage area is much lower than that in conventional bubble memory, to retrieve a block of data, fewer propagation cycles are needed with a resultant decrease in the likely overall propagation error rates.

The total packaged power dissipation is dominated therefore by the current-access major tracks and is estimated as 0.5 Watts and 0.7 Watts for the 5 Mbit and 1 Gbit devices respectively. This compares favourably with 1.1 Watts, 2.0 Watts, and 2.9 Watts for Fujitsu, Hitachi and Intel's 4 Mbit devices respectively [104]. Increases in architectural complexity will necessitate an increase in major track length and thus power dissipation. Any chosen architecture will be a compromise between increase in power dissipation and decrease in access time.

3.4 Conclusion

The operational concepts and expected performance of VBL memory have been examined. While development of the technology is in the very early stages, as yet no fundamental flaws in its conception have been identified. A negative VBL pair is a stable winding twist in a domain wall and, providing a passive potential well structure is used, the non-volatility of the memory is assured. It is solid state therefore requiring low maintenance. The advantages which make bubble memory unique are therefore common to VBL memory at higher densities with lower access time and lower power requirements.

Error rates are more difficult to estimate without practical devices although care must be taken to avoid Bloch point injection which would annihilate VBL pairs.

This discussion has been limited to the most likely conditions of operation although many others are possible. Almost any shape of perpendicular pulse field will produce a net forward motion of VBL as there is a coercive force associated with VBL displacement. Hidaka and Matsutera [91] have experimentally shown that a 5ns wide 30 Oe pulse field is capable of inducing VBL propagation in 5μm stripe width materials. It should not be assumed, however, that a propagation frequency of 200 MHz is possible, as the relaxation time for domain wall displacement is very large in a wall containing VBLs. A long settling time is necessary for the wall to reach on equilibrium state before the next pulse is applied. Care must also be taken that the domain wall velocity, especially at the stripe head, does not exceed that for punch-through, equation 3.2.1, or spontaneous nucleation of VBLs will corrupt the data. The more gentle drive field with comparatively slow rise and fall times discussed in this work is felt more capable of propagating random bit patterns and demonstrating wider operating margins.

Using present day technology, densities in excess of 64 Mbits/cm^2 and single chip capacities of 128 Mbits would appear feasible. With improvements in industrial fabrication technology single chip devices of up to 1 Gbit may be possible although this is quite a few years in the future. In the immediate future priority must be given to an all-function demonstration chip including read, write, and a few bits of storage. A current-access approach, using conductors or an apertured-sheet to define bit position would have several advantages

for an experimental device, giving external control of potential well restoring forces and gyrotropic drive forces on a VBL pair. Direct comparison with the theoretical models which have proved useful in the initial development of VBL memory would be possible, further increasing confidence in them.

Industrial development of VBL memory is undertaken at present only by N.E.C. of Japan who hold certain key patents in the technology. The presently-stated position of the other Japanese bubble memory manufacturers, Hitachi and Fujitsu, is that they will wait until the basic technical feasibility of the scheme has been demonstrated, i.e., a small read/write/propagate chip has been fabricated, before themselves undertaking active research and development. Whether or not VBL data storage devices will finally appear as commercial products is still a somewhat open question. There is room, however, for justified optimism and with the gathering pace of research in Japan and elsewhere there is every prospect that questions of basic technical feasibility will largely be answered by late 1985 or early 1986. If this phase is successful, then the prospect of ultra-high density micromagnetic memory sharing bubble memory's attributes of providing rugged, solid-state, low power, non-volitile storage but with device capacities of greater than 64 Mbits, access times of the order 4ms and data transfer rates in excess of 1 MHz is highly likely.

CHAPTER IV

ANALYSIS OF DOMAIN AND DOMAIN WALL DYNAMIC BEHAVIOUR BY COMPUTER MODELLING

4.1 Introduction

The two-dimensional numerical solution of the equations of motion for a domain wall having a twisted wall structure, is already well established. Such solutions as bubble transport by Hayashi and Mikami [105] and stripe domain dynamics by Matsuyama and Konishi [95], have shown the capability of two-dimensional simulation in predicting the motion of Vertical Bloch Lines (VBL) at low wall velocities. The simulation of dynamic wall conversion due to Horizontal Bloch Line (HBL) punch through, initially solved numerically by MacNeal and Humphrey [106], has characterised plane wall motion at high velocities. In addition, the recent interest in VBL memory has encouraged various numerical studies of both HBL and VBL dynamics [98, 107]. All these simulations assume a plane wall with respect to wall position, q, and magnetisation azimuthal angle, ϕ_M, either in the plane of the film or through the film thickness. There remain, however, many features of VBL memory which require a three-dimensional approach for detailed study. Examples include VBL injection at the stripe head for write, stripe domain chopping for read, and localised material thinning for stripe domain stabilisation. To estimate the feasibility of a three-dimensional

calculation, the existing dynamic domain wall theory, initially proposed by Slonczewski [108], has been modified to permit treatment of a domain of arbitrary shape with associated twisted wall structure. The theory has been applied to the case of a translating unichiral bubble (i.e. without VBLs) with the intention of extending it to situations considered in VBL memory. The criterion for the simulation is that it be capable of illustrating wall motion at a sufficiently high velocity to include the formation, propagation, and punch-through of Bloch curves, using a realistic calculation time.

Section 4.2 summarises the derivation of the equations of motion by equating the Landau-Liftshitz-Gilbert equations to the functional derivatives of wall energy. The derivation is similar to that previously reported [39]. An additional term arises from the spatial variation of (ϕ_m - ϕ_{ip}), (the magnetization and stray field azimuthal angles), measured in the plane of the film. The increases in wall energy due to curvature and exchange terms, $\nabla^2 q$ and $\nabla^2 \phi_m$, are evaluated in three-dimensions. The assumptions made are that the exchange energy term is small and the wall is of constant width.

The numerical method of solution by the substitution of finite difference expressions is outlined in Section 4.3. A bubble of radius 3μm is represented by a q and ϕ_m defined at each of 3552 points. As treatment of this comparatively large increase in point number requires a relatively long computation time, methods to reduce computation cost are included. The Dufort-Frankel scheme for evaluating the 2nd order spatial partial differentials, $\nabla^2 q$ and $\nabla^2 \phi_m$, is modified to maintain stability at a practical computation time-step interval.

The single most time-consuming numerical process is the

demagnetising and stray in-plane field calculation. Section 4.4 describes a economical method of obtaining these fields. A circulating current of 2M emu/cm flowing on the domain wall is assumed, as discussed by O'Dell [41], and Biot-Savart's Law is integrated over the wall surface. The effect of localised wall curvature has been maintained. Distortion greatly removed from the observation point is ignored by integrating analytically through the film thickness.

The results shown in Section 4.5 illustrate the capability of the simulation. Examples of bubble transport between low, 0.5 Oe/μm, and high, 4.0 Oe/μm, drive fields are demonstrated by instantaneous skew angle, velocity, bubble locus, time-averaged velocity, domain shape, and magnetisation distribution configurations.

Finally in Section 4.6, the capabilities and limitations of the calculation are discussed with regard to further bubble dynamics and possible applications to VBL memory.

4.2 The Equations of Motion

The discussion is based on the Landau-Lifshitz-Gilbert equations integrated through the wall thickness as illustrated by Malozemoff and Slonczewski [39],

$$\frac{\delta\sigma}{\delta\phi_H} = \frac{2M}{\gamma}\left(\dot{q} - \alpha\Delta_0\,\dot{\phi}_H\right) \qquad \ldots\ldots 4.1$$

$$\frac{\delta\sigma}{\delta q} = -\frac{2M}{\gamma}\left(\dot{\phi}_H + \frac{\alpha}{\Delta_0}\,\dot{q}\right) \qquad \ldots\ldots 4.2$$

where $\frac{\delta\sigma}{\delta\phi_m}$ and $\frac{\delta\sigma}{\delta q}$ are functional partial derivatives of magnetisation azimuthal angle, ϕ_m, and wall position, q. γ is the gyromagnetic constant, α is the Gilbert damping parameter, Δ_o is the wall width parameter, and M is the spontaneous magnetization. The coercive field is assumed zero.

A bubble is defined in the XYZ co-ordinate system, or laboratory frame, as shown in Figure 4.2.1a. The bubble is represented numerically by a grid matrix of 3552 points (a compromise between computation cost and accuracy resulting in 96 points around the circumference at 37 levels through the thickness), for each of which a local co-ordinate frame, RSQ, is defined as shown in Figure 4.2.1b. The S axis is taken as tangential to the wall in the XY plane, the R axis tangential to the wall and perpendicular to S, and the Q axis orthogonal to the RS plane or normal to the domain wall. The sense of Q points to the direction of down magnetisation, i.e., into the bubble domain. Each wall point is made to displace normal to the domain wall.

Having defined our co-ordinate system at point P such that q is parallel to the Q axis, we may express the wall energy density in the vicinity of P projected on the RS plane and expanded to first order in curvature, exchange and magnetostatic terms as,

$$\sigma = \sigma_o (1 + \tfrac{1}{4} (\nabla q)^2) + 2A\Delta_o (\nabla\phi_m)^2 + 4\pi\Delta_o M^2 \sin^2 (\phi_m-\phi_t)$$

$$- \pi\Delta_o M \{H_t \cos (\phi_m-\phi_t) + H_n \sin (\phi_m-\phi_t)\} - 2MH_z\, q \qquad .....4.3$$

where σ_o is the wall energy per unit area ($=4(AK)^{\frac{1}{2}}$), A is the exchange constant, H_t and H_n are the wall tangential and normal in-plane field components respectively, H_z is the sum of fields perpendicular to the film plane, and ϕ_t is the wall tangent azimuthal

where $\frac{\delta\sigma}{\delta\phi_m}$ and $\frac{\delta\sigma}{\delta q}$ are functional partial derivatives of magnetisation azimuthal angle, ϕ_m, and wall position, q. γ is the gyromagnetic constant, α is the Gilbert damping parameter, Δ_o is the wall width parameter, and M is the spontaneous magnetization. The coercive field is assumed zero.

A bubble is defined in the XYZ co-ordinate system, or laboratory frame, as shown in Figure 4.2.1a. The bubble is represented numerically by a grid matrix of 3552 points (a compromise between computation cost and accuracy resulting in 96 points around the circumference at 37 levels through the thickness), for each of which a local co-ordinate frame, RSQ, is defined as shown in Figure 4.2.1b. The S axis is taken as tangential to the wall in the XY plane, the R axis tangential to the wall and perpendicular to S, and the Q axis orthogonal to the RS plane or normal to the domain wall. The sense of Q points to the direction of down magnetisation, i.e., into the bubble domain. Each wall point is made to displace normal to the domain wall.

Having defined our co-ordinate system at point P such that q is parallel to the Q axis, we may express the wall energy density in the vicinity of P projected on the RS plane and expanded to first order in curvature, exchange and magnetostatic terms as,

$$\sigma = \sigma_o (1 + \tfrac{1}{4} (\nabla q)^2) + 2A\Delta_o (\nabla\phi_m)^2 + 4\pi\Delta_o M^2 \sin^2 (\phi_m-\phi_t)$$

$$- \pi\Delta_o M (H_t \cos (\phi_m-\phi_t) + H_n \sin (\phi_m-\phi_t)) - 2MH_z q \qquad .....4.3$$

where σ_o is the wall energy per unit area ($=4(AK)^{\frac{1}{2}}$), A is the exchange constant, H_t and H_n are the wall tangential and normal in-plane field components respectively, H_z is the sum of fields perpendicular to the film plane, and ϕ_t is the wall tangent azimuthal

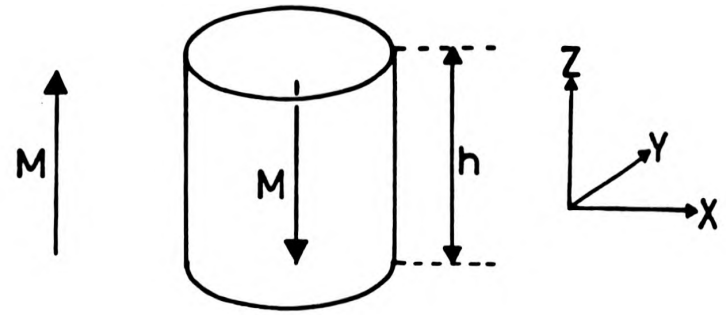

(a)

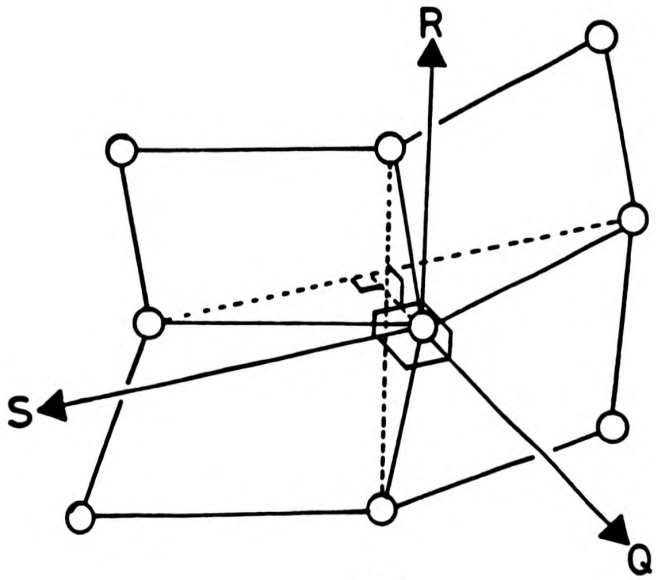

(b)

Fig.4.2.1 a) Laboratory co-ordinate system. b) Local co-ordinate system.

angle. The wall's internal demagnetising field has been replaced by a local approximation corresponding to the term $4\pi\Delta_0 M^2 \sin^2(\phi_m-\phi_t)$. Evaluating the functional derivatives defined by

$$\frac{\delta\sigma}{\delta q} = \frac{\partial\sigma}{\partial q} - \nabla \cdot \frac{\partial\sigma}{\partial(\nabla q)} \qquad .....4.4$$

and equating with equations 4.1 and 4.2, we obtain the equations of motion for a domain wall. With the substitution $\phi_t = \partial q/\partial S$ for small ϕ_t, the functional derivatives are given by,

$$\frac{\delta\sigma}{\delta\phi_m} = 2\Delta_0 M\, F(\phi_m) - 4\Delta_0 A\nabla^2\phi_m \qquad .....4.5$$

$$\frac{\delta\sigma}{\delta q} = -2MH_z - \sigma_0\nabla^2 q + 2\Delta_0 M \frac{\partial}{\partial S}(F(\phi_m)) \qquad .....4.6$$

where

$$F(\phi_m) = 2\pi M \sin 2(\phi_m-\phi_t) - \frac{\pi}{2}(H_n \cos(\phi_m-\phi_t) - H_t \sin(\phi_m-\phi_t)). \qquad .....4.7$$

Replacing H_t and H_n with $H_{ip}(\cos(\phi_{ip}-\phi_t))$ and $H_{ip}(\sin(\phi_{ip}-\phi_t))$ respectively, where H_{ip} is the in-plane field magnitude and ϕ_{ip} is the in-plane field azimuthal angle, $F(\phi_m)$ becomes,

$$F(\phi_m) = 2\pi M \sin 2(\phi_m-\phi_t) + \frac{\pi}{2} H_{ip} \sin(\phi_m-\phi_{ip}) \qquad .....4.8$$

Finally, equating equations 4.5 and 4.6 with equations 4.1 and 4.2 and separating the time differentials, dq/dt and $d\phi_m/dt$, we are left with the equations of motion,

$$\dot{q} = \frac{\gamma\Delta_0}{(1+\alpha^2)} \{F(\phi_m) - \frac{2A}{M} \nabla^2\phi_m + \alpha(H_z + \frac{2A}{M\Delta_0} \nabla^2 q - \Delta_0 \frac{\partial}{\partial S} F(\phi_m))\} \quad \ldots\ldots 4.9$$

$$\dot{\phi}_m = \frac{\gamma}{(1+\alpha^2)} \{H_z + \frac{2A}{M\Delta_0} \nabla^2 q - \Delta_0 \frac{\partial}{\partial S} F(\phi_m) - \alpha(F(\phi_m) - \frac{2A}{M} \nabla^2\phi_m)\} \ldots 4.10$$

where the 2nd order spatial partial differentials, $\nabla^2 q$ and $\nabla^2\phi_m$, representing increase in wall energy due to wall curvature and exchange energy respectively, are evaluated in three dimensions with respect to the RSQ frame, i.e.,

$$\nabla^2 q = \frac{\partial^2 q}{\partial R^2} + \frac{\partial^2 q}{\partial S^2} \quad \ldots. 4.11$$

$$\nabla^2\phi_m = \frac{\partial^2\phi_m}{\partial R^2} + \frac{\partial^2\phi_m}{\partial S^2} \quad \ldots. 4.12$$

Although for the purpose of evaluating equations 4.9 and 4.10 we measure ϕ_m, ϕ_t, and ϕ_{ip} from the S axis, we can define for convenience all azimuthal angles as being measured from a fixed line in the laboratory frame, the X axis, noting that the values $(\phi_m - \phi_t)$ and $(\phi_m - \phi_{ip})$ are independent of this definition.

To solve equations 4.9 and 4.10 numerically, the time and spatial differentials are replaced with finite difference expressions and

solved in the RSQ frame for the incremental displacements in q and ϕ_m over a time step ΔT. The laboratory frame is subsequently updated and the process continues. As each point is made to displace in a direction normal to the wall, successive calculations would lead to convergence or divergence of wall points. After each calculation step, therefore, the wall points must be rearranged to maintain stability. As described in Section 4.3, this may be achieved using available knowledge of the wall shape and spatial distribution of ϕ_m.

The material parameters used are $4\pi M$ = 195 G; h = 4.27μm; l = 0.616μm; γ = 1.83 x 10^7 $(Oe.s)^{-1}$; A = 2.63 x 10^{-7} erg/cm; and Ku = 8230 erg/cm^3; and, unless otherwise stated, α = 0.11, assuming a typical $(YSmLuCa)_3(GeFe)_5O_{12}$ garnet.

4.3 The Numerical Method

If we look at a section of wall, Figure 4.3.1, shown for simplicity in the SQ plane only, in the past, (n-1), present, (n), and future, (n+1), positions, we can see that the velocity of the wall point $q_{i,n}$ may be expressed in the finite form,

$$\dot{q} = \frac{\Delta q_{n+1} + \Delta q_n}{2\Delta T} \qquad \ldots.4.13$$

where Δq_{n+1} and Δq_n are the incremental displacements in wall position over successive time steps ΔT. Similarly, magnetisation angular velocity may be written as,

$$\dot{\phi}_m = \frac{\Delta\phi_{n+1} + \Delta\phi_n}{2\Delta T} \qquad \ldots.4.14$$

solved in the RSQ frame for the incremental displacements in q and ϕ_m over a time step ΔT. The laboratory frame is subsequently updated and the process continues. As each point is made to displace in a direction normal to the wall, successive calculations would lead to convergence or divergence of wall points. After each calculation step, therefore, the wall points must be rearranged to maintain stability. As described in Section 4.3, this may be achieved using available knowledge of the wall shape and spatial distribution of ϕ_m.

The material parameters used are $4\pi M$ = 195 G; h = 4.27μm; l = 0.616μm; γ = 1.83 x 10^7 $(Oe.s)^{-1}$; A = 2.63 x 10^{-7} erg/cm; and Ku = 8230 erg/cm^3; and, unless otherwise stated, α = 0.11, assuming a typical $(YSmLuCa)_3(GeFe)_5O_{12}$ garnet.

4.3 The Numerical Method

If we look at a section of wall, Figure 4.3.1, shown for simplicity in the SQ plane only, in the past, (n-1), present, (n), and future, (n+1), positions, we can see that the velocity of the wall point $q_{i,n}$ may be expressed in the finite form,

$$\dot{q} \simeq \frac{\Delta q_{n+1} + \Delta q_n}{2\Delta T} \qquad \ldots.4.13$$

where Δq_{n+1} and Δq_n are the incremental displacements in wall position over successive time steps ΔT. Similarly, magnetisation angular velocity may be written as,

$$\dot{\phi}_m \simeq \frac{\Delta \phi_{n+1} + \Delta \phi_n}{2\Delta T} \qquad \ldots.4.14$$

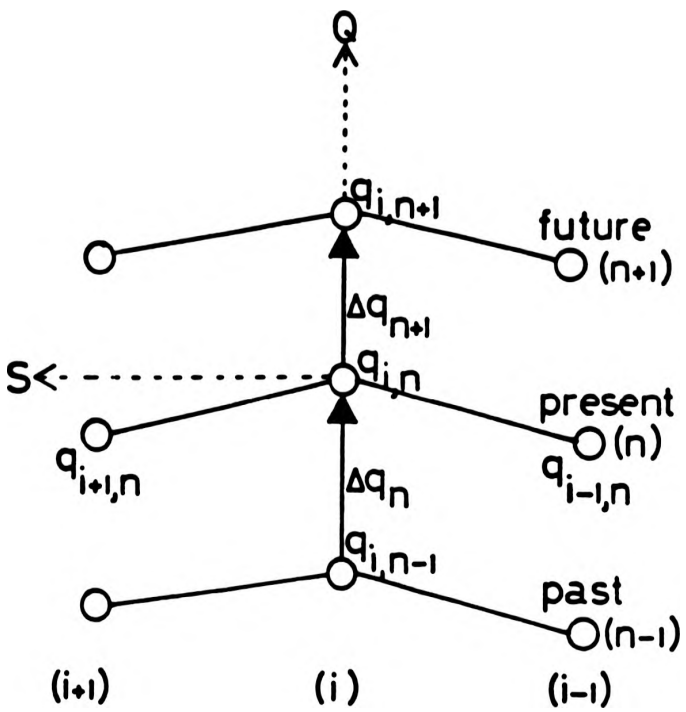

Fig.4.3.1 Numerical representation of domain wall in the QS plane in past, present and future positions.

The 2nd-order spatial partial differentials are replaced by a modified form of the Dufort-Frankel scheme. If we consider $\partial^2 q/\partial S^2$, and bearing in mind that the same procedure applies to $\partial^2 q/\partial R^2$, $\partial^2 \phi_m/\partial^2 S$ and $\partial^2 \phi_m/\partial R^2$, the Dufort-Frankel finite difference is given by

$$\frac{\partial^2 q}{\partial S^2} \approx \frac{q_{i+1,n} - q_{i,n+1} - q_{i,n-1} + q_{i-1,n}}{(\Delta S^2)} \qquad \ldots.4.15$$

where $q_{i,n}$ is the position of the i^{th} point at time n measured in the local co-ordinate frame. Converting to incremental displacements by substituting

$$q_{i,n+1} = q_{i,n} + \Delta q_{n+1} \qquad \ldots.4.16$$

$$q_{i,n-1} = q_{i,n} - \Delta q_n \qquad \ldots.4.17$$

we get,

$$\frac{\partial^2 q}{\partial S^2} \approx \frac{q_{i+1,n} - 2q_{i,n} + q_{i-1,n}}{(\Delta S)^2} + \frac{\Delta q_n - \Delta q_{n+1}}{(\Delta S)^2} \qquad \ldots.4.18$$

Equation 4.18 can be seen to be the finite difference form of a 2nd-order differential in its simplest form, plus what is essentially a stability term dependent on the difference in incremental displacement between successive time steps and which reduces to zero during steady state motion (i.e., $\Delta q_n = \Delta q_{n+1}$). In this simulation, in addition to those reported by Fujita et al [107], Konishi et al

[95, 98] and more recently Krumbholz et al [109], this term is increased by 50%, greatly improving the stability of the calculation. The partial differential is therefore taken as,

$$\frac{\partial^2 q}{\partial S^2} \triangleq \frac{q_{i+1,n} - 2q_{i,n} + q_{i-1,n}}{(\Delta S)^2} + \frac{3}{2}\left(\frac{\Delta q_n - \Delta q_{n+1}}{(\Delta S)^2}\right) \qquad ....4.19$$

with similar expressions used for $\partial^2 q/\partial R^2$ and $\nabla^2 \phi_m$. From the heat conduction equation, we know the finite difference solution of a one-dimensional partial differential equation should theoretically converge as $\Delta T \to 0$, and $\Delta T/\Delta S \to 0$. Although our case is more complex, provided ΔT is not excessively large and ΔS not too small, little effect of this modification would be expected, or can be seen from the bubble dynamics. For the configuration under consideration a compromise value of $\Delta T = 0.1$ ns was chosen, as opposed to a maximum ΔT of 0.01-0.02 ns using the standard form of equation 4.15.

Substituting the above finite difference expressions in equation 4.9 and 4.10, and separating future, (n+1), terms we are left with a pair of simultaneous equations in Δq_{n+1} and $\Delta \phi_{n+1}$,

$$AA\ \Delta q_{n+1} - \Delta_o\ BB\ \Delta \phi_{n+1} = CC \qquad ....4.20$$

$$AA\ \Delta \phi_{n+1} + \frac{1}{\Delta_o}\ BB\ \Delta q_{n+1} = DD \qquad ....4.21$$

The variables AA, BB, CC and DD, which are defined in Appendix 4.1, may be determined at any given time from the material and numerical parameters, the wall shape, the distribution of ϕ_m, and the applied

fields. Solving for the incremental displacements Δq_{n+1} and $\Delta \phi_{n+1}$ and updating the laboratory frame, the new wall position and magnetisation configuration are obtained. Replacing Δq_n and $\Delta \phi_n$ with Δq_{n+1} and $\Delta \phi_{n+1}$ respectively allows the calculation to proceed to the next time step.

As each wall point is made to displace normal to the wall, and therefore successive calculations would lead to an uneven distribution of wall points, the grid matrix must be repositioned after each calculation step. Figure 4.3.2 illustrates this process, each point being made to displace at a tangent to the wall, going to a given radial angle (to be called the reference angle, θ) from the bubble centre at a given level, i.e. Z co-ordinate, through the thickness. The wall position may be determined from simple trigonometry with the associated magnetisation azimuthal angle given by

$$\phi'_m = \phi_m + \vec{DS} \cdot \left(\frac{\partial \phi_m}{\partial S}, \frac{\partial \phi_m}{\partial R}, 0\right) \qquad \ldots.4.22$$

where $\vec{DS}$ is the three-dimensional vector, $(\Delta S, \Delta R, 0)$, from the wall point position before re-arrangement to that after re-arrangement. In addition, as the past wall displacements Δq_n and $\Delta \phi_n$ are needed for the next calculation step, these also must be adjusted in the same manner using the appropriate gradients.

Surface boundary conditions are imposed such that $\partial^2 q/\partial Z^2$ and $\partial^2 \phi_m/\partial Z^2$ are zero [106].

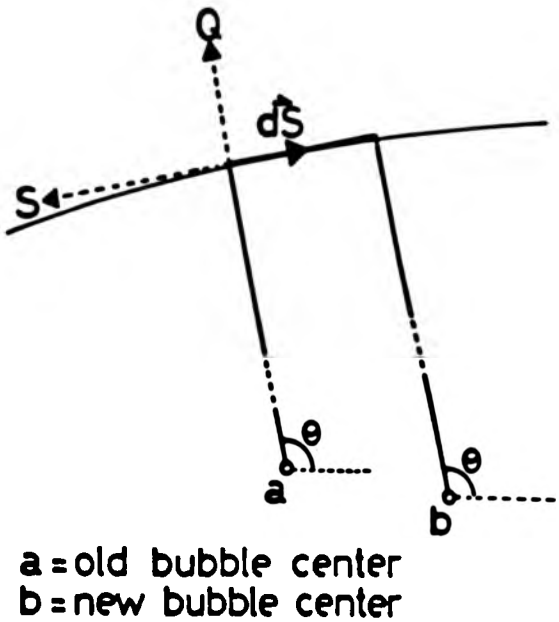

Fig.4.3.2 Repositioning wall points to prevent convergence or divergence with succession of calculation.

4.4 The Demagnetising and Stray Fields

By far the most time consuming section of the numerical solution is the derivation of the demagnetising and stray in-plane fields. Emphasis has been placed on reducing computation time while accounting, as accurately as possible, for wall distortion in three dimensions.

For the purpose of calculating these fields, a circulating current density of 2M emu/cm is assumed to flow on the domain wall. The effective field resulting from this current may be obtained at any point by integrating using Biot-Savart's Law over the wall surface. With reference to Figure 4.4.1, the field at point P, due to a current flowing in a direction ($\cos \phi_t$, $\sin \phi_t$, 0), in an element of width $Rd\theta$ and height dZ, a distance and direction $\vec{r}$ from P, is given by

$$\vec{dH}_p = 2M \frac{Rd\theta \, (\cos \phi_t, \sin \phi_t, 0) \times \vec{r}}{|r|^3} dZ \qquad \ldots.4.23$$

The total field at P is the surface integral

$$\vec{H}_p = 2M \int_0^{2\pi} \int_0^h \frac{R \, (\cos \phi_t, \sin \phi_t, 0) \times \vec{r}}{|r|^3} d\theta \, dZ \qquad \ldots.4.24$$

The stray field is the in-plane component and the demagnetising field is the Z component of $\vec{H}p$. Performing such a calculation numerically, with the inclusion of every grid point, would not only exceed the

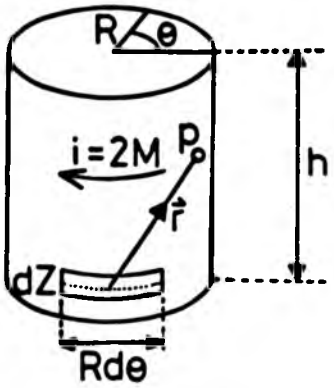

Fig.4.4.1 Demagnetising and in-plane field calculation.

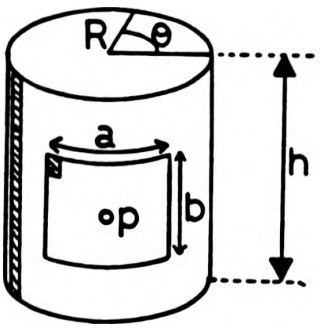

Fig.4.4.2 Window method for surface integral.

required accuracy of the simulation, but also be unrealistic in terms of computation time (The c.p.u. time to simulate 100ns is estimated as 4 days). Looking again at equation 4.23, it can be seen that the resultant field due to an element varies inversely as a function of the square of the distance from the point in question. This leads us to the conclusion that only the area in the immediate vicinity of P need be treated explicity. Our calculation, therefore, treats the area outside a predetermined "window", as shown in Figure 4.4.2, by assuming thickness-averaged values and integrating equation 4.24 analytically with respect to Z (see Appendix 4.2). The final integral around the bubble circumference is evaluated numerically by summation of the contributions of each element, as is the surface integral within the aforementioned window. $\vec{H}p$ is the sum of the fields from the two areas. For a bubble of radius 3μm, in a film of thickness 4.27μm, the chosen values of window width, a, and height, b, are 4.7μm and 2.4μm respectively. Even with the enormous saving in computation using this 'window method', to evaluate at every point, including every point for calculation, would still be unrealistic. Instead, the fields are determined at every 8th point, using every 8th point for calculation, the remainder being obtained by linear interpolation. Ideally, the choice of calculation point should be determined by the areas of greatest distortion, as suggested by Hayashi and Mikani [105], although this has been avoided in the three-dimensional case for numerical reasons.

It should be noted that $\vec{dH}p$ is discontinuous at $\vec{r} = 0$ and this would suggest that the above integral is numerically indeterminate. It was found, however, that by taking the tangential components of circulating current density as opposed to the non-physical straight

wall segments between grid points, and summing the contributions from nearest neighbouring wall segments, the demagnetizing field could be calculated to within 0.5% of that predicted for a bubble by Thiele [40] while avoiding the discontinuity at $\vec{r} = 0$. This is largely independent of the number of circumferential grid points in the range 20-200 and was thus considered adequate for the required accuracy of the calculation. Also, unphysical logarithmic divergences in the in-plane components of $\vec{Hp}$ arise at the film surfaces. These are avoided by calculating the field one grid point from the surfaces and extrapolating linearly. A surface in-plane field magnitude of 1.2 times $4\pi M$ is obtained which is in reasonable agreement with that expected [11]. In addition, as the so called critical points for Bloch line nucleation and punch-through are a comparatively long distance from the surfaces ($\approx 2.5\pi\Delta_0$) the inclusion of finite wall width in equation 4.24 would not significantly effect $\vec{Hp}$ at these points, and it was therefore considered unnecessary.

It is worth noting that the above method may be used to include the effect of localised material thinning. As shown in Figure 4.4.3, the thinned area creates a wall between regions of magnetization M and zero and may therefore be represented by a current density of M emu/cm. The influence of this thinned region may be included in a simple manner by integrating using Biot-Savart's Law as before.

4.5 Transport of a Three-Dimensional Bubble

Figure 4.5.1a and 4.5.1b show the domain shape and magnetisation azimuthal angle of a unichiral bubble stablised in a bias field of 75 Oe for 80 ns by which time an equilibrium state was reached, these

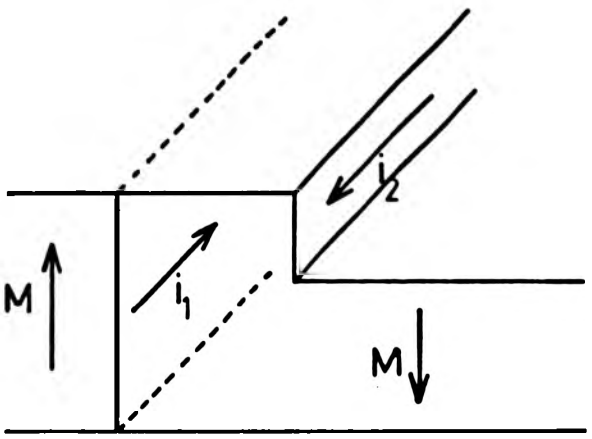

Fig.4.4.3 Including material thinning in demagnetising and in-plane field calculations.

being the initial conditions for bubble transport. The bubble assumes a barrel shape, a difference of 0.12μm in radii from surface to mid-plane being due to the variation in demagnetising field (see Figure 4.5.2a). An average bubble radius of 2.99μm is in good agreement with that expected from the two-dimensional theory. The 180^{o} twisted wall structure through the film thickness (Figure 4.5.1b) is a result of ϕ_m tending towards the stray in-plane field direction (Figure 4.5.2b). Also shown for comparison in Figure 4.5.2a is the field calculated assuming a uniform cylinder of 3μm radius. The wall curvature through the thickness tends to reduce the variation of demagnetising field from surface to mid-plane. The effect of wall curvature on the in-plane field was found to be negligible.

For bubble transport a field gradient, Hgrad Oe/μm, is superimposed to the bias field as,

$$H_z = H_{bias} + H_{grad}\,(X_C - X) \qquad ....4.25$$

Taking X_C-X as the bubble X co-ordinate measured from the bubble centre, bias field compensation is obtained, reducing domain distortion due to bubble expansion.

Bubble transport as expected was found to fall into three categories:-

(a) at low drive, < 0.85 Oe/μm, there was no Bloch curve formation,

(b) at medium drive fields, between 0.85 Oe/μm and 2.13 Oe/μm, there was Bloch curve nucleation without punch-through and

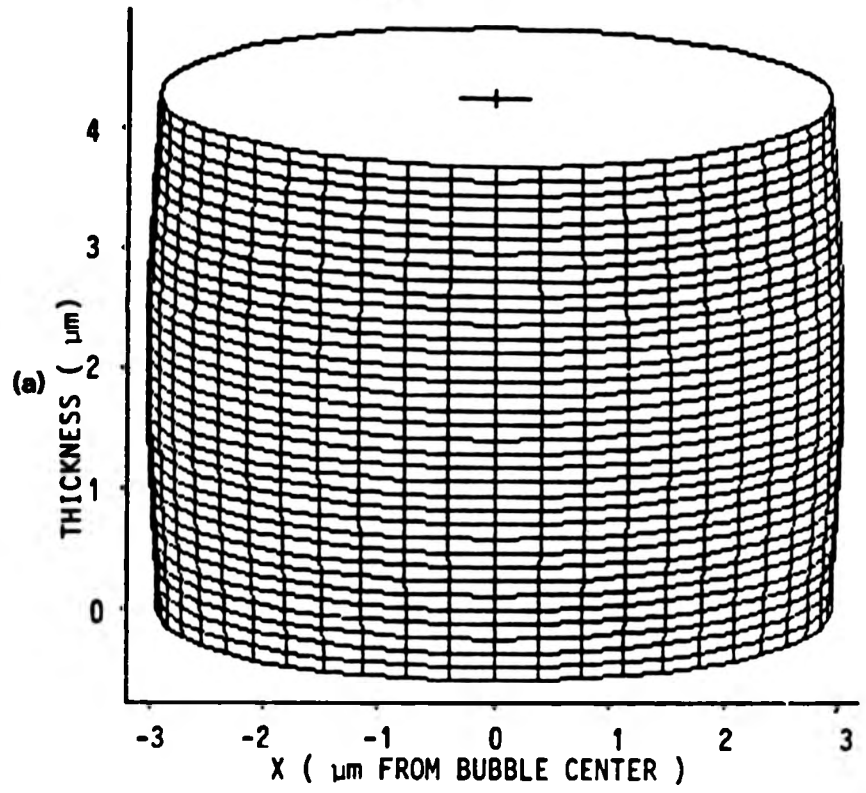

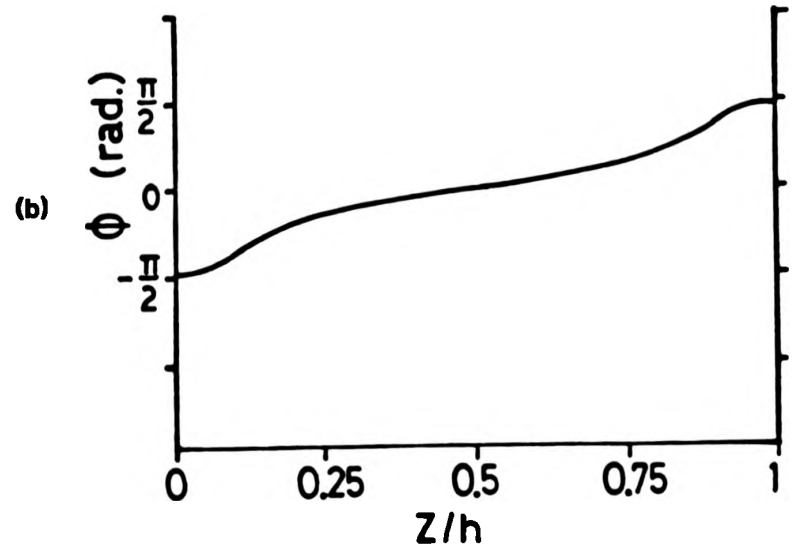

Fig.4.5.1 a) A bubble stabilised for 80 ns in a bias field of 75 Oe. Only 25% of the grid points are shown for clarity. b) Azimuthal angle of magnetisation measured from wall tangential direction as a function of position through film thickness.

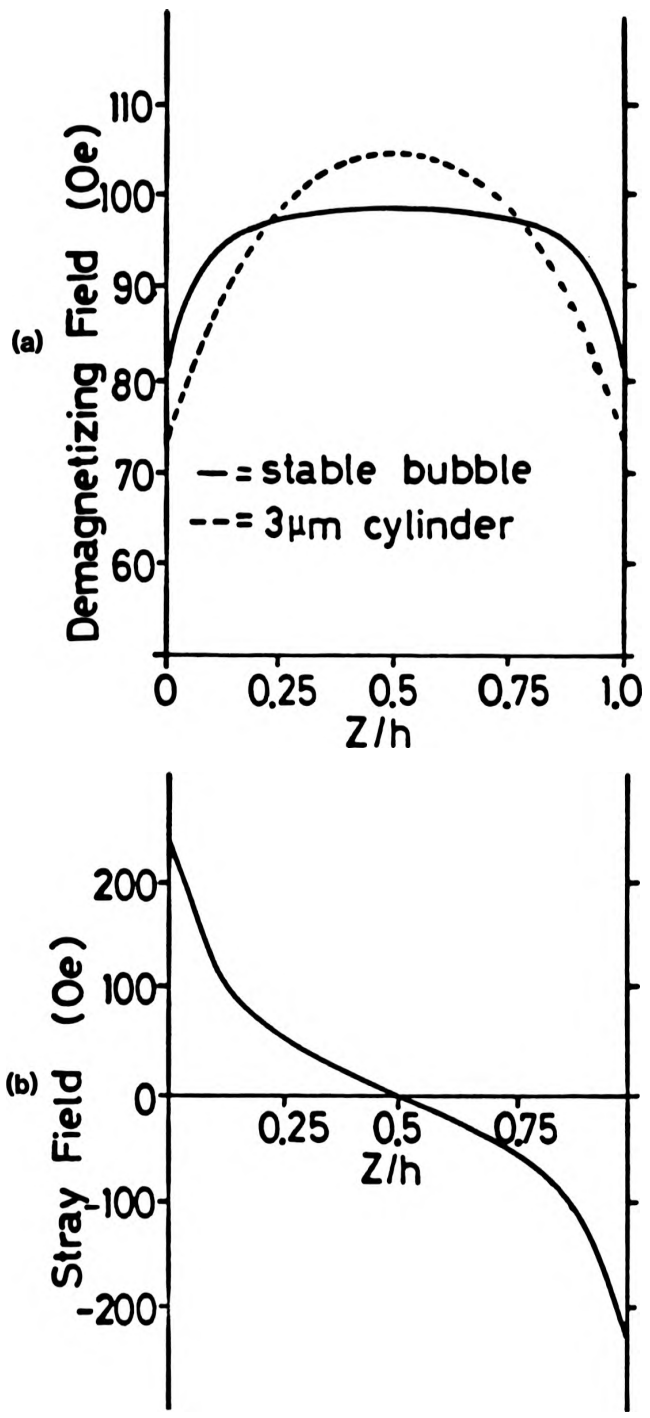

Fig.4.5.2 a) Demagnetising field and b) stray in-plane field both measured on the wall of the stable bubble as a function of position through film thickness.

(c) at high drive field, > 2.13 Oe/μm, there was Bloch curve punch-through with the formation of two VBL per Bloch curve.

Figure 4.5.3 illustrates the bubble skew angle at a low drive field, 0.5 Oe/μm, for three values of damping parameter α. Agreement with the two-dimensional theory [111, 112], shown in dotted line, which in turn is known to be in good agreement with experiment, is excellent. The simulated low drive field mobility of 9.39m/s/Oe also compares well with the theoretical value of 9.40m/s/Oe $((\gamma/\alpha)(A/K)^{\frac{1}{2}})$. Figure 4.5.4 shows the bubble instantaneous velocity and skew angle at drive fields of 0.5 Oe/μm, 1.5 Oe/μm and 3.5 Oe/μm corresponding to the low, medium and high drive field regions mentioned above. At medium drive field Bloch curves nucleate on the leading and trailing edges of the bubble causing the instantaneous velocity to decrease. Punch-through does not occur at this drive field and the velocity eventually approaches that expected with a linear mobility of 9.4m/s/Oe. This decrease in velocity and subsequent recovery as the Bloch curves propagate through the material thickness is similar to that discussed by Hagedorn [110]. The corresponding skew angle decreases at approximately the time the Bloch curves pass through the centre of the material thickness and also recovers to a skew angle similar to that of the low drive region. The drop in skew angle is attributed to the Bloch curves tending to centre about the X axis, i.e. the direction of maximum field gradient, as opposed to the initial direction of propagation along the low drive skew angle. At high drive field the Bloch curves punch-through as they reach the opposite surface forming two VBL per Bloch curve. New Bloch curves nucleate after punch-through causing the process to repeat and the

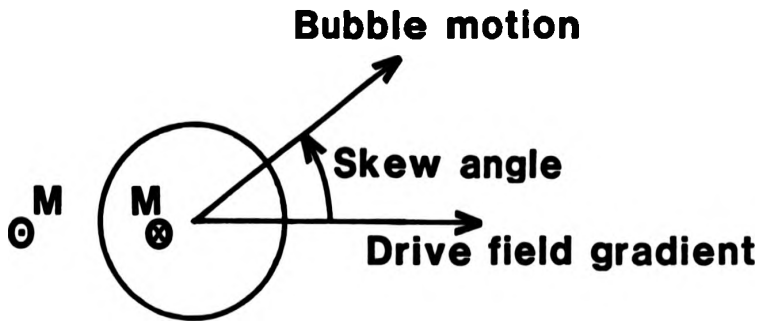

Fig.4.5.3a Definition of bubble skew angle.

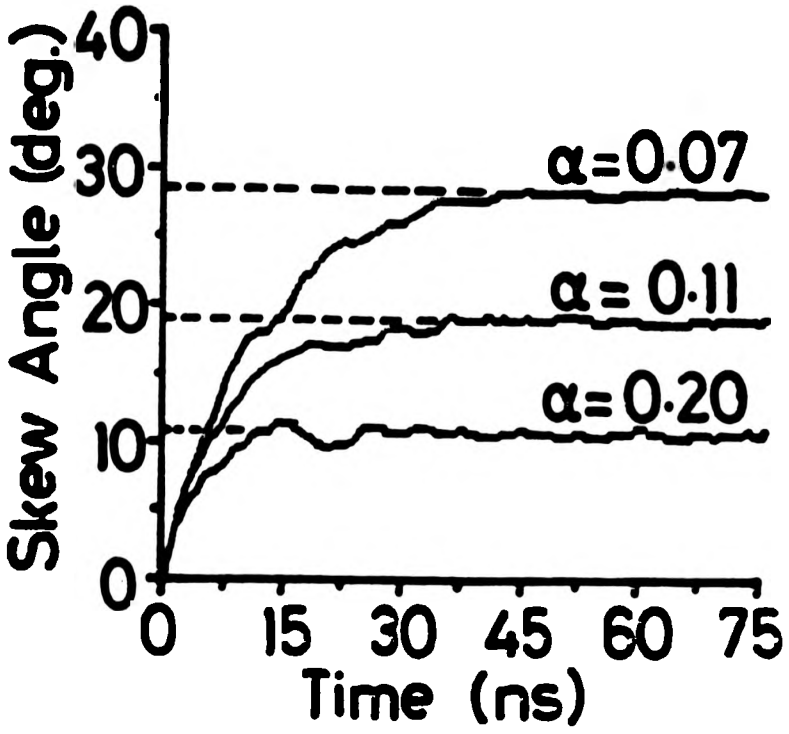

Fig.4.5.3b Bubble skew angle as a function of time for three values of damping parameter. Drive field is 0.5 Oe/μm. The dotted lines show the theoretical skew angles.

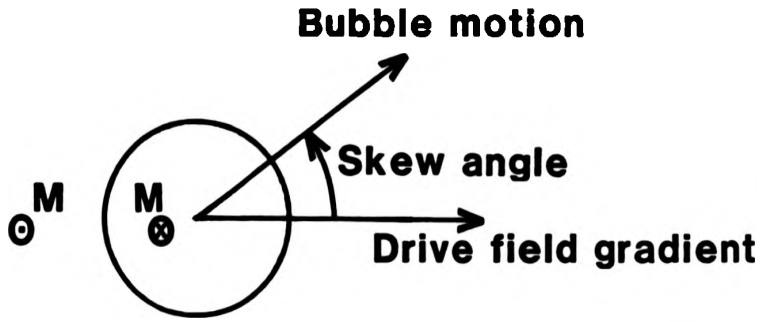

Fig.4.5.3a Definition of bubble skew angle.

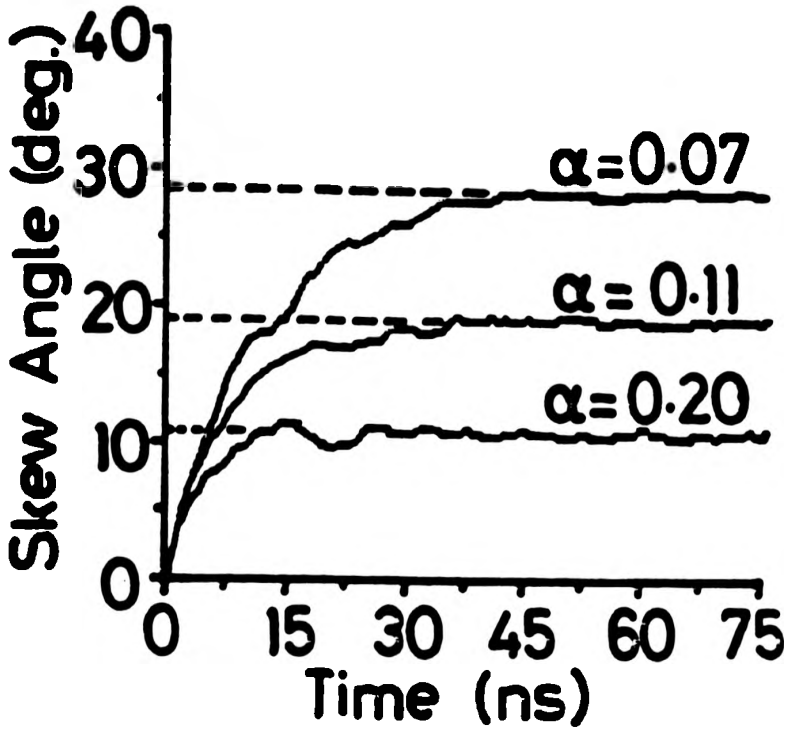

Fig.4.5.3b Bubble skew angle as a function of time for three values of damping parameter. Drive field is 0.5 Oe/μm. The dotted lines show the theoretical skew angles.

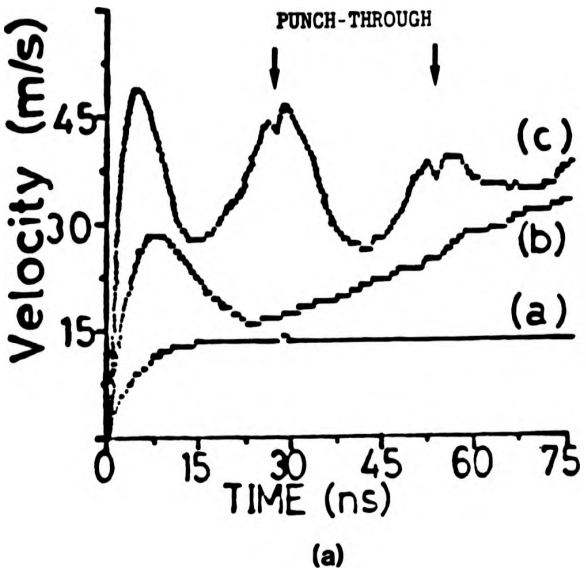

(a)

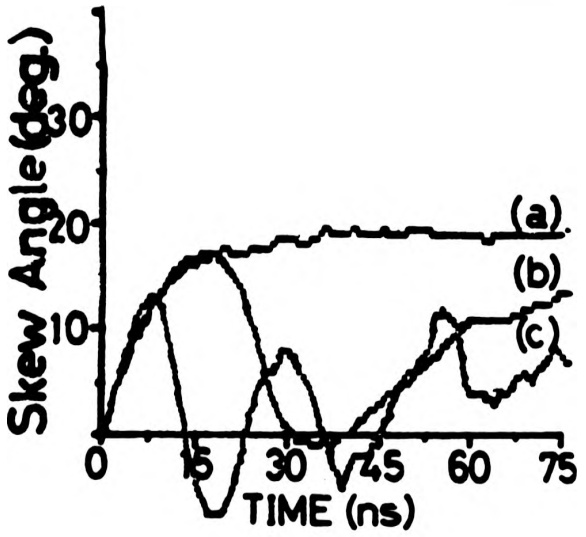

(b)

Fig.4.5.4 a) Bubble instantaneous velocity and b) instantaneous skew angle at drive fields of (a) 0.5 Oe/μm, (b) 1.5 Oe/μm, and (c) 3.5 Oe/μm.

velocity oscillates in an approximately periodic manner. The skew angle also demonstrates a similar periodicity although it is more erratic due to the additional gyrotropic forces associated with the propagating VBLs. For the drive field illustrated, 3.5 Oe/μm, punch-through occurs at 28.3ns and 54.2ns and is accompanied by a small decrease in bubble velocity. A plot of the bubble centre locus is included in Figure 4.5.5 for 0.5 Oe/μm and 3.5 Oe/μm drive fields. As expected from the plot of bubble skew angle the locus at high drive field is erratic and the average skew angle is much lower, 4.5^{o}, than that at low drive field, 19.1^{o}.

Figure 4.5.6 shows the bubble shape and Bloch curve positions at 10, 20, 30 and 40ns for a drive field of 3.5 Oe/μm. A dot and cross convention is used to define the direction of magnetisation at the centre of the Bloch lines. For the choice of bubble chirality (x-) a Bloch curve nucleates near the bottom surface on the leading edge and vice versa on the trailing edge. Associated with Bloch curve propagation is moderate domain distortion as would be expected from previous numerical solutions of plane wall dynamics [106, 107]. By 20ns the Bloch curve velocities have decreased considerably as they approach their respective surfaces. Punch-through on the leading edge occurs a few ns before that on the trailing edge (see Figure 4.5.6c), the difference becoming less noticeable at higher drive fields. The reason for such assymetrical punch-through can be seen from the bubble shape as the Bloch curves approach their respective surfaces. The bubble radius at the surface through which the leading edge Bloch curve punches is always less than the radius at the surface which the trailing edge Bloch curve is approaching, resulting in a slightly tapered-shape of bubble. The effective field at the

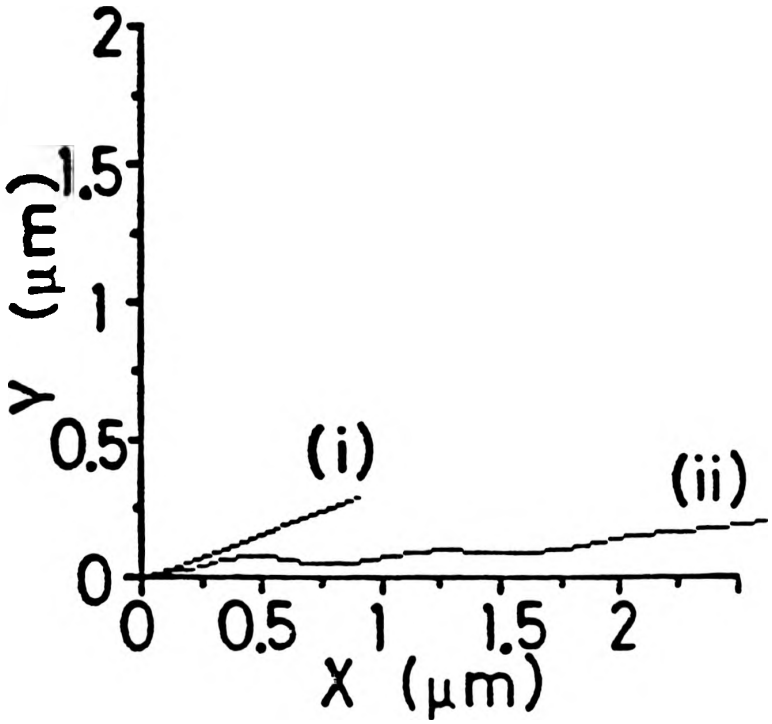

Fig.4.5.5 Bubble centre locus at drive fields of (i) 0.5 Oe/μm, and (ii) 3.5 Oe/μm.

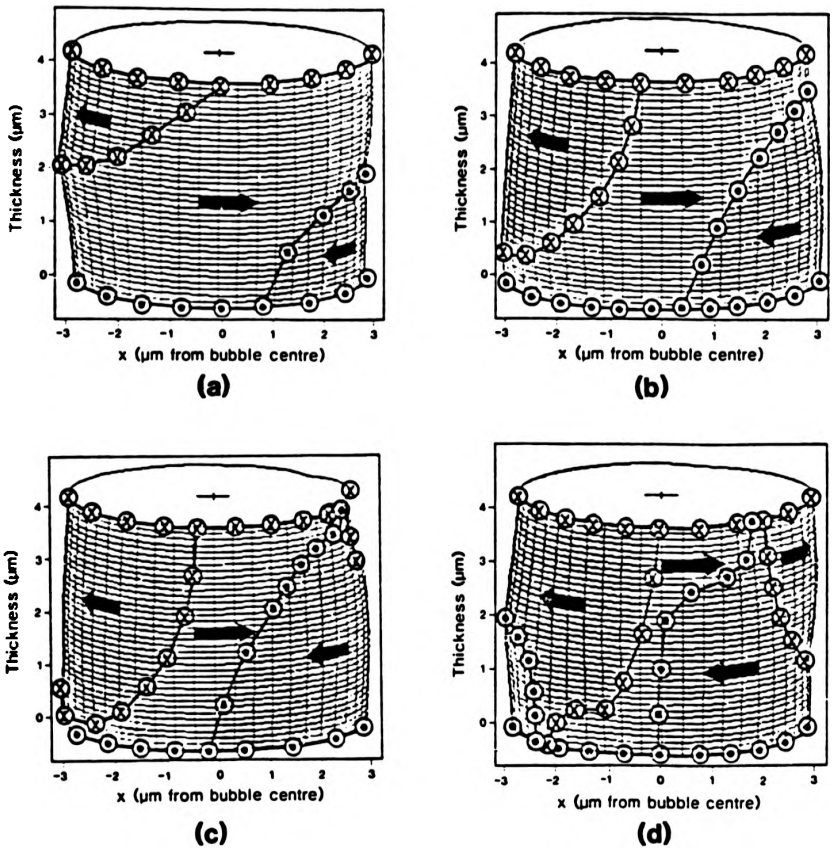

Fig.4.5.6 Bubble shape and Bloch curve positions for a drive field of 3.5 Oe/μm at a) 10 ns, b) 20 ns, c) 30 ns, and d) 40 ns. The X axis is centred on the bubble gravity centre with leading and trailing edges at +3 and -3 μm respectively.

surface with small radius is therefore greater causing the leading edge Bloch curve to punch-through first. This is true irrespective of initial bubble chirality. By 40ns both Bloch curves have punched-through and the VBLs converge on the flanks of the propagating bubble. The domain of Figure 4.5.6d has in total four VBL (two shown and two on the opposite wall) and two Bloch curves. The VBL are clearly seen to be three-dimensional structures with a rotation of magnetisation of 360^{o} at one surface and zero at the other.

From Figure 4.5.7 the time-averaged velocity at high drive field can be seen to decrease to a saturation velocity of 35m/s although the instantaneous velocity (Figure 4.5.4a) increases beyond 50m/s. Such high instantaneous velocities would probably not be observed experimentally as the time and spatial resolutions of the simulation (0.1ns and < 1nm) are unlikely to be obtained practically. Figure 4.5.8 plots both the time-averaged velocity and initial peak instanteous velocity as a function of drive field resolved in the direction of propagation across the bubble radius. The three regions of propagation are clearly seen. Below 2.4 Oe a Bloch curve does not nucleate and the simulated mobility agrees well with the theoretical value of 9.4 m/s/Oe. In this region the bubble dynamics are virtually identical to those obtained from the much less complex two-dimensional simulation and, as such, if the velocity can be limited to these values the simpler calculation is much preferable. The apparent drop in averaged velocity above 2.4 Oe/μm is a result of averaging over a relatively short time period of 80ns. As averaging time increases the averaged velocity will approach that corresponding to a mobility of 9.4 m/s/Oe as observed in Figure 4.5.4a. Beyond 6.25 Oe Bloch curves punch-through causing the instantaneous velocity

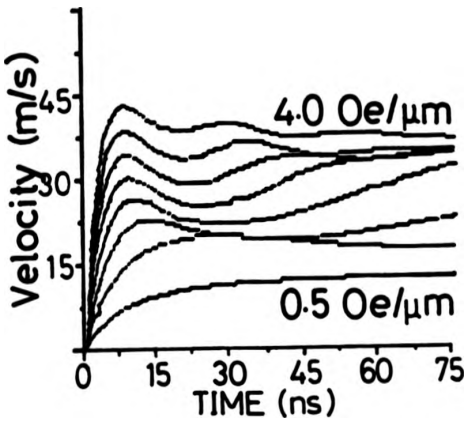

Fig.4.5.7 The bubble time-averaged velocity as a function of averaging time for various values of drive field gradient. A saturation velocity of 35 m/s is observed.

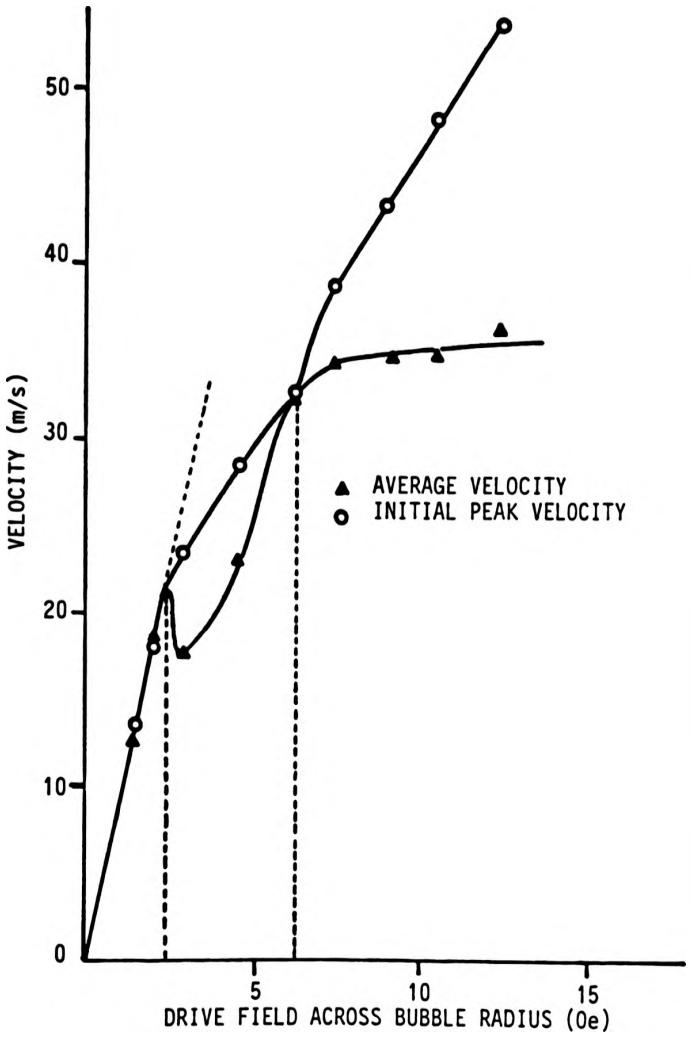

Fig.4.5.8 The bubble average velocity and initial peak velocity as a function of drive field magnitude across the bubble radius.

to break down and the averaged velocity to saturate. There is now continual formation, propagation and punch-through of Bloch curves which, by analogy to VBL motion in a domain wall as discussed in section 1.3, would suggest that there should be a high drive mobility of approximately α^2 times the low drive mobility. Here again, however, the averaging time was limited to 80ns to save on computation cost which is insufficient to quantify these values accurately. The initial instantaneous peak velocity continues to rise linearly with drive field at a gradient of 3.0 m/s/Oe.

The simulated saturation velocity of 35 m/s is higher than that expected. Malozemoff et al [45], using a quasi-static state model in the limit $\alpha = 0$, have calculated a saturation velocity for the case of punch through of 0.42 Vp where Vp is the so-called plane wall peak velocity. This model however explicitly excludes the possibility of the instantaneous velocty increasing beyond Vp as has been found in this work for this choice of material parameters. Hagedorn [110] has discussed the difficulties of quantifying saturation velocity and has illustrated the wide range of values that could be obtained experimentally depending on which type of averaging is used. It would seem reasonable, however, to assume that if the instantaneous velocity continues to increase above the peak wall velocity at which punch-through occurs then a succession of punches through and the resulting damping effect of nucleated VBL will tend to decrease the saturation velocity to that of the peak wall velocity. While the simulated saturation velocity is slightly larger than that given for the punch-through threshold velocity by Slonczewski (equation 3.2.1), it is in good agreement with a numerically-calculated value of 35.1 m/s for plane wall dynamics [107] using the same material

parameters, and a theoretical value of 34.97 m/s given by $2M\gamma\Delta_0(h/h-\pi\Lambda))$ [113]. While the value simulated is therefore not unreasonable, clearly the calculation must be compared more directly with experiment as is intended in the near future.

Finally, bubble overshoot was briefly examined by terminating a drive field of 3.5 Oe/μm at 20, 25 and 35ns as shown in Figure 4.5.9. After pulse termination the velocity decreases sharply and settles to a "steady state" motion as the Bloch curves unwind. For the case of a 35ns drive field pulse, punch-through occurs and the bubble overshoot is comparatively small as the nucleated VBL are metastable on the bubble flanks. The momentum stored in the Bloch curves and VBL is clearly conserved. Also of note from the case of punch-through is that after the pulse turns off the velocity drops to zero. This is due to the nucleated VBL preferring a vertical configuration to minimise the total VBL length and therefore Bloch line energy. Such a rapid straightening of the VBL is not observed during normal propagation as the gyrotropic force associated with domain wall motion is insufficient for the VBL head (2π rotation) to traverse rapidly to the bubble flanks and is in opposition to the required motion of the tail (zero rotation). After pulse termination, however, the domain is simply trying to reach an equilibrium state and the total VBL length is reduced by the 'tail' moving directly under the 'head'. Such movement is in opposition to that dictated by the direction of propagation and therefore requires an energy which is apparent in the extra reduction in velocity. One could visualise negative velocities occurring due to this mechanism although none were observed.

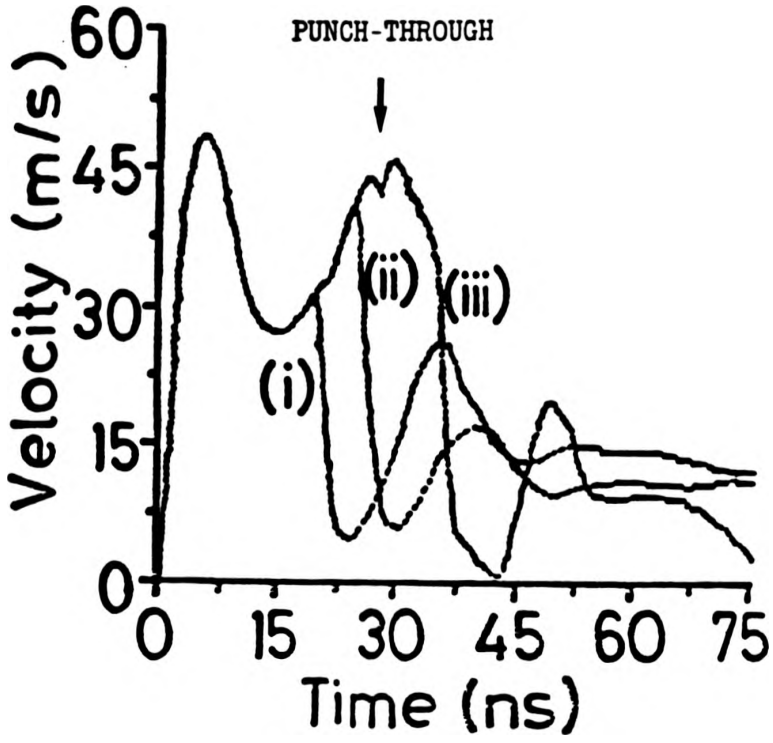

Fig.4.5.9 Bubble overshoot observed when a drive field of 3.5 Oe/μm is terminated at (i) 25 ns, (ii) 30 ns, and (iii) 35 ns. For case (iii) punch-through occurs.

4.6 Discussion and Summary

The feasibility of a three-dimensional simulation of an arbitrary shaped domain wall with an associated domain wall magnetisation structure has been demonstrated by applying the numerical solution to the case of a translating bubble. By employing a combination of analytical and numerical methods in the demagnetising and stray field calculation, a significant saving in computation time has been achieved. The simulation has been written in Fortran, each calculation step of 0.1ns taking 0.75 seconds c.p.u. time using a Fujitsu FACOM M-329 computer. The simulated time was limited to 80ns to minimise total computation cost. It is felt that with present-day computational capability simulation times in excess of 100-200ns are prohibitive and therefore simulation of VBL dynamics, as in the previously discussed context of VBL memory, is as yet unrealistic in three-dimensions. Apart from a general increase in understanding of Bloch line dynamics, the three-dimensional simulation would appear best suited to punch-through at the stripe head and stripe domain chopping in VBL memory as both these processes are relatively short, < 100ns. Punch-through at the stripe head should be similar to that on the leading edge of the bubble, although this has not yet been simulated. Stripe domain chopping has been studied in three-dimensions by Ohbo and Konishi [114].

The simulated bubble deflection angle and velocity at low drive field was found to be in good agreement with previous theory. At high drive field the physical picture of Bloch curve nucleation, propagation, and punch-through with oscillation of velocity, punch-through at velocity peaks, decrease in skew angle, and

ballistic overshoot is consistent with existing models. A relatively high, although not unrealistic, saturation velocity was observed. Clearly a more direct comparison with experiment and simulation over a wide range of material parameters is desirable and will be undertaken in future work. A promising approach to direct experimental comparison is the three-dimensional dynamic bubble collapse model of Fujita et al [115]. In the case of radial collapse, circular symmetry is conserved and thus the equations of motion need only be applied to one point at each level through the thickness. Approximately one hundreth of the previously-mentioned computation time is required allowing the program to run on a personal computer (NEC PC-9801). Such a calculation is probably better suited to experimental comparison and application over a wide range of parameters due to its low cost.

The attractive force between VBL, as discussed by the point charge model in Chapter 3 has not been included in the bubble transport simulation. The forces involved are very small in comparison to those required for punch-through and therefore their inclusion is felt unnecessary for this case. An attempt was made to include the distributed charge of a VBL in a three-dimensional straight wall but this involves an additional calculation of similar numerical complexity to the demagnetising field. In addition, as VBL dynamics exhibit a comparatively long time constant the overall computation time was found to be excessive. As computation capability increases in the future, no doubt this term will be included.

CHAPTER V

CONCLUSIONS

The use of magnetic bubble computer storage is gradually becoming more widespread. Clearly it is now aimed at a low volume rather specialised commercial market as it is unable to compete with much cheaper forms of mass storage such as magnetic tape or disc technologies. Its unique attributes, however, make it the only possible storage medium in hostile environments and where data integrity is of paramount importance. As such, its main uses are at present military and aerospace applications although the rapid decrease in system cost is now opening further markets where low power and high density are relevant considerations. Magnetic bubble technology has continually offered storage densities of 4-16 times that of semiconductor storage and with the introduction of VBL memory the gap is likely to widen further. This work has investigated some novel aspects of bubble technology, in particular the high-speed dual-conductor current-access device and the ultra high density VBL memory. Combining the attributes of both these concepts a high performance solid-state non-volatile magnetic memory which has capacities of up to 1 Gbit and data transfer rates in excess of 1 MHz appears a distinct possibility.

The fabrication of dual-conductor apertured-sheet current-access propagation patterns has been undertaken using dry processing technology. The final devices were of only limited quality due to the

poor second layer registration and the difficulties of RIE of Al/4% Cu using CCl_4. On this latter point, it is felt that a non-chemical etching process such as ion milling using Ar would be better suited to delineation of conductor layers. Such a system was not available during this project and realistically would only be available if it was deemed necessary for associated microfabrication projects. The problems associated with second layer registration have subsequently been alleviated by the improvement of picture quality of the EBM in SEM mode. These difficulties are obviously related to fabrication equipment quality and not in any way to the fundamental concepts of current-access bubble memory. It became apparent during the course of this work, and with hindsight is obvious, that high quality lithography is extremely difficult without very high quality fabrication equipment and clean room facilities. The financial commitment and manpower necessary to maintain such equipment was unavailable within the limited resources of the magnetic bubble research group at Manchester University. Consequently, the initial aim of this work, i.e. the design and testing of current-access propagation circuits with the intention of improving bubble memory device performance, was not fulfilled. It is recommended that future work on actual device fabrication should therefore rely more heavily on collaborative research with, in particular, industry. Industrial commitment to magnetic bubble technology in the U.K. is non-existent and therefore such collaborative efforts must be established abroad. This is at present being pursued in the context of VBL memory with similar research groups in Japan, Germany and France.

The possibility of coding data as micromagnetic twists in a domain wall as in VBL memory offers the potential of single device

storage densities of 1 Gbit. The concept of VBL memory and its presently-expected mode of operation has been discussed in detail. By applying simple design rules, it would appear that, although the ultimate device density is perhaps a factor of four less than that initially anticipated, access times, data transfer rates and power dissipation compare favourably with conventional bubble memory at densities greatly increased over the latter. These projections were performed using the simple major-minor loop or 'disc lookalike' architecture which has proved so popular with bubble memory manufacturers and undoubtedly more complex designs incorporating bubble logic, cache loops or chip partitioning will further enhance operational characteristics. Applications for such ultra-high density memory are as yet largely unconsidered. Clearly there is a potential for archival uses although, as with bubble devices, the cost of VBL memory is unlikely to be able to compete with tape and disc media. Apart from applications common to conventional bubble memory, where ruggedness and reliability are of interest, it is anticipated that the higher density of VBL memory will make it more attractive in portable or low-weight systems.

As yet VBL technology is in its infancy and the number of possible areas for future work are unlimited. It is apparent however that simulation of device behaviour will play a major role in its development. Numerical techniques to solve the equations of motion for a domain wall having an associated twisted wall structure have been studied in this work. The solution has been extended to three-dimensions and applied to the case of a translating magnetic bubble. Translational velocities exceeding that for dynamic wall-state conversion and the subsequent formation of VBL by the

punch-through of Bloch curves have been studied, an area directly relevant to the write process in VBL memory. The simulated domain dynamics at low velocities are in good agreement with those theoretically predicted, while at high velocities they appear consistent with previous Bloch line models. There remains, however, a need to compare more directly the simulated results with those found experimentally and this should be one of the major considerations in future theoretical research. This is also generally true of research on VBL memory. While confidence in device simulation is justifiably high, the vast majority of work on VBL memory so far has been theoretical. It is essential that in the near future correlation between these theoretical results and experimental device behaviour is established. It is anticipated that such correlation will be possible when the initial test devices are produced within the next few months. Hopefully design of these test structures will be based on a current-carrying conductor approach giving external control over both potential wall structures and gyrotropic drive forces. Such a device is likely to undergo many design changes before a commercial product is available. In many ways this early work on VBL memory is akin to that of early bubble technology. Innovative propagation patterns and methods of read/write are anticipated. Such early research has two distinct advantages over that of bubble technology. Firstly, the magnetic media is similar to that already used in bubble devices and there is a readily-available device-quality supply, and secondly, VBL physics have been widely documented over the past decade. As such, providing the fundamental functions can be demonstrated in a fully-functioning test device, advances are expected to occur at a rapid pace. To its

disadvantage, however, is the difficulty of observing such fine structures, a technique which has proved useful in early magnetic bubble research. In addition the independent potential-well structure and drive force is arguably a higher degree of control over data propagation or an added complexity. Which of these it proves in practice remains yet to be seen.

There is room for justifiable optimism with regard to VBL memory. As yet no fundamental flaws in its conception have been identified. It is, however, a technology of the future. Although it is estimated that using today's lithographic capabilities devices of the order 64-128 Mbits are possible, these would not be anticipated in the next two or three years. Certainly devices of the order 1 Gbit will not become available until the necessary fabrication techniques are possible in industry and even optimistically would not be expected before the 1990's. Such a device, if it were to be produced at a price which enabled wide availability, would greatly condense the increasing volume of binary-coded data and could produce a minor revolution in information technology.

APPENDIX 1

UNITS AND SYMBOLS

A1.1 Commonly-Used Symbols

h	Thickness of magnetic garnet
Q	Quality factor
α	Gilbert damping parameter
M	Magnetisation
K	Anisotropy constant
γ	Gyromagnetic ratio
H	Magnetic field strength
σ_o	Wall energy density
l	Characteristic length
A	Exchange constant
μ_w	Wall mobility
Δ_o	Wall width parameter
Λ	Bloch line width parameter
ϕ	Azimuthal angle of magnetisation
θ	Polar angle of magnetisation
q	Wall position
Sw	Stripe width
d	Bubble diameter
r	Bubble radius or VBL pair bit position

A1.2 Comparison of SI and cgs Units

Quantity	Units		Conversion ratio
	cgs	SI (Sommerfeld Convention)	
Magnetisation	G	Am^{-1}	$10^3/4\pi$
Anisotropy	erg/cm^3	Jm^{-3}	10^{-1}
Exchange constant	erg/cm	Jm^{-1}	10^{-5}
Gyromagnetic ratio	$(s.Oe)^{-1}$	$(s.Am^{-1})^{-1}$	$4\pi/10^3$
Gilbert damping parameter	——	——	1
Magnetic field strength	Oe	Am^{-1}	$10^3/4\pi$
Wall energy density	erg/cm^2	Jm^{-2}	10^{-3}
Characteristic length	cm	m	10^{-2}
Wall mobility	cm/s/Oe	$m^2s^{-1}A^{-1}$	$4\pi \times 10^{-5}$
Quality factor	——	——	1

To convert value in cgs to value in SI, multiply by conversion ratio.

APPENDIX 2

FABRICATION CHARACTERISATION

A2.1 Characteristics of Sputter Deposition

A2.2 Reactive Ion Beam Etching

A2.3 End-Point Detection Noise Reduction

A2.4 Electron Beam Resists

A2.5 Test Equipment

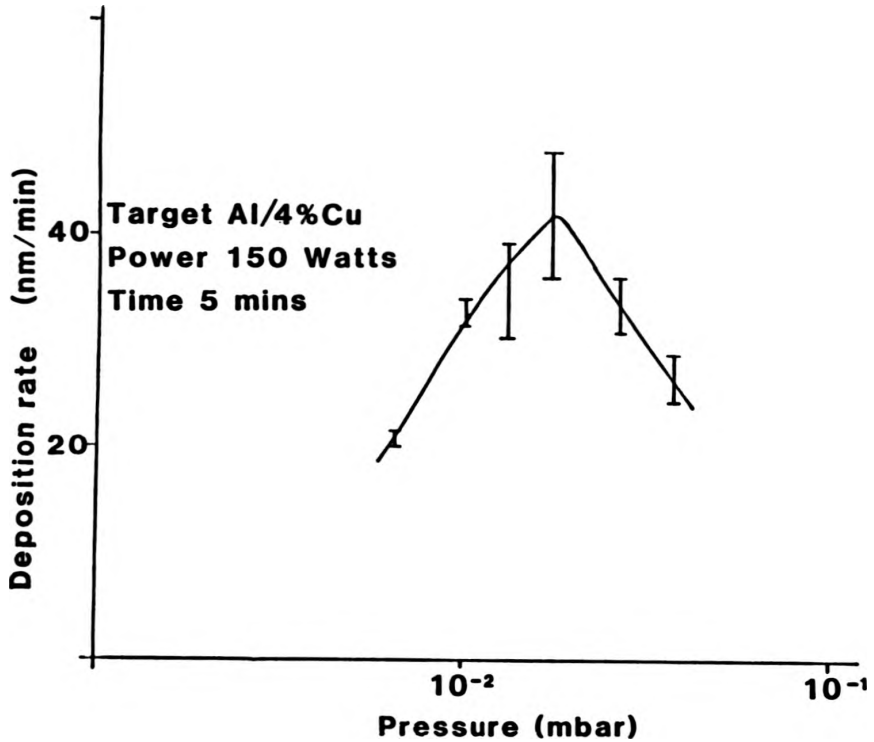

Fig.A2.1 Sputter deposition rate of Al/4%Cu as a function of pressure. The target diameter is 10.6cm and the substrate-target spacing is 4cm.

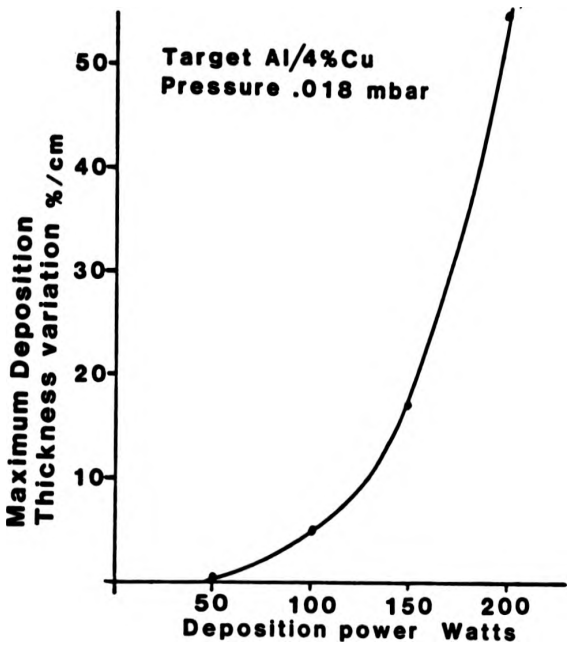

Fig.A2.2 Deposition uniformity as a function of power.

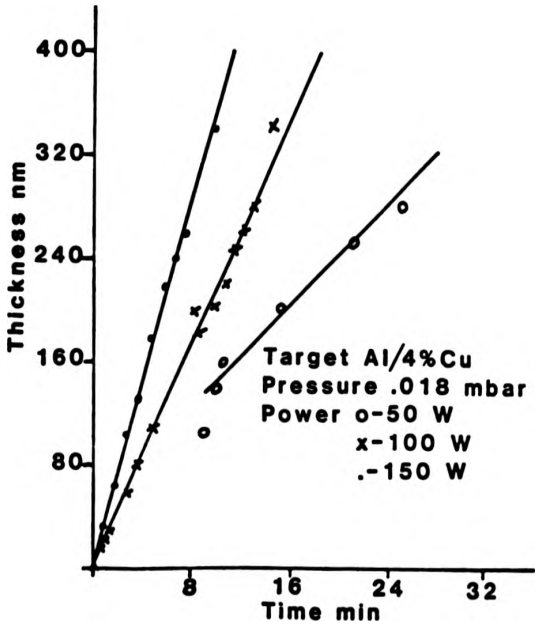

Fig.A2.3 Sputter deposition thickness as a function of deposition time.

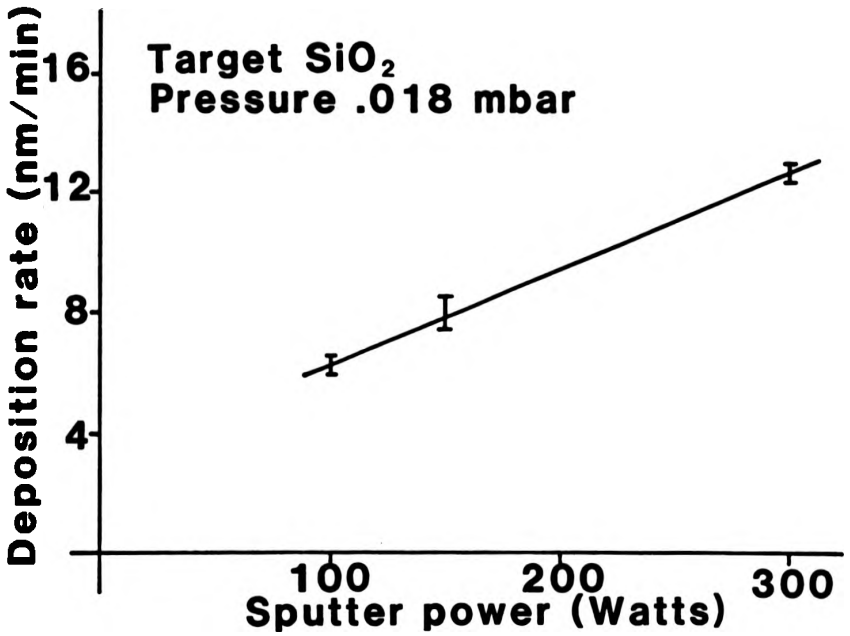

Fig.A2.4 Sputter deposition rate as a function of power.

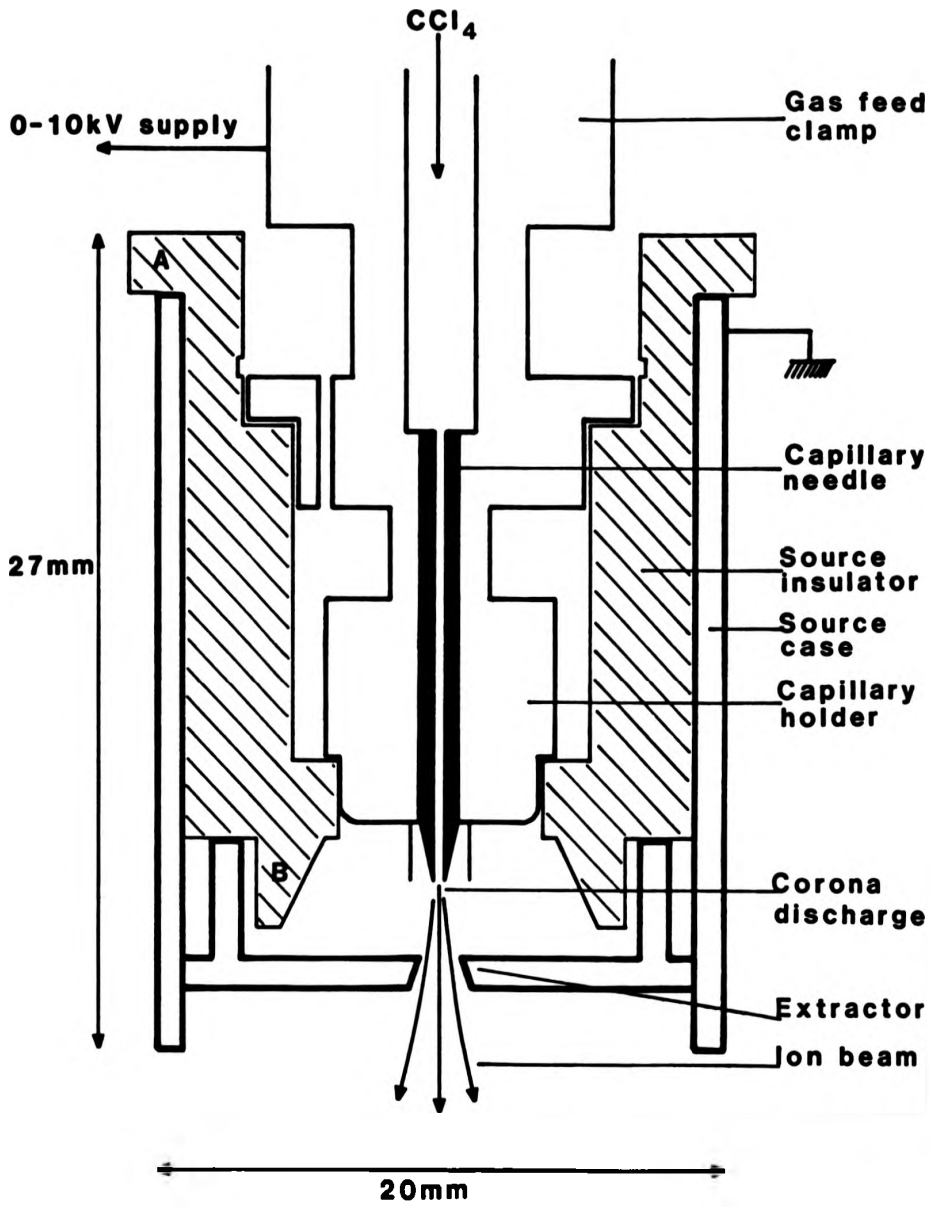

Fig.A2.5 Cross section of the ion source and modified insulator. A voltage on the capillary needle causes a corona discharge, ionising the reactive gas. The ion beam is accelerated by the pressure differential across the source and by the voltage across anode and extractor. The origional source insulator (ground glass) was replaced with PTFE and modified at A and B to discourage high voltage breakdown.

APPENDIX 2.3

NOISE REDUCTION IN END POINT DETECTION

The optical switch, S1, of Figure A2.6 is physically positioned so that when it is open circuit the input to the monochromator is optically isolated. The photomultiplier output (noise only) is amplified with a negative gain through IC3. With S1 closed the monochromator is exposed to the optical emission from the plasma discharge and the resultant photomultiplier output (noise + signal) is amplified with a positive gain through IC3. The output low pass filter averages the signal, greatly improving the signal-to-noise ratio for the system.

This circuit is now incorporated in test equipment for the study of S.A.W. devices.

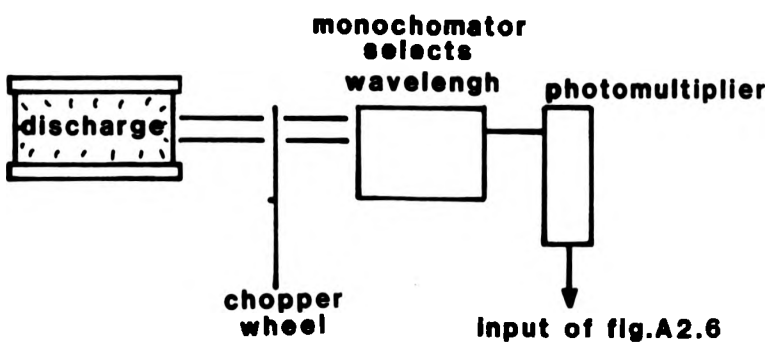

Fig.A2.6a Optical spectroscopy.

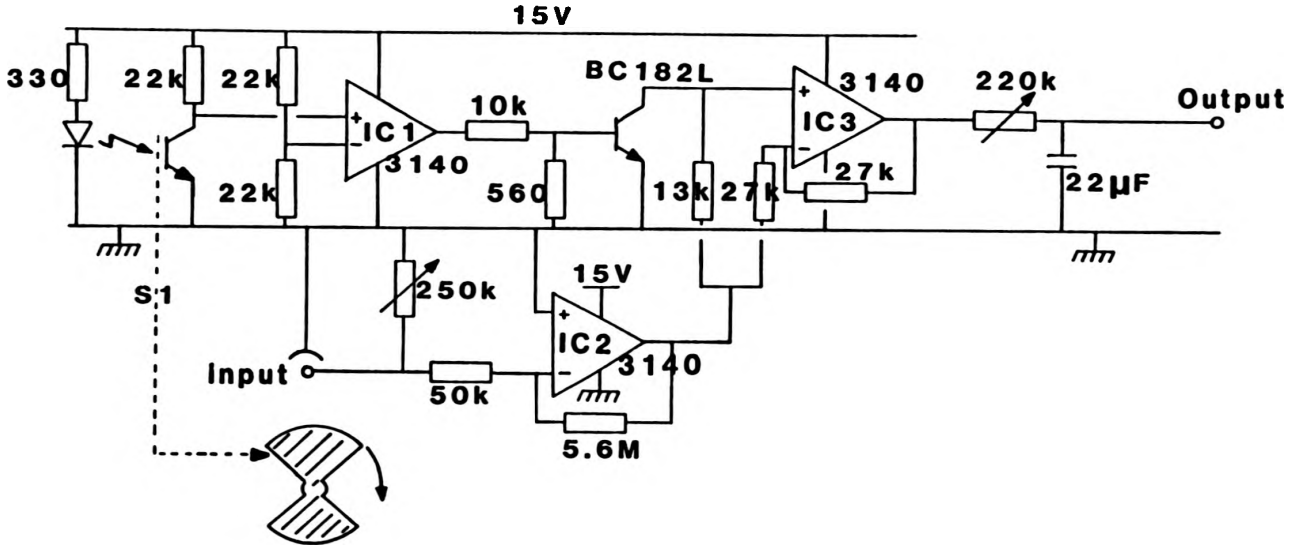

Fig.A2.6b The noise-reduction chopper circuit used in the optical spectroscopy equipment for end-point detection in RIE.

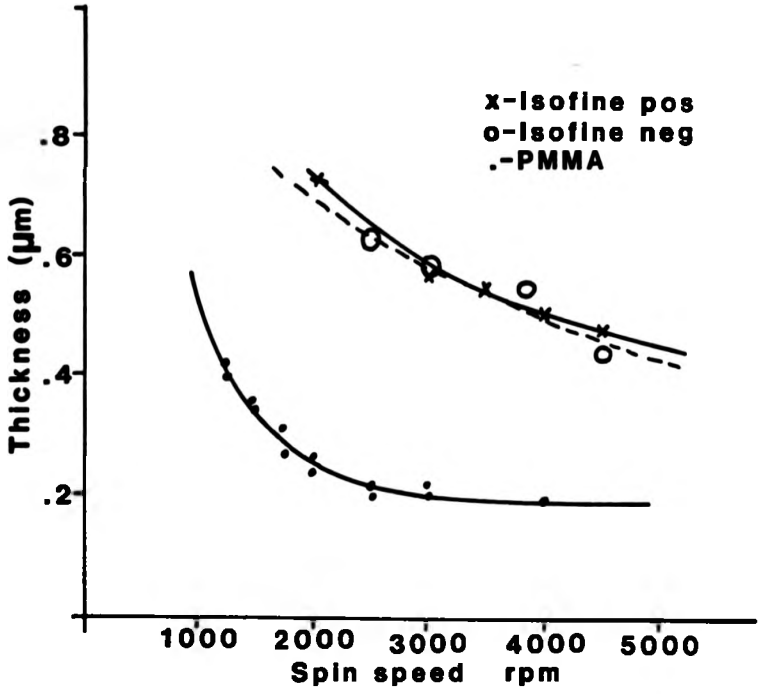

Fig.A2.7 Electron beam resist thickness as a function of spin speed.

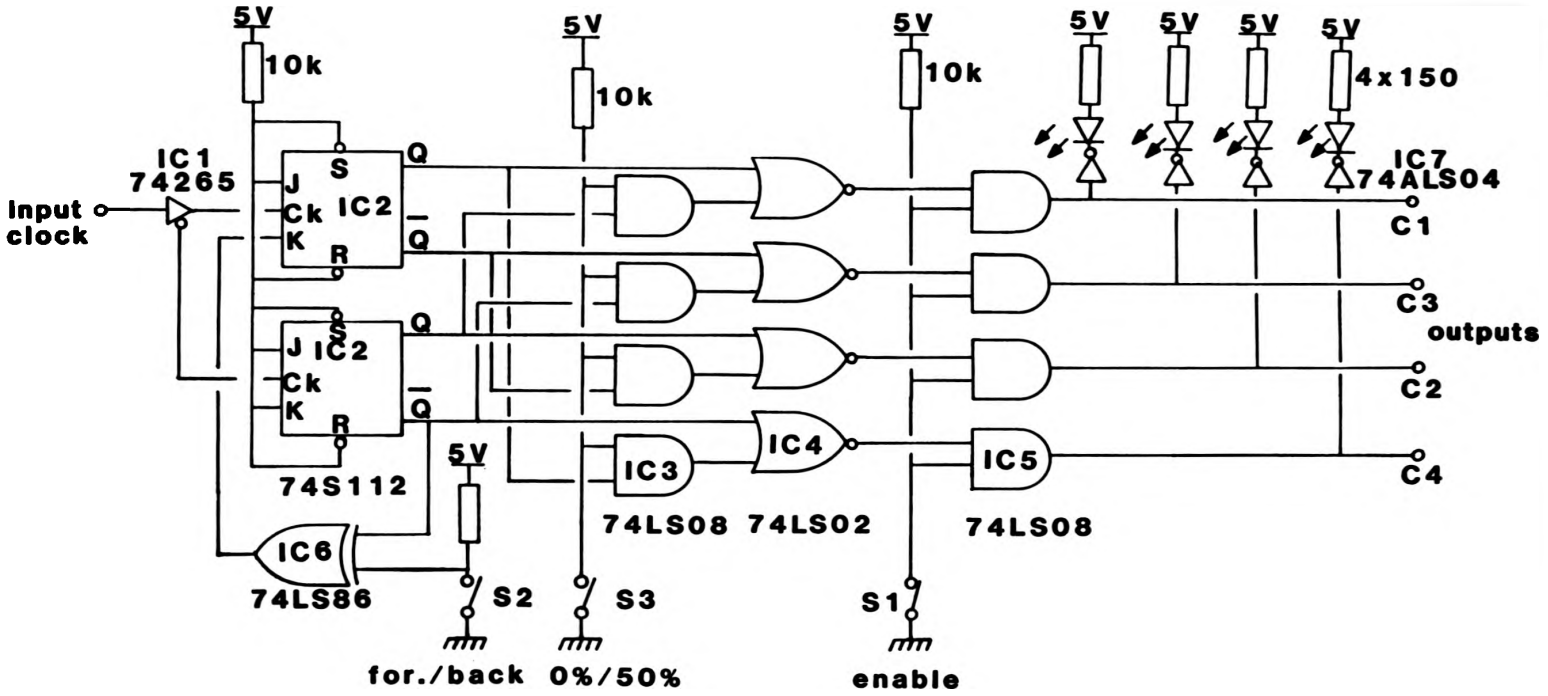

Fig.A2.8 The current-access clock generator circuit. Output sequence is C1,C2,C3,C4 with C1 and C3 generating the drive for one layer and C2,C4 for the other.

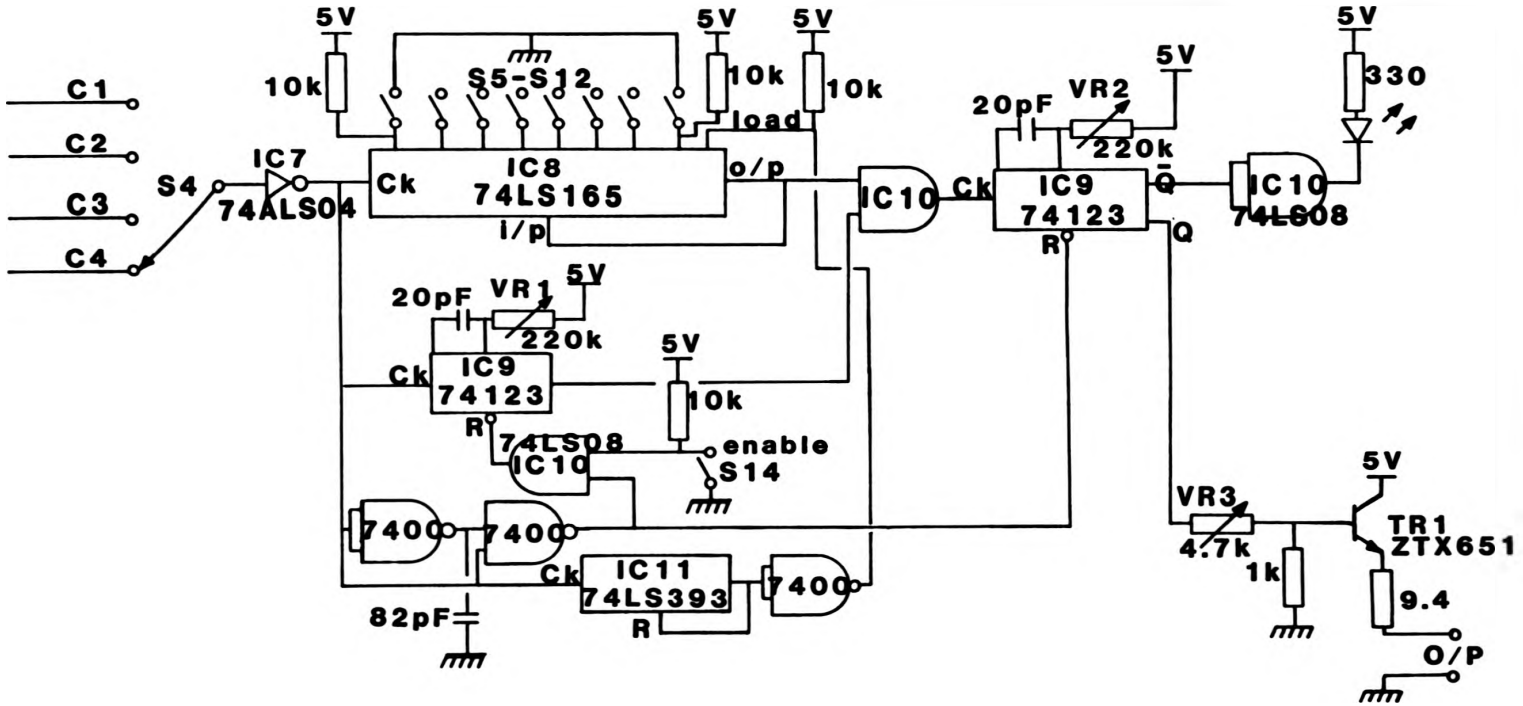

Fig.A2.9 The bubble nucleator control and drive circuit.

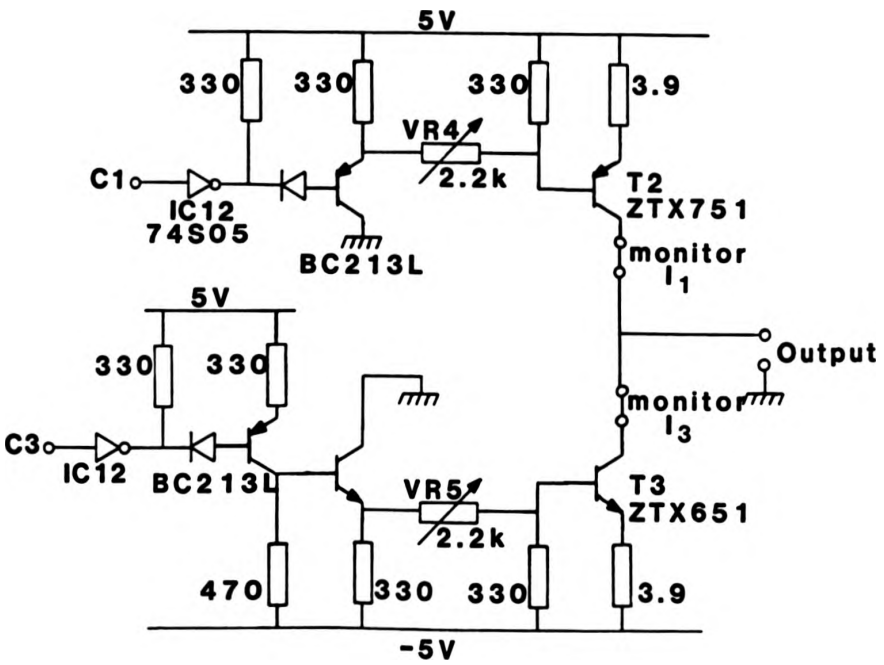

Fig.A2.18 The output current driver circuit (one for each layer).

APPENDIX 3

VBL MEMORY

Appendix 3.1 Power Requirements for Current Access Major Track

Assume	Track width,	W_1,	=	5 Sw
	Slot width,	W_2,	=	$0.5W_1$
	Conductor thickness,	t,	=	$0.3\mu m$
	Aluminium resistivty,	ρ,	=	2.4×10^{-8} Ωm
	Track length,	L,	=	1cm
	No. of layers/track,	n,	=	2
	Current density,	J,	=	$2mA/\mu m$
	Stripe width,	Sw,	=	$5\mu m$
	Track duty cycle,	D,	=	75%
	Track resistance,		=	R.

Power, $W = I^2RDn$

$$\triangleq Dn\, J^2 W_1^2 \, \frac{\rho L}{tW_1} \cdot \frac{W_1}{W_2}$$

$$= 0.25 \text{ Watts.}$$

APPENDIX 4

NUMERICAL ANALYSIS

Appendix 4.1 The Finite Difference Equations of Motion

Substituting the finite difference expressions for $\dot{q}$, $\dot{\phi}_m$, $\nabla^2 q$, $\nabla^2 \phi_m$, in equations 4.9 and 4.10 and separating future, (n+1), terms we are left with the simultaneous equations:

$$AA\ \Delta q_{n+1} - \Delta_o\ BB\ \Delta\phi_{n+1} = CC \qquad \ldots(A1)$$

$$AA\ \Delta\phi_{n+1} + \frac{1}{\Delta_o}\ BB\ \Delta q_{n+1} = DD \qquad \ldots(A2)$$

where

$$AA = \frac{1}{\gamma\Delta T} + \frac{6\alpha A\ (\Delta S^2 + \Delta R^2)}{(1+\alpha^2)\ M\ (\Delta S^2\ \Delta R^2)} \qquad \ldots(A3)$$

$$BB = \frac{6A\ (\Delta S^2 + \Delta R^2)}{(1+\alpha^2)\ M\ (\Delta S^2\ \Delta R^2)} \qquad \ldots(A4)$$

$$CC = \frac{2\Delta_o}{1+\alpha^2}\left(F(\phi_m) - \alpha\Delta_o \frac{\partial}{\partial S} F(\phi_m) + \alpha H_z - \frac{2A}{M}\left(FT - \frac{\alpha}{\Delta_o} CT\right)\right) - \frac{1}{\gamma\Delta T}\Delta q_n \qquad \ldots(A5)$$

$$DD = \frac{2}{(1+\alpha^2)} \{H_z - \alpha F(\phi_m) - \Delta_o \frac{\partial}{\partial S} F(\phi_m) + \frac{2A}{M} (\alpha FT + \frac{1}{\Delta_o} CT)) - \frac{1}{\gamma \Delta T} \Delta\phi_n \quad \ldots(A6)$$

$$CT = \nabla^2 q + \frac{3}{2} \Delta q_{n+1} (\frac{1}{\Delta S^2} + \frac{1}{\Delta R^2}) \quad \ldots(A7)$$

$$FT = \nabla^2 \phi_m + \frac{3}{2} \Delta\phi_{n+1} (\frac{1}{\Delta S^2} + \frac{1}{\Delta R^2}) \quad \ldots(A8)$$

The variables AA, BB, CC, and DD may be determined at any given time from the material parameters, the numerical parameters, the present and past wall shape and magnetisation distribution, and the applied fields. The simultaneous equations, A1 and A2, are solved in each local frame for the incremental displacements Δq_{n+1}, and $\Delta\phi_{n+1}$. By subsequently updating the laboratory frame and repositioning the points, the new wall position and magnetisation distribution are obtained.

Appendix 4.2 The Demagnetising and Stray Field Integrals

The demagnetising and stray fields are calculated by assuming a current density of 2M emu/cm to flow on the domain wall and integrating using Biot-Savart's Law over the wall surface. Biot-Savart's Law states:

$$\vec{dHp} = 2M \frac{\vec{d\ell} \times \vec{r}}{|r|^3} dZ \qquad \ldots(A9)$$

where (see Figure A4.1) $\vec{d\ell}$ is assumed to lie in the film plane and $\vec{r}$ is the vector from the point P to the element in question, i.e.,

$$\vec{d\ell} = Rd\theta\ (\cos \phi_t,\ \sin \phi_t,\ 0) \qquad \ldots(A10)$$

$$\vec{r} = (r_x,\ r_y,\ r_z) \qquad \ldots(A11)$$

$$= (X_p - X\ ,\ Y_p - Y\ ,\ Z_p - Z\ ) \qquad \ldots(A12)$$

The total field at P is the surface integral over the domain wall. Evaluating the vector product $\vec{d\ell} \times \vec{r}$ the X, Y and Z components are given by,

$$H_x = 2M \int_0^{2\pi} \int_0^{h} \frac{R \sin \phi_t\ r_z}{|r|^3}\, dz\, d\theta \qquad \ldots(A13)$$

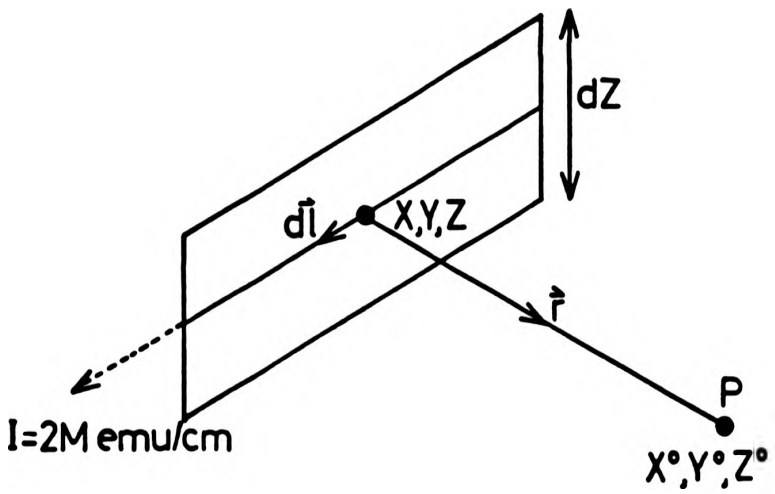

Fig.A4.1 The demagnetising and stray in-plane field calculation.

$$H_y = -2M \int_0^{2\pi} \int_0^{h} \frac{R \cos \phi_t \, r_z}{|r|^3} \, dz \, d\theta \qquad \ldots(A14)$$

$$H_z = 2M \int_0^{2\pi} \int_0^{h} \frac{R \, (\cos \phi_t \, r_y - \sin \phi_t \, r_x)}{|r|^3} \, dz \, d\theta \qquad \ldots(A15)$$

Within the aforementioned window area these integrals are evaluated with respect to Z and θ by summation of the contributions from each element. For the remainder of the wall surface, equations A13-A15 are integrated analytically with respect to Z using thickness-averaged values of R, ϕ_t, X, and Y. Between the limits 0 and h we get,

$$H_x' = 2M \int_0^{2\pi} R \sin \phi_t \left[\frac{1}{(r_x^2+r_y^2 + (h-Z_o)^2)^{1/2}} - \frac{1}{(r_x^2+r_y^2 + Z_o^2)^{1/2}} \right] d\theta \qquad \ldots(A16)$$

$$H_y' = -2M \int_0^{2\pi} R \cos \phi_t \left[\frac{1}{(r_x^2+r_y^2 + (h-Z_o)^2)^{1/2}} - \frac{1}{(r_x^2+r_y^2 + Z_o^2)^{1/2}} \right] d\theta \qquad \ldots(A17)$$

$$H_z' = 2M \int_0^{2\pi} \frac{R(\cos \phi_t \, r_y - \sin \phi_t r_x)}{(r_x^2+r_y^2)} \left[\frac{h - Z_o}{(r_x^2+r_y^2+(h-Z_o)^2)^{1/2}} + \frac{Z_o}{(r_x^2+r_y^2+Z_o^2)^{1/2}} \right] d\theta \qquad \ldots(A18)$$

The final integral with respect to θ is obtained numerically as before. The in-plane components are the stray field and the Z-component is the demagnetising field. i.e.,

$$H_{ip} = \{(H_x + H_x')^2 + (H_y + H_y')^2\}^{\frac{1}{2}} \qquad \ldots(A19)$$

$$\phi_{ip} = \tan^{-1} \frac{(H_y + H_y')}{(H_x + H_x')} \qquad \ldots(A20)$$

$$H_d = H_z + H_z' \qquad \ldots(A21)$$

In comparison to the two-dimensional case, Hd is the thickness-averaged value of H_z' with the stray in-plane field obviously zero.

The final integral with respect to θ is obtained numerically as before. The in-plane components are the stray field and the Z-component is the demagnetising field. i.e.,

$$H_{ip} = \{(H_x + H_x')^2 + (H_y + H_y')^2\}^{\frac{1}{2}} \qquad \ldots(A19)$$

$$\phi_{ip} = \tan^{-1} \frac{(H_y + H_y')}{(H_x + H_x')} \qquad \ldots(A20)$$

$$H_d = H_z + H_z' \qquad \ldots(A21)$$

In comparison to the two-dimensional case, Hd is the thickness-averaged value of H_z' with the stray in-plane field obviously zero.

APPENDIX 5

PUBLICATIONS AND PRESENTATIONS

5.1 G. Ronan and S. Konishi, "3-Dimensional Simulation of Bubble Translation", 26th Japanese Magnetic Bubble Applications Conference, Tokyo, July 1984 (unpublished).

5.2 G. Ronan and S. Konishi, "3-D Computer Simulation of a Translating Magnetic Bubble", Proc. 8th Japanese Magnetic Applications Conference, Hiroshima, D-8, pp. 90, November 1983 (Proc. to be translated and published by IEEE Translation Services).

5.3 G. Ronan, W. Clegg and S. Konishi, "A Theoretical Study of Bloch Curve Motion and Punch-Through in Garnet Films by Computer Simulation", Paper MN27, Proc. I.O.P. Solid State Physics Conference, Southampton, December 1984 (unpublished).

5.4 G. Ronan, "Progress in Vertical Bloch Line Ultra-High Density Computer Storage". University of Manchester, Elec. Eng. Colloquium, February 1985 (unpublished).

5.5 G. Ronan and W. Clegg, "Recent Progress in the Development of Vertical Bloch Line Memory Devices". Paper II, I.O.P. Conference on Current Research in Magnetism, London, April 1985 (unpublished).

5.6 G. Ronan and S. Konishi, "A Three-Dimensional Computer Simulation of a Translating Magnetic Bubble", J. Appl. Phys. Vol. 57(1), pp. 4074-4076, April 1985.

5.7 G. Ronan, W. Clegg and S. Konishi, "Material Considerations for Vertical Bloch Line Memory", To be published, J. de Physique, Sept. 1985.

5.8 G. Ronan, K. Matsuyama, E. Fujita, M. Ohbo, S. Kubota and S. Konishi, "A Three-Dimensional Computer Model of Domain Wall Motion in Magnetic Bubble Materials", To be published, IEEE Trans. Magn., Nov. 1985. (This paper has been extracted from Chapter 4 of this thesis).

18aD-8

第8回日本応用磁気学会学術講演概要集 (1984 11)

バブルトランスポートの三次元シミュレイション

3-D SIMULATION OF A TRANSLATING MAGNETIC BUBBLE.

G. Ronan* and S. Konishi, Dept. of Elec. Eng., Kyushu University.
*On leave from Dept. of Elec. Eng., Manchester University, England.

The dynamic characteristics of a translating magnetic bubble are studied by a three dimensional numerical solution of the equations of motion for a domain with twisted wall magnetization structure. The azimuthal angle of wall magnetization and the wall center position for a unichiral (X-) bubble of radius 3μm are defined at 3552 points distributed regularly on the domain wall. Demagnetizing and stray in-plane fields are calculated by assuming a circulating current of 2M emu/cm flowing on the domain wall and integrating Biot-Savart's Law over the wall surface. The detailed numerical method is to be presented elsewhere (1). A typical garnet ($(YSmLuCa)_3(GeFe)_5O_{12}$) is assumed with film thickness = 4.27 μm, $4\pi M$ = 195 Gauss, exchange const. = 2.63×10^{-7} erg/cm, gyromagnetic const. = 1.83×10^{7} 1/(Oe.s) and, unless otherwise stated, damping parameter α = 0.11.

The initial conditions for transport are a bubble stabilized in a bias field of 75 Oe. The bubble assumes a slightly barrel shape due to the variation of demagnetizing field from surface to mid plane of the film. The azimuthal angle of magnetization tends toward the stray in-plane field direction, stabilizing in the classic Bloch line mode, as proposed by Slonczewski (2). A field gradient is superimposed to the bias field and thus field compensation is employed to prevent bubble expansion during translation.

Bubble transport as expected was found to fall into three catagories:- (a) below 0.85 Oe/μm, no Bloch curve formation, (b) between 0.85 and 2.13 Oe/μm, Bloch curve nucleation and propagation without punch through and, (c) above 2.13 Oe/μm, Bloch curve punch through with the formation of 2 vertical Bloch lines (VBL) per Bloch curve. Fig.1 illustrates the bubble skew angle at a low drive field, 0.5 Oe/μm, for three values of damping parameter. Agreement with the two dimensional theory (shown in dotted line) is excellent. In fig.2 the three catagories of transport are shown by the time dependence of bubble instantaneous velocity. For case (a), 0.5 Oe/μm, velocity reaches steady state motion, a simulated mobility of 9.39 m/s/Oe agreeing well with the 9.40 m/s/Oe expected theoretically. In case (b), 1.5 Oe/μm, Bloch curves nucleate on the leading and trailing edges causing the velocity to decrease. As punch through does not occur the velocity eventually approaches that expected with a mobility of 9.4 m/s/Oe. At high drive field, case (c), 3.5 Oe/μm, punch through occurs on the velocity peaks at 28.3 ns and 54.2 ns with, in total, eight VBLs formed by 55 ns. The velocity oscillates in an approximately periodic manner and the time averaged velocity saturates at 35 m/s. A bubble propagating in a drive field of 3.5 Oe/μm is shown in fig.3, 20 ns after the field gradient was applied. The position and polarity of the Bloch curves on the leading (X=3μm) and trailing (X=-4μm) edges are shown by the usual dot and cross convention. Large distortion accompanies Bloch curve propagation, similar to that previously observed for plane wall dynamics. Finally bubble overshoot has been examined by terminating a field gradient of 3.5 Oe/μm at (i) 20 ns, (ii) 25 ns and (iii) 35 ns as illustrated in fig.4. After pulse termination the velocity decreases sharply and settles to a "steady state" motion as the Bloch curves unwind. For the case (ii), i.e. after punch through, the overshoot is comparatively small as the VBLs are metastable on the bubble flanks. The momentum stored in the Bloch curves and VBLs is clearly observed.

The bubble dynamics simulated numerically are in good agreement with the two dimensional theory at low drive fields while they appear inconsistent with the Bloch line model at high drive fields.

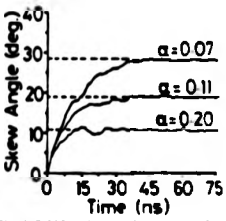

Fig.1 Bubble skew angle vs time for three values of damping parameter. Drive field is 0.5 Oe/μm.

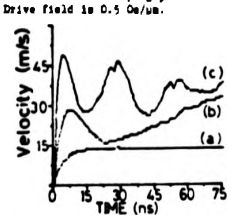

Fig.2 Instantaneous bubble velocity for drive fields of (a) 0.5, (b) 1.5, and (c) 3.5 Oe/μm.

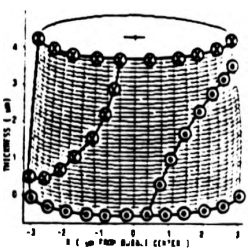

Fig.3 Bubble shape and Bloch curve positions at 20 ns in a drive field of 3.5 Oe μm.

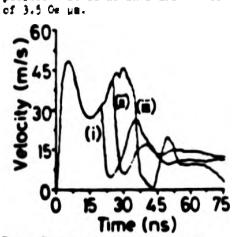

Fig.4 Overshoot observed when a gradient of 3.5 Oe/μm is terminated at (i) 20 ns, (ii) 25 ns, (iii) 35 ns.

1. G. Ronan et al., To be published
2. J. Slonczewski, Int. J. Magnetism, Vol. 2, p.85, 1972.

A THEORETICAL STUDY OF BLOCH CURVE MOTION AND PUNCH-THROUGH IN GARNET FILMS BY COMPUTER SIMULATION.

G. RONAN, W. CLEGG AND S. KONISHI*, DEPARTMENT OF ELECTRICAL ENGINEERING, MANCHESTER UNIVERSITY, MANCHESTER M13 9PL.
* DEPARTMENT OF ELECTRICAL ENGINEERING, KYUSHU UNIVERSITY, FUKUOKA, JAPAN.

Our recent interest in Vertical Bloch Line memory has encouraged the development of a three dimensional numerical solution of the equations of motion for a domain wall with an associated twisted wall magnetization structure in garnet films. The simulation has been applied to the case of a translating magnetic bubble at velocities at which Bloch curve formation, propagation and punch-through occur. The azimuthal angle of wall magnetization and the wall centre position for a unichiral (χ-) bubble of radius 3μm are defined at 3552 points distributed regularly on the domain wall. Demagnetizing and stray in-plane fields are calculated by assuming a circulating current of 2M emu/cm flowing on the domain wall and integrating Biot-Savart's Law over the wall surface. The detailed numerical method is to be presented elsewhere. A typical bubble garnet film [$(YSmLuCa)_3(GeFe)_5O_{12}$] is assumed.

Bubble transport as expected was found to fall into three categories: (a) below 0.85 Oe/μm, no Bloch curve formation, (b) between 0.85 and 2.13 Oe/μm, Bloch curve nucleation and propagation without punch-through and, (c) above 2.13 Oe/μm, Bloch curve punch-through with the formation of two Vertical Bloch lines (VBL) per Bloch curve. The bubble skew angle and mobility at low drive field, (a), are in excellent agreement with the two dimensional theory for a range of material damping parameters. At high drive field, case (c), the velocity oscillates in an approximately periodic manner as proposed by Slonczewski, Bloch curve punch-through occurring on the velocity peaks. The VBLs formed by punch-through propagate to opposite flanks of the bubble causing elliptical distortion. Bubble overshoot has been examined by terminating a field gradient of 3.5 Oe/μm before and after punch-through. After pulse termination the velocity decreases sharply and settles to a "steady state" motion as the Bloch curves unwind. When the gradient is terminated after punch-through, the overshoot is comparatively small as the VBLs are metastable on the bubble flanks. The momentum stored in the Bloch curves and VBLs is clearly conserved.

The bubble dynamics simulated numerically are in good agreement with the two dimensional theory at low drive fields while they appear consistent with the Bloch line model at high drive fields.

Electrical Engineering Colloquium

PROGRESS IN VERTICAL BLOCH LINE ULTRA-HIGH DENSITY COMPUTER STORAGE

by

Mr. Gerry Ronan

Department of Electrical Engineering.

With magnetic bubble devices approaching the limits of the technology, interest is now turning to a related form of micromagnetic computer storage, vertical Bloch line (VBL) memory, where information is coded in the domain wall, as opposed to using the domain itself. Due to the intrinsically smaller scale of the domain wall, densities of the order 100-400 Mbits/cm^2 are anticipated with improvements on the operating characteristics of conventional bubble devices.

The concept of VBL memory will be outlined with emphasis on the individual functions of write, propagation and read. Densities, operating characteristics and fabrication tolerances are considered in comparison to conventional bubble technology.

Wednesday February 20th, 1985.

Lecture Room B at 2.00 p.m.

Electrical Engineering Department (Dover Street)

ALL ARE WELCOME

Electrical Engineering Colloquium

RECENT PROGRESS IN THE DEVELOPMENT OF VERTICAL BLOCH LINE MEMORY DEVICES

G. Ronan and W. Clegg.

Department of Electrical Engineering,
University of Manchester,
MANCHESTER M13 9PL

Summary

With magnetic bubble devices approaching the limits of the technology, interest is now turning to a related form of micromagnetic computer storage, vertical Bloch line (VBL) memory, where information is coded in the domain wall, as opposed to using the domain itself. Due to the intrinsically smaller scale of the domain wall, densities in excess of 100 Mbits/cm^2 are anticipated with enhanced operating characteristics compared with conventional bubble devices.

The concept of VBL memory will briefly be considered. Densities, operating characteristics and fabrication requirements will be discussed.

Present research concerned with computer modelling of Bloch line dynamics will be outlined.

A three-dimensional computer simulation of a translating magnetic bubble

G. Ronan[a)] and S. Konishi
Department of Electrical Engineering, Kyushu University, Fukuoka, 812 Japan

The dynamic characteristics of a translating magnetic bubble are studied by a three-dimensional numerical solution of the equations of motion for a twisted domain wall structure. The azimuthal angle of magnetization ϕ and wall center position q for a bubble of radius 3 μm are defined at 3552 points distributed regularly on the domain wall. Demagnetizing and stray in-plane fields are calculated by assuming a circulating current density of $2M$ emu/cm flowing on the domain wall and integrating Biot–Savart's Law over the wall surface. A typical $(YSmLuCa)_3(GeFe)_5O_{12}$ garnet of film thickness 4.27 μm is assumed. Instantaneous bubble skew angle and velocity are illustrated at drive fields from 0.5 to 4.0 Oe/μm. Bubble dynamics are seen to fall into three categories, transport without Bloch curve nucleation, with Bloch curve propagation, and with Bloch curve punch through. At low drive field both skew angle and velocity are in good agreement with earlier theory. At high drive field the time averaged velocity saturates as the instantaneous velocity oscillates due to Bloch curve punch through. A comparatively high saturation velocity of 35 m/s and an instantaneous peak velocity of 54 m/s are observed.

INTRODUCTION

Our recent interest in VBL memory[1] has encouraged the development of a numerical method to investigate the motion of a domain wall, with an associated twisted wall magnetization structure, in three dimensions. To establish the feasibility of calculation, the theory[2] has been applied to the case of a translating magnetic bubble. Existing two-dimensional numerical solutions assume a uniform wall position q and azimuthal angle of magnetization ϕ either in the plane of the film or through the film thickness. The three-dimensional simulation is intended to remove these restrictions, in particular, to investigate the formation of vertical Bloch lines (VBL) by the punch through of Bloch curves.

NUMERICAL METHOD

The coupled nonlinear equations of motion, initially derived by Slonczewski,[2] and extended to the three-dimensional case[3] are

$$\dot{q} = \gamma\Delta\left(f(\phi) - \frac{2A}{M}\cdot\nabla^2\phi\right) + \alpha\Delta\dot{\phi}, \tag{1}$$

$$\dot{\phi} = \gamma\left(Hz + \frac{2A}{M\Delta}\cdot\nabla^2 q + \Delta\frac{\partial}{\partial x}[f(\phi)]\right) - \frac{\alpha}{\Delta}\dot{q}, \tag{2}$$

$$f(\phi) = 2\pi M\cdot\sin 2(\phi - \phi_t) + \frac{\pi}{2}\cdot Hs\cdot\sin(\phi - \phi_s), \tag{3}$$

where M is the magnetization, A is the exchange constant, α is the Gilbert damping parameter, γ is the gyromagnetic ratio, Δ is the wall width parameter, Hs is the stray in-plane field magnitude, Hz is the sum of the fields perpendicular to the film, and ϕ_t and ϕ_s are the azimuthal angles of wall tangent and stray in-plane field, respectively. For a bubble of radius 3 μm, q and ϕ are defined at 96 points on the bubble circumference at 37 levels through the thickness, this being a grid matrix of 3552 points. The above equations are solved numerically by the explicit method in the vicinity of each point, all displacements being made normal to the three-dimensional wall. Surface boundary conditions are imposed such that the second order spatial partial differentials with respect to Z of q and ϕ are zero. A finite time step interval of 0.1 ns was chosen and the translation time was limited to 80 ns to minimize computation cost.

By far the most time consuming section of the simulation is the demagnetizing and stray in-plane field calculation. For the purpose of evaluating these fields, we assume a circulating current of density $2M$ emu/cm to flow on the domain wall, as discussed by O'Dell,[4] and integrate Biot–Savart's Law over the wall surface. A considerable saving in computation time is achieved by our so-called window method, whereby distortion greatly removed from the observation point is ignored by integrating analytically through the film thickness. The effect of distortion in the vicinity of the observation point is maintained by evaluating the surface integral numerically. A more detailed explanation of the numerical method is to be reported elsewhere.[3]

A drive field is superimposed to the bias field as

$$H_{\text{total}} = H_{\text{bias}} + H_{\text{drive}}(X_c - X), \tag{4}$$

where Xc–X is the X coordinate of wall position measured from the bubble center. This provides bias field compensation as the bubble translates, removing domain distortion due to expansion. The material parameters used in the simulation are $4\pi M = 195$ G, $A = 2.63\times10^{-7}$ erg/cm, $\alpha = 0.11$, $\gamma = 1.83\times10^7$/Oe/s, $\Delta = 0.0565$ μm, and film thickness $h = 4.27$ μm, assuming a typical $(YSmLuCa)_3(GeFe)_5O_{12}$ garnet.

RESULTS

The initial conditions for transport are taken as a unichiral bubble stabilized in a bias field of 75 Oe for 80 ns. The bubble assumes a slightly barrel shape, with maximum, minimum, and thickness averaged radii of 3.028, 2.93, and 2.986 μm, respectively. The azimuthal angle of magnetization tends towards the in-plane field direction, stabilizing in the classic

[a)] On leave from Department of Electrical Engineering, Manchester University, England.

 0021-8979/85/014074-03$02.40

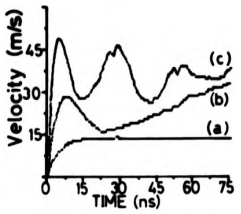

FIG. 1. Time dependence of instantaneous bubble velocity at drive fields of (a) 0.5 Oe/μm, (b) 1.5 Oe/μm, and (c) 3.5 Oe/μm.

180° twisted wall structure through the thickness, as proposed by Slonczewski.[2]

Bubble transport can be divided into three sections: (a) without Bloch curve nucleation, (b) with Bloch curve formation and propagation, and (c) with Bloch curve punch through. The time dependence of instantaneous bubble velocity and skew angle are plotted in Figs. 1 and 2 for three drive fields corresponding to these forms of propagation. At a low drive field (case a, 0.5 Oe/μm), velocity and skew angle rise to their steady states of 13.2 m/s and 19.1°, these values being within 0.5% of those given by previous theory.[5] Domain distortion is minimal and there are no Bloch curves. At a medium drive field (case b, 1.5 Oe/μm), first velocity, and later skew angle, break down due to Bloch curve formation on the leading and trailing edges of the bubble. As the Bloch curve reach the opposite surfaces both velocity and skew angle approach their steady state values. At a high drive field (case c, 3.5 Oe/μm), the punch through of Bloch curves cause velocity and skew angle to breakdown in an approximatley periodic manner. For the example shown, the initial velocity peaks at 5.3 ns just before Bloch curve nucleation, with punch through occurring on subsequent peaks at 28.3 and 54.2 ns. Two VBL's are formed per Bloch curve punch through, which propagate to opposite flanks of the bubble causing elliptical distortion. The initial peak in skew angle at 8.3 ns occurs as the Bloch curves passs through approximately the midplane of the film, the subsequent erratic propagation path being due to the complex gyrotropic forces accompanying multiple horizontal and vertical Bloch line motion. A time averaged skew angle of 4.5° is very much lower than that found at 0.5 Oe/μm. In Fig. 3 the domain shape and Bloch curve positions at 20 and 40 ns are shown for a drive field of 3.5 Oe/μm. At 20 ns the Bloch curves have nearly reached the top surface on the leading edge and the bottom surface on the trailing edge. By 40 ns both Bloch curves have punched through forming in total four VBL's. In addition, a new pair of curves are moving from top to bottom surface on the leading edge and vice versa on the trailing edge. The VBL's are clearly seen to be three-dimensional structures with a ϕ rotation of 360° at one surface decreasing to zero at the other.

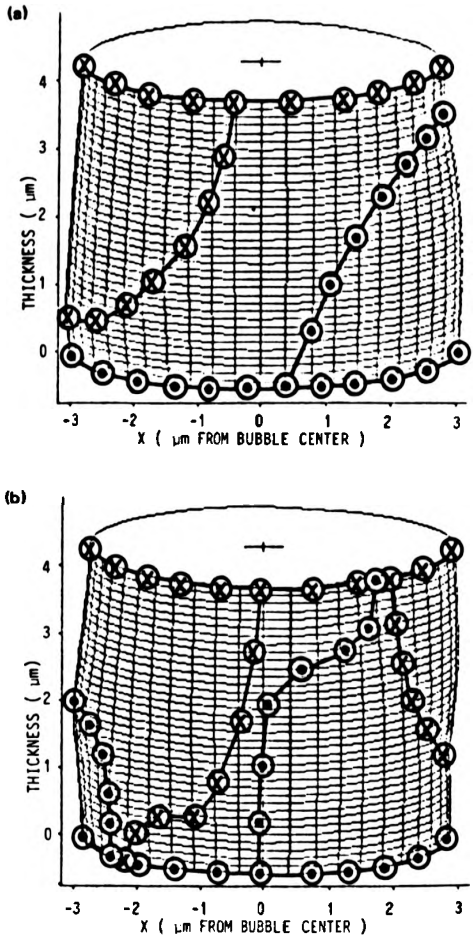

FIG. 3. Domain shape and Bloch curve positions for a drive field of 3.5 Oe/μm at (a) 20 ns and (b) 40 ns. The bubble is propagating from left to right.

The time averaged velocities for a range of drive fields are plotted against averaging time in Fig. 4. At high drive fields the averaged velocity decreases to a saturation velocity of 35 m/s, although the initial peak velocity has been seen to exceed 50 m/s. In Fig. 5 the average velocity at 80 ns and initial instantaneous peak velocity are plotted against drive field (resolved to the direction of propagation) across the bubble radius. Below 2.4 Oe a Bloch curve does not nucleate.

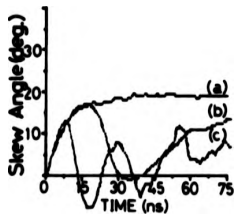

FIG. 2. Time dependence of bubble skew angle at drive fields of (a) 0.5 Oe/μm, (b) 1.5 Oe/μm, and (c) 3.5 Oe/μm.

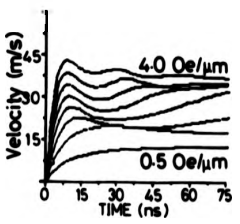

FIG. 4. Time averaged bubble velocity vs averaging time for drive fields 0.5, 1.0, 1.5, 2.0, 2.5, 3.0, 3.5, and 4.0 Oe/μm.

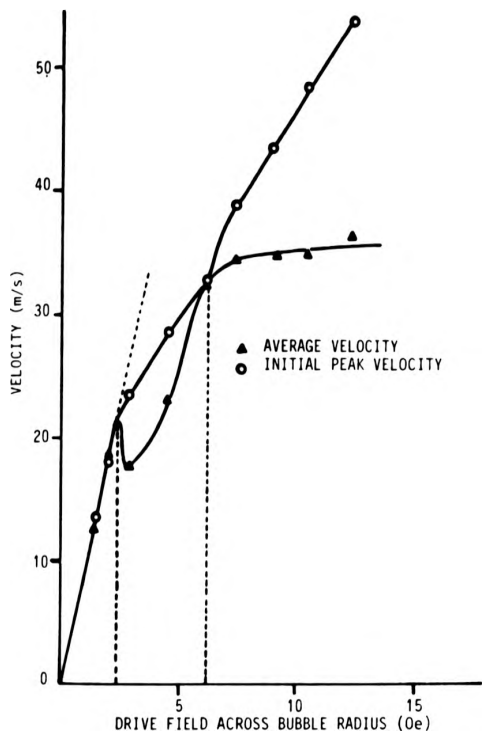

FIG. 5. Initial instantaneous peak velocity and averaged bubble velocity at 80 ns vs drive field (resolved to direction of propagation) across bubble radius.

A simulated mobility of 9.39 m/s/Oe agrees well with the theoretical value of 9.4 m/s/Oe. Between 2.4 and 6.25 Oe Bloch curves form but do not punch through. The apparent drop in velocity is a result of averaging over a relatively short time. As averaging time increases the averaged velocity will approach that expected with a mobility of 9.4 m/s. Beyond 6.25 Oe Bloch curves punch through at the surfaces causing the instantaneous velocity to breakdown and the averaged velocity to saturate at 35 m/s. The initial instantaneous peak velocity continues to rise linearly with drive field at a gradient of 3.0 m/s/Oe. The simulated saturation velocity is much higher than the 12.5 m/s expected theoretically,[6] although it is close to a previously calculated value of 35.1 m/s for so called peak velocity in plane wall dynamics.[7]

CONCLUSION

A three-dimensional simulation of domain wall motion has been established and applied to the case of a translating bubble. The feasibility of calculating motion of an arbitrary shaped wall with Bloch curve nucleation, propagation, and punch through has been shown. The physical picture of Bloch line wind up appears consistent with previous models although the saturation velocity is higher than expected. The simulation is currently being applied to domain configurations considered in VBL memory.

ACKNOWLEDGMENT

The authors would like to thank Y. K. K. Fasteners [U.K.] Ltd. for the financial support of G. Ronan through the Y.K.K. Scholarship Scheme.

[1] S. Konishi, IEEE Trans. Magn. **MAG-19**, 1838 (1983).
[2] J. C. Slonczewski, Int. J. Magnetism **2**, 85 (1972).
[3] G. Ronan and S. Konishi (to be published).
[4] T. H. O'Dell, *Magnetic Bubbles* (Macmillian, New York, 1974), p. 27.
[5] J. C. Slonczewski, A. P. Malozemoff, and O. Voegeli, AIP Conf. Proc. **10**, 458 (1973).
[6] A. P. Malozemoff, J. C. Slonczewski, and J. C. DeLuca, AIP Conf. Proc. **29**, 58 (1976).
[7] E. Fujita, H. Kawahara, S. Sakata, and S. Konishi, IEEE Trans. Magn. **MAG-20**, 1144 (1984).

Material Consideration for Vertical Bloch Line Memory.

G. Ronan*, W. Clegg* and S. Konishi+.

* Department of Electrical Engineering, University of Manchester, Manchester M13 9PL, England.

+ Department of Electrical Engineering, Kyushyu University, Fukuoka, Japan.

Résumé - Un modèle simplifié de la paroie séparant deux domaines est employé afin d'envisager les exigences d'un materiau qui conduirnient à l'élaboration d'un film de garnet à bulles typiquement adapté aux besoins specifiques de la mémoire VBL. Un materiau à large Q, basse épaisseiur ($h \approx 3\text{-}4\ell$) et grand σ paraitrait pouvoir optimiser la force gyrotropique du champ agissant et minimiser l'attraction VBL paire-paire non-désirée. Cependent, pour minimiser l'amplitude du puits de potentiel et celle du champ agissant, il apparaîtrait avantageux d'accroître la separation entre bits pour être de l'ordre de 0.8 s_w.

Abstract - A simplified model of a domain wall is employed to consider some of the material requirements that would tailor a typical bubble garnet film to the specific needs of VBL memory. A large Q, low thickness ($h \approx 3\text{-}4\ell$), high σ material would appear to optimise drive field gyrotropic force and minimise the undesirable VBL pair-pair attraction. Even so, to minimise the required potential well and drive field amplitudes, it would appear expedient to increase the bit separation to be of the order of 0.8 s_w.

Introduction

In the proposed VBL memory (1) the presence or absence of a pair of negative VBL injected in a stripe domain wall act as a binary '1' or '0'. A periodic in-plane field potential well structure defines the bit position and a perpendicular drive field provides a gyrotropic force sufficient to propagate a VBL pair out of one potential well into the next. For this discussion we assume a VBL is represented as a point magnetic charge and consider the in-plane field component parallel to the wall arising from convergence (or divergence) of magnetisation in the flanking Bloch wall regions. This so called 'σ-charge' gives rise to a non local effect which interacts with similar poles at different positions on the wall. If we consider a VBL as a line with regions of wall magnetisation angle ϕ_w=0 and π on either flank then the magnetic moment of the VBL is simply 2M. Including the wall width, $\pi\Delta$, and the material thickness, h, then the total magnetic charge, m, is given by $2\pi M\Delta h$. Our model therefore assumes a point charge as opposed to the charge distribution which would require a very much more detailed study, and ignores variation of charge through the thickness. (This latter point shall be considered in conclusion.) The magnetic field parallel to the wall resultant from this point charge is m/r^2, and the force acting on the charge due to a magnetic field is m.H.

Attractive Force Between VBL Pairs

Let us consider the effective field resultant from a pair of negative VBL as shown in Figure 1. The field at p a distance x from the centre of the VBL pair is

$$H_p = 2M\pi\Delta h\left\{\frac{1}{(x+\frac{\pi\Delta}{2})^2} - \frac{1}{(x-\frac{\pi\Delta}{2})^2}\right\} \qquad \ldots (1)$$

$$\approx -4\pi M\Delta\pi\Lambda\, h/x^3 \qquad \ldots (2)$$

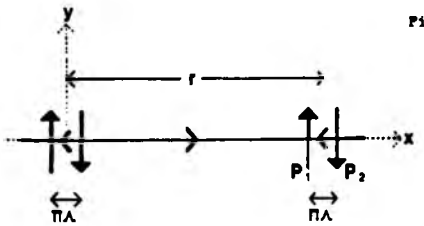

Fig. 1. VBL pairs in adjacent bit positions at a separation of r.

for the VBL spacing, $\pi\Lambda_1 << x$. With reference to Figure 1 the attractive force on a pair of VBL a distance r from the initial pair is given by,

$$F_{att} = 2\pi M\Delta h\, H(p_1) - 2\pi M\Delta h\, H(p_2) \qquad \ldots (3)$$

where $H_{(p)}$ is the field at p. Therefore

$$F_{att} = 2\pi M\Delta h.\pi\Lambda.\left(\frac{\delta H}{\delta x}\right)_{x=r} \qquad \ldots (4)$$

which from equation (2) is

$$F_{att} = 24\pi^4 M^2\Delta^2\Lambda^2 h^2/r^4 \qquad \ldots (5)$$

Substituting $\Delta = \iota/2Q$ ... (6)
and $\Lambda = \iota/2\sqrt{Q}$ ... (7)

we are left with

$$F_{att} = 3\pi^3 \frac{A}{Q^2}\, \iota^2 h^2/r^4 \qquad \ldots (8)$$

Potential Well Restoring Force

If we assume a sinusoidal potential well of the form

$$H_w = H_m \cos \frac{2\pi}{r} x \qquad \ldots (9)$$

then in a similar manner to equ. 4 the restoring force on a VBL pair is

$$F_R = -2\pi^2 M\Delta\Lambda h \frac{2\pi}{r} H_m \sin \frac{2\pi}{r} x \qquad \ldots (10)$$

which is a maximum at $x = r/4$ and $x = 3r/4$. Ideally as $F_{att} \propto 1/r^4$ it would be preferable to have the maximum restoring force at $x = 0$ and $x = r$ reducing the required amplitude of H_m and thus the magnitude of the drive field. A simple solution would be a triangular potential well as shall be discussed at a later date. For the present, however, we shall consider the case of maximum restoring force at $x = 0$, r and with the substitutions of equ. 6 and 7,

$$F_{Rmax} = 2\pi^2 M\Delta\Lambda h 2\pi H_m/r \qquad \ldots (11)$$

$$= -\frac{\pi^2}{Q}\sqrt{2\pi A}\; H_m \iota h/r \qquad \ldots (12)$$

Drive Field Gyrotropic Force

The gyrotropic force associated with a perpendicular drive field is more ambiguous as it is directly related to the density of VBL in the domain wall. The gyrotropic

force on a VBL is (2)

$$F_g = \frac{2\pi M}{\gamma} h v_y \qquad \ldots (13)$$

v_y is the domain wall velocity which from the mobility of a 'hard' wall (i.e., r = $2\pi\Delta$) is

$$v_y = \alpha\gamma\Delta H_z \qquad \ldots (14)$$

where H_z is the sum of perpendicular components of effective fields, i.e., demagnetising, wall curvature and applied fields. Our initial assumption for f_{att} however was that $r \gg \pi\Delta$ which would suppose that the wall would move at a higher velocity although not that of a 'soft' wall given by

$$v_y = \frac{\gamma\Delta}{\alpha} H_z \qquad \ldots (15)$$

As $\alpha \ll 1$ there would appear to be a considerable uncertainty as to the magnitude of the gyrotropic force (although this may be estimated by numerical solutions of domain wall motion (3)). Combining equ. 13 and 14 one can however say that this force is in excess of

$$F_{gmin} = 2\pi M\alpha\Delta h H_z \qquad \ldots (16)$$

$$= \sqrt{\frac{2\pi A}{Q}}\, \alpha h H_z \qquad \ldots (17)$$

which is suffice for the present discussion.

Material Considerations

Comparing the three forces equations 8, 12 and 17 the requirements to be met are minimise f_{att} so that the potential well magnitude H_m is minimised reducing the required gyrotropic force while maintaining the bit period r low. Of the variables in question ι can be taken as $S_W/8$ and the exchange constant A can be assumed constant at $\simeq 2 \times 10^{-7}$ erg/cm. Immediately obvious is that a low h ($\simeq 3\text{-}4\iota$) high Q ($\simeq 4$) material reduces the relative effect of F_{att} and that a high α ($\simeq 0.1 - 0.2$) increases F_{gmin}. This latter one would intuitively expect as large damping decreases domain distortion and large VBL oscillatory effects during propagation (3). The upper limit on α can be seen from the ratio of VBL velocity to wall velocity (4),

$$v_{VBL} \propto \frac{1}{\alpha} v_{wall} \qquad \ldots (18)$$

i.e., a large damping increases the ratio v_{wall}/v_{VBL} increasing the required wall displacement and thus H_z (remembering that H_z is an effective field resultant from drive, demagnetising and wall bending effects). The criterion high Q is straight forward as one would require large Q to maintain VBL stability. A possible disadvantage of a thin material (h = $3\text{-}4\iota$) might be in detection (magnetoresistive detection of bubble domains) although as it is only the detector that is to be of permalloy a thin film detector with high signal:noise could be employed.

In conclusion to estimate density (r) we consider a material with $\alpha = 0.1$, $Q = 4$, $h = 4\iota$, $\iota = S_{W/8}$ and $A = 2 \times 10^{-7}$ erg/cm.

Density

It would clearly be desirable to have $F_{Rmax} \gg F_{att}$ not only to ensure stability of the bit positions, but also for successful propagation of a random bit pattern. Taking therefore $F_{Rmax} = 10\ F_{att}$ and combining equations 8 and 12, a relationship between potential well depth (H_m) and bit period:stripe width ratio (r/s_w) can be

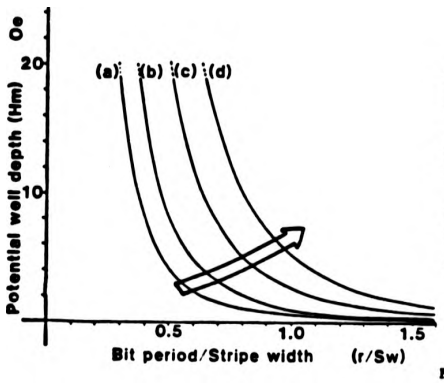

Fig. 2. Potential well depth as a function of bit period:stripe width ratio for strip width of (a) 5μm, (b) 2.5μm, (c) 1.0μm, (d) 0.5μm.

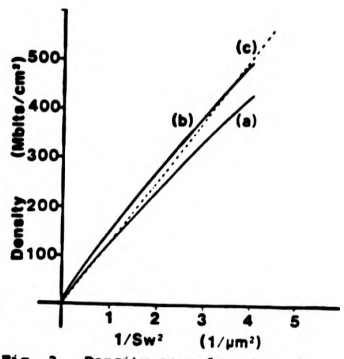

Fig. 3. Density as a function of $1/S_w^2$ for (a) the simple charge model, (b) the revised charge model accounting for charge variation through thickness and (c) r = 0.8Sw.

obtained as shown for various stripe widths in Fig. 2. The expected potential well depth for decreasing stripe width is shown approximately as an arrow from which an estimation of the bit period can be made. (The positioning of the arrow is derived from previous numerical calculations of VBL propagation (3) and unpublished results, but it can be seen to correspond approximately to the 'knee' of the curves.) As is expected potential well depth increases sharply with decreasing bit period and the corresponding densities (= 1/r x S_w bits/cm^2) varies approximately as a function of $1/S_w^2$. (See Fig. 3.)

A more detailed estimation of VBL magnetic charge accounting for variation of wall magnetisation angle through the material thickness, gives a smaller VBL charge and (following the same argument as above) as shown on Fig. 3 a density which approaches 500Mbits/cm^2 for 0.5μm stripe width. We must therefore conclude that the above model is conservative and that in practice some gain in density would be achieved. However as a rule of thumb, bit spacing of the order 0.8S_w (four times the VBL pair width) could be used. This may be considered somewhat analogous to the required bit spacing of four times the bubble diameter in a conventional bubble device although in that case the relevant force is repulsive.

Conclusion

Design rules have been proposed for VBL memory using a simple point charge model. Although the model is considered conservative two important conclusions can be drawn from it. Firstly a low thickness (h ≈ 4t) material reduces the relative effect of the mutual attraction between VBL pairs and secondly the bit period should be of the order 0.8 S_w. In comparison to a conventional bubble memory cell area (16 S_w^2) an increase in density of twenty fold is expected. Considerations of fabrication requirements for such a device while beyond the scope of this present work are to be covered at a later date.

References

1. Konishi, S., I.E.E.E. Trans. Magn., Mag-19, p. 1838, 1983.
2. Malozemoff and Slonczewski, "Magnetic Domain Walls in Bubble Materials", Applied Solid State Science, p. 162, Academic Press Inc., 1979.
3. Matsuyama, K. and Konishi, S., I.E.E.E. Trans. Magn., Mag-20, p. 1141, 1984.
4. Konishi, S., Matsuyama, K., Chida, I., Kubota, S., Kawahara, H., and Ohbo, M., I.E.E.E. Trans. Magn., Mag-20, p. 1129, 1984.

REFERENCES

[1] A. H. Bobeck, "Properties and Device Applications of Magnetic Domains in Orthoferrites", Bell Sys. Tech. J., Vol. 46, 8, pp. 1901-1925, 1967.

[2] H. Urai, K. Mizuno, S. Asada, N. Takada, N. Yoshioka, H. Gokan and K. Yoshimi, "4Mb On-Chip-Cache Bubble Memory Chips with 4μm Period Ion-Implanted Propagation Patterns", IEEE Trans. Magn., MAG-20, 5, pp. 1072-1074, 1984.

[3] H. Jouve, Manager, Magnetic Microelectronics Laboratory. L.E.T.I., France, Private Communication, Sept. 1984.

[4] G. Nelson, Senior Electrical Engineer, Advanced Materials and Devices, Corporate Technology Centre, Sperry Corporation, U.S.A., Private Communications, Nov. 1984,

[5] S. Konishi, Professor, Department of Electrical Engineering, Kyushu University, Japan, Private Communication Regarding 1981 Study Visit to U.S.S.R.

[6] M. Ohashi, T. Miyashita, Y. Satoh, K. Betsui and K. Komenou, "Design of 2μm-Period Minor Loops in Hybrid Bubble Memory Devices", To be published, IEEE Trans. Magn., Sept. 1985.

[7] K. Hirota, Y. Akiba and K. Kawamoto, "New Drive System and Packaging Method for Magnetic Bubble Memory", To be published, IEEE. Trans. Magn. Sept. 1985.

[8] T. J. Nelson, R. Wolfe, S. L. Blank and W. A. Johnson, "Reliable Propagation of Magnetic Bubbles with 8μm Period Ion Implanted Patterns", J. Appl. Phys., Vol. 50, 3, pp. 2261-2263, 1979.

[9] A. H. Bobeck, S. L. Blank, A. D. Butherus, F. J. Ciak and W. Strauss, "Current-Access Magnetic Bubble Circuits", Bell Sys. Tech. J., Vol. 58, 6, pp. 1453-1540, 1979.

[10] S. Konishi, "A New Ultra-High Density Solid State Memory: Bloch Line Memory", IEEE Trans. Magn., MAG-19, 5, pp. 1838-1840, 1983.

[11] J. A. Copeland, J. P. Elward, W. A. Johnson, and J. G. Ruch, "Single-Conductor Magnetic Bubble Propagation Circuits", J. Appl. Phys. 42, 4, pp. 1266-1267, 1971.

[12] T. J. Walsh and S. H. Charap, "Novel Bubble Drive", AIP Conf. Proc., 24, pp. 550-551, 1974.

[13] B. A. Calhoun, J. S. Eggenberger, L. L. Rosier and L. F. Shew, "Column-Access of a Bubble Lattice, Column Translation and Lattice Translation": IBM J. Res. and Dev., Vol. 20, 4, pp. 368-375, 1976.

[14] G. L. Nelson, D. R. Krahn, R. H. Dean, M. C. Paul and C. H. Tolman, "Self-Structured Current Aperture Approach for High Data Rate, High Density, Defect Tolerant, Low Power Bubble Memory", To be published, IEEE Trans. Magn., Sept. 1985.

[15] E. H. L. J. Dekker, K. L. L. van Mierloo and R. de Werdt, "Combination of Field and Current Access Magnetic Bubble Circuits", IEEE Trans. Magn., MAG-13, 5, pp. 1261-1263, 1977.

[16] K. Takahashi and H. Urai, "Chip Architecture for Large Capacity Bubble Memories", Presented at the Third Joint INTERMAG-MMM Conference, Montreal, Canada, July 1982.

[17] R. L. Smith and M. H. Kryder, "Dynamic Effects in Current-Access Dual-Conductor Perforated Sheet Magnetic Bubble Logic Grates", to be published, IEEE Trans. Magn., MAG-21, Sept. 1985.

[18] N. Hayashi, Y. Tsukizaki, A. Itoh and K. Kawanishi, "Operation of Magnetic Bubble Domain Dynamically-Ordered Dual-Conductor Shift Registers", IEEE Trans. Magn., MAG-20, 5, pp. 1090-1092, 1984.

[19] D. J. Breed and A. G. H. Verhulst, "High Frequency Magnetic Bubble Devices", Microelectronics Journal, Vol. 12, 5, pp. 15-18, 1981.

[20] M. H. Kryder, "Current Accessed Magnetic Bubble Devices: Projections of Performance", IEEE Trans. Magn., MAG-17, 5, pp. 2392-2400, 1981.

[21] J. P. Hwang, B. S. Han and H. Chang, "Can Perforated-Sheet Bubble Devices be Scaled Down from 2 to 0.2 Micron Features", IEEE Trans. Magn., MAG-17, 6, pp. 2680-2682, 1981.

[22] R. H. Dean, D. R. Krahn, G. L. Nelson and M. C. Paul, "Feasibility of Self-Structured Current Accessed Bubble Devices in Spacecraft Recording Systems", NASA Contractor Report 172554, April 1985 (Unclassified).

[23] G. L. Nelson, Advanced Materials and Devices, Corporate Technology Centre, Sperry Corporation, St. Paul, U.S.A., Private Communications, May 1985.

[24] H. N. Carlson, A. J. Perneske, L. F. Rago, G. J. Rothauser and W. D. P. Wagner, "Field Access Bubble to Bubble Logic Operations", IEEE Trans. Magn., MAG-8, 3, pp. 367, 1972.

[25] P. I. Bonyhard, Y. S. Chen and J. L. Smith, "Magnetic Bubble Logic Gate", IEEE Trans. Magn., MAG-9, 4, pp. 708-709, 1973.

[26] K. Matsuyama, H. Ural and K. Yoshimi, "Optimum Design Consideration for Dual Conductor Bubble Devices", IEEE Trans. Magn., MAG-19, 2, pp. 111-119, 1983.

[27] D. Shenton, S. H. Charap, H. David and M. H. Kryder, "Simulation of Dual Conductor Current Access Magnetic Bubble Devices", IEEE Trans. Magn., MAG-17, 6, pp. 2677-2679, 1981.

[28] J. C. Wu, J. P. Hwang and F. B. Humphrey, "Operation of Mangetic Bubble Logic Devices", IEEE Trans. Magn., MAG-20, 5, pp. 1093-1095, 1984.

[29] J. P. Hwang, J. C. Wu and F. B. Humphrey, "Magnetic Bubble VLSI Logic System", IEEE Trans. Magn., MAG-20, 5, pp. 1096-1098, 1984.

[30] J. P. Hwang, "VLSI Intelligent Magnetic Bubble Memories", Ph.D. Thesis, Carnegie-Mellon University, U.S.A. April 1985.

[31] F. B. Humphrey, Professor, Department of Electrical and Computer Engineering, Carnegie-Mellon University, U.S.A., Private Communication, May 1985.

[32] Y. Sugita, Chief Scientist, Central Research Laboratory, Hitachi Limited, Japan, Private Communication, Sept. 1984.

[33] S. Orihara, Manager (Bubble Memory Devices), Component Technology Laboratory, Fujitsu Laboratories Limited, Japan, Private Communication, September 1984.

[34] J. Fairholme, Manager, Bubble Memory Products, Motorola Corporate Research and Development, Tempe, Arizona, U.S.A., Private Communication, June 1985.

[35] M. Poirier, SAGEM, France, Private Communication, June 1985.

[36] Y. Hidaka, Research Manager, Memory Research Laboratory, NEC, Japan, Private Communication, September 1984.

[37] C. Kooy and U. Enz, "Experimental and Theoretical Study of the Domain Configuration in Thin Layers of $BaFe_{12}O_{19}$", Philips Research Report, Vol. 15, pp. 7-29, 1960.

[38] G. Ronan, M.Sc. Thesis, Chapter 5, Victoria University of Manchester, 1981.

[39] A. P. Malozemoff and J. C. Slonczewski, "Magnetic Domain Walls in Bubble Materials", Applied Solid State Science, Advances in Materials and Device Research, Supplement 1, Academic Press, Inc., (London) Limited, 1979.

[40] A. A. Thiele, "The Theory of Cylindrical Magnetic Domains", Bell Sys. Tech. J., Vol. 48, pp. 3287-3335, 1969.

[41] T. H. O'Dell, "Magnetic Bubbles", Chapter 2, The MacMillan Press Limited, 1974.

[42] P. J. Grundy and S. R. Herd, "Lorentz Microscopy of Bubble Domains and Changes in Domain Wall State in Hexaferrites", Phys. Stat. Sol. (a) 20, pp. 295-307, 1973.

[43] G. P. Vella-Coleiro, "Overshoot in the Translational Motion of Magnetic Bubble Domains", J. Appl. Phys., 47, pp. 3287-3290, 1976.

[44] S. Konishi, T. Hsu, and B. R. Brown, "On the Punch-Through of Bloch Loops in Magnetic Bubbles", Appl. Phys. Lett., 30, pp. 497-498, 1977.

[45] A. P. Malozemoff, J. C. Slonczewski and J. C. DeLuca, "Translational Velocities and Ballistic Overshoot of Bubbles in Garnet Films", A.I.P. Conf. Proc. 29, pp. 58-64, 1976.

[46] G. Ronan and S. Konishi, "A Three-Dimensional Computer Simulation of a Translating Magnetic Bubble", J. Appl. Phys. 57, 8, pp. 4074-4076, 1985.

[47] G. Ronan, K. Matsuyama, E. Fujita, M. Ohbo, S. Kubota and S. Konishi, "A Three-Dimensional Computer Model of Domain Wall Motion in Magnetic Bubble Materials", To be published, IEEE Trans. Magn., Nov. 1985.

[48] L. Landau and E. Lifshitz, Physik A, Soviet Union, Vol. 8, pp. 153, 1935.

[49] A. A. Thiele, "Steady-State Motion of Magnetic Domains", Phys. Rev. Lett. 30, pp. 230-233, 1973.

[50] S. Konishi, T. Hsu and B. R. Brown, "Effect of Ion-Implantation on Bubble Translation Velocity", J. Appl. Phys. 49, pp. 1894-1896, 1978.

[51] T. J. Beaulieu and B. A. Calhoun, "Dependence of Bubble Deflection Angle on the Orientation of an In-Plane Field", Appl. Phys. Lett., 28, pp. 290-292, 1976.

[52] S. Konishi, K. Matsuyama, Y. Yoshida and K. Narita, "Large Automation of an S=½ Bubble", Jap. J. Appl. Phys., 17, No. 12, pp. 66-67, 1978.

[53] W. J. Tabor, A. H. Bobeck, G. P. Vella-Coleiro, and A. Rosencwaig, "A New Type of Cylindrical Magnetic Domain (Bubble Isomers)", Bell Sys. Tech. J., Vol. 51, 6, pp. 1427-1430, 1973.

[54] J. R. Garside and R. M. Pickard, "A Position-Controlled Rectangular-Coordinate Table", J. Phys. E. Sci. Instrum., Vol. 16, pp. 223-226, 1983.

[55] C. J. Hardy, J. R. Garside, P. L. Jones, R. M. Pickard and R. S. Quayle, "Electron Beam Direct-Write Customisation of Uncommitted Logic Arrays. The Implications for Wafer Throughput of Increased Chip Complexity and Finer Structures", Proceedings of Microcircuit Engineering Conference, pp. 83-90, 1983.

[56] D. Bollinger and R. Fink, "A New Production Technique: Ion Milling", Solid State Tech., Vol. 23, 12, pp. 97-103, 1980.

[57] D. F. Downey, W. R. Bottoms and P. R. Hanley, "Introduction to Reactive Ion Beam Etching", Solid State Tech., Vol. 24, 2, pp. 121-127, 1981.

[58] M. W. Geis, G. A. Lincoln and N. Efremow, "A Novel Anisotropic Dry Etching Techniques", Paper K2, 16th Symposium on Electron, Ion and Photo Beam Technology, Dallas, U.S.A., May 1981.

[59] W. Beinvogl and H. Mader, "Reactive Dry Etching for Fabrication of Very-Large-Scale Integrated Circuits", Siemens Forsch.-u. Entwickl.-Ber. Bd., Vol. 11, 4, pp. 180-189, 1982.

[60] A. Weiss, "Plasma Etching of Aluminium: Review of Process and Equipment Technology", Semiconductor Int., Vol. 5, pp. 69-84, Oct. 1982.

[61] R. A. M. Wolters, "Selectivity Aspects in Aluminium Plasma Etching", 3rd Symp. of Plasma Etching and Deposition Electrochemical Society, 1982.

[62] R. Iscoff, "Trends in Metallisation Materials", Semiconductor Int., Vol. 5, pp. 57-65, Oct. 1982.

[63] J. F. Mahoney, J. Perel and A. T. Forrester, "Capillaritron: A New, Versatile Ion Source", Appl. Phys. Lett., Vol. 38, 5, pp. 320-322, 1981.

[64] P. J. Revell and A. C. Evans, "Ion Beam Etching Using Saddle Field Sources", Thin Solid Films, Vol. 86, pp. 117-123, 1981.

[65] G. K. Herb, R. F. Caffrey, E. T. Eckroth, Q. T. Jarrett, C. L. Fraust and J. A. Fulton, "Plasma Processing: Some Safety, Health and Engineering Considerations", Solid State Tech., Vol. 26, 8, pp. 185-193, 1983.

[66] C. J. Hardy, Department of Electrical Engineering, University of Manchester, Private Communication, 1982.

[67] N. Norstrom and H. O. Blom, "R.F. Sputtering Characteristics and Power Supply Coupling Conditions", Thin Solid Films, Vol. 86, pp. 255-265, 1981.

[68] J. M. Frary and P. Seese, "Lift-off Techniques for Fine Line Metal Patterning", Semiconductor Int., Vol. 4, pp. 72-88, Dec. 1981.

[69] G. R. Sheriff and S. Bull, Department of Electrical Engineering, University of Manchester, Project Report, May 1981.

[70] A. G. H. Verhulst, T. W. Bril, A. B. Voermans and G. J. Koel, "High Frequency Propagation of Magnetic Bubbles in Dual Conductor Devices", J. Appl. Phys., Vol. 52, 3, pp. 2371-2373, 1981.

[71] D. Bollinger and R. Fink, "A New Production Technique: Ion Milling", Solid State Tech., Vol. 23, 11, pp. 79-84, 1980.

[72] G. R. Hoffman, E. W. Hill and J. K. Birtwistle, "Thin Film Magnetoresistive Vector Sensors with Submicron Gap Width", IEEE Trans. Magn., MAG-20, 5, pp. 957-959, 1984.

[73] R. W. Light, "Reactive Ion Etching of Aluminium/Silicon", J. Electrochem. Soc., Solid-State Science and Tech., Vol. 130, 11, pp. 2225-2230, 1983.

[74] B. J. Curtis, "Optical End-Point Detection for the Plasma Etching of Aluminium", Solid State Tech. Vol. 23, 4, pp. 129, 1980.

[75] E. S. Bulat, G. F. Doyle and B. Gelernt, "Optical Emission and Pressure Correlation During Plasma Etching", Semiconductor Int., Vol. 5, pp. 113-118, Nov. 1982.

[76] D. Webb, Ph.D. Thesis, Victoria University of Manchester, 1975.

[77] T. Tada, "Crosslinked Poly(2,2,2 - Trichlorethyl Methacrylate) as a Highly Sensitive Positive Electron Resist", J. Electrochem. Soc., Vol. 126, 9, pp. 1635-1636, 1979.

[78] E. D. Roberts and C. E. Fuller "A Positive-Working Cross-Linked Electron Resist with Improved Resistance to Plasma-Etching Processes", Proc. of Microcircuit Engineering, 83, pp. 297-304, 1983.

[79] A. D. Weiss, "Photoresist Technology Update", Semiconductor Int., Vol. 6, pp. 82-87, April 1983.

[80] R. G. Poulsen "Plasma Etching in Integrated Circuit Manufacture, A Review", J. Vac. Sci. Technol. Vol. 14, 1, pp. 266-274, 1977.

[81] G. Ronan and W. Clegg, "A Microprocessor-Based Cursor Measuring System", Laboratory Practice, Vol. 32, 2, pp. 74-76, 1983.

[82] W. F. Mohamad, Ph.D. Thesis, Victoria University of Manchester, 1980.

[83] H. L. Berkowitz and R. L. Lux, "Critical Edge Proximity Effect Corrections", Proc. 10th Int. Conf. on Electron and Ion Beam Science and Technol. pp. 261-265, 1982.

[84] P. L. Jones, Department of Electrical Engineering, University of Manchester, Private Communication, Sept. 1985.

[85] S. C. P. Lim, "Reduction of Hillock Formation in Aluminium Thin Films", Semiconductor Int., Vol. 5, pp. 135-145, April 1982.

[86] G. J. Zimmer, T. M. Morris and F. B. Humphrey, "Transient Bubble and Stripe Domain Configurations in Magnetic Garnet Materials", IEEE Trans. Magn., MAG-10, 5, pp. 651-654, 1974.

[87] T. M. Morris, G. J. Zimmer and F. B. Humphrey, "Dynamics of Hard Walls in Bubble Garnet Stripe Domains", J. Appl. Phys., 47, 2, pp. 721-726, 1976.

[88] L. J. Schwee, "Proposal on Cross-Tie Wall and Bloch Line Propagation in Thin Magnetic Films", IEEE Trans. Magn., MAG-8, 5, pp. 405-407, 1972.

[89] Y. Hidaka, K. Matsuyama and S. Konishi, "Experimental Confirmation of Fundamental Functions for a Novel Bloch Line Memory", IEEE Trans. Magn., MAG-19, 5, pp. 1841-1843, 1983.

[90] S. Konishi and Y. Hidaka, "1 Gbit/cm^2 High Density Solid State Magnetic Memory is Realised: Bloch Line Memory", Nikkei Electronics, No. 323, pp. 141-167, Aug. 1983 (In Japanese).

[91] Y. Hidaka and H. Matsutera, "Bloch Line Stabilisation in Stripe Domain Wall for Bloch Line Memory", IEEE Trans. Magn., MAG-20, 5, pp. 1135-1137, 1984.

[92] D. Klein and J. Engemann, "Bloch Line Memory: Dams for Stripe Domain Confinement", J. Appl. Phys., 58, 8, pp. 4071-4073 1985.

[93] J. C. Wu and F. B. Humphrey, "Operation of a VBL Memory Write Gate", To be published, IEEE Trans. Magn., MAG-21, 5, 1985.

[94] S. Konishi, K. Matsuyama and K. Narita, "Formation and Punch-Through of Horizontal Bloch Line in a Stripe Domain Wall", Jap. J. Appl. Phys., Vol. 18, 9, pp. 1855-1856, 1979.

[95] K. Matsuyama and S. Konishi, "Computer Simulation of Domain Wall and Vertical Bloch Line Motion in a Bubble Garnet Film", IEEE Trans. Magn., MAG-20, 5, pp. 1984.

[96] K. Matsuyama, H. Asada and S. Konishi, "Bloch Line Propagation in Straight Domain Walls", Digest of the 8th Japanese Conference on Magnetics, pp. 94, 1984 (In Japanese).

[97] K. Matsuyama, H. Asada and S. Konishi, "Computer Simulation of Vertical Bloch Line Propagation Around Stripe Domain Head", To be published, IEEE Trans. Magn., MAG-21, 5, 1985.

[98] S. Konishi, K. Matsuyama, I. Chida, S. Kubota, H. Kawahara and M. Ohbo, "Bloch Line Memory, An Approach to Gigabit Memory", IEEE Trans. Magn., MAG-20, 5, pp. 1129-1134, 1984.

[99] L. Arnaud and F. Boileau, "Stripe Domain Stablisation for Bloch Line Memory", To be published, J. de Physique, Sept. 1985.

[100] J. Engemann, J. Theile and J. Heidmann, "Domain Wall and Bloch Line Phenomena in (111) - and (110) - Orientated Garnets and its Application to Bloch Line Memory", To be published, J. de Physique, Sept. 1985.

[101] F. B. Humphrey and J. C. Wu, "Vertical Bloch Line Memory", To be published, IEEE Trans. Magn., MAG-21, 5, 1985.

[102] Y. Yonekura, T. Yanase, T. Majima and H. Watanabe, "Study on Less-Than-4μm-Period Permalloy Propagation Tracks using a New Narrow-Gap Delineation Technique", To be published, IEEE Trans. Magn., MAG-21, 5, 1985.

[103] D. Pierce, "Bubble Memories - Still a Powerful Option", New Electronics, Vol. 17, pp. 102-111, Nov. 13th, 1984.

[104] N. Williams, "The Adaptable Bubble", Systems International, pp. 92-93, May, 1984.

[105] N. Hayashi and H. Mikami, "Computer Simulation of Magnetic Bubble Domain Bloch Lines Motion", Jap. J. Appl. Phys., Vol. 19, pp. 295-306, Feb. 1980.

[106] B. MacNeal and F. Humphrey, "Horizontal Bloch Line Motion in Magnetic Bubble Materials", IEEE Trans. Mag., Vol. MAG-15, pp. 1272-1284, Sept. 1979.

[107] E. Fujita, H. Kawahara, S. Sakata, and S. Konishi, "Dynamic Behaviour of Plane Wall in Bubble Garnet Films (Computer Simulation)", IEEE Trans. Mag., Vol. MAG-20, pp. 1144-1146, Sept. 1984.

[108] J. C. Slonczewski, "Theory of Domain-Wall Motion in Magnetic Films and Platelets", J. Appl. Phys., Vol. 44, pp. 1759-1770, April 1973.

[109] D. Krumbholz, J. Heidmann and J. Engemann, "Domain Wall Dynamics in Orthorhombic Garnets", To be published, J. de Physique, Sept. 1985.

[110] F. Hagedorn, "Dynamic Conversion During Magnetic Bubble Domain Wall Motion", J. Appl. Phys., Vol. 45, pp. 3129-3140, July 1974.

[111] A. A. Thiele, "Applications of the Gyrocoupling Vector and Dissipation Dyadic in the Dynamics of Magnetic Domains", J. Appl. Phys., Vol. 45, pp. 377-393, Jan. 1974.

[112] J. C. Slonczewski, A. P. Malozemoff and O. Voegeli, "Statics and Dynamics of Bubbles Containing Bloch Lines", A.I.P. Conf. Proc., No. 10, pp. 458-477, 1973.

[113] S. Konishi, "Bubble Wall Structure and Dynamics", Jarect, Vol. 10, Recent Magnetics for Electronics, Ohmsha Limited and North-Holland Publishing Co., pp. 3-13, 1983.

[114] M. Ohbo and S. Konishi, "3-D Simulation of Stripe Domain Chopping", Digests of the 8th Japanese Conference on Magnetics, pp. 91, 1984 (In Japanese).

[115] E. Fujita, Y. Saegusa and S. Konishi, "3-D Simulation of Dynamic Bubble Collapse", Digests of the 8th Japanese Conf. on Magnetics, pp. 92, 1984 (In Japanese).

[116] A. H. Eschenfelder, "Magnetic Bubble Technology", Springer Series in Solid-State Sciences, 14, Chapter 6, Springer-Verlag, Berlin, Heidelberg, New York, 1981.